PHYSICAL AND NUMERICAL MODELING OF STEEL WIRE ROD FRACTURE DURING UPSETTING FOR COLD HEADING OPERATIONS

by

Nicholas Nickoletopoulos

Department of Mining and Metallurgical Engineering
McGill University
Montreal, Canada

A Thesis Submitted to the
Faculty of Graduate Studies and Research
in partial fulfillment of the requirements for the degree of
Doctor of Philosophy

February, 2001

0-612-70113-1

ABSTRACT

A comprehensive methodology to physically and numerically model upsetting in cold heading was developed.

The physical model was a Drop Weight Test with a guided pocket-die set capable of approximating industrial cold heading conditions. The results show that the test is sensitive to the critical parameters for cold heading. These include surface quality, residual element level, nitrogen content, microstructure, decarburization, and specimen geometry. The test is capable of assessing the fracture behavior of cold heading materials.

One goal of the study was to reveal differences in fracture behavior with varying steel sources. Accordingly, the matrix of test materials consisted of grade 1038 steels from three different steel sources.

Material preparation and conditioning of test materials approximated industrial procedures for cold heading materials. These procedures included hot rolling, controlled rod cooling, descaling, straightening, lime coating and lubricating, and wire drawing. Spheroidization of test specimens was performed in an industrial batch furnace using an industrial heat treatment cycle.

A finite element program (FEM) enabled the simulation of upsetting in cold heading. The inputs required to model the cold heading process include flow stress behavior and friction conditions representative of cold heading. These inputs were obtained using the CANMET Cam Plastometer and the Friction Ring Test.

The Cockcroft and Latham fracture constants for an as-rolled and a spheroidize annealed 1038 material were computed by FEM modeling and the critical values were calibrated using the Drop Weight Test. The fracture criterion constant was found to be independent of strain path for upsetting in cold heading and thus is material-related.

RÉSUMÉ

Nous avons mis au point une méthode pour simuler physiquement et numériquement l'écrasement d'un acier lors de la frappe à froid.

Nous avons effectué les simulations physiques à l'aide d'un essai représentatif de l'étape d'écrasement lors de la frappe à froid. Nos résultats montrent que l'essai sait reconnaître les paramètres qui dictent la performance des matériaux à la frappe, soit l'état de surface, le niveau des elements résiduels, la teneur en azote, la microstructure, la cote de décarburisation, et enfin, la géométrie de l'éprouvette. L'essai permet, en particulier, de chiffrer les déformations à la rupture des matériaux destinés à la frappe à froid.

Un des buts de l'étude était de faire ressortir le comportement des matériaux à la frappe en fonction du schéma d'élaboration des aciers. Nous avons utilisé des matériaux en provenance de trois aciéries, en l'occurrence, des aciers de nuance 1038.

Lors de la préparation de nos échantillons, nous avons pris soin de suivre de près les opérations annexes à la frappe à froid : laminage à chaud du fil machine, refroidissement contrôlé, décapage, rectification, dépôt d'une couche d'apprêt poreuse, adjonction de lubrifiants complémentaires, et enfin, tréfilage. Nous avons ensuite effectué un traitement de globularisation des carbures à l'aide d'un cycle utilisé couramment dans un four industriel.

Un programme d'éléments finis (EF) a été utilisé pour simuler l'écoulement plastique en forgeage axisymétrique. Les données requises pour une simulation comprennent la loi d'écoulement plastique du matériau ainsi que le coefficient de frottement entre la matrice et la pièce à déformer. Les courbes d'écoulement ont été générées à partir d'un plastomètre à came, tandis que le coefficient de frottement a été determiné par l'essai de l'anneau.

La simulation par EF a permis de calculer l'évolution du paramètre d'endommagement de Cockcroft et Latham pour des aciers bruts de laminage et des aciers à structure globularisée. Les valeurs critiques du paramètre ont été étalonnées par des essais d'écrasement. La valeur du paramètre est constante pour un matériau donné, et est indépendante du parcours de déformation.

ACKNOWLEDGEMENTS

I thank Dr. Michel Hone for his friendship, support and patience. Dr. Hone's dedication to higher learning and excellence was an inspiration to me. Dr. Priti Wanjara for her friendship, advice, and laboratory assistance were invaluable.

Ivaco Rolling Mills provided me with the generous opportunity to pursue my goals. I thank the Rod Mill Production personnel who scheduled trial rollings for this work. The assistance of the Quality Assurance personnel was much appreciated.

I express my gratitude to my thesis supervisors, Professors John J. Jonas, James Nemes and Steve Yue, for their support and guidance. Special thanks go to Professor Yves Verreman for his valued dedication to the project, and to Professor André Laplante for his inspirational teaching during my undergraduate years.

Thanks to Darryl Seaman, Dr. Don Baragar, Lorraine Mello, John Tsekeris, Edwin Fernandez, George Dedic and George Tewfik for their hard work, to Transvalor for the use of the Forge2 software.

On a personal level I thank my parents, siblings, and extended family for their unconditional love and support. Finally, I thank my wife Paula for her love, encouragement, and the sacrifices she made for the realization of this project.

TABLE OF CONTENTS

LIST OF FIGURES

Chapter 2

Chapter 4

Chapter 5

Chapter 6

Chapter 7

List of Tables

Chapter 4

Chapter 6

Appendix A

List of Symbols

α	$d\varepsilon_z/d\varepsilon_\theta$ = strain path slope
α^{l}	friction parameter
β	temperature coefficient
ε_o	strain hardening regulation term ~ 0.0001
ε	strain
$\dot{\varepsilon}_{eq}$	equivalent strain rate[s^{-1}]
$\dot{\varepsilon}$	strain rate [s^{-1}]
ε_θ	circumferential strain
ε_{eq}	equivalent strain = $f[\varepsilon_\theta, \varepsilon_r, \varepsilon_z]$ – von Mises
$\varepsilon_{eq.f.}$	equivalent strain to fracture
ε_r	radial strain
$\{\dot{\varepsilon}\}$	strain rate tensor
ε_z	axial strain
η	constant that penalizes volumetric strain rate
θ_m	total angle subtended by cam lobe [degrees]
θ	angle from the start of the cam lobe [degrees]
κ	consistency [MPa]
ξ	constant true strain rate [s^{-1}]
ρ	density [kgm^{-3}]
σ	stress [MPa]
σ_θ	circumferential stress [MPa]
σ_r	radial stress [MPa]
σ_z	axial stress [MPa]
σ_I	maximum principal tensile stress [MPa]
σ_{eq}	equivalent stress = $f[\sigma_\theta, \sigma_r, \sigma_z]$ – von Mises [MPa]
σ_m	hydrostatic stress = $[\sigma_\theta+\sigma_r+\sigma_z]/3$ [MPa]
σ_{cal}	stress calculated by Norton-Hoff relation [MPa]
σ_{exp}	stress from CP testing [MPa]
τ_s	interface shear stress [MPa]
ω	speed of cam rotation [degrees/s]
Ω	volume of the domain occupied by the body at a given time t
a	acceleration [ms^{-2}]
A	Oyane fracture criterion constant
B	Oyane fracture criterion constant
C	Cockcroft and Latham fracture criterion constant [MPa]
C_p	heat capacity [$Jkg^{-1}K^{-1}$]
D	final diameter [mm]
D_o	initial diameter [mm]
E_{DWT}	energy of DWT experiment [J]
E_{SP}	energy absorbed by the test specimen [J]

E_{BASE}	energy absorbed by the base and floor [J]
E_{LOST}	energy lost as heat, friction, and noise [J]
F	force [N]
F_{DWT}	force measured from DWT experiment [oscilloscope] [N]
F_{SP}	resistive force of the test specimen [N]
F_{BASE}	resistive force of the base and floor [machine compliance] [N]
g	gravitational pull = 9.81 ms^{-2}
h	final gauge height [mm]
h_o	initial gauge height [mm]
H	final height [mm]
H_o	initial height [mm]
ΔH	change in specimen height in time [mm]
ΔH_{final}	total change in specimen height [mm]
J	Johnson-Cook constant
K	strength coefficient
K_o	strength coefficient
L	specimen length [mm]
L_o	initial specimen length [mm]
m	strain rate sensitivity
$\overline{m}$	shear friction factor
M	mass [kg]
n	work hardening coefficient
N	number of data points
P	velocity factor
r	cam radius at any point [mm]
r_o	base radius of the cam [mm]
R_i	inner radius [mm]
$R_{i,f}$	final inner radius [mm]
R_o	outer radius [mm]
R_n	neutral radius [mm]
R_{actual}	barrel-corrected radius in time [mm]
R_{final}	final radius measured on specimen [mm]
$R_{th,final}$	final theoretical radius for no barreling [mm]
R_{th}	theoretical radius for no barreling in time [mm]
S	displacement [mm]
S_o	initial displacement [mm]
S_f	final displacement [mm]
S	distance between micro-switches [m]
S_{data}	final DWT specimen displacement [mm]
S_{final}	displacement at end of DWT test or FEM simulation [mm]
S_{DWT}	displacement from DWT experiment [mm]
S_{SP}	displacement of the test specimen [mm]
S_{BASE}	displacement of the base and floor (machine compliance) [mm]
S_c	the contact surface of the domain occupied by the body at a given time t
$\{s\}$	deviatoric stress tensor

t	time [s]
t_f	time for complete deformation [s]
t_s	time between signals [s]
T	temperature [°C]
T_m	melting temperature [K]
T_r	reference temperature [K]
v	velocity [ms^{-1}]
v_i	initial crosshead velocity [ms^{-1}]
v_o	crosshead velocity at impact [ms^{-1}]
V	tangential velocity (metal minus die)
w	final gauge width [mm]
w_o	initial gauge width [mm]
W	final width [mm]
W_o	initial width [mm]
W_{strain}	strain energy [J]
$\dot{W}_{total}$	total power [J/s]
$\dot{W}_{friction}$	friction power [J/s]
Y	material yield stress in shear [MPa]

CHAPTER 1

INTRODUCTION

Cold heading is a forging operation that is performed without an external heat source. The operation involves a force being applied to the free end of a metal workpiece contained between a die and a punch. The force is applied by one or several blows of the punch and it displaces (upsets) the metal to form a pre-determined contour [Upsetting, 1988; Davis, 1988].

Cold heading is used to produce a variety of fasteners such as bolts, rivets and nuts. The automotive, construction, aerospace, railway, mining and electrical product sectors are the major consumers [Barrett, 1997]. The ability to assess the formability of cold heading materials to model the cold heading process is of great importance since failures result in equipment downtime, material waste and the possibility of a very costly product recall. However, it is difficult to quantitatively define the ability of a material to be cold headed [Sowerby et al., 1984]. The forming process involves an interplay between material structure, temperature, deformation rate, tool and workpiece geometry, and friction at the interface of tool and workpiece [Sowerby et al., 1984]. Other critical factors include the surface quality of the workpiece and the amount of cold work (pre-draw) performed on the workpiece prior to cold heading [Muzak et al., 1996; Turner et al., 1984; Maheshwari et al., 1978].

Conventional testing methods employed for determining the formability of cold heading materials include the tensile test and the simple compression (upset) test. These methods allow comparisons between various materials, as well as surface quality assessment. However, they do not accurately simulate the cold heading process in terms of factors such as stress and displacement boundary conditions, strain rate, and workpiece temperature [Nickoletopoulos et al., 2000; Kurko, 1998].

This thesis is divided into the following chapters: Chapter 2 presents a literature review of cold heading, including a description of different types of cold heading operations, wire rod material requirements and cold heading parameters that affect cold heading. This chapter also examines types of defects common in cold heading, as well as conventional tests used to evaluate cold headability of materials, ductility criteria, shear banding, and constitutive modeling.

Chapter 3 presents the objectives of this thesis. Chapter 4 explains the design of the matrix of test materials, and details conditioning and characterization of these materials. Chapter 5 gives a detailed description of the methods used in this work - the Cam Plastometer (CP), the Drop Weight Test (DWT), the Friction Ring Test (FRT), and the Finite Element Method (FEM). Chapter 6 presents the experimental results, and these are discussed in Chapter 7. Conclusions of the thesis are presented in Chapter 8. Recommendations for future work and contributions to original knowledge follow Chapter 8.

CHAPTER 2

LITERATURE REVIEW

2.1 Heading Operations

Cold heading can involve several types of operations [National Machinery Co. 1997; Dove, 1989B]. The most common of these is the heading operation, also refered to as upsetting (Figure 2.1a). Other operations include forward and backward extrusion (Figures 2.1b and 2.1c), in which the workpiece is formed by forcing the metal to flow plastically through a die orifice. In forward extrusion, the die and punch are at opposite ends of the extrusion stock, and the product and punch travel in the same direction. In backward extrusion, product and punch travel in opposite directions.

Trimming is sometimes employed in cold heading machines for the removal of possible surface defects or for final sizing on the head itself (Figure 2.1d). Piercing is mainly used for shearing or punching holes or slots for the production of rivets and nuts (Figure 2.1e).

Many of the concepts discussed in this thesis are valid for both heading and extrusion. However, special emphasis is placed on the heading operation itself, particularly when dealing with ductile fracture criteria.

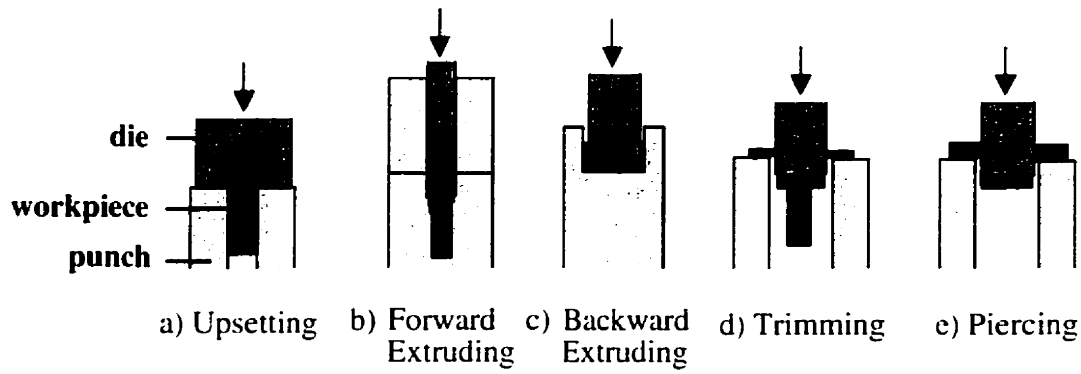

Figure 2.1 Cold heading manufacturing operations.

2.2 Rod Wire Material Requirements

There are many factors to consider for the study of cold heading. These factors and their interaction must be considered in the interpretation of the results to test the validity of a cold heading test.

There are two sets of requirements for cold heading quality materials. One set speaks to the properties necessary for cold forming operations that require a material that has 'good' cold headability [Maheshwari et al., 1978]. The other set addresses the properties relating to product specifications which differ according to product end use [Matsunaga and Shiwaku, 1980].

2.2.1 Surface

The workability of wire rod in industrial cold heading operations can be influenced by the presence of longitudinal and transverse surface defects [Joffret and Perrier, 1996; Jenner and Dodd, 1981]. It is believed by many researchers [Maheshwari et al., 1978; Matsunaga and Shiwaku, 1980; Jenner and Dodd, 1981; Thomason, 1990A] that these surface defects act as circumferential stress raisers, thereby reducing the formability and allowing the material to fracture on the equatorial surface during heading operations. Turner et al. [1984] speculated that the acuity of a surface notch decreases with equatorial expansion during heading, and therefore question the role of surface defects as stress raisers. Instead, they concluded that surface defects are strain discontinuities that may lead to localization of fracture on the equatorial surface of the upset.

Surface defects typically arise during billet casting operations, wire rod rolling and cooling operations, and coil handling. The most common of these include billet seams (Figure 2.2a), rolling laps (Figure 2.2b), slivers, and mechanical abrasions.

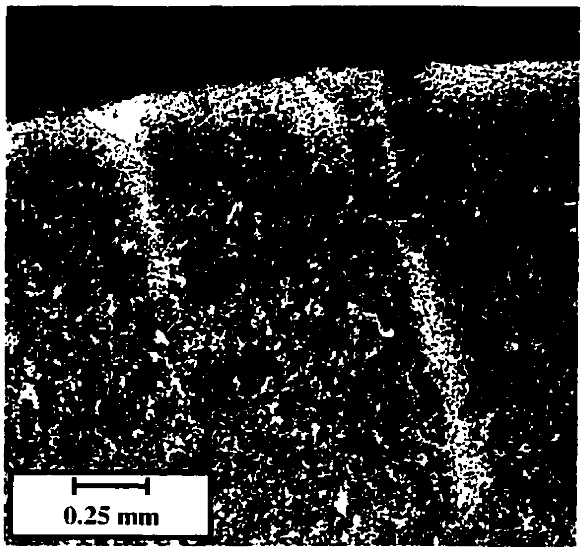

Figure 2.2a Billet seam (9% depth).

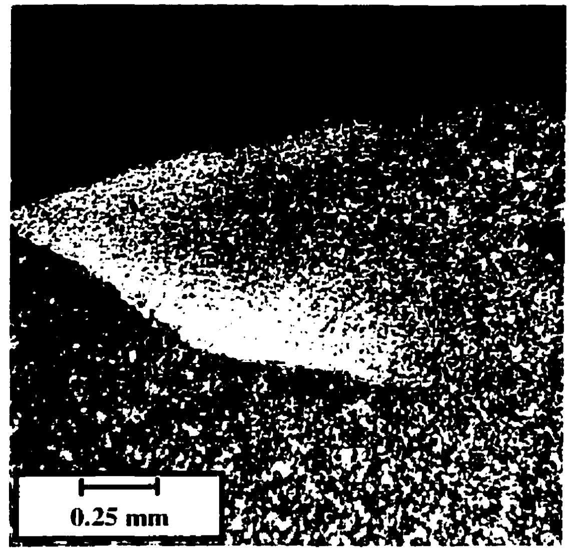

Figure 2.2b Rolling lap (7% depth).

Material destined for cold heading applications should never contain any type of surface defect. Through the use of surface billet conditioning, hot eddy-current testing and visual inspection, all wire rod destined for cold heading applications should possess surface integrity. Although this is not always the case, for the purpose of this thesis, it is assumed that test materials are free of surface defects, unless otherwise stated.

2.2.2 Cleanliness

Heavy silicate, sulphide, alumina and globular oxide inclusions are unacceptable for cold heading quality material [Maheshwari et al., 1978]. These act as stress raisers and can promote microvoid nucleation, growth and coalescence leading to ductile fracture [Thomason, 1990B].

The primary method of controlling the quantity of non-metallic inclusions is by sound steelmaking practice, controlled raw material selection, and the addition of deoxidizers such as silicon or aluminum in the ladle.

There are standards (i.e. ASTM E45 [1997]) that define cleanliness in cold heading materials. The cleanliness of the test materials used in this work is representative of such materials. Cleanliness ratings for these materials are presented in Chapter 5.

2.2.3 Chemical Composition

Chemical composition affects the ductility of cold heading materials. Raising the carbon content increases yield strength but adversely affects impact and toughness properties of the final product as well as the tool life of heading equipment [Maheshwari et al., 1978]. Higher carbon (0.30-0.40%) material is also more susceptible to surface decarburization during billet reheating and rod spheroidize annealing operations.

It is common practice to employ lower carbon materials (as low as 0.10%) in cold heading applications. A balance must be found in terms of strength and ductility for particular applications. Strength may be achieved through subsequent quench and temper operations on the cold headed product.

The properties of carbon and alloy steels can be adversely affected by residual elements (copper, nickel, chromium, molybdenum, tin) in steel produced by recycling scrap [Yalamanchili et al., 1999]. Residuals increase material hardness and decrease ductility [Matsunaga and Shiwaku, 1980]. Common industrial practice is to control copper to roughly below 0.15%, nickel and chromium to below 0.10%, molybdenum to below 0.02% and tin to below 0.01%. The sum of these residuals should not exceed 0.25% for optimal headability. On the other hand, additions of nickel, chromium and molybdenum are used where enhanced toughness and hardenability are required.

Nitrogen must also be controlled. Free nitrogen is a major contributor to the embrittlement of ferrite and strain aging, which in turn can lead to head bursts, shear cracking, and increased machine wear [Cao et al., 1998]. Matsunaga and Shiwaku [1980] stated that free nitrogen results in increased hardness and poor response to heat treatment and has a negative impact on the ductility of cold heading materials.

The matrix of materials used in this thesis was designed to assess the sensitivity of the cold heading test by varying the amounts of the residual elements (i.e. copper, chromium) and nitrogen. However, the objective of this work was to develop a test for evaluating cold headability, not to perform an in-depth study of the effect of residual elements or nitrogen.

2.2.4 Microstructure

The microstructure of cold heading material comprises a ferrite matrix with varying amounts of lamellar pearlite (Figure 2.3 – grade 8650). This microstructure resists deformation due to the fine lamellar carbides (Fe_3C) that subdivide the ferrite.

A spheroidize annealed (Figure 2.4 – grade 8650) microstructure is often desired in cold heading materials, particularly with low alloy and medium carbon steels [Samuels, 1980; Blake, 1986]. Spheroidal carbide particles are evenly dispersed in the ferrite matrix, resulting in a tougher and more ductile microstructure [Muzak et al., 1996]. This microstructure may also be required in low carbon cold heading materials, particularly for elaborate geometries [Matsunaga and Shiwaku, 1980].

Industrial spheroidize annealing is performed in batch or continuous furnaces with a non-oxidizing atmosphere to prevent surface decarburization and the formation of heavy oxide scale. This involves heating below the lower critical temperature (1340 F / 725°C) for a time sufficient to produce the correct amount of spheroidization [Samuels, 1980 and 1988.]. The full operation requires approximately 24 hours and represents about 15 percent of the total cost of producing a fastener.

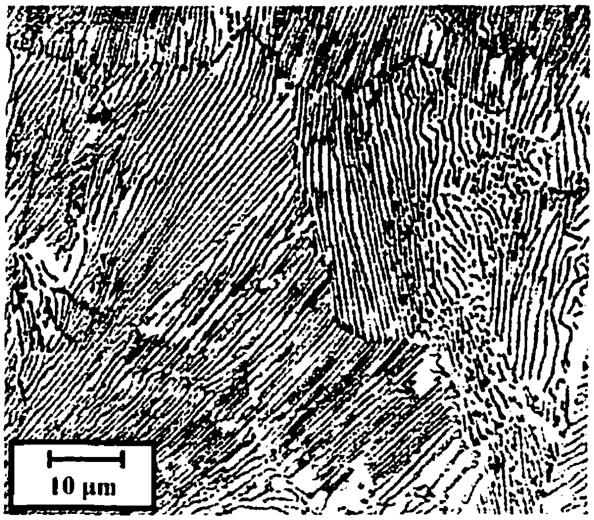

Figure 2.3 Lamellar carbide.

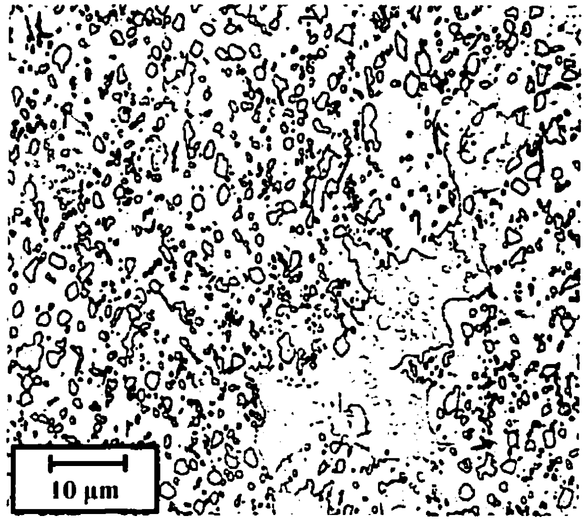

Figure 2.4 Spheroidal carbide.

The laws of thermodynamics dictate that there will always be a drive to reduce the energy of a microstructure. One way to achieve this is by reducing the interfacial area between matrix and second phases. The shape that has the minimum surface area per unit volume is the sphere. As such, the particles of a phase are driven to adopt a spherical shape. In addition, these spheres will try to grow as large as possible by consuming smaller spheres, which are of higher surface area per unit volume. The net result is a reduction in surface energy per unit volume [Samuels, 1980].

To understand the role of microstructure the materials used in this thesis were tested in both the as-rolled pearlite and spheroidize annealed conditions.

2.2.5 Decarburization

Surface decarburization is another parameter that must be controlled for cold heading quality materials, particularly those in the medium to higher carbon ranges (0.20-0.40%). Decarburization results when the reheat furnace atmosphere reacts with carbon in the steel billet. Wire rod decarburization can also result during spheroidize annealing. In the absence of carbon, the surface material is softer, and provides more ductility for the heading operation. However, subsequent threading as well as quench and temper operations will be jeopardized since the free ferrite can no longer be hardened to the desired final product specification.

The extent to which the zone is depleted of carbon is defined according to industry standards such as ASTM E1077 [1997] and IFI 140 [1993]. Decarburization evaluations presented in Chapter 4 show that test materials used in this thesis meet industry standards, except for one case where the material was purposely decarburized.

2.3 Cold Heading Parameters

Process parameters can also have a large influence on the cold heading operation. In particular, strain rate and temperature during deformation, pre-draw prior to cold heading, and lubrication between die and workpiece must be accounted for in developing a practical cold heading model.

2.3.1 Strain Rate and Temperature

Cold heading is a high-rate deformation process, with overall strain rates in the range 100-200 s^{-1} [Yoo et al., 1997]. Cescutti [1986] reports local equivalent strain rates between 400 and 3000 s^{-1} during cold heading. Mechanical properties, such as strength and ductility, may vary with strain rate. Therefore, it is necessary to determine these properties close to the deformation rates observed during cold heading [Follansbee, 1989]. It is well known that at constant temperature, the flow stress increases with increasing strain rate [Dieter, 1984A]. However, many metals exhibit a decrease in the stress for plastic deformation with increasing strain (flow softening behavior) at high temperatures [Thirukkonda et al., 1994].

Deformation during cold heading is essentially adiabatic. The flow stress decreases with increasing temperature and hence promotes instability since the more deformed regions are softened to a greater extent by the deformation heat [El-Magd et al., 1997]. Hartley et al.

[1986] have shown and Osakada [1989] has stated that the workpiece temperature may increase by as much as 400°C during the heading operation. In certain cases, local temperatures, particularly in the base region of headed components, can exceed the transformation temperature A_{c1} (723°C) when shear bands form. Section 2.7 of this chapter provides a description of this phenomenon.

The equation $\sigma = K\varepsilon^n\dot{\varepsilon}^m$ is one of many available to describe the flow stress of a material (see for example Wagoner and Chenot, 1996). Here, K is the strength coefficient, ε is the strain, $\dot{\varepsilon}$ is the strain rate, n is the work hardening coefficient, and m is the strain rate sensitivity.

The effects of strain rate and temperature are taken into account in the experimental testing of the materials, as well as in the determination of flow stress data.

2.3.2 Pre-draw

A pre-draw operation serves to increase the ductility of the material [Sarruf et al., 1998], to strengthen less-worked portions of a headed product (i.e. the shaft), and to improve the surface finish of the final product [Davis, 1988].

Material ductility is a strain-history dependent parameter. Many researchers have demonstrated that wire drawing following a process anneal operation can increase material ductility for subsequent operations [Jenner and Dodd, 1981]. In particular, a pre-draw of 35% reduction-of-area through dies with included angles in the range of 12-20° improves the cold-headability of steel [Jenner and Dodd, 1981].

All test materials received a pre-draw of approximately 10%. The intent was not to determine the effect of the pre-draw, but to simulate as accurately as possible the procedures employed in industrial cold heading.

2.3.3 Lubrication

Approximately 50% of the deformation energy required for cold heading is dissipated in friction [Turner et al., 1984]. Friction results from relative motion between metal surfaces are not smooth and not perfectly lubricated [Dieter, 1984A]. The friction increases the deformation force, which in turn increases the propensity for fracture [Dieter, 1984A].

Friction at the die-workpiece interface may result in non-uniform or localized plastic deformation and surface bulging (Figure 2.5). Surface bulging generates secondary tensile stresses that result in longitudinal cracking or plastic instability (flow localization) at the equatorial surface of the workpiece [Semiatin and Jonas, 1984]. Flow localization may also manifest itself in regions of intense shear bands and lead to shear cracks [Dieter, 1984A]. Bulge severity is proportional to friction and inversely proportional to specimen aspect (height/diameter) ratio [Latham et al., 1968A, 1968B; Nguyen, 1984; Sarruf et al., 1998].

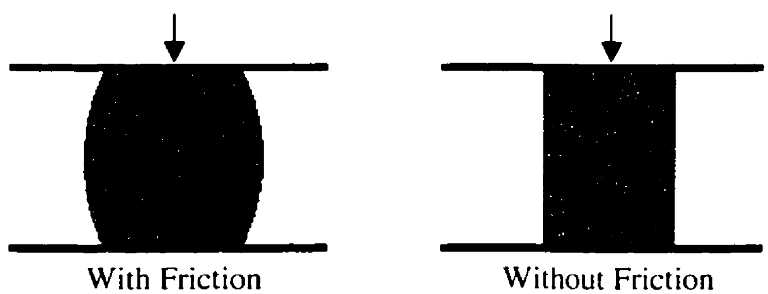

Figure 2.5 Simple compression of cylindrical specimen.

The punch force, F, multiplied by its velocity, v, yields strain power, $\dot{W}_{strain}$, as given by:

$$Fv = \dot{W}_{strain} + \dot{W}_{friction} \qquad (2.1)$$

If a frictional power term is introduced, then the right-hand side of the equation is increased since the strain power remains constant. As a result, Fv must also increase. Since v is constant, this can only be accomplished by increasing the force of the punch, F, which in turn increases die stresses. Thus, a benefit of proper lubrication is improved die longevity.

In the context of this thesis, friction is taken into consideration in finite element method simulations using experimentally determined friction values.

2.4 Typical Fastener Defects

Two types of surface defects are commonly found on the surface of cold headed products. The first is the longitudinal defect (Figure 2.6), which originates in the billet casting or wire rod rolling operation (i.e. seams, laps).

Longitudinal defects are parallel to the axis of the product and can run the full length. This defect can be revealed with an eddy current tester during rolling, by simple compression testing, or with an acid pickle test. These defects can also be due to the exhaustion of material ductility and that the plastic limit of the material has been exceeded [Levaillant,1986].

Oblique defects (Figure 2.7) are typically characterized by a 45° shear crack in the upset portion. The presence of such a defect is indicative of localization due to flow softening. Flow softening in turn may be caused by such factors as deformation heating, high friction, and die misalignment. As such, shear cracks are only possible when there is negative work hardening.

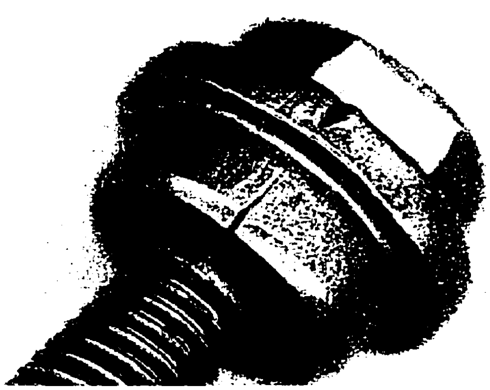

Figure 2.6 Longitudinal defect.

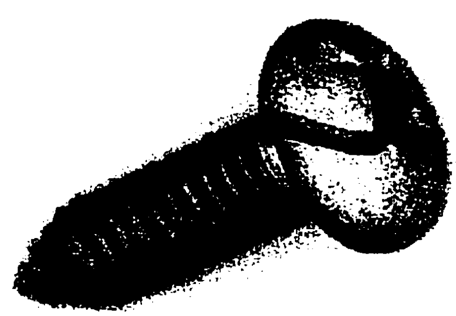

Figure 2.7 Oblique (shear) defect.

Okamoto et al. [1973] developed a classification system for cracks found in cold forging operations. External longitudinal and shear cracks (Figures 2.6 and 2.7) were classified as alpha (α)-type cracks. A crack occurring at the boundary between the top and bottom dead metal (i.e. the axial centerline) was identified as a theta (θ)-type. This internal defect is caused by excessive upsetting. It results in the splitting of fastener heads due the presence of microscopic cracks. More recent work by Bai and Dodd [1992] has shown that this type of defect is closely related to adiabatic shear banding.

Although theta-type cracks are of concern to the cold heading industry, the primary focus of this thesis is the alpha-type crack.

Most researchers have focused their efforts on the effect of gross seam or lap-like defects. Little work has been performed regarding near-surface defects due to casting inhomogeneities and microscopic surface imperfections such as pitting (due to weathering) and die scratches. These are the most prevalent defects. One of the test matrix materials has been selected to test the sensitivity of upsetting in cold heading to such defects.

2.5 Mechanical Tests

Workability measures material ductility under the particular imposed stress system. Cockcroft and Latham [1968] proposed a theory that workability is a function of material and process variables. For a test to be representative of the cold heading process, it is imperative that all material and process variables be accounted for.

Conventional laboratory tests (i.e. tensile test, simple compression) have two primary weaknesses with regard to obtaining reliable ductility parameters for cold upsetting. The first is that the strain rates are not representative of the cold heading process [Turner et al., 1984]. Also, the variations in a heat or a particular coil obliges one to perform a large number of tests to establish statistically significant results.

2.5.1 Tensile Test

The tensile test is commonly employed to evaluate cold heading materials, and offers several advantages: well-established stress state, relatively low cost, and ease of use. Tensile testing is usually conducted at low strain rates (10^{-2} to 10^{-4} s^{-1}). It is capable of providing mechanical properties such as yield and tensile strengths, as well as ductility parameters such as elongation and reduction of area. Elongation is dominated by the uniform elongation, which increases with the strain hardening capacity of the material [Dieter, 1984B]. Initially, the stress-state during tensile testing is simple uniaxial tension. Once necking begins, the stress system changes: a component of hydrostatic tensile stress is added to the axial stress [Cockcroft and Latham, 1968]. The probability of fracture is greater as the neck becomes deeper since the hydrostatic tensile stress increases.

Indeed, Dieter [1961A] stated that the tensile strength value is of use for only very restrictive conditions of tensile loading. Bhatnagar [1978] affirmed that the tensile test for assessing cold heading materials suffers from the disadvantage that, after some strain, the specimen necks and fails prematurely.

Work by Ollilainen [1995] showed that there are major limitations in the prediction of flow stress using the tensile test at very high strain rates, and also when there are very large strains ($\varepsilon > 1$). Hosford and Caddell [1983A] stated that bulk formability does not correlate well with tensile ductility, particularly when fracture initiates at a surface. Osakada [1989] stated that it is difficult to predict fracture using material property data since it is not expressed in terms of energy.

Olsson et al. [1986] stated that the tensile test is not suitable for the characterization of cold forging ductility because fracture in tensile testing does not initiate at the surface as in cold forging; the stress and strain states at the crack initiation site are different. Turner et al. [1984] concluded that there is no direct correlation between tensile properties and the upset ductility of cold heading quality materials.

2.5.2 Simple Compression Test

The simple compression test involves compressing a cylindrical wire rod workpiece between parallel dies and circumvents the necking problem associated with tensile testing. The test is employed to obtain flow stress as a function of strain and to estimate the headability of cold heading quality materials. However, the frictional effects at the interface between the dies and the workpiece can lead to barreling (Figure 2.8).

The severity of bulging increases with increasing friction and with decreasing specimen aspect (height/diameter) ratio. In order to avoid buckling, the aspect ratio should generally be kept below two [Lee and Kuhn, 1984]. The lower limit is usually in the range 0.75-1.75, and is based on a height suitable for the application of grid marks.

Strain measurements (Figure 2.8) can be made by measuring the spacing between grid marks, which are placed on the equatorial surface where cracks are usually observed. Alternatively, a critical value of $\Delta h/h$ may be determined through upset testing. The critical strain measurements can be determined through finite element modeling of the upset test. Such a procedure could be more accurate than the grid mark method if the finite element model and its inputs (i.e. flow curve data, friction conditions) are representative of the test conditions and the material. This is the procedure used in this work.

The following relationships [Lee and Kuhn, 1973] can be used in upset testing:

$$\varepsilon_Z = \text{global axial strain} = \ln\left(\frac{H}{H_o}\right) \quad (2.2)$$

$$\varepsilon_\theta = \text{global hoop strain} = \ln\left(\frac{W}{W_o}\right) = \ln\left(\frac{D}{D_o}\right) \quad (2.3)$$

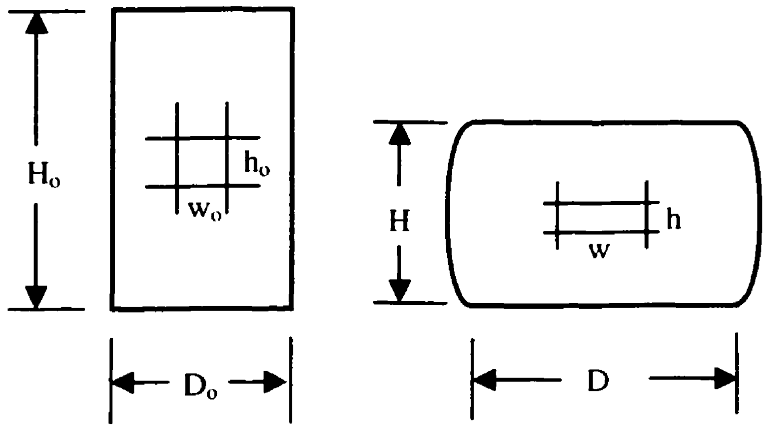

Figure 2.8 Strain measurement grids [Dieter, 1984A].

Here, h_o and h represent the initial and final gauge heights, respectively, w_o and w represent the initial and final gauge widths, and D_o and D represent the initial and final workpiece diameters. Since the radial surface stresses are zero, the axial (compressive) and hoop (circumferential tensile) stresses can then be determined from the Levy-Mises stress-strain relations [Kudo et al., 1968]. It has been shown in laboratory compression tests by Kudo et al. [1968], and through the use of neutron diffraction [Nickoletopoulos et al., 2000; Rogge et al., 2000], that the circumferential strain is uniform around the circumference of the barreled surface.

Stress-strain conditions can be tested by varying the aspect ratio and friction conditions for a given material at a particular strain rate and temperature. The strain paths followed during testing are solely a function of the process parameters, and the point where the fracture line crosses the ordinate is representative of material ductility. It has been shown by Lee and Kuhn [1973, 1984], Shah [1974], and Kuhn [1978] that such a diagram (Figure 2.9) may be constructed by plotting the hoop strain, ε_θ, versus the axial strain, ε_z, and by joining all the fracture points. Cylindrical compression test data usually fit a straight line with a slope of one-half for all materials. For frictionless homogeneous compression, where no bulging occurs, test data are parallel to the strain path, and therefore no fracture can occur in ductile steels. Only strain paths that deviate (curve upward) away from the frictionless compression line will cross the fracture locus and result in fracture. The height of the fracture line and the point of contact on the ordinate (ε_θ) change with material and process conditions.

Shabaik et al. [1993] found that the single slope fracture locus was not always valid. Their results show that as the aspect ratio changes, a dual slope fracture locus is encountered with many materials tested at room and elevated temperatures.

Shah and Kuhn [1986], Kuhn [1978], and Shah [1974] also found that lower friction values and higher aspect ratios decrease bulge curvature and the degree of non-uniformity, thereby delaying fracture. With increasing friction and decreasing aspect ratio, the strain path rotates clockwise, thus increasing the negative slope ($d\varepsilon_\theta/d\varepsilon_z$) [Kuhn, 1978].

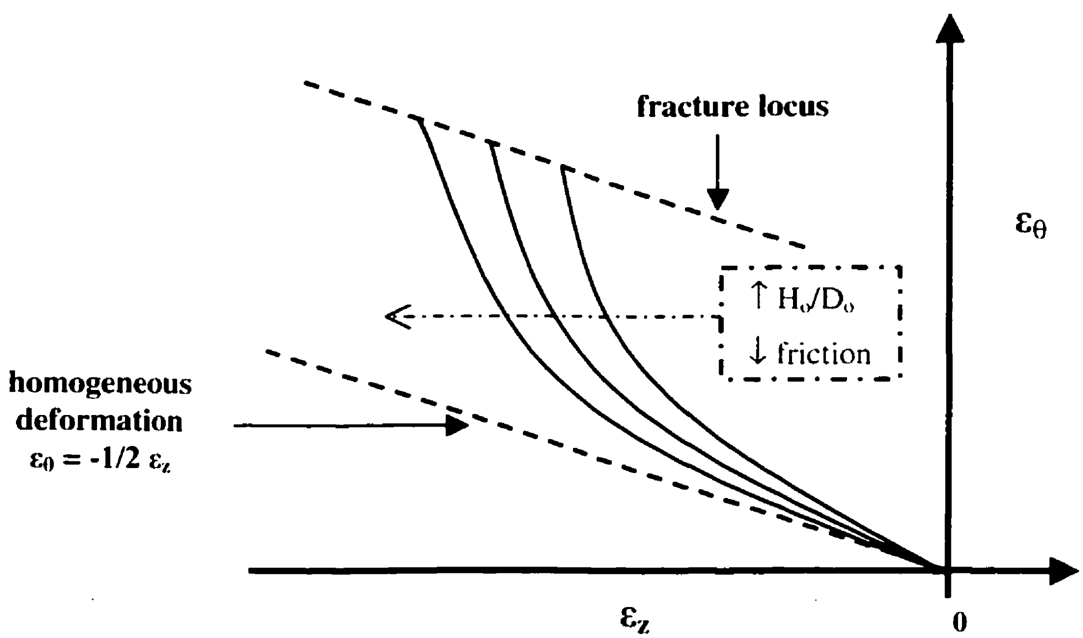

Figure 2.9 Fracture limit diagram for the grooved-die compression test.

During the start of compressive deformation, the deformation is homogeneous and $d\varepsilon_\theta = d\varepsilon_r$. The constant volume ($d\varepsilon_\theta + d\varepsilon_r + d\varepsilon_z = 0$) relation may therefore be expressed as $2d\varepsilon_\theta + d\varepsilon_z = 0$.

From this,

$$\frac{d\varepsilon_z}{d\varepsilon_\theta} = -2 \tag{2.4}$$

After appreciable deformation, $\varepsilon_\theta \to \infty$, and the deformation becomes inhomogeneous. The result is that the ratio $d\varepsilon_z/d\varepsilon_\theta$ approaches zero. Therefore, from the onset of compressive deformation, the following relation is true [Darvas, 1984]:

$$-2 \leq \frac{d\varepsilon_z}{d\varepsilon_\theta} < 0 \tag{2.5}$$

Although the forming limit diagram is a valuable tool for the study of ductile fracture during upsetting, it is difficult to apply to other geometries.

Shabara et al. [1996] show that existing ductile fracture criteria, such as the Cockcroft and Latham and Oyane criteria (see section 2.6.3), may be expressed exclusively in terms of the negative slope ($d\varepsilon_z/d\varepsilon_\theta$) in the case where finite element methods are not accessible, or when a more explicit mathematical analysis is desired.

One major setback of the simple compression test is the difficulty in producing cracks on the surface due to the small strains that can be achieved. There have been several efforts to increase the tensile hoop strain in compression tests through various workpiece and test designs [Shivpuri et al., 1988A, 1988B]. One of these is the collared cylinder (Figure 2.10) design proposed by Sowerby et al. [1984]. The collar eliminated the need for a surface grid since the axial and circumferential strains can be obtained by measuring its diameter and thickness. This design was found to be successful in increasing the hoop strains at the equatorial surface. However the workpiece geometry is altered, thereby changing the process conditions [Shivpuri et al., 1988A, 1988B].

Shivpuri et al. [1988A, 1988B] proposed another design that employs concentric grooves (Figure 2.11) at the die-workpiece interface. Differing die relief angles eliminate variability at this boundary. They concluded that sticking friction results in the development of high circumferential tensile stresses, thus rendering this test very sensitive to inherent surface defects. Sticking friction conditions may be a positive aspect of this test since many cold heading operations are performed under such conditions (closed-die upsetting), particularly when the aspect ratio exceeds buckling limitations.

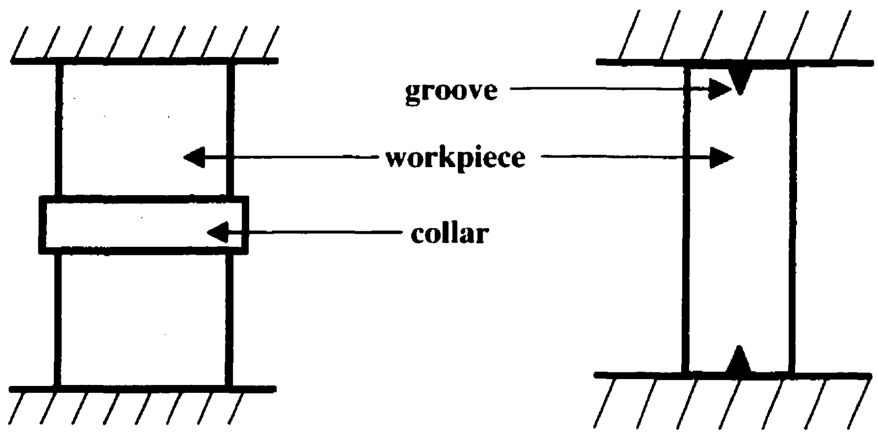

Figure 2.10 Collar test. **Figure 2.11 Grooved-die design.**

The test for the initiation of cracking is visual in these methods and therefore subjective [Woodall and Schey, 1978]. In addition, it is difficult to reproduce the stress-strain conditions, the strain rates and the temperatures observed in industrial cold heading [Muzak et al., 1996]. Furthermore, the assumption that the maximum strain is located on the equatorial surface is not valid, as indicated by finite element modeling of the heading operation by Kobayashi et al. [1989] and Verreman et al. [2000]. Hence, a fracture criterion based solely on surface stress or strain state may not be appropriate for upsetting.

Compression testing can be used to compare various cold heading materials [Sowerby et al., 1984] and to generate a ductile fracture criterion for upsetting at a given strain rate and initial temperature. It may also be employed to acquire flow stress data at low strain rates.

Non-instrumented compression testing is commonly employed on a production basis to reveal surface defects on wire rod.

In fact, low strain rate compressive MTS testing and high strain rate cam plastometer testing was performed on many of the matrix materials used in this work.

2.5.3 Drop Weight Impact Test

The drop weight impact machine enables a falling weight to compress a workpiece. It is capable of generating strain rates in the range 100-200 s^{-1}, rates that cannot be obtained by servo-hydraulic machines [Follansbee, 1989]. Instrumentation allows the acquisition of load-history data. Guthrie [1981] employed a drop weight tester to investigate metal flow under constant load conditions. The test may also be used to determine fracture strains to compare materials. The design of a proper die-set that does not fracture during testing is a challenge [Sarruf, 2000; Shivpuri et al., 1988A].

The drop weight impact tower is the equipment of choice for this work. More detailed descriptions of the machine and test are provided in Section 5.2.

2.6 Ductility and Ductility Criteria

Ductility can be defined as the ability of a material to withstand deformation without fracture. Two approaches have been proposed to predict the onset of ductile fracture. The first is the micromechanical or local approach, which accounts for the effect of damage in constitutive equations. The local approach involves studying the effect of inclusions, microvoid nucleation, growth and coalescence. In the second approach, the global approach, stress and strain fields are calculated at each stage of the deformation process and are incorporated into a ductile fracture criterion [Alberti et al., 1994].

2.6.1 Micromechanical Approach to Ductile Fracture

Inclusions do not behave elasto-plastically as does the matrix material. They can cause non-uniform deformation and strain concentrations that can result in decohesion of the inclusion-matrix interface or even fracture of the inclusion [Levaillant, 1986].

Ductile fracture comprises three stages [Dieter, 1984A; Dieter, 1997]. The first stage is microvoid nucleation (Figure 2.12) at second phase particles, inclusions or existing voids. Microvoid nucleation is a stress-controlled process. The second stage is microvoid growth, and is a strain-controlled process. As the microvoids elongate, the matrix material between them thins. The last stage of ductile fracture is microvoid coalescence, where microvoids link [Thomason, 1990B]. This stage is a precursor to ductile fracture. In cold forming, the fracture strain is affected by the characteristics of the non-metallic inclusions. Their size, type, orientation, and location will affect the nucleation of voids [Ollilainen, 1995; Shivpuri et al., 1988A; Kuhn, 1978].

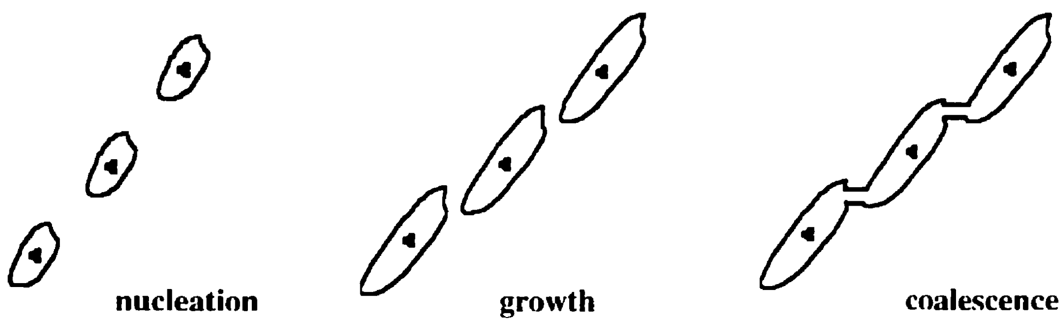

Figure 2.12 Schematic representation of microvoid nucleation, growth and coalescence.

Levaillant [1986] states that many continuum mechanics-based damage models have been developed. These include the models proposed by Garland and Plateau, Tanaka et al., Argon, Gurson, Tvergaard and Needleman, and Lemaître. Levaillant [1986] states that some of the most cited metallurgically-based (dislocation theory) models include those of Ashby, Argon et al., and Goods and Brown. These models are valuable in providing an understanding of damage evolution. However, they are difficult to apply since an enormous amount of experimentation is required. Micromechanical models are complex and difficult to apply on a macroscopic level. The application of such models to the cold heading process requires a great number of assumptions involving microvoid sizes and distributions.

2.6.2 Flow Localization

Flow localization and instability can lead to shear cracks on the equatorial surface of a cold headed specimen. This may be attributed [Semiatin and Jonas, 1984] to friction, which leads to non-uniform deformation and bulging of the surface. It may also be attributed to the depletion of strain-hardening capacity due to deformation heating (flow softening), a chain of events that leads to higher concentrated strains.

Hill developed a local instability criterion that is applicable [Levaillant, 1986] to a simple grooved-die compression test (see Figure 2.13).

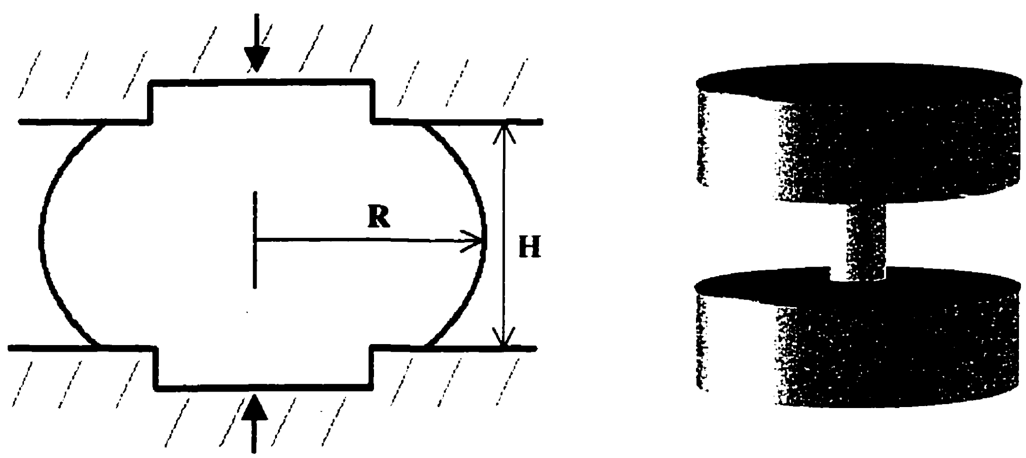

Figure 2.13 Grooved-die compression test (2D and 3D view).

For a Hollomon material ($\sigma = K\varepsilon^n$), the Hill criterion for stability is as follows:

$$\frac{n}{\varepsilon_0} \geq \frac{1+\alpha}{\sqrt{1+\alpha+\alpha^2}} \tag{2.6}$$

where

n = work hardening coefficient
ε_θ = circumferential or hoop strain

$$\alpha = \frac{d\varepsilon_z}{d\varepsilon_\theta} \tag{2.7}$$

When the left hand side of the Hill criterion (equation 2.6) is less than the right hand side, there is instability. The instability may result in fracture in the form of a 45° shear crack(s) at the surface [Levaillant, 1986].

During frictionless compression, α is equal to –2 and therefore the right hand side of the criterion equals $-\sqrt{3}/3$. Since the work hardening coefficient is positive in the absence of deformation heating or of other flow softening mechanisms, the circumferential strain is always positive and there cannot be instability leading to fracture under these conditions. This criterion shows that instability cannot occur unless α becomes greater than –1, at which point the right hand side of the equation becomes positive. Alternatively, deformation heating can initiate a vicious circle, as already discussed above.

Such a criterion explains why it may be beneficial to employ materials with a high work hardening coefficient for cold heading, such as dual phase steels. It also provides further evidence of the importance of the workability diagram and the strain path slope.

2.6.3 Global Approach to Ductile Fracture

As stated earlier, the global approach involves the calculation of stress and strain fields at each stage of the deformation process until fracture occurs. These stress and strain fields can then be used to develop ductile fracture criteria for specific deformation processes (i.e.

sequence of stress states), or they can be introduced into an existing ductile fracture criterion to predict fracture for a specific process such as cold heading.

The onset of cracking is dependent on the intrinsic ductility of the material and the stress system to which it is subjected. Musak et al. [1996] state that fracture initiation is obvious on a load-displacement curve for compression. In this work the load-displacement curves did not exhibit discontinuities related to fracture initiation. Cockcroft and Latham proposed a fracture criterion that enables the prediction of fracture under complex conditions [Cockcroft and Latham, 1968]. They speculated that such a criterion would be analogous to the prediction of yielding under complex stress conditions using either the von Mises or Tresca yield criteria.

The Cockcroft and Latham criterion states that fracture will occur when the work done by the maximum tensile stress attains a critical work energy density value 'C' (equation 2.8), a material property [Jenner and Dodd, 1981; Dieter, 1984A; Cockcroft and Latham, 1968; Ollilainen, 1995; Shivpuri et al., 1988A; Woodall and Schey, 1978; Levaillant, 1986; Wifi et al., 1998; Frater and Petrus, 1990; Gilormini and Montheillet, 1985; Wright et al., 1987]. In tensile testing, the maximum tensile stress acts on the centerline, where fracture is initiated [Cockcroft and Latham, 1968]. During upsetting, the maximum tensile stress is at the equatorial surface in the circumferential direction [Wright et al., 1987], where fracture is initiated. According to this criterion, ductile fracture occurs when:

$$\int_0^{\varepsilon_{eq,f.}} \sigma_1 d\varepsilon_{eq} = C \qquad (2.8)$$

where

C	= fracture criterion constant [MPa]
$\varepsilon_{eq,f.}$	= equivalent strain to fracture
σ_1	= maximum principal tensile stress [MPa]
ε_{eq}	= equivalent strain = von Mises equivalent strain
	= $\int \dot{\varepsilon}_{eq} dt$

and

$\dot{\varepsilon}_{eq}$	= equivalent strain rate [s^{-1}]
t	= time [s]

This criterion recognizes the coupled roles of tensile stress and plastic strain in promoting ductile fracture [Cockcroft and Latham, 1968]. When the tensile strain energy per unit volume reaches a critical value, fracture occurs [Dieter, 1984A]. When only compressive stresses are operating, e.g., in hydrostatic compression, σ_I is equal to zero and no fracture can occur.

Hosford and Caddell [1983A] point out that when the maximum principal tensile stress, σ_I, becomes negative, the criterion predicts an accumulation of 'negative damage'. Nevertheless, this criterion has been successfully employed in a variety of deformation processes, including tensile, torsion, bending, and extrusion tests [Cockcroft and Latham, 1968].

Microstructure, the presence of second phases, alloy content, grain size and cleanliness are metallurgical parameters that have a significant impact on the value 'C' [Frater and Petrus, 1990]. Jenner and Dodd [1981] determined that the Cockcroft and Latham criterion is accurate enough to predict the onset of surface fracture in cold upsetting and that it is empirically correct.

In the context of this work, upset testing is performed using a drop weight test machine to determine the critical $\Delta H/H_o$ (reduction limit) of various materials. The Cockcroft and Latham criterion will be numerically integrated using finite element simulations of the experimental test to predict the onset of fracture in upsetting for different aspect ratios. For a particular material, the equation should produce the same fracture criterion constant, C, for upset testing regardless of the aspect ratio.

Oyane proposed a 2-parameter ductile fracture criterion (equation 2.9) that emphasizes the role of hydrostatic stress (σ_m) [Jenner and Dodd, 1981; Levaillant, 1986, Ollilainen, 1995; Oyane et al., 1980; Oyane, 1972, Wifi et al., 1998; Gilormini and Montheillet, 1985; Takuda et al., 1997]. According to the Oyane criterion, ductile fracture occurs when:

$$B = \int_0^{\varepsilon_{eq,f}} \left(1 + \frac{A\sigma_m}{\sigma_{eq}}\right) d\varepsilon_{eq} \tag{2.9}$$

where

A and B = fracture criterion constants
σ_m = hydrostatic stress = $(\sigma_\theta + \sigma_r + \sigma_z)/3$ [MPa]
σ_{eq} = equivalent stress = von Mises equivalent stress $= f(\sigma_\theta, \sigma_r, \sigma_z)$ [MPa]

This semi-empirical criterion is more difficult to use since there are two material constants (A and B), which must be determined through experiments on the material in question [Thomason, 1990C; Levaillant, 1986]. The additive factor ($A\sigma_m/\sigma_{eq}$) takes into account the detrimental effect of tensile stress triaxiality.

The material constants (A and B) are determined using a procedure similar to the one used to determine the Cockcroft and Latham constant. The reduction limit at fracture for various materials is determined experimentally, while the equivalent strain to fracture and the integral term are determined through finite element method simulations of the upset test. A plot of the equivalent strain to fracture versus the integral term yields a straight line with a slope equal to $-1/A$. The material constant, B, is determined from the intersection of the line and the ordinate.

The Oyane criterion has been used successfully in simple grooved-die upsetting tests with various workpiece geometries and lubrication conditions [Oyane et al., 1980]. It has also been used successfully as a ductile fracture criterion for finite element method simulation of sheet forming [Takuda et al., 1997].

2.7 Shear Banding

During the plastic deformation of metals, work is partly stored as cold work (elastic strain energy), while the remainder is converted into heat [Rogers, 1983]. At room temperature, approximately 90-95% of the work is converted into heat [Rogers, 1983; Bai and Dodd, 1992]. If the strain rate is high, as in cold heading, there is not enough time for the heat to diffuse away from the deforming zone [Bai and Dodd, 1992; Field et al., 1994]. This results in local heating and a form of thermal softening known as thermo-mechanical coupling. When the strength loss due to thermal softening becomes greater than the increase in strength due to strain hardening, the plastic deformation localizes in the hottest region [Hartley et al., 1986; Bai and Dodd, 1992; Roessig and Mason, 1999A and 1999B]. This results in heterogeneous plastic deformation and the formation of a shear band that spans many grains [Semiatin et al., 1983].

Shear bands are uncommon during low strain rate tensile testing because fracture occurs before bands can form [Rogers, 1983]. During compressive loading, on the other hand, void nucleation and fracture are suppressed, thus producing large local strains, and intensifying the local heating [Rogers, 1983; Bai and Dodd, 1992].

There exist two different types of shear bands: deformed bands and transformed bands. Deformed bands are zones of intense plastic shear resulting from a rapid decrease in flow stress due to thermal softening [Bai and Dodd, 1992; Meyers, 1994]. Transformed bands are intense zones of shear within which a phase transformation has taken place. Meyers [1994] stated that other researchers, e.g., Zener and Hollomon, have shown that for steel, the temperature rise in a shear band can readily exceed 1000°C; as a result, ferrite transforms to austenite. The high temperature shear band then cools very rapidly in contact with the surrounding material. This results in a transformation from austenite to martensite, and possibly in the formation of cracks across the band [Rogers, 1983; Bai and Dodd, 1992]. Transformation shear bands in cold heading may lead to component failure during a sequence of impact events, during subsequent processing, or in service.

Increasing thermal softening rate and decreasing work hardening coefficient promote shear band formation [Rogers, 1983; Semiatin et al., 1983]. The flow stress of the test material is another critical factor in the formation of shear bands. The higher the flow stress, the more heat is generated [Rogers, 1983]. Materials most resistive to shear band formation have low strength, high work hardening coefficient, and good resistance to thermal softening

[Rogers, 1983; Roessig and Mason, 1999A; Bai and Dodd, 1992]. Roessig and Mason [1999A] have shown that certain steels exhibit a decrease in punch energy at higher punch speeds. This may be an indication that shear localization has occurred. Materials with high work hardening coefficient, e.g., dual phase steels, are more resistant to shear banding.

Although shear band cracks (θ-type) are not directly related to the surface cracks (α-type) that are the primary focus of this thesis, they are of great importance to the cold heading industry. Alpha-type cracks can be detected during final surface inspection of components. On the other hand, θ-type cracks are usually revealed by destructive testing. Theta-type cracks are more elusive because fasteners are typically quench and tempered, thereby eliminating the microstructural evidence of prior shear banding.

The test methodology developed for this work can be employed to foster a better understanding of shear band defects.

2.8 Constitutive Relations

Numerous empirical relations are available to describe the flow stress of a material. Although many of these approximate the stress-strain curve, this does not imply that the relations have physical interpretations. In fact, plastic deformation is path dependent and is therefore not uniquely dependent on the dislocation structure of the material. Nevertheless, these relations are required in the mathematical modeling of metal forming processes.

The Ludwik-Hollomon equation

$$\sigma_{eq} = \sigma_o + K\varepsilon_{eq}^{n} \tag{2.10}$$

is the most commonly used relation to describe plastic response in metals. In this equation, K is a constant and the exponent, n, is the work hardening coefficient. The exponent is a function of the material, the temperature, the strain, and the strain coefficient [Meyers, 1994; Meyers and Chawla, 1999]. For steel, n generally varies between 0.2 and 0.25 at room temperature and decreases significantly with increasing temperature. When the work hardening coefficient is equal to zero, the response describes ideal plastic behavior.

The Ludwik-Hollomon equation is limiting because it predicts a slope of infinity when the strain is zero (i.e. at the yield point), which is not the case; furthermore, the stress increases ad infinitum with strain, which is not realistic since stress saturates at high strains [Meyers and Chawla, 1999].

The Johnson-Cook constitutive equation

$$\sigma_{eq} = \left(\sigma_o + K\varepsilon_{eq}^n\right)\left(1 + J\ln\frac{\dot{\varepsilon}_{eq}}{\dot{\varepsilon}_o}\right)\left[1 - \left(\frac{T - T_r}{T_m - T_r}\right)^m\right] \tag{2.11}$$

where

$\dot{\varepsilon}_o$ = reference strain rate
J = Johnson-Cook constant
T_r = reference temperature [K]
T_m = melting temperature [K]

is a more realistic relation that takes into account strain rate and temperature effects. Indeed, it is well known that the flow stress increases with increasing strain rate and decreasing temperature. There are three groups of terms representing work hardening, strain rate, and temperature effects [Meyers and Chawla, 1999]. The parameters K, J, m and n are all material constants.

In the Norton-Hoff relation

$$\sigma_{eq} = \kappa\sqrt{3}\left(\sqrt{3}\dot{\varepsilon}_{eq}\right)^m \tag{2.12}$$

the stress is linked to the equivalent strain rate through the consistency, κ, and the strain rate sensitivity, m [Forge2, 1998]. The consistency is a function of the thermo-mechanical conditions and may take various forms, for example

$$\kappa(T,\varepsilon_{eq}) = K_o\left(\varepsilon_{eq} + \varepsilon_o\right)^n \exp\frac{\beta}{T} \tag{2.13}$$

where

K_o = strength coefficient
ε_o = strain hardening regulation term ~ 0.0001
n = work hardening coefficient
β = temperature coefficient

Here, the strain-hardening power law is coupled with the Arrhenius law for the temperature. The exponential term is included to take into account the effect of absolute temperature. Beta (β) is a constant that must be determined experimentally. This empirical relation is one of the constitutive models available in the finite element method code used in this work (Forge2).

2.9 Summary

Cold heading encompasses numerous material and process aspects, and their relevance to the present work has been outlined in this chapter.

CHAPTER 3

OBJECTIVES

The cold heading industry uses intuition and rule-of-thumb standards based on decades of trial-and-error. In the hope of ensuring an adequately ductile material for a particular application, wire rod producers customarily supply material qualities that exceed the requirements of the application since expensive product recalls and injury may result when substandard material is provided. This 'excess' quality can result in higher raw material and processing costs. To address these concerns, the present research project was initiated.

The specific objectives of this project were:

- Development of a drop weight test apparatus, a die-set configuration, and a technique for evaluating material ductility during upsetting in cold heading.
- Development of a scientific foundation for ongoing studies of upsetting in cold heading using:
    - constitutive equations
    - ductile fracture criteria
    - friction values
    - finite element methods

- Development of a methodology to validate and calibrate fracture criteria for upsetting in cold heading.

- Determination of the sensitivity of the drop weight test to material and process parameters.

Chapter 4

SELECTION, CONDITIONING AND CHARACTERIZATION OF MATERIALS

4.1 Selection of Test Materials

Grade 1038 steel was selected for testing. This material is a medium-carbon cold heading quality steel. The material matrix was designed to evaluate the impact of varying material parameters, i.e., surface quality, copper level, nitrogen content, and microstructure, and steel sources, i.e., ingot versus continuous cast, on fracture behavior.

Table 4.1 lists the chemical composition of the materials selected for testing. Three billet sources were selected for the matrix. Açominas supplies a high quality ingot cast steel with a very low residual element content (~ 0.05 wt.%) employed in more demanding cold heading applications. QIT Fer & Titane produces a continuous cast steel from pig iron smelted from ilmenite ore. This steel has low residual element content (~ 0.15 wt.%). The Ivaco Steel Plant produces a continuous cast steel from scrap steel with varying levels of residual elements (~ 0.5-1.0 wt.%). The latter steels are used in less demanding cold heading applications. In addition, most grades are supplied as aluminum killed (AK), silicon-aluminum killed (SiAK) and silicon killed (SK). All but one of the materials selected for the test matrix were silicon killed.

Heats numbered 1 to 3 were used to test the effect of low and high copper (Heat 2 versus Heat 3) and nitrogen (Heat 1 versus Heat 2). Fast rod cooling on the Stelmor conveyor is known to have a negative impact on cold heading materials since it causes the maximum amount of nitrogen to remain in solution [Taheri et al., 1995A, 1995B]. This increases the influence of dynamic strain aging. To reduce the solute nitrogen level after hot working, a slow cooling rate after hot rolling of wire rod could be employed [Taheri et al., 1995A]. All test materials were fast cooled following hot rolling on a Stelmor conveyor, using the same cooling rate, to maximize the effect of nitrogen. Heats 4 and 5 were intended to test the effect of low and high nitrogen on QIT material. Heats 6 and 7 are low residual element, low nitrogen ingot cast cold heading steels. Heat 6 is an aluminum-killed steel with a substandard surface quality. Visual inspection and optical microscopy analysis revealed a corroded and slightly pitted surface. This heat was included in the test matrix to evaluate the sensitivity of the methodology to the effect of surface nonconformity. Heat 7 was a silicon-killed material with a chemistry similar to that of Heat 5, and provided a baseline for comparison with the other billet suppliers.

Billet Source	Heat No.	Heat	C (wt. %)	Mn (wt. %)	P (wt. %)	S (wt. %)	Si (wt. %)	Cu (wt. %)
Ivaco	1	A47870	0.38	1.04	0.018	0.009	0.24	0.16
Ivaco	2	A49056	0.38	0.99	0.007	0.015	0.22	0.15
Ivaco	3	A34595	0.37	0.96	0.024	0.004	0.24	0.35
QIT	4	T50391	0.41	0.78	0.007	0.002	0.23	0.05
QIT	5	T45893	0.41	0.80	0.007	0.009	0.22	0.04
Açominas	6	Z41909	0.36	0.72	0.016	0.006	0.20	0.00
Açominas	7	Z26787	0.39	0.79	0.016	0.009	0.25	0.00
Billet Source	**Heat No.**	**Ni (wt. %)**	**Cr (wt. %)**	**Mo (wt. %)**	**Sn (wt. %)**	**Al (wt. %)**	**N (wt. %)**	**Sum of Residuals**
Ivaco	1	0.06	0.25	0.026	0.009	0.005	0.0107	0.51
Ivaco	2	0.07	0.26	0.020	0.011	0.004	0.0060	0.51
Ivaco	3	0.09	0.33	0.033	0.016	0.007	0.0078	0.82
QIT	4	0.07	0.04	0.006	0.004	0.006	0.0101	0.17
QIT	5	0.07	0.04	0.006	0.004	0.004	0.0044	0.16
Açominas	6	0.02	0.03	0.010	0.003	0.044	0.0035	0.06
Açominas	7	0.01	0.03	0.000	0.003	0.002	0.0040	0.04

Table 4.1 Chemical analyses of test matrix materials.

Three rod specimens from each heat were re-analyzed to ensure that the chemical composition was comparable to that of the heat certificate.

In summary, the test matrix materials were selected to enable fracture strain comparisons to be made between high and low nitrogen heats, high and low copper levels, and three billet suppliers; they were also intended to ascertain the sensitivity of the test methodology to billet quality and chemistry.

4.2 Conditioning and Characterization of Materials

The test specimen preparation procedure is shown in Figure 4.1.

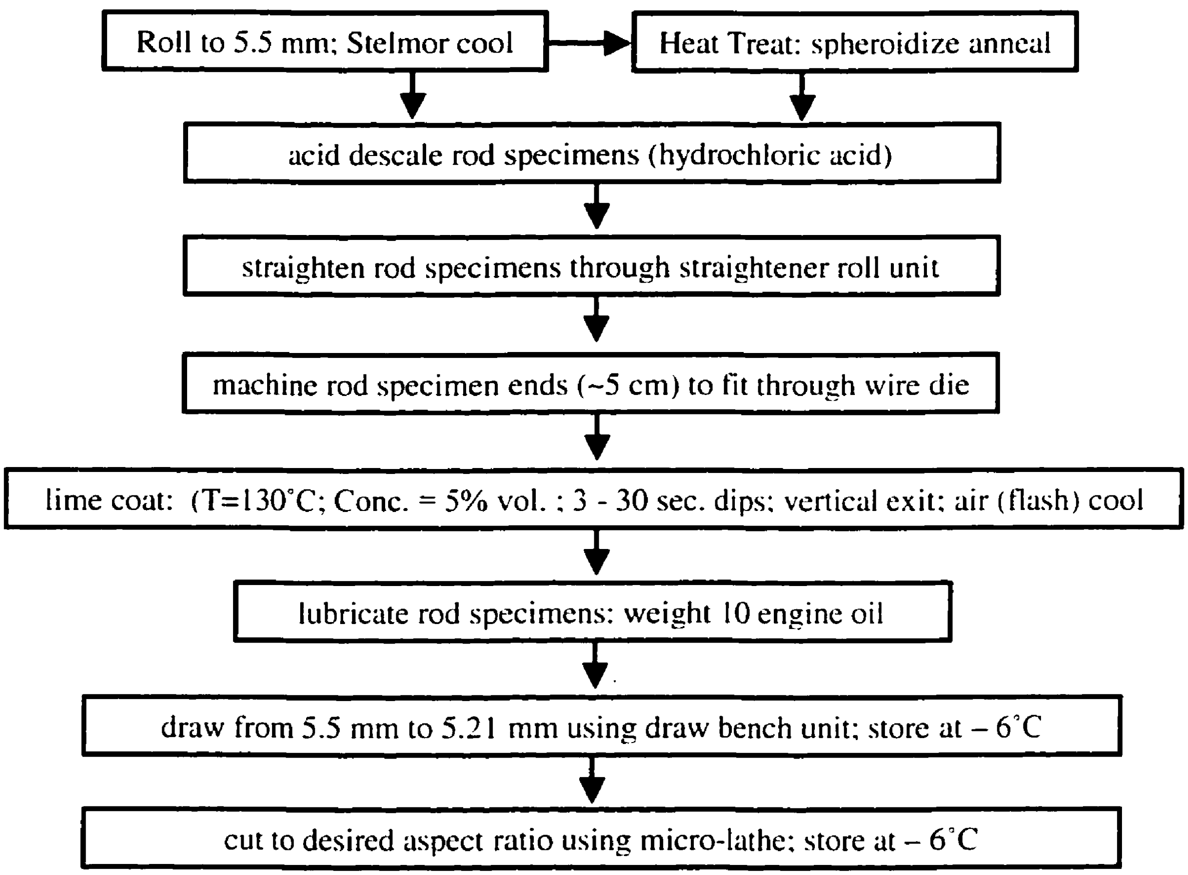

Figure 4.1 Flowchart of specimen preparation.

4.2.1 Descaling

Rod specimens, 18-23 cm in length, were cut from wire rod coils, and then pickled to remove the oxide scale developed during wire rod cooling. Pickling was performed by immersion in a hot (90°C) acid solution (50% HCl / 50%H_2O) for 5 to 7 minutes.

4.2.2 Straightening

Specimens cut from wire rod coils retained a radius of curvature of a little over 1 m. Compression specimens need to be as straight as possible for compression testing to simulate an axisymmetric forming operation, and to prevent buckling. A laboratory roll unit was assembled to straighten the wire specimens (see Figure 4.2). The wire rod specimens were inserted into the first set of rolls and hammered through the roll assembly.

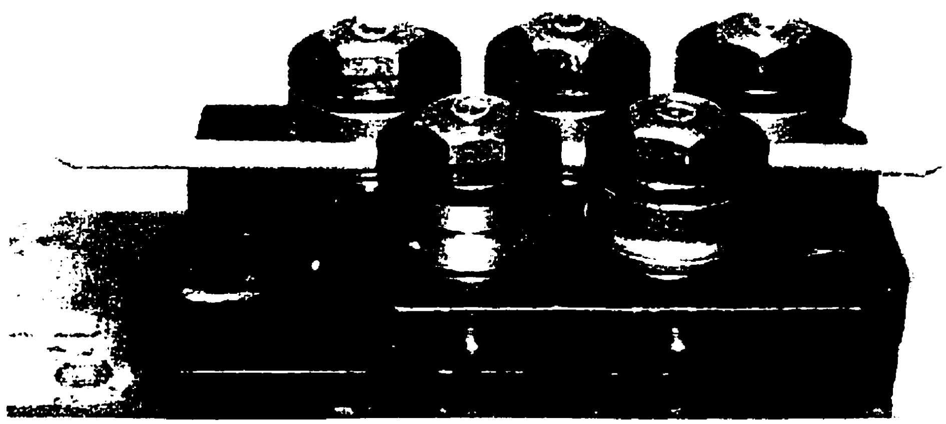

Figure 4.2 Laboratory straightener unit.

4.2.3 Machining

The next step in specimen preparation was to machine a 5 cm long step to a diameter below 5.2 mm using a micro-lathe. This allowed wire rod specimens to pass through the wire drawing die and into the gripping jaw in the ensuing wire-drawing step. Figure 4.3 illustrates the machined portion of a wire rod specimen passing though a wire drawing die.

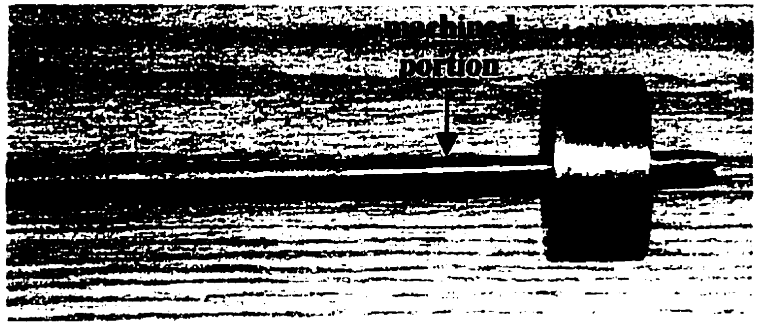

Figure 4.3 Machined wire rod specimen with wire drawing die.

4.2.4 Characterization of As-Rolled Materials

Tensile testing was performed on the as-rolled specimens using a Tinius Olsen Super L testing machine. Tables 4.2 and 4.3 illustrate the ultimate tensile strength (UTS) and reduction-of-area (ROA) results for the 7 heats following hot rolling. Three wire rod specimens from a population of about 40 rods were tensile tested for each heat.

All 7 heats were fast cooled using the same cooling schedule following hot rolling. Heat 1 exhibits slightly higher UTS and lower ROA values than Heat 2. This is consistent with the fact that Heat 1 contains twice the amount of nitrogen. The UTS results for Heat 3 ranged from 900 to 1200 MPa. The larger range and the much higher average UTS may be related to the much higher copper and residual element content. The ROA results for this heat are consistent with the higher UTS.

Heats 4 and 5 (from QIT) exhibited lower UTS and slightly higher ROA values than Heats 1 to 3 (from Ivaco). This is probably due to the lower residual element content in Heats 4 and 5, particularly chromium. The property ranges are also quite small, indicating better chemical and microstructural uniformity.

Heats 6 and 7 (from Açominas) exhibit UTS and ROA results comparable to those of Heats 5 and 6. These two sets of heats have low residual element and nitrogen contents.

Heat No.	Heat	UTS minimum [MPa]	UTS maximum [MPa]	UTS average [MPa]
1	A47870	876	989	925
2	A49056	830	867	851
3	A34595	919	1221	1119
4	T50391	795	800	798
5	T45893	758	764	761
6	Z41909	693	703	697
7	Z26787	726	735	731

Table 4.2 Ultimate tensile strength (UTS) results for as-rolled rod specimens.

Heat No.	Heat	ROA minimum [%]	ROA maximum [%]	ROA average [%]
1	A47870	61.4	65.0	63.0
2	A49056	64.7	67.8	66.4
3	A34595	60.5	63.6	61.8
4	T50391	66.6	69.5	68.1
5	T45893	66.5	67.2	67.0
6	Z41909	68.3	70.1	69.2
7	Z26787	66.2	68.5	67.0

Table 4.3 Reduction-of-area results (ROA) for as-rolled rod specimens.

Wire rod specimens for metallographic evaluation were mounted in Lucite, ground using successively finer silicon carbide papers (60, 120, 240 and 600 grit), polished using 6 and 1 micron diamond paste, and etched in a 4% nital solution. A JEOL JSM-840A scanning electron microscope (SEM) was used to photograph the microstructure of the specimens.

SEM microscopy revealed a microstructure consisting of lamellar pearlite in a ferrite matrix for all 7 as-rolled heats (see Figures 4.4 to 4.10). The fact that Heats 1 to 7 were Stelmor-cooled using similar rod cooling practice allowed objective comparisons between the as-rolled materials. Variations in microstructure are expected because of dissimilar cooling around the circumference of coil rings.

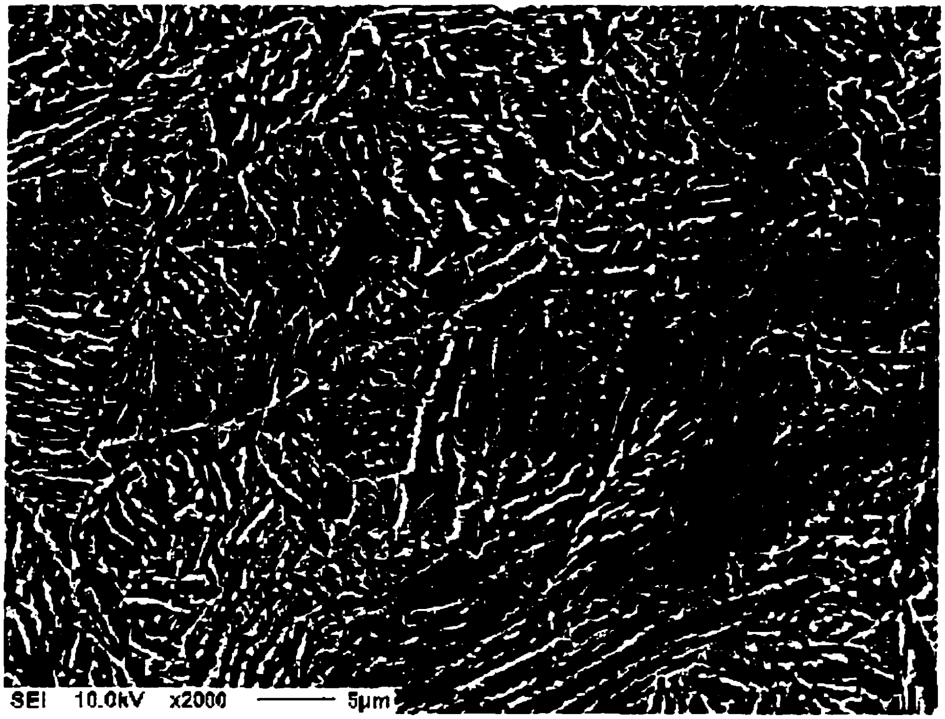

Figure 4.4 As-rolled microstructure of Heat 1.

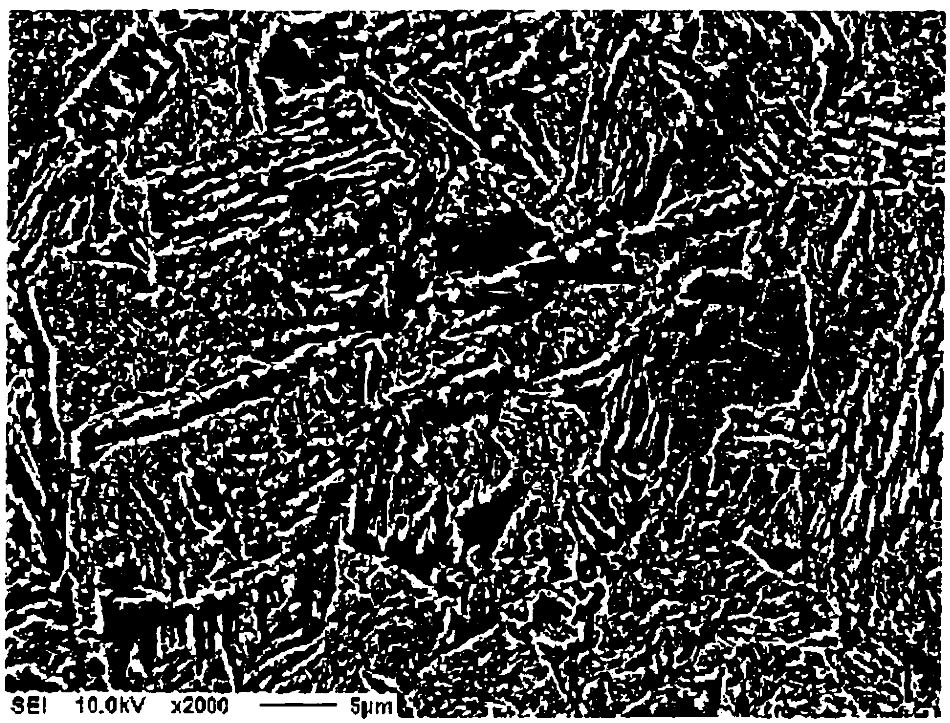

Figure 4.5 As-rolled microstructure of Heat 2.

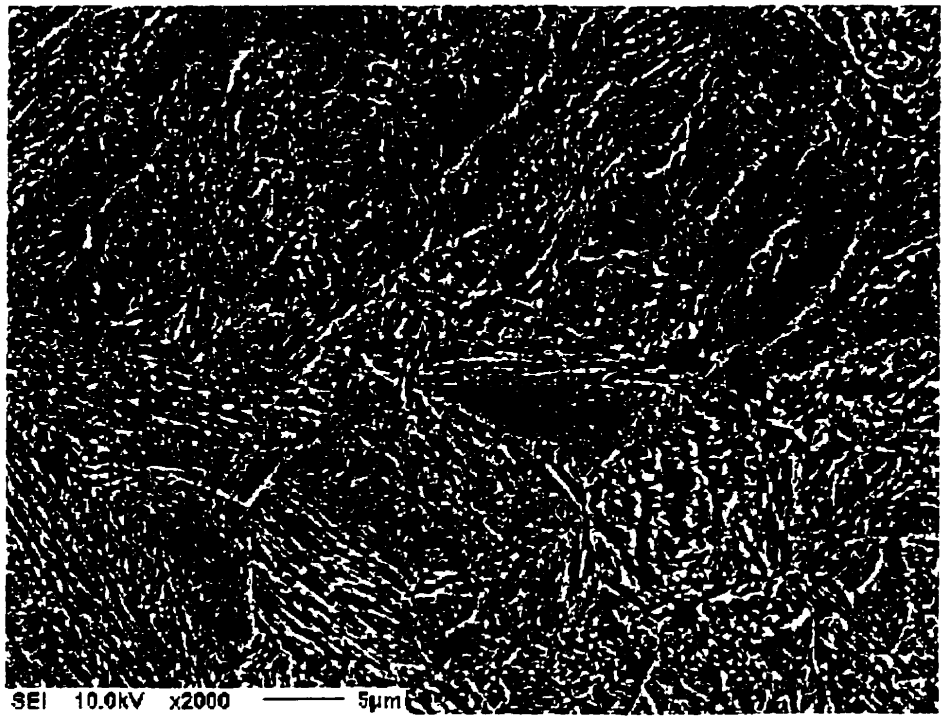

Figure 4.6 As-rolled microstructure of Heat 3.

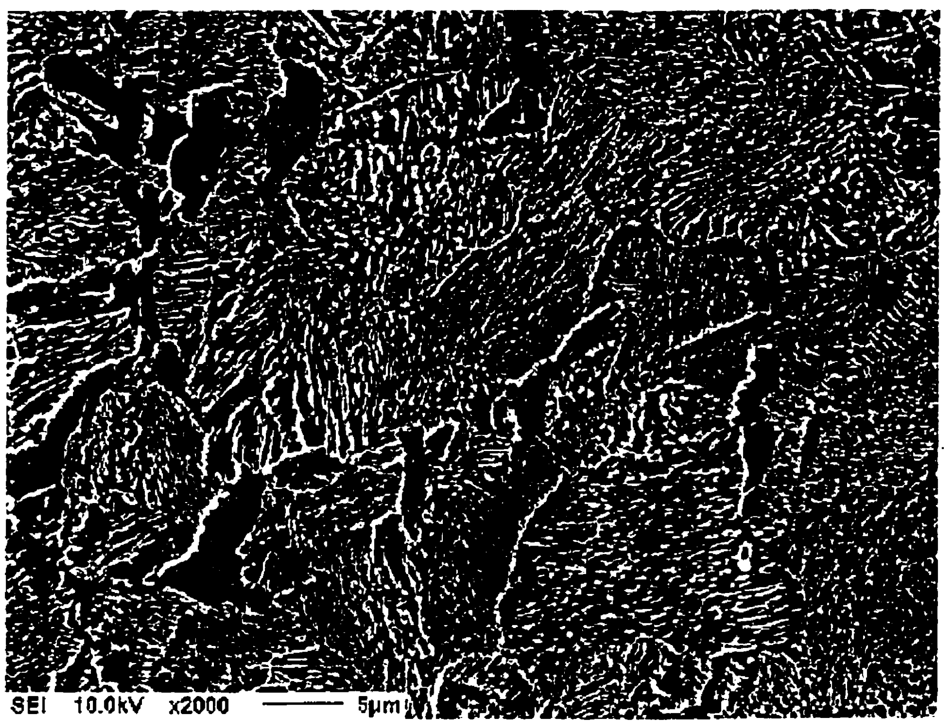

Figure 4.7 As-rolled microstructure of Heat 4.

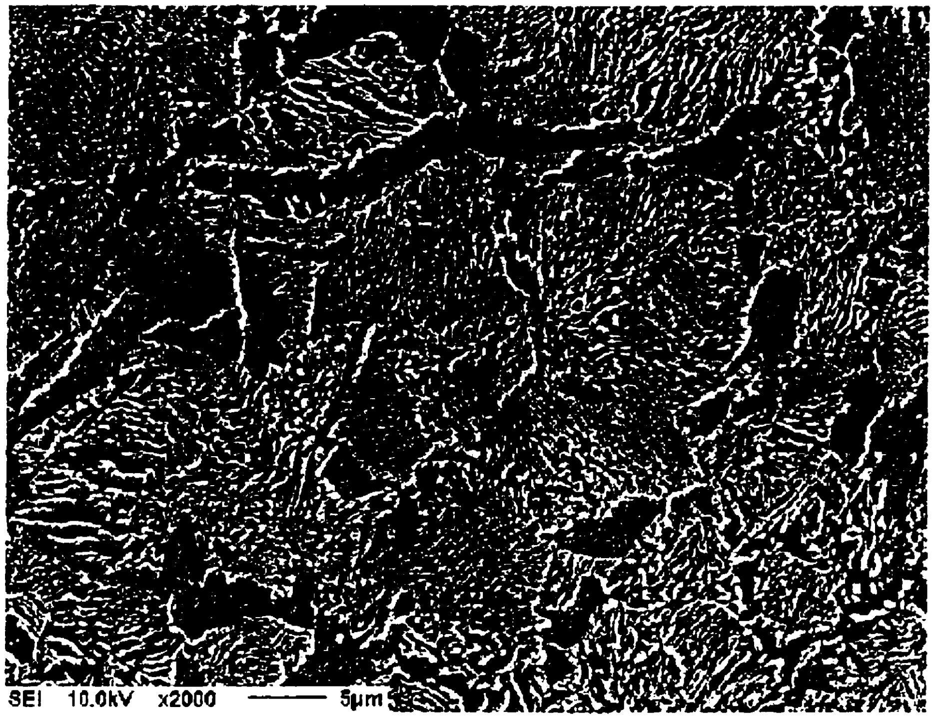

Figure 4.8 As-rolled microstructure of Heat 5.

Figures 4.9 As-rolled microstructure of Heat 6.

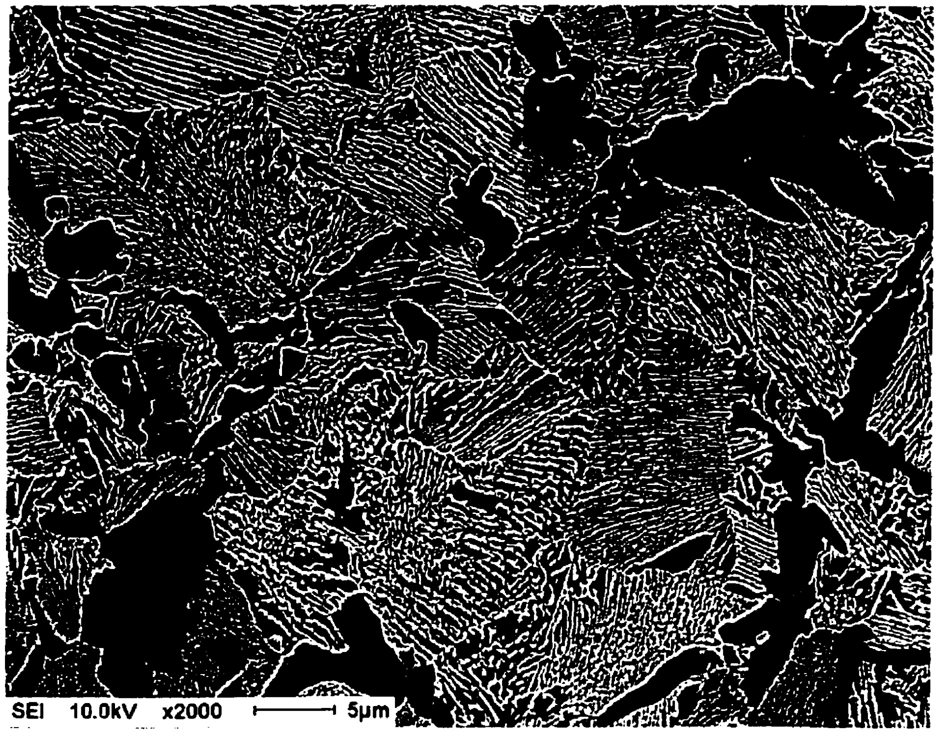

Figure 4.10 As-rolled microstructure of Heat 7.

4.2.5 Spheroidize Annealing and Characterization of Test Materials

To assist the subsequent spheroidization process, the test matrix heats were cooled quickly from the rod rolling temperature. This promoted the development of fine pearlite known to increase the spheroidization rate due to a decrease in diffusion distance [Samuels, 1980, 1988]. Wire rod materials consisting of a lamellar pearlite in a ferrite matrix microstructure are seldom used in a cold heading application. They are usually spheroidize annealed to yield a more ductile microstructure [Samuels, 1980].

As mentioned earlier, one objective of this work was to evaluate the sensitivity of the test methodology to microstructure. Accordingly, the test matrix specimens were split into two batches: as-rolled pearlite and spheroidize annealed cementite.

Wire rod specimens from Heats 1 to 6 were spheroidize annealed in an atmosphere-controlled industrial batch furnace (see Figure 4.11) at Sivaco Ontario (Ingersoll, Ontario). These specimens were processed together to ensure consistent heat treatment.

A capsule (610 mm length by 160 mm diameter) was constructed to hold the rod specimens during the spheroidize anneal cycle (see Figure 4.12). The capsule prevented surface decarburization during heat treatment. A 150 mm long pipe with a 50 mm inner diameter was attached to the capsule in order to relieve any pressure buildup during the heat treatment operation. The small pipe contained electrode carbon between two layers of Kaowool, a silica alumina ceramic-fiber. The electrode carbon provided additional protection against oxidation.

The heat treatment cycle employed in this work is common for 1038 steel in industry. The furnace was heated to 749°C (1380°F) and held at that temperature for 8 hours. The furnace was then cooled to 677°C (1250°F) over a 2-hour period, and held at this temperature for 6 hours. The furnace was then allowed to cool slowly to room temperature.

Optical microscopy showed that rod specimens from all test matrix heats were spheroidized to an acceptable level of 80-85% at a magnification of X500, as per industrial standards. Figures 4.13 to 4.17 illustrate spheroidized microstructures for the test matrix materials.

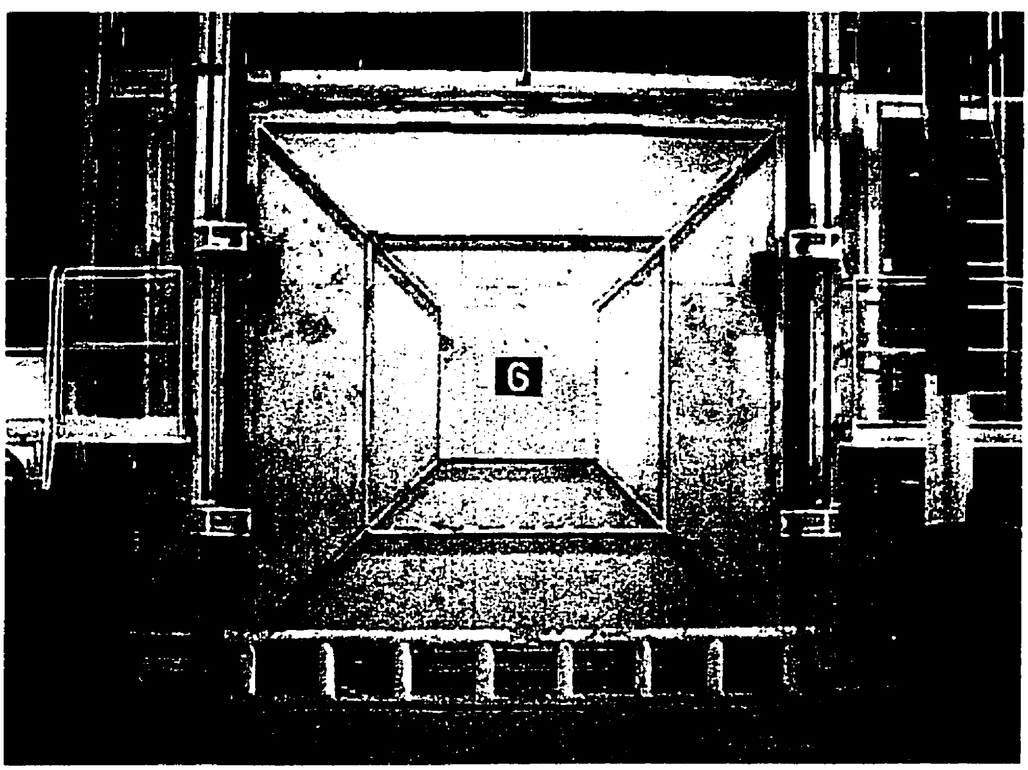

Figure 4.11 Spheroidizing furnace.

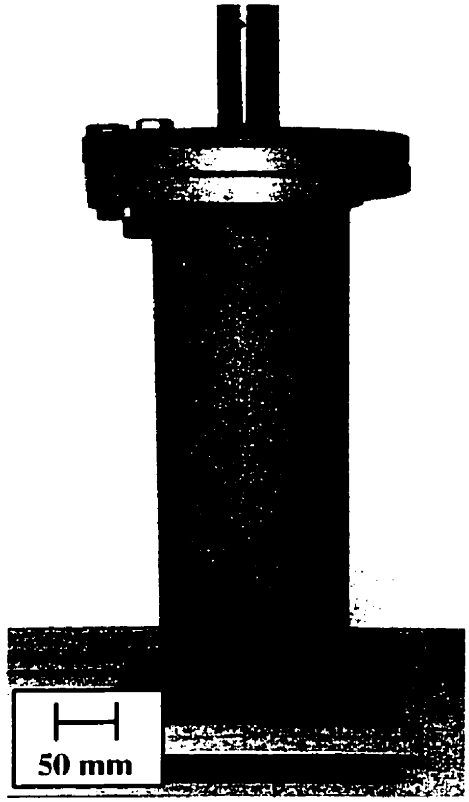

Figure 4.12 Heat treatment capsule.

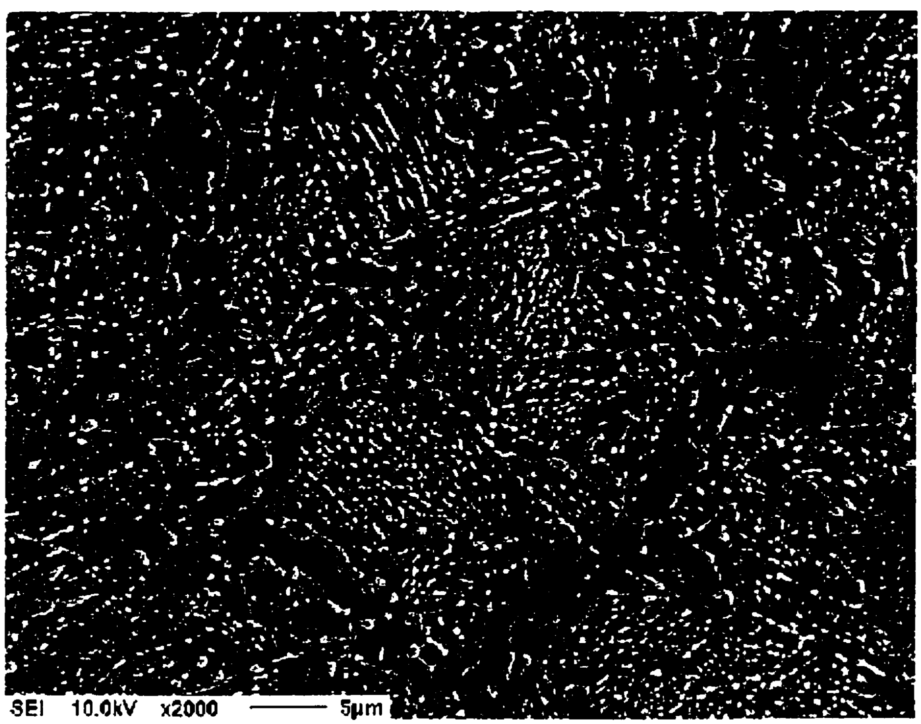

Figure 4.13 Spheroidize annealed microstructure of Heat 1.

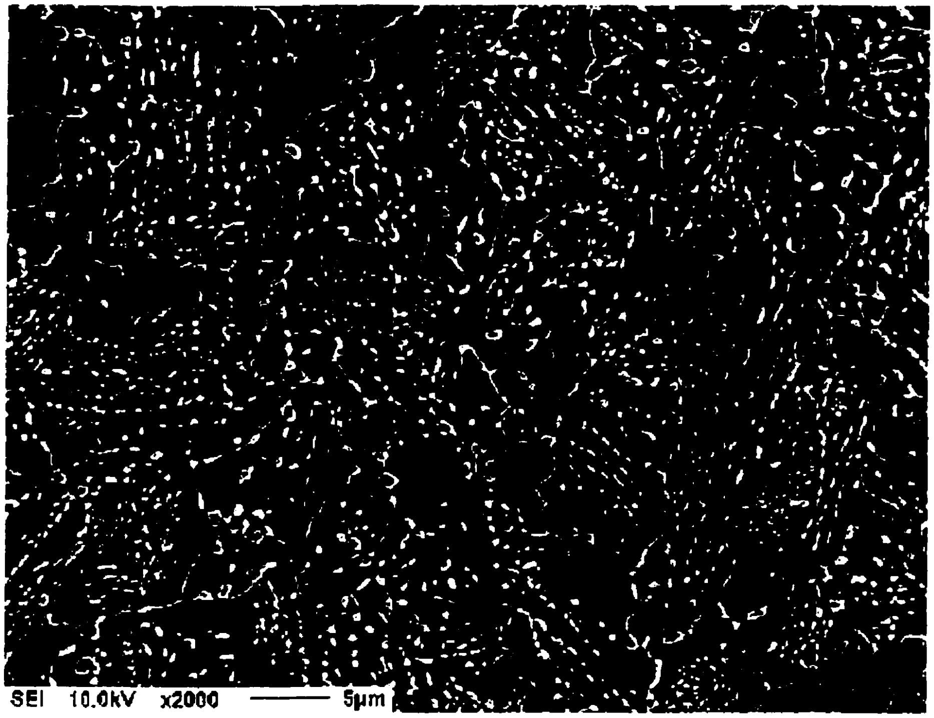

Figure 4.14 Spheroidize annealed microstructure of Heat 2.

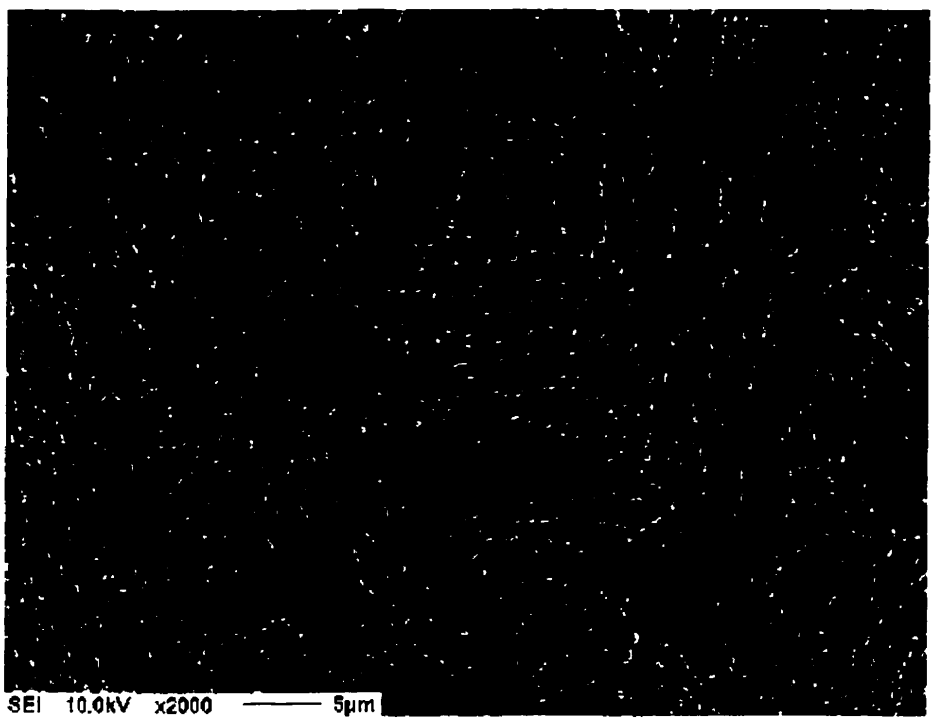

Figure 4.15 Spheroidize annealed microstructure of Heat 3.

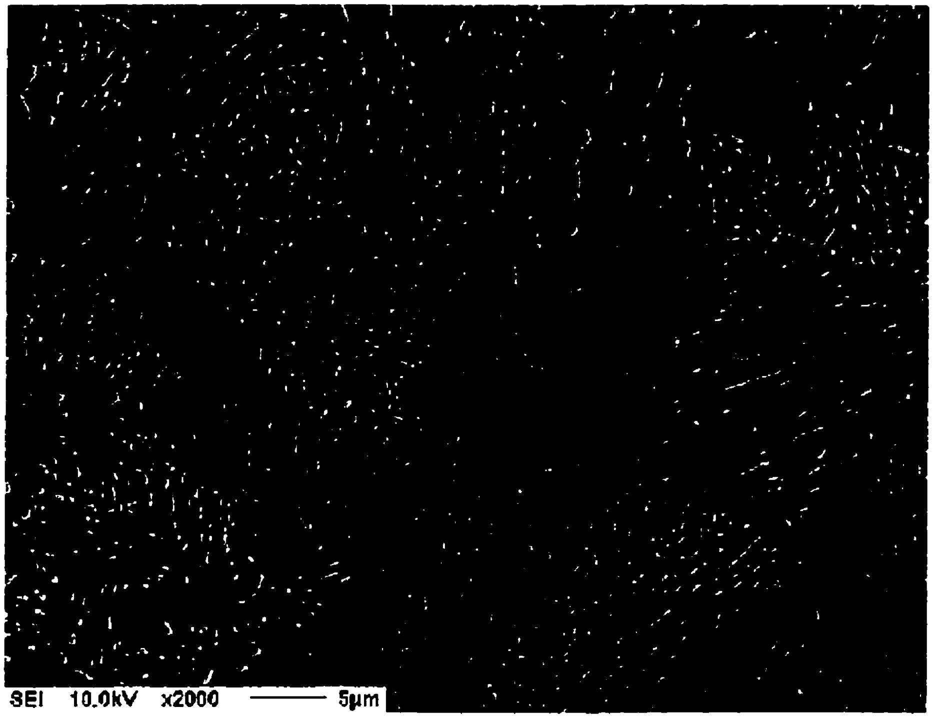

Figure 4.16 Spheroidize annealed microstructure of Heat 4.

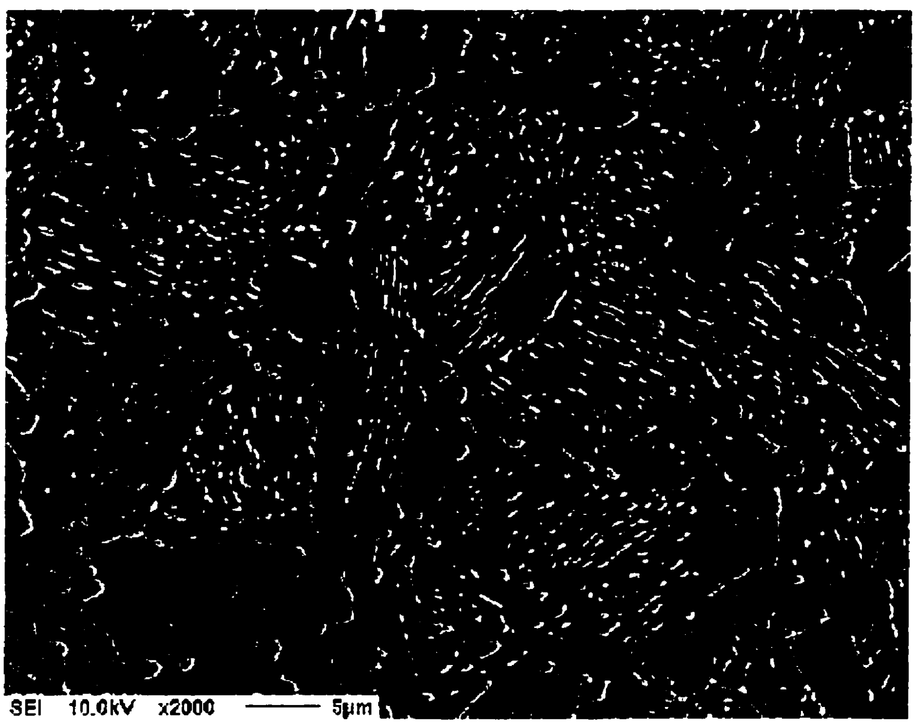

Figure 4.17 Spheroidize annealed microstructure of Heat 5.

Specimens from Heat 7 were spheroidize annealed without the use of the heat treatment capsule to promote surface decarburization. The purpose was to permit evaluation of this non-conformity on fracture behavior. Figure 4.18 is a SEM micrograph of a typical cross-section. The fully decarburized layer has a thickness of 100 μm. As discussed in Chapter 2, decarburization provides added ductility at the surface during upset testing. However, the carbon-depleted layer cannot be hardened during subsequent quench and tempering operations.

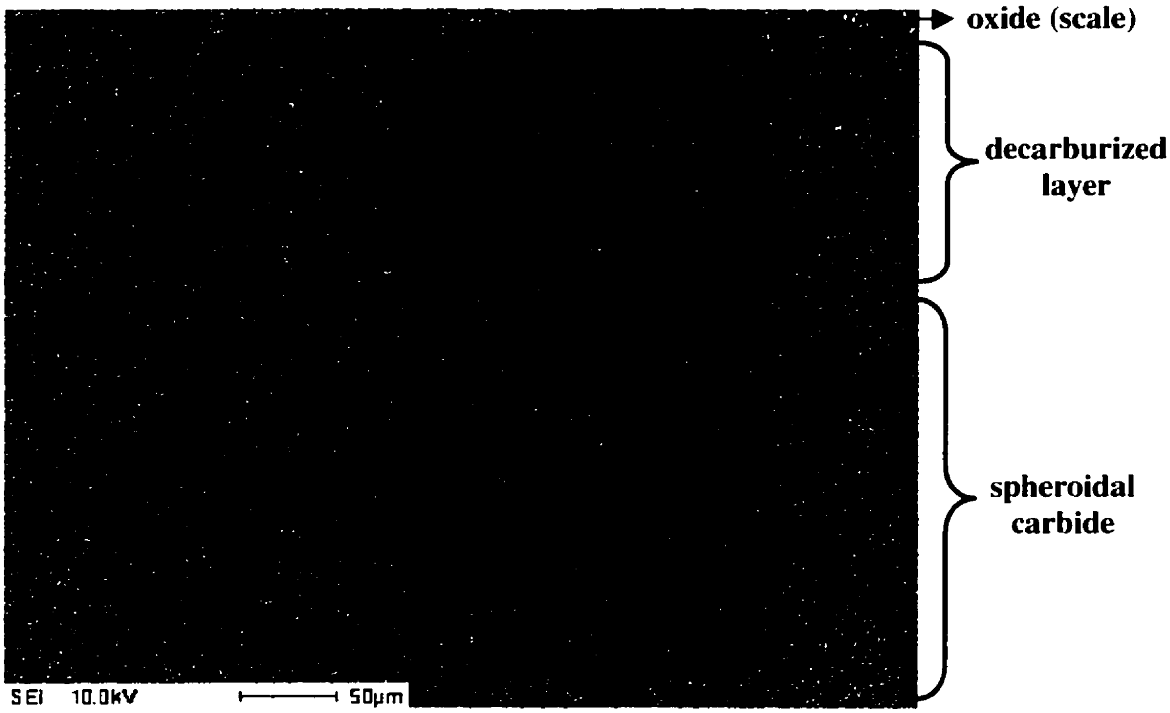

Figure 4.18 Spheroidized Heat 7 specimen exhibiting surface decarburization.

Tensile testing was also performed on the spheroidize annealed rod specimens using a Tinius Olsen Super L testing machine. Tables 4.4 and 4.5 illustrate the ultimate tensile strength (UTS) and reduction-of-area (ROA) results for Heats 1 to 5 following spheroidize annealing. Once again, 3 rod specimens were tensile tested for each heat. The sensitivity of the test methodology to surface non-conformities was determined on as-rolled Heat 6 and 7 materials, and was not repeated for the spheroidized Heat 6 and 7 materials. It was therefore not necessary to determine and report tensile properties for these heats.

Heat No.	Heat	UTS maximum [MPa]	UTS minimum [MPa]	UTS average [MPa]
1	A47870	565	553	560
2	A49056	534	525	529
3	A34595	585	573	579
4	T50391	513	509	511
5	T45893	517	504	509

Table 4.4 Ultimate tensile strength for spheroidize annealed rod specimens.

Heat No.	Heat	ROA maximum [%]	ROA minimum [%]	ROA average [%]
1	A47870	74.8	73.9	74.3
2	A49056	75.5	75.2	75.3
3	A34595	75.6	74.9	75.3
4	T50391	73.9	73.2	73.5
5	T45893	74.5	74.1	74.3

Table 4.5 Reduction-of-area results for spheroidize annealed rod specimens.

4.2.6 Lime Coating, Lubricating, and Wire Drawing

As mentioned in the literature section, industrial practice is to pre-draw the wire rod prior to cold heading. This serves to strengthen less-worked portions of a headed product, i.e., the shaft, to present the correct cross-section to the heading dies, to heat-up the wire rod, and to improve the surface finish of the final product. Predraw may also serve to increase the ductility of the material by allowing it to overcome Lüders band instabilities while compression.

A laboratory wire drawing unit (see Figure 4.19) was constructed to draw the matrix materials. The unit consists of an R-5 conical wire die (Figure 4.20) in a holder assembly that maintains the die case in compression (not shown in Figure 4.19), and a gripping jaw unit attached to a threaded rod, and crank. The machined end of the wire rod specimen is passed through the die and gripped in the jaw. The crank assembly pulls the wire rod specimen where it is reduced to the test diameter (5.21 mm).

A lime coating was applied to the wire rod before drawing. The lime acts as a carrier for the lubricant and provides a certain degree of lubrication itself. Specimens were immersed for 30 seconds in a 5% (vol.) solution of lime and water heated to 130°C, pulled out vertically, and cooled in still air. The procedure was repeated three times to yield a thick lime coat. The specimens were then immersed in 10W engine oil for additional lubrication.

The rod specimens were drawn from an initial diameter of 5.50 ± 0.10 mm to a final diameter of 5.21 ± 0.01 mm, a 10% reduction. Typical industrial pre-draw reductions range from 8 to 14%. Materials were then stored at - 6°C to minimize aging after cold working.

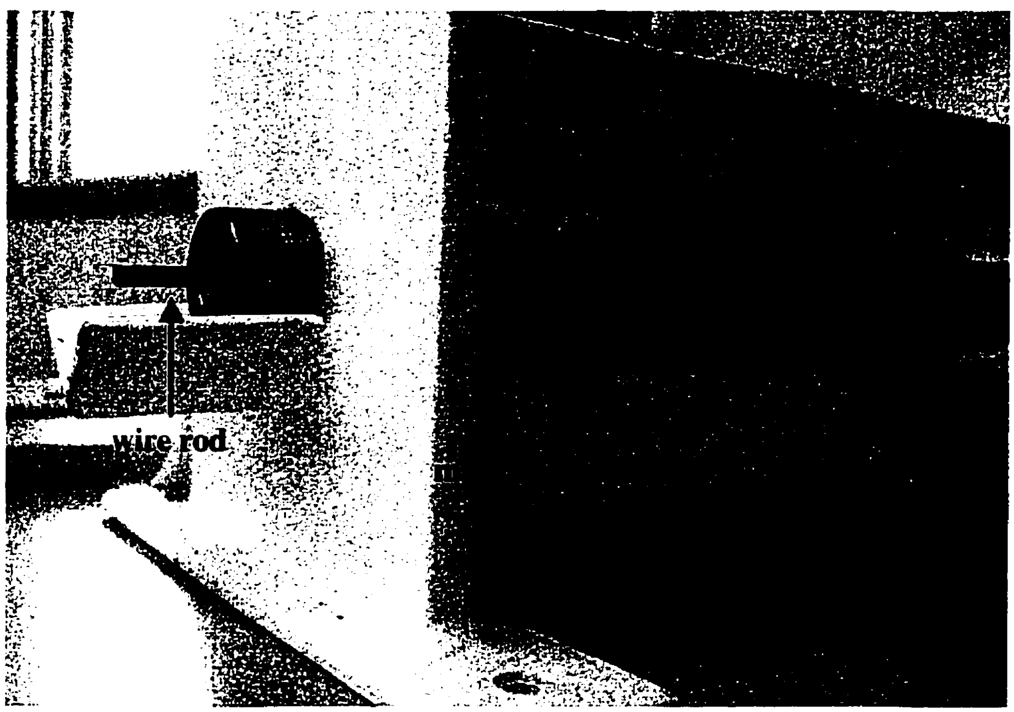

Figure 4.19 Laboratory wire drawing unit.

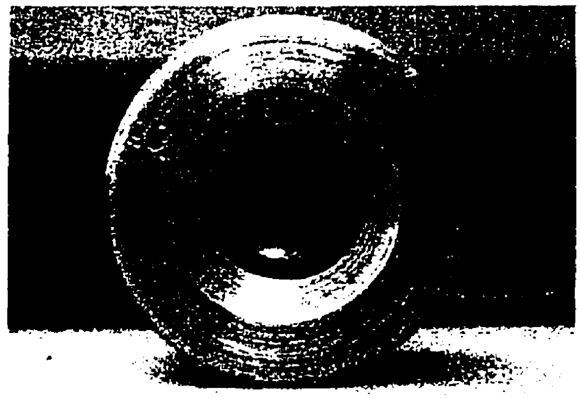

Figure 4.20 Wire die for drawing unit.

4.2.7 Cutting

The aspect ratio is another parameter considered in the testing schedule. It influences the fracture behavior of the material, as evidenced by workability diagrams (Chapter 2).

The drawn wire specimens were cut to the desired aspect ratio using a micro-lathe. The aspect ratios were maintained at or below 1.6 to prevent buckling.

Metallographic analysis was performed at a magnification of X100 using an optical microscope to determine decarburization and cleanliness ratings of spheroidized materials from Heats 1 to 5 and hot rolled materials from Heats 6 and 7. The ASTM E1077 [1997] and IFI 140 [1993] standards were used for the decarburization evaluation. The ASTM E45 [1984] standard was used for the cleanliness rating; acceptable cleanliness for cold heading materials is A2H, B2H, C2H and D2H maximum.

The 'partial' decarburization results (Table 4.6) easily pass the acceptability standards. The 'total' decarburization was determined to be nil for all the test materials. The cleanliness results (Table 4.7) are equally acceptable. Criteria for decarburization and cleanliness often depend on customer specifications. The results presented for the test materials exceed the more stringent criteria observed in most customer specifications for cold heading materials.

Material	Decarburization Results (ASTM E1077 rating) [mm]
Heat 1 – spheroidized	0.008 0.008 0.008 0.000
Heat 2 – spheroidized	0.008 0.008 0.000 0.000
Heat 3 – spheroidized	0.008 0.008 0.008 0.000
Heat 4 – spheroidized	0.000 0.000 0.000 0.000
Heat 5 – spheroidized	0.000 0.000 0.000 0.000
Heat 6 – as-rolled	0.000 0.000 0.000 0.000
Heat 7 – as-rolled	0.000 0.000 0.000 0.000
Heat 7 – spheroidized	0.1 0.1 0.1 0.1

Table 4.6 Decarburization evaluation of test materials.

Material	Cleanliness Results (ASTM E45 rating)
Heat 1	A1; D1
Heat 2	A1; C1; D1
Heat 3	A1; D1
Heat 4	D1
Heat 5	A1; D1
Heat 6	A1; D1
Heat 7	A1; D1

Table 4.7 Cleanliness evaluation of test materials.

CHAPTER 5

METHODS

A finite element method (FEM) program was used to simulate the upset stage of the cold heading process. Numerous inputs are required for an accurate simulation of the cold heading process as shown in Figure 5.1. These inputs include the configuration of specimen and dies, the stress-strain relationship of the material, i.e., constitutive model and parameters, a fracture criterion, the friction conditions, and the kinematics of the process.

These inputs were obtained using the Cam Plastometer (CP) Test, the Drop Weight Test (DWT), and the Friction Ring Test (FRT). The Cam Plastometer is employed to determine the flow stress at low and high strain rates, and at two nominal temperatures. The Drop Weight Test is utilized to compress specimens to failure and to determine the fracture limit of test materials. The Friction Ring Test is employed in conjunction with the DWT to determine friction values.

Once the input parameters have been determined and the FEM models are satisfactory, the models may be used as predictive tools.

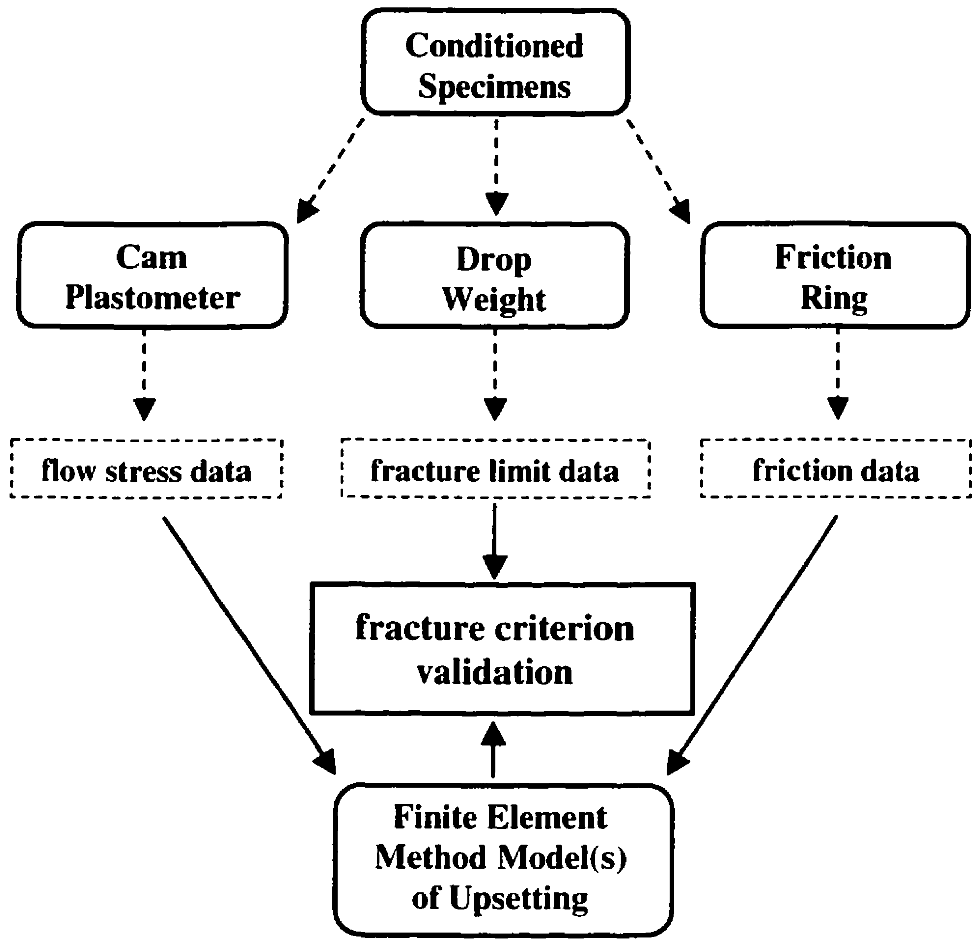

Figure 5.1 **Schematic of test design.**

5.1 Cam Plastometer

The original intent for determining flow stress data was to combine uniaxial tensile test results with high strain rate Hopkinson Pressure Bar Test (HPBT) results. The HPBT offers several advantages, in particular, the calculation of stress within the deforming workpiece without the use of a load cell and the measurement of strain without monitoring the specimen length [Follansbee, 1986]. In addition, it can achieve the strain rates observed during upsetting in industrial cold heading (100-200 s^{-1}) [Yoo et al., 1997]. However, the HPBT is only able to obtain constitutive parameters for small strains (0.1-0.2). Axial strains in cold heading typically exceed 1. Re-testing previously compressed specimens following re-machining of the barrel is possible; however, this is difficult due to the size of the specimens. In addition, the accumulated heat of deformation would be lost. For these reasons, it was decided that the CP would be better suited for obtaining flow stress data.

The CP is a compression testing machine that is capable of achieving strain rates of up to 200 s^{-1} and performing constant true strain rate experiments over a large range of strains and testing temperatures [Atack, 1984; Follansbee, 1989]. In addition, the CP can compress cylindrical specimens homogeneously to a 70% reduction in height (axial strains over 1), depending on the formability of the material being tested, the friction conditions at the interface, and the specimen aspect ratio. The major advantage of the CP is that it allows the determination of constitutive parameters such as σ_o, K, m, n and β (see equations 2.12 and 2.13).

The test involves compressing cylindrical specimens between two flat dies. An axial compressive load is transferred to the test specimen from a large rotating flywheel via a cam. The cam follower is inserted between the cam and the lower die that is driven upwards while the upper die remains stationary. The cam is driven at a known speed by a variable-speed d.c. motor through two multiple-speed transmissions [Baragar, 1989]. The total compressive load is applied in one pass of the cam lobe, and the specimen is compressed to a pre-determined extent.

The cam plastometer employed for this investigation is located at the Metals Technology Laboratories – CANMET (Figures 5.2 to 5.5). The rotational speed of the cam is measured by a magnetic pickup from a 120-tooth sprocket on the flywheel shaft [Baragar, 1989]. The rotational speed may be varied from 100 to 1200 rpm, providing strain rates ranging from 5 to 160 s^{-1} on the specimen design height (14.5 mm).

A photo cell is used to determine the position of the cam lobe relative to the hit position. A MINC PDP 11/23 microcomputer administers the testing. The microcomputer receives signals from the photocell, and synchronizes the firing of the cam follower into the hit position. The specimen is actually compressed on the next rotation of the cam lobe. The microcomputer then retracts the cam follower to prevent secondary specimen compression. A hydraulic wedge pulls towards the direction of the cam rotation to accommodate the gap in the load train that is created during the compression.

Specimens for high temperature testing are drilled along the diameter at half-height. A chromel-alumel K-thermocouple is inserted into the hole and held in place by peening the surrounding metal. The output of the thermocouple is displayed on a strip-chart recorder.

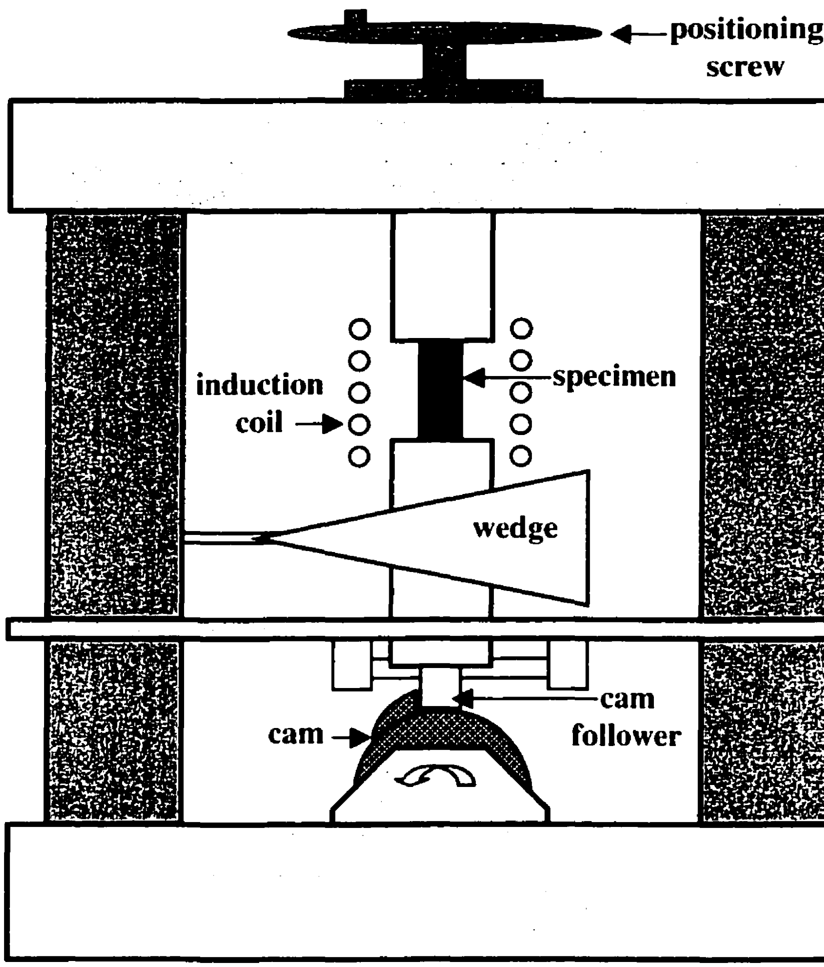

Figure 5.2 Schematic of the cam plastometer [Baragar, 1989].

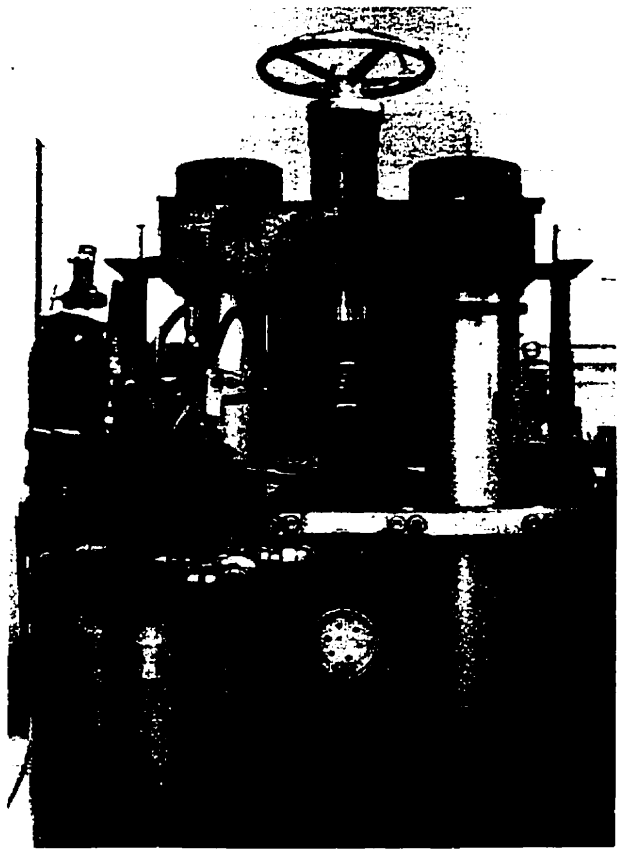

Figure 5.3 Photograph of the cam plastometer at CANMET.

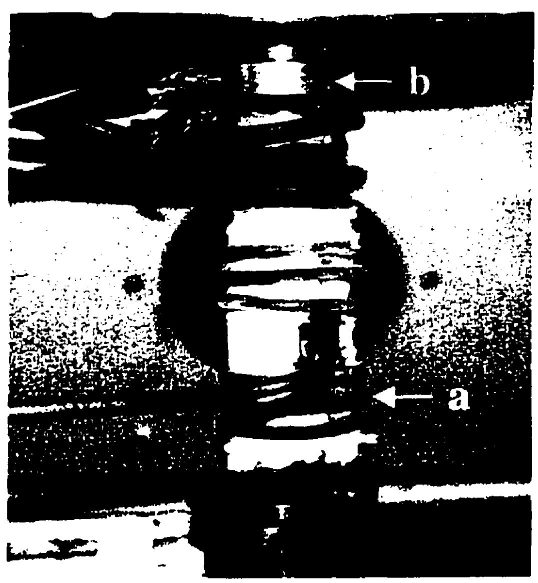

Figure 5.4 Photograph of the die assembly: (a) the induction coil, and (b) the load cell on the cam plastometer.

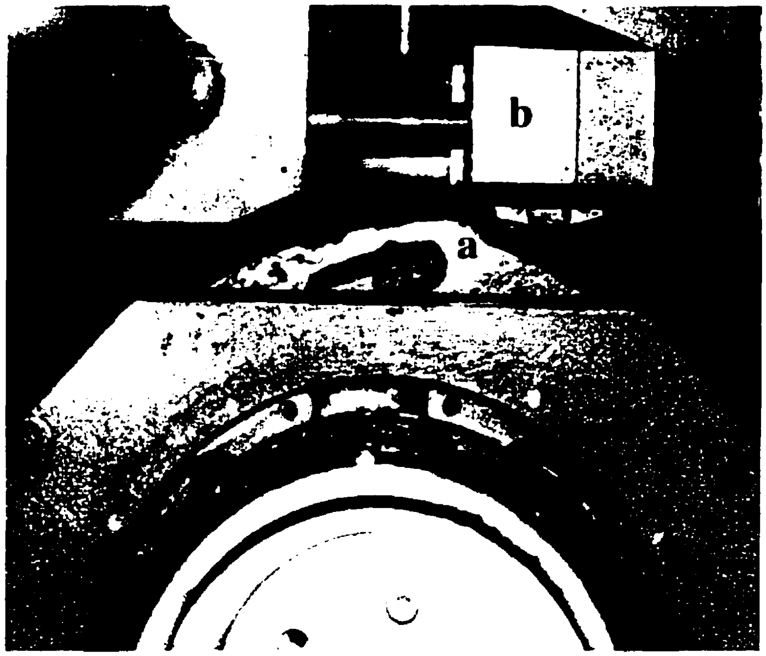

Figure 5.5 Photograph of the (a) cam and (b) cam follower on the cam plastometer.

An induction heating unit makes high temperature testing possible. The specimen is shrouded in argon during heating and testing to prevent oxidation. The maximum attainable testing temperature is 1300°C.

The load signal is acquired using a Kisler quartz load cell and amplifier. The signal is fed into a Tektronix 2430 digital oscilloscope that has an acquisition rate of 100 MHz with eight-bit resolution. The load signal data are transferred to the microcomputer for conversion to true stress and true strain. The length of the test specimen is calculated from knowledge of the cam lobe profile, the cam angle, and the test time.

The theory of the cam design is presented below [Baragar, 1989]:

$$\varepsilon = \ln \frac{L}{L_o} \tag{5.1}$$

where

ε = true strain (< 0 since $L < L_o$)
L_o = initial specimen length [mm]
L = specimen length [mm]

The true strain rate is achieved by designing the load-applying mechanism in the form of a logarithmic cam.

$$\frac{d\varepsilon}{dt} = \dot{\varepsilon} = \frac{1}{L}\frac{dL}{dt} \tag{5.2}$$

where

$\dot{\varepsilon}$ = strain rate [s^{-1}]
t = time [s]

Therefore, the radius of the cam increases or decreases to satisfy equation 5.3, which holds at any time, t, and only for a constant true strain rate test [Baragar, 1989; Follansbee, 1989].

$$\varepsilon = \xi t = \ln\frac{L}{L_o} \tag{5.3}$$

where

ξ = constant true strain rate assuming specimen design height (14.5 mm) (s^{-1})

The specimen length may be computed at any time during the deformation from equation 5.4:

$$L = L_o e^{\xi t} \tag{5.4}$$

The cam lobe height is equal to the decrease in specimen length. The cam radius at any point is equal to:

$$r = r_o + (L_o - L) \tag{5.5}$$

where

r = cam radius at any point [mm]
r_o = base radius of the cam [mm]

By manipulation of equations 5.4 and 5.5:

$$r = r_o + L_o(1 - e^{\xi t}) \tag{5.6}$$

The time for complete deformation, t_f, and the time at any point during the deformation, t, are computed by equations 5.7 and 5.8:

$$t_f = \theta_m / \omega \tag{5.7}$$

$$t = \theta / \omega \tag{5.8}$$

where

t_f = time for complete deformation [s]
θ_m = total angle subtended by cam lobe [degrees]
θ = angle from the start of the cam lobe [degrees]
ω = speed of cam rotation [degree/s]

The cam profile may be defined by combining equations 5.6 and 5.8:

$$r = r_o + L_o(1 - e^{\frac{\xi\theta}{\omega}}) \tag{5.9}$$

For any given cam, L_o, r_o, and θ_m are fixed quantities. In addition, the ratio ξ/ω is constant. When $\theta = \theta_m$:

$$r = r_o + (L_o - L_f) \tag{5.10}$$

Substituting 5.10 into 5.9:

$$L_f = L_o e^{\frac{\xi\theta_m}{\omega}} \tag{5.11}$$

where

L_f = final specimen length (mm)

Substituting 5.3 into 5.11:

$$\frac{\xi}{\omega} = \frac{\varepsilon_t}{\theta_m} \tag{5.12}$$

where

L_f = L at time t

ε_t = true strain at time t

The profile of the cam lobe that results in a constant true strain rate experiment is determined by substituting ξ from equation 5.12 into equation 5.6:

$$r = r_o + L_o\left(1 - e^{\frac{\varepsilon_t \theta}{\theta_m}}\right) \tag{5.13}$$

The CP test is homogeneous as long as the friction is minimized at the interface between the platens and the specimen ends. Proper lubrication using a molybdenum-disulphide grease reduces barreling. A correction factor (equation 5.14) for barreling is used in interpreting the results, i.e., the stress is based on R_{actual}. Equation 5.14 is based on the final barreled radius and the theoretical radius for no barreling.

$$R_{actual} = R_{th} + \left(\Delta H / \Delta H_{final}\right)\left(R_{final} - R_{th.final}\right) \tag{5.14}$$

where

R_{actual}	= barrel-corrected radius in time [mm]
R_{th}	= theoretical radius for no barreling in time [mm]
ΔH	= change in specimen height in time [mm]
ΔH_{final}	= total change in specimen height [mm]
R_{final}	= final radius measured on specimen [mm]
$R_{th.final}$	= final theoretical radius for no barreling [mm]

The cam plastometer at CANMET was designed for a specimen length of 14.5 mm. If the specimen length is not equal to the design length, the strain rate during testing will vary. Baragar [1989] has shown that small variations in strain rate do not have a marked effect on the measured flow stress.

5.2 Drop Weight Test (DWT)

The drop weight test machine (Figure 5.6) consists of a tower enabling interchangeable weight plates to be dropped from a height of up to 3 m., a compression fixture, and stop blocks. The compression fixture transfers the impact load from the crosshead to the workpiece through a shaft. The whole die set configuration rests on a central column that is welded to the base of the DWT machine. The machine is anchored with grade 8 alloy bolts to a concrete floor.

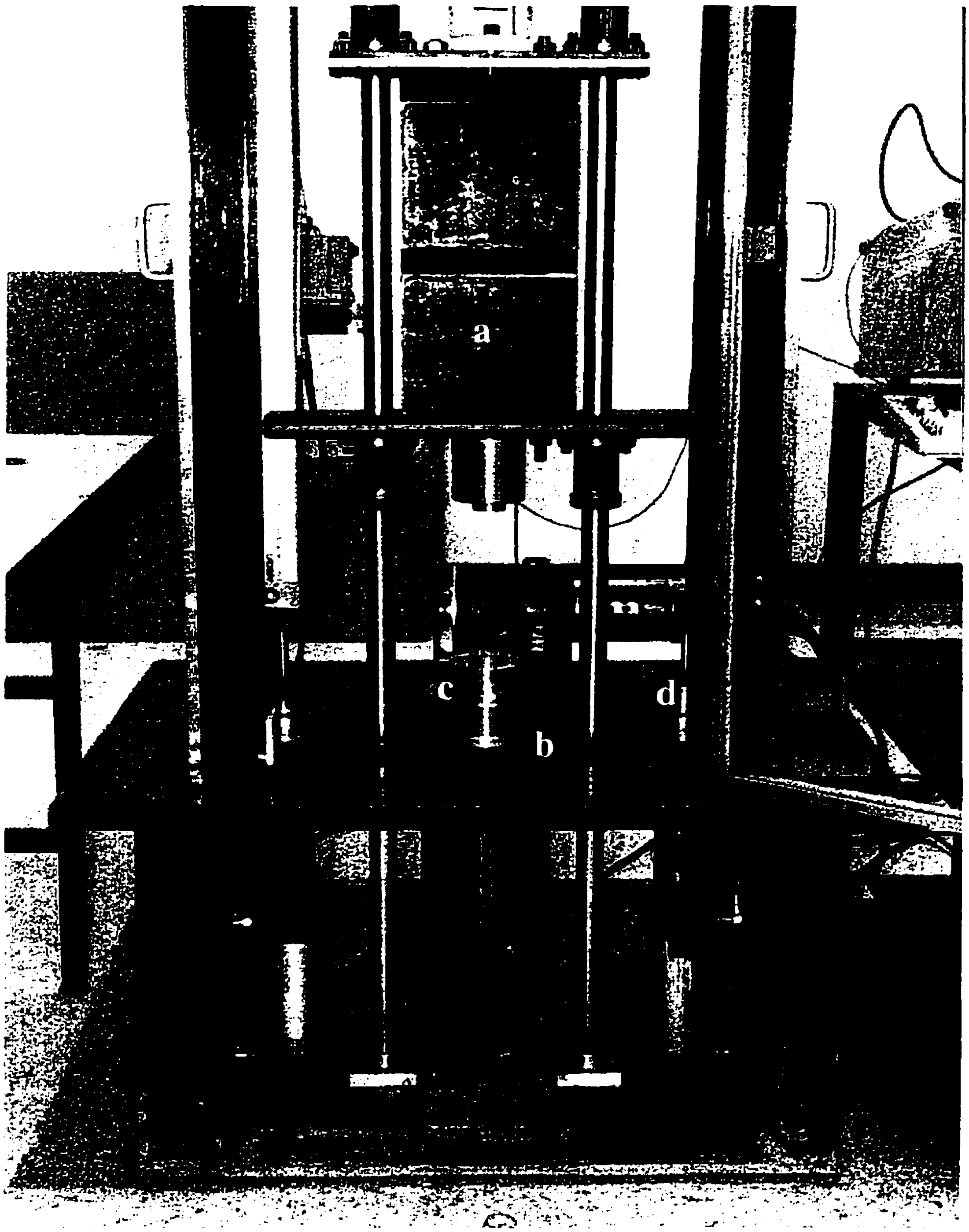

Figure 5.6 Drop weight test machine – (a) weight plates, (b) load cell, (c) die-set configuration, and (d) pneumatic shock absorbers.

A load cell located between the die-set assembly and the central column acquires voltage versus time data. Double integration of these data yields displacement versus time information that may be plotted in terms of load versus displacement. The area under this curve represents the energy absorbed by the test specimen. Pneumatic shock absorbers avoid secondary loading due to rebounding.

A guided cylindrical-pocket die-set was designed for the DWT machine (Figure 5.7).

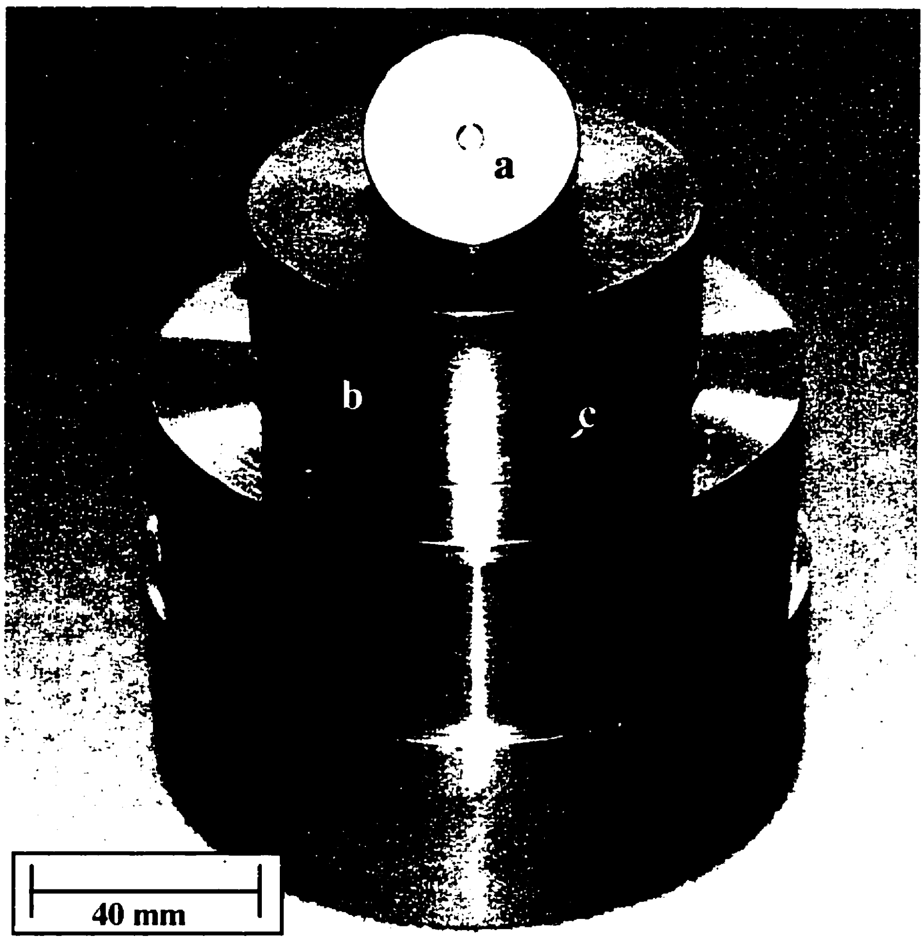

Figure 5.7 Photo of guided cylindrical-pocket die-set for DWT – (a) lower die, (b) die sleeve, and (c) air vent.

A sleeve acts to guide the dies and to reduce die movement during testing. Air vents in the sleeve prevent pressure build-up. The die set is machined from S2 shock resistant alloy tool steel. S2 is designed for maximum toughness and is used for pneumatic tools, punches, and stamps. It has a nominal composition of 0.50% carbon, 0.40 % manganese, 1.10% silicon, and 0.45% molybdenum. Steel blocks were annealed by heating slowly to 780°C and soaking for several hours, followed by cooling at an approximate rate of 25°C per hour. The steel blocks were machined to the desired shape, and the die pockets were drilled into the dies. The finished dies were re-heated to about 880°C, soaked for a few hours and quenched in water. Finally, the dies were tempered to a Rockwell C hardness of 61.

Figure 5.8 is an exploded representation of the drop weight test die-set assembly including the die protection cap, the upper and lower pocket dies, a test specimen, the die sleeve, and the load cell. Figure 5.9 presents a photograph of a test specimen between the upper and lower dies. This assembly rests atop the load cell.

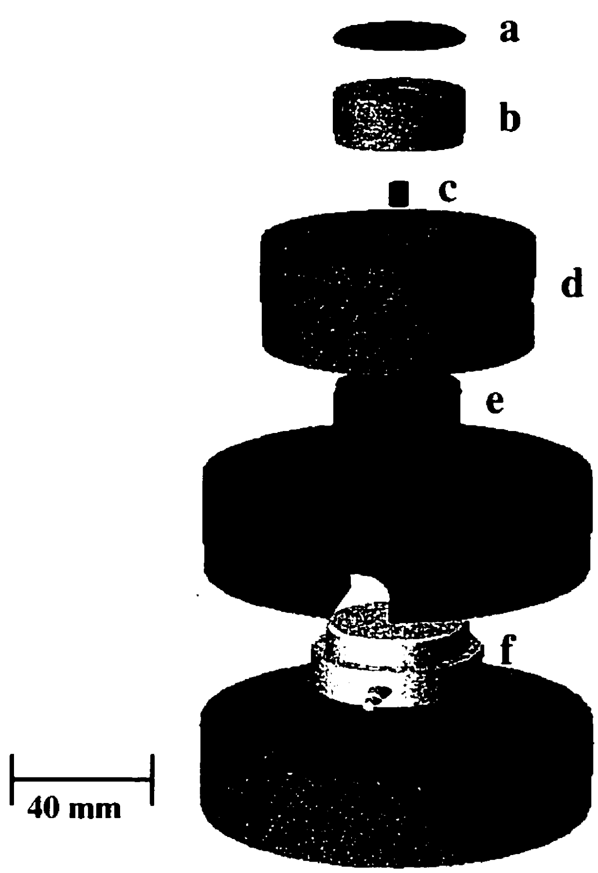

Figure 5.8 Exploded view of the die-set assembly for the DWT including: (a) die protection cap, (b) upper die, (c) test specimen, (d) die sleeve, (e) lower die, and (f) load cell.

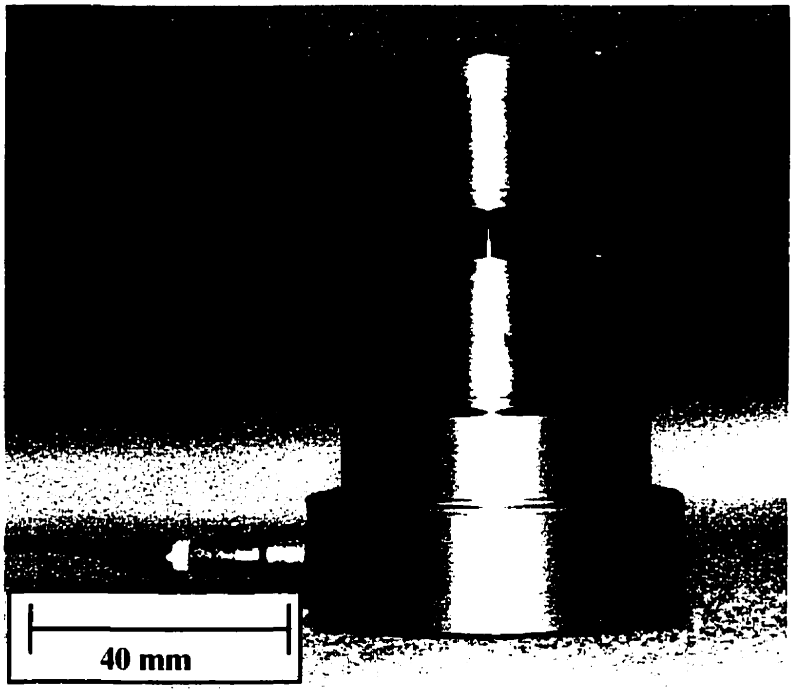

Figure 5.9 Photograph of test specimen between the upper and lower dies. The assembly rests atop the load cell.

The instrumentation of the drop weight test machine consists of a 222 kN PCB quartz force sensor, and a 100 MHz oscilloscope. The oscilloscope records the voltage throughout the DWT experiment. The oscilloscope was set to obtain a total of 10,000 data points in a time frame of 4 ms. The triggering level was set at 150 mV, corresponding to a force of 6.67 kN. This high triggering level was necessary to avoid false triggering due to background noise. Once triggered, the oscilloscope also retained 500 data points prior to triggering. The voltage-time history was converted into load-time history using the linear voltage-load relation. The calibration of the load cell employed for the experiments is traceable to NIST, and complies with ISO 10012-1 and former MIL-STD-45662A.

Drop weight testing can be performed by varying the drop weight or the drop height. In this work, the drop height was kept constant. This ensures a constant initial strain rate, since the crosshead velocity is solely a function of gravitational pull and the drop height.

The drop weight was varied until the deformation to fracture ($\Delta H/H_o$) was determined for each material. The load cell measurements were converted to a load-displacement curve to estimate the energy absorbed by the specimen. The experimental energy results were then compared to a finite element simulation of the DWT. The experimental and simulated deformations were then compared.

In the DWT, the strain rate decreases as the specimen is being compressed until the velocity reaches zero. The initial drop height was selected to yield a much larger strain rates than that used in industry to facilitate fracture.

Once the FEM model has been validated, the parameters of a fracture criterion (see Chapter 2.6.3) may be computed for different materials and microstructures. For a fracture criterion to be valid, the value of the constant(s) for a particular material must be the same for all aspect ratios. The effect of material and process parameters may be determined individually or in combination once the FEM model of the DWT is calibrated.

5.2.1 Fracture Evaluation

Qualitative determination of fracture onset is subjective. Significant attributes for this determination include the crack type (shear versus longitudinal) and the intensity of the crack at the equatorial surface.

Crack type is easily ascertained through visual observation of the specimen. In some cases, an X8 magnifying glass is necessary.

The crack intensity is the more subjective of the two attributes. A three-level crack intensity chart was devised to provide visual interpretation of crack type. Figure 5.10 illustrates the three longitudinal crack intensity levels for DWT specimens: (a) 'no crack', (b) 'ghost-line' crack, and (c) 'open' crack. Figure 5.11 illustrates shear cracks for DWT specimens. Shear cracks are not very common in industry.

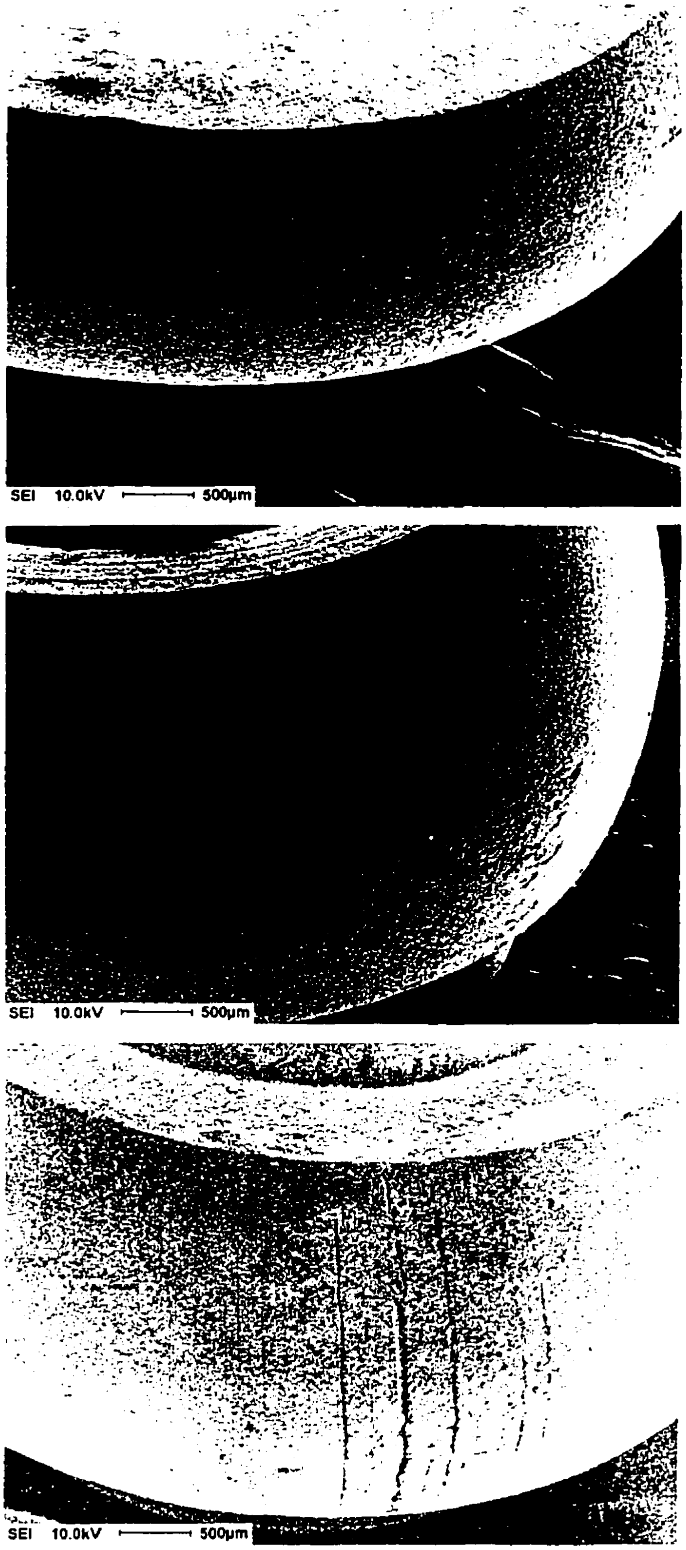

(a) Level 0 - No Crack

(b) Level 1 - Ghost-Line Crack

(c) Level 2 – Open Crack

Figure 5.10 Illustration of longitudinal-crack intensity levels for DWT specimens.

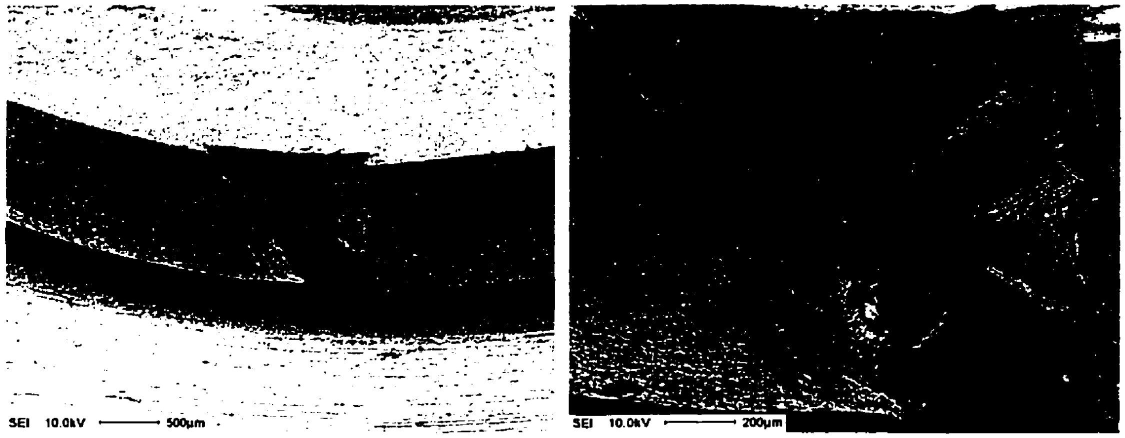

Figure 5.11 Illustration of shear cracks for DWT specimens.

There is no industry standard available to evaluate the surface quality of cold headed parts. Some manufacturers use 100% visual product inspection, while others employ eddy current or laser equipment to detect the presence of surface discontinuities. In this work, the presence of a ghost-line crack (Level 1) signifies specimen failure. A Bausch and Lomb stereo microscope set at X25 was employed to determine fracture initiation, and to evaluate crack intensity. Meticulous attention was paid to regions of undeformed material in the die pockets, just above and below a crack, to ensure that there was no evidence of prior surface irregularities such as wire drawing scratches or mechanical damage. Questionable specimens were discarded, and new specimens tested. However, Heat 6 specimens were tested in spite of containing pits and scratches to determine the sensitivity of the DWT to surface condition.

Photographs of typical DWT specimens, examined using a JEOL JSM-840A scanning electron microscope, are presented in Chapter 6.

5.2.2 Velocity and Displacement Determination

Force, velocity, displacement, and acceleration are interrelated, and this fact may be used to further the analysis of the DWT system. The relationship between these can be derived from first principles by considering an equilibrium diagram of the system. There is a downward force (F_1) equal to the product of the falling mass (M) and the gravitation pull (g), and an opposing force (F_2) that is the product of the falling mass and the deceleration (a). The sum of these forces (F) is:

$$F = Ma - Mg \tag{5.15}$$

$$a = g + \frac{F}{M} = \frac{dv}{dt} \tag{5.16}$$

Therefore,

$$dv = gdt + \frac{F}{M}dt \tag{5.17}$$

where

v	= velocity
t	= time

By integrating both sides

$$\frac{dS}{dt} = v = v_o + gt + \frac{1}{M}\int_{t=0}^{t_1} Fdt \tag{5.18}$$

where

S = displacement

since v = dS/dt and by integration,

$$S_f - S_o = \int_{t=0}^{t_1} vdt \tag{5.19}$$

where

S_o	= initial displacement
S_f	= final displacement

Equation 5.18 may be used to convert the load-time curves to velocity-time curves for an ideal system. The crosshead velocity at impact, v_o, may be computed by equating the kinetic and potential energies.

All the experiments were performed using the same drop height (1.5 m). The maximum theoretical initial velocity was calculated to be 5.42 ms^{-1}. Since the DWT crosshead is not actually in a free fall; there is friction and air resistance that slows the crosshead velocity. This value had to be measured experimentally. Two micro-switches were separately placed at a distance of 1.5 m, each connected to a different channel of the oscilloscope. Upon release of the crosshead, the top micro-switch moved to the closed position, and channel one began recording a signal. Once the drop hammer reached the bottom micro-switch, the switch closure triggered a signal on channel 2. Both signals were recorded and the time difference between them was used to calculate the experimental crosshead velocity at impact.

Assuming the acceleration is constant, the following set of equations was used for computation of the experimental crosshead velocity at impact:

$$S = \frac{1}{2} a t_s^{\,2} + v_i t_s \tag{5.20}$$

where

v_i = initial crosshead velocity [ms^{-1}]
S = distance between micro-switches [m]
t_s = time between signals [s]

The initial crosshead velocity was zero in these experiments.

Therefore,

$$a = \frac{2S}{t_s^2} = \frac{dv}{dt} \tag{5.21}$$

By integration,

$$v_o = \frac{2S}{t_s} \tag{5.22}$$

Experimental determination of the crosshead velocity at impact is presented in Section 6.2.2.

5.3 Friction Ring Test

Friction plays an important role in metal forming operations, and the FRT is commonly employed to determine the shear friction factor ($\bar{m}$) [Danckert and Wanheim, 1988; Sahi et al., 1996; Ellingson, 1999]. The test involves upsetting cylindrical ring specimens between flat parallel dies under given conditions of specimen geometry, strain, strain rate and temperature [Andersson et al., 1996; Sahi et al., 1996]. The change in internal and external diameters of the ring depends on the friction at the die-workpiece interface. If the friction at the interface is zero, the ring deforms as a solid disc, with each element flowing radially outward at a rate proportional to its distance from the center [Kobayashi et al., 1989]. The internal diameter of the ring decreases when the friction is high, and increases when the friction is low (see Figure 5.12) [Sahi et al., 1996].

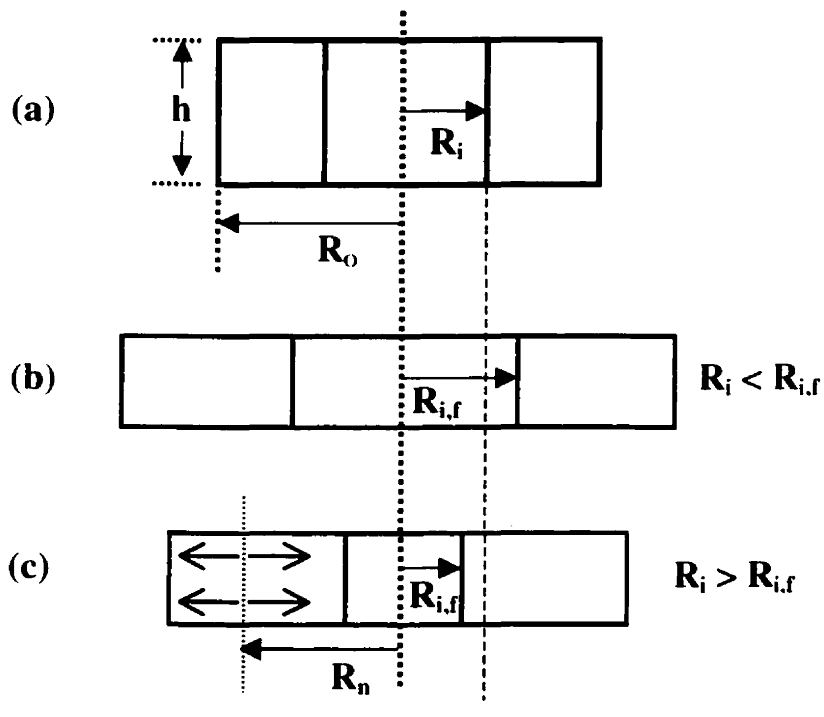

Figure 5.12 Diagram of friction ring testing: (a) undeformed ring specimen, (b) low friction upsetting, and (c) high friction upsetting.

At the neutral radius, R_n, all points are stationary. The value of this neutral radius is directly related to the shear friction factor. If the friction is high, the neutral axis is located within the ring itself ($R_n > R_i$). If the friction is low, the neutral axis radius is smaller than the initial internal radius.

In the FRT, friction produces a tangential (shear) force at the interface between the die and the specimen, and restricts the movement of the specimen [Goetz et al., 1991]. As such, friction has a pronounced influence on forming loads, material flow and wear [Danckert and Wanheim, 1988].

The FRT offers several advantages, in particular no direct load or strain measurements are required, and no yield strength values of the deforming material are needed to determine the friction parameter [Male and Depierre, 1970]. The FRT is easy to conduct, and can be used over a wide range of strain rates and temperatures [Kalpakjian, 1984A; Wagoner and Chenot, 1996]. To determine friction parameters for a particular upsetting operation, actual ring and die materials must be used. Process parameters such as strain rate, temperature and lubrication must also be the same.

Numerous theoretical analyses have resulted in the development of ring calibration curves, including the early works by Avitzur [1968] who performed the analysis through an upper bound mathematical solution, and Hayward and Johnson [1966] who used a stress analysis approach. Theoretical friction ring calibration curves were developed for different ring geometries from these works. The theoretical analyses are based on the following assumptions:

a) there is no non-uniform distortion due to friction (no barreling)
b) the material obeys the Lévy-von Mises stress-strain rate laws with no strain hardening
c) the friction factor, $\overline{m}$, is constant

Since strain hardening occurs, friction ring results must be interpreted with caution. The general assumption is that the ratio of shear stress to yield stress remains constant, and therefore the friction factor remains constant. This can be reasonably justified when the analysis is performed for a small increment of deformation [Male and Depierre, 1970].

Equation 5.23 represents one relation that describes friction in metal forming:

$$\tau_s = -\alpha' Y V^P \tag{5.23}$$

where
- τ_s = interface shear stress
- α^l = friction parameter
- Y = material yield stress in shear [von Mises: Y = yield stress/$(3)^{1/2}$]
- V = tangential velocity (metal with respect to die)
- P = velocity factor

By extension, friction may be described by the shear friction factor relation [Goetz et al., 1991; Dellavia et al., 1977; Tan et al., 1998; Altan et al., 1983]. The shear friction factor, $\overline{m}$, is a function of the specimen material, the lubrication, and the roughness of the die surface:

$$\overline{m} = \frac{-\tau_s}{Y} \tag{5.24}$$

where
- $\overline{m}$ = shear friction factor
- Y = material yield shear stress [MPa]

In equation 5.23, if P equals zero, then $\tau_S = -\alpha^l Y$, where α^l is equivalent to $\overline{m}$. The value of $\overline{m}$ varies from 0.0 to 1.0.

The construction of calibration curves is based on equation 5.24. The change in internal diameter as a function of reduction in height represents a simple method for determining the shear friction factor [Sahi et al., 1996; Altan et al., 1983; Tan et al., 1998; Danckert and Wanheim, 1988; Dellavia et al., 1977; Goetz et al., 1991; Kalpakjian, 1984B]. A common specimen geometry has a 6:3:2 ratio for outer diameter, inner diameter, and thickness.

Figure 5.13 is a theoretical friction ring calibration chart for the 6:3:2 geometry as adapted from Kalpakjian [1984B]. The cylindrical surfaces of the ring specimen tend to barrel slightly. Therefore, it is important to measure the average diameter.

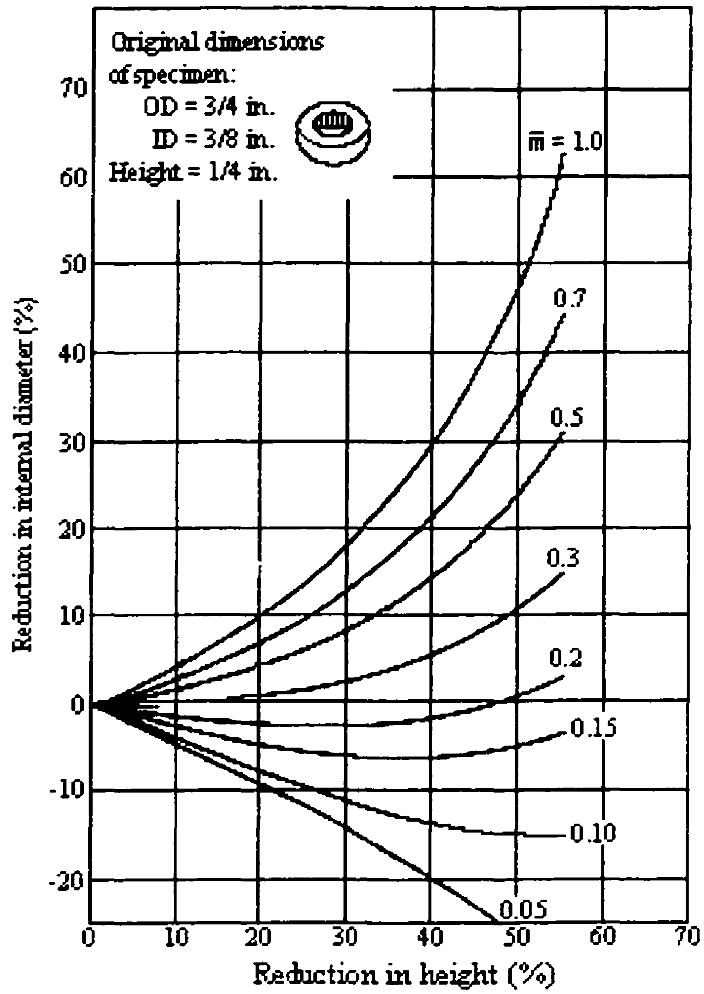

Figure 5.13 Theoretical friction ring calibration chart for the 6:3:2 geometry as adapted from Kalpakjian [1984B].

Another method of determining the friction parameter is to use FEM simulations of the FRT [Andersson et al., 1996]. This may be accomplished by varying the friction parameter until the final geometry of the simulation matches the experimental one. For the present work, the friction parameter will be determined using FEM simulations. Friction ring calibration charts will only be used as a check.

A flat die set of the same material as the DWT dies (S2 tool steel), lubricated with the same type and quantity of molybdenum-disulphide employed in the DWT, was used in this FRT work. A stopper was used to arrest the upper die at approximately 50% deformation, as suggested in the literature. The stopper is composed of Celazole Polybenzimidazole (PBI), an engineering thermoplastic that has the highest mechanical properties of any plastic up to 205°C. A photograph of the FRT set-up is shown in Figure 5.14.

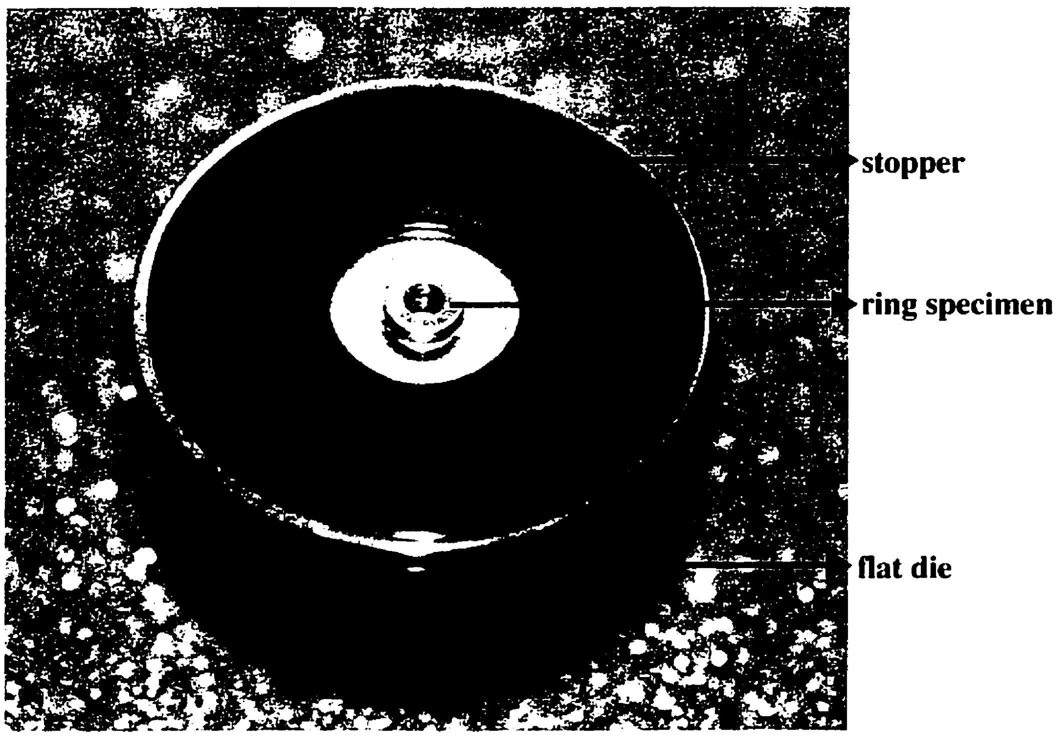

Figure 5.14 FRT set-up including ring specimen, stopper, and flat die.

5.4 Forge2 – Finite Element Method

Many FEM packages are capable of simulating plastic deformation of metals. Forge2 was developed approximately 20 years ago at the Ecole des Mines de Paris. The Forge2 code is capable of handling metal flow during forging and other metal forming operations. Problem symmetry decreases computational requirements.

Forge2 was developed for two-dimensional plane strain, or axisymmetrical operations such as upsetting. It is Windows-based, and includes automatic mesh generation and re-meshing capabilities. The general organization of Forge2 is illustrated in Figure 5.15.

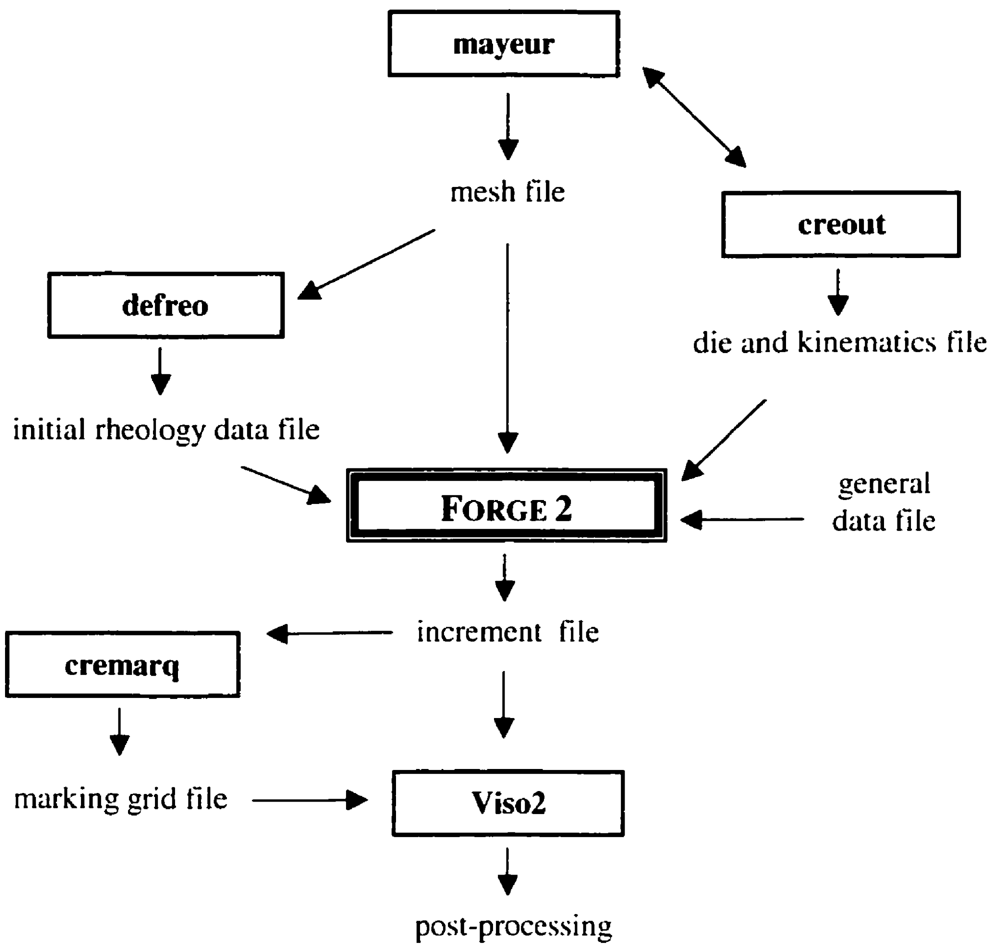

Figure 5.15 General organization of Forge2.

The *mayeur* function is used to create the initial specimen contour and the mesh, and to define eventual symmetry axes. The *creout* function allows the user to define the geometry of the dies, the velocity and the piloting of the tools (constant velocity, tool drop, mechanical press, etc.). A general data file allows the user to define the materials rheology, the friction conditions, the mean strain allowed for each time increment, and the user parameters such as the Cockcroft and Latham ductile fracture parameter. The *defreo* function allows the user to set initial values at nodal positions.

The Forge2 function utilizes all the inputs from *mayeur*, *creout*, and *defreo*, and performs the FEM computations. The results of each increment are recorded in an increment file for use by the post-processor. The *Viso2* post-processor reads the increment files, and displays the simulation results in graphical form. At any chosen increment, *Viso2* can generate plots of the deformed mesh, including the dies and the contact nodes. In addition, it is capable of plotting strain and stress distributions, and any user-defined parameters. It is also capable of providing the evolution of the total forging load.

During the simulation, the code may become unable to perform additional computations due to mesh distortion or to mesh penetration into the dies. The Forge2 code is capable of automatically remeshing a distorted mesh. The *mayeur* function regenerates a new mesh within the contour of the deformed geometry, and the *defreo* function interpolates cumulated strains at the new nodal positions [Verreman, 1996; Forge2, 1998]. Forge2 then restarts with the appropriate historical data from the general data file. Clearly, the re-meshing capability is of great value.

Automatic re-meshing is only possible with triangular, three-node or six-node elements. The use of triangular, six-node elements makes visualization of the deformed mesh difficult. Numerous re-meshing steps that may be required during a particular forging operation further complicate the visual interpretation of the deformed mesh. To overcome this difficulty, a tool (*cremarq*) has been added to Forge2 that creates a marking grid composed of square elements superimposed on the initial mesh. It aids the user to better visualize the deformation.

In this work, the Forge2 code was used to simulate rigid-plastic material behavior. Forge2 assumes that the material obeys the Lévy-von Mises incremental flow rule according to equations 5.25 [Verreman, 1996; Verreman, 1998, Le Floc'h, 1986]:

$$\frac{\{s\}}{\sigma_{eq}} = \frac{2\{\dot{\varepsilon}\}}{3\dot{\varepsilon}_{eq}} \quad (5.25)$$

where

$\{s\}$ = deviatoric stress tensor
σ_{eq} = equivalent stress
$\{\dot{\varepsilon}\}$ = strain rate tensor
$\dot{\varepsilon}_{eq}$ =equivalent strain rate

Here the equivalent stress is related to the equivalent strain rate using the Norton-Hoff relation:

$$\sigma_{eq} = \kappa\sqrt{3}\left(\sqrt{3}\dot{\varepsilon}_{eq}\right)^m \quad (5.26)$$

where

κ = consistency = $f(\varepsilon_{eq},T) = K_o(\varepsilon_o+\varepsilon_{eq})^n \exp(\beta/T)$
ε_{eq} = von Mises equivalent strain = $f(\varepsilon_0, \varepsilon_r, \varepsilon_z)$
m = strain rate coefficient
ε_o = strain hardening regulation term ~ 0.0001
K_o = strength coefficient (~ yield constant)
n = work hardening coefficient
β = temperature coefficient
T = temperature

The code must determine nine unknowns for small time increments (Δt). The unknowns include the 6 stresses (σ_{ij} where i, j = 1, 2, 3) and the 3 velocities (v_i where i = 1, 2, 3). This is accomplished using nine equations: 3 equilibrium equations and 6 equations from the Lévy-von Mises rigid plastic behavior law. At each time increment, the Forge2 code loops by repeating the following steps [Verreman, 1996]:

(a) compute the velocity field (see variational formulation below) and corresponding strain rate and stress tensors at time t

(b) determine the time increment (see below)

(c) update the configuration for next increment of deformation (equations 5.27 and 5.28):

$$X(t+\Delta t) = X(t) + \bar{v}(t)\Delta t \tag{5.27}$$

$$\varepsilon_{eq}(t+\Delta t) = \varepsilon_{eq}(t) + \varepsilon_{eq}\Delta t \tag{5.28}$$

Once the user-defined criterion for the simulation is met, e.g., final deformation height or velocity criterion, Forge2 terminates the computation.

(a) Details for computation of velocity field at time t

The velocity field is computed by the FEM at each increment from a variational formulation derived from the virtual power principle and the boundary conditions $(\bar{v}_{metal} - \bar{v}_{die})\bar{n} = 0$. The functional that needs to be minimized is essentially the sum of the three terms: the strain power, the condition of constant volume, and the friction power [Verreman, 1998].

$$\varphi(\bar{v}) = \int_{\Omega} \frac{\kappa}{m+1}\left(\sqrt{3}\dot{\varepsilon}_{eq}\right)^{m+1} d\Omega + \frac{1}{2}\eta \int_{\Omega} \kappa\left(\mathrm{div}(\bar{v})\right)^2 d\Omega + \int_{S_c} \frac{\alpha' \kappa}{P+1}\left\|\Delta\bar{v}\right\|^{P+1} dS_c \tag{5.29}$$

where

Ω = volume of the domain occupied by the body at a given time t
S_c = contact surface of the domain occupied by the body at a given time t
η = large positive ($\sim 10^7$-10^9) constant penalizing the volumetric strain rate
α' = friction parameter
P = velocity factor

The first term in the functional accounts for strain power, the second term accounts for volume conservation, and the third term accounts for friction power.

The functional is discretized by the code, and the velocities (v_x and v_y for 2D) at each node of the mesh are obtained. Minimization of the functional gives a system of non-linear equations that are solved using the Newton-Raphson method through an iteration loop until the convergence criteria are satisfied [Verreman, 1996, 1998].

(b) Details for determination of time increment

The time increment is determined once node and tool contact exists, or when one of the following limiting criteria is met:

$$\Delta\varepsilon_{eq} = \dot{\varepsilon}_{eq}\Delta t = x\% \tag{5.30}$$

$$\left(\Delta\varepsilon_{eq}\right)_{max} = 2.5x\% \tag{5.31}$$

The criteria presented in equations 5.30 and 5.31 ensure that the chosen time increment is sufficiently small so that the loss in volume during the simulation step is minimal. The value of the x% criterion was set to 2% for the FEM simulations in this work. This value should be reduced if the total volume loss during the simulation becomes unacceptable (> 2-3%).

Chapter 6

RESULTS

6.1 Cam Plastometer

Flow curve parameters and constitutive relations can be developed by testing under conditions representative of the process being modeled. The test conditions include stress and strain state, strain rate, and temperature.

6.1.1 Test Results

Flow curves were obtained for 4 of the 7 matrix materials in the as-rolled and spheroidize annealed conditions. The materials are from the same grade, i.e., 1038, but the residual element content differs from heat to heat. This can affect flow behavior. Indeed, indications of such differences were evident in the tensile and reduction-of-area results presented in Chapter 4.

Heats from each of the three billet suppliers were selected for CP testing: Heat 1 (Ivaco), Heats 4 and 5 (QIT) and Heat 6 (Açominas). The two QIT heats were chosen to determine the effect of nitrogen level. Heat 1 was chosen for comparison purposes since it has a nitrogen content similar to that of Heat 4. Heat 3 (Ivaco) was not selected since preliminary DWT showed this heat would be unacceptable for cold heading applications. Heat 6, with its low nitrogen and residual element content, was selected as a benchmark.

Flow stress data was obtained at two strain rates and in two temperature ranges. CP testing was performed at two nominal strain rates, 20 and 150 s^{-1}, up to strains of approximately one. Ambient temperature testing was performed at both strain rates since this is roughly the temperature at which cold heading begins. CP testing was also performed at a nominal temperature of 500°C to ascertain the flow behavior at the temperature encountered during flow localization. Table 6.1 illustrates the test parameters for determining the constitutive model data.

Temperature	Strain Rate [s^{-1}]
ambient temperature	20 and 150
500°C	20 and 150

Table 6.1 CP test parameters for determining constitutive model data.

As mentioned in Chapter 5, the CP is capable of performing constant strain rate tests on specimens of standard height (14.5 mm). Since the diameter was fixed at 5.21 mm in this work, it was not possible to use standard specimens due to the probability of buckling with an aspect ratio approaching 3. In addition, the crosshead distance was fixed at 3.94 mm, thus limiting the amount of strain that could be achieved on larger specimens. To allow the axial strain to at least approach one during compression, an aspect ratio of 1.17 was selected. For this reason, the strain rate was not constant throughout testing. The nominal strain rate of 20 s^{-1} actually ranged from 7 to 22 s^{-1}, while the nominal strain rate of 150 s^{-1} ranged from 75 to 180 s^{-1}. The actual strain rate corresponding to each data point in a given range was calculated and taken into account when determining the constitutive parameters.

Figures 6.1 to 6.8 present the true stress versus true strain behavior of the 4 matrix materials chosen for CP testing in the as-rolled and spheroidize annealed conditions. Each figure presents the data obtained at the two strain rates and the two nominal test temperatures.

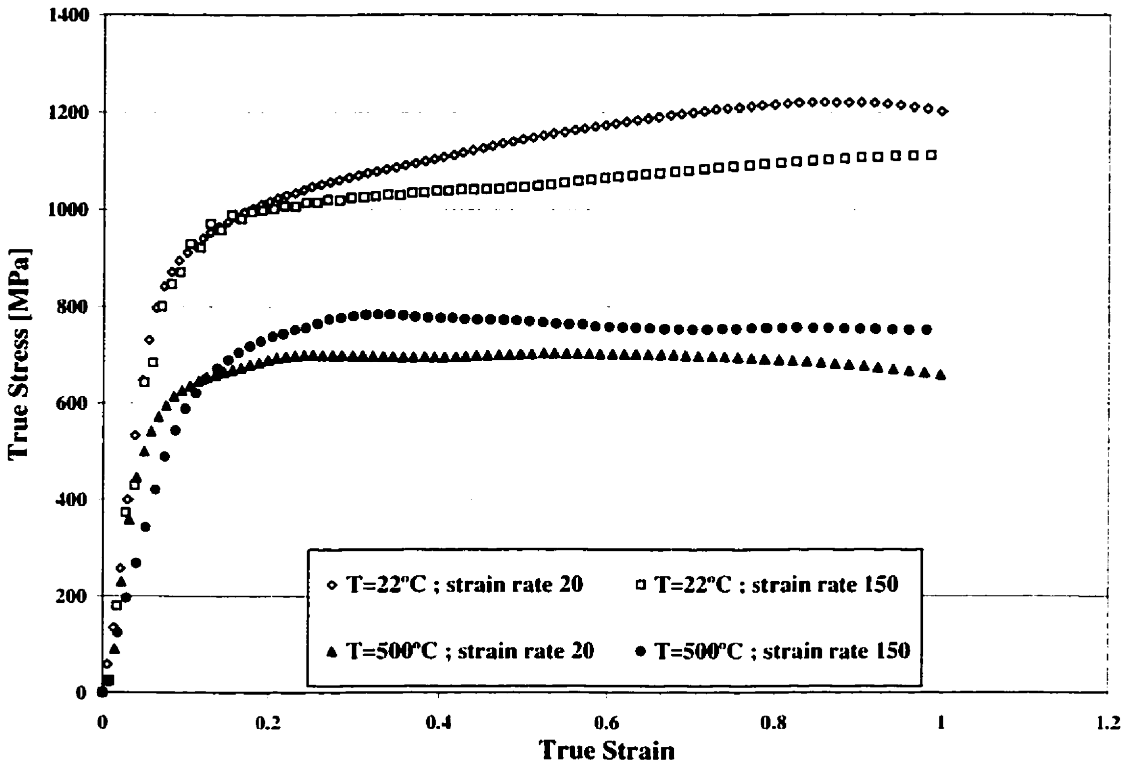

Figure 6.1 Heat 1 as-rolled. CP true stress-true strain results.

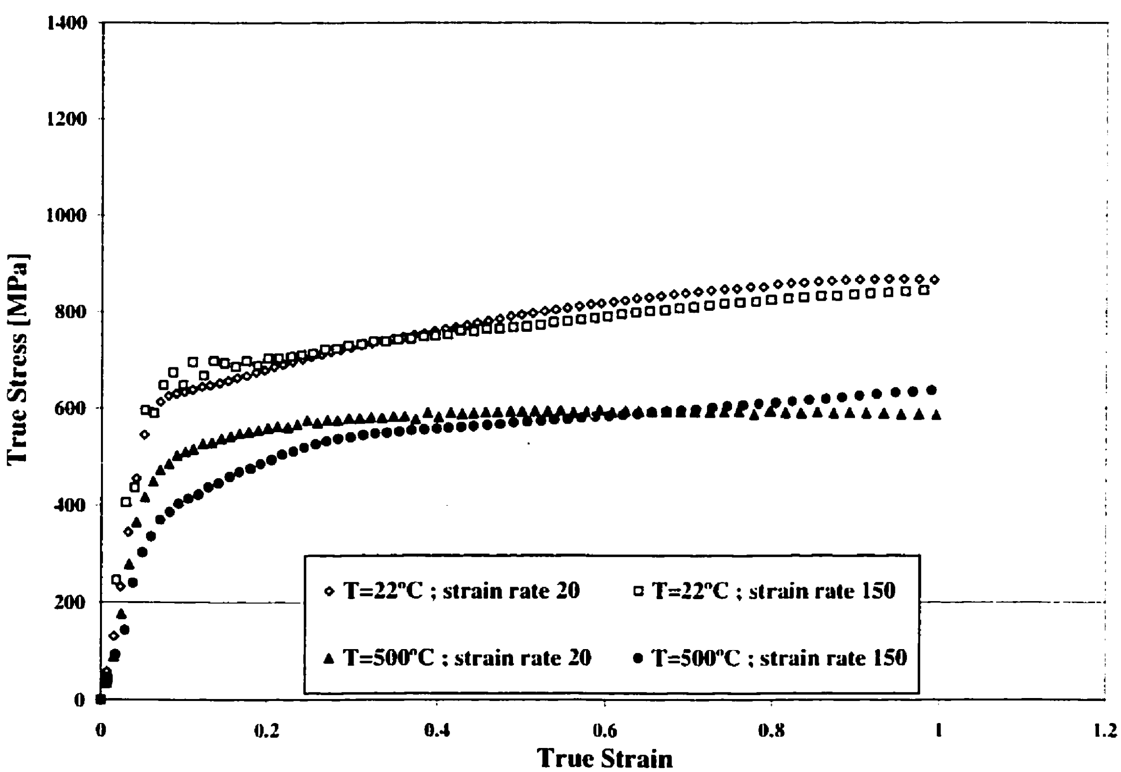

Figure 6.2 Heat 1 spheroidized. CP true stress-true strain results.

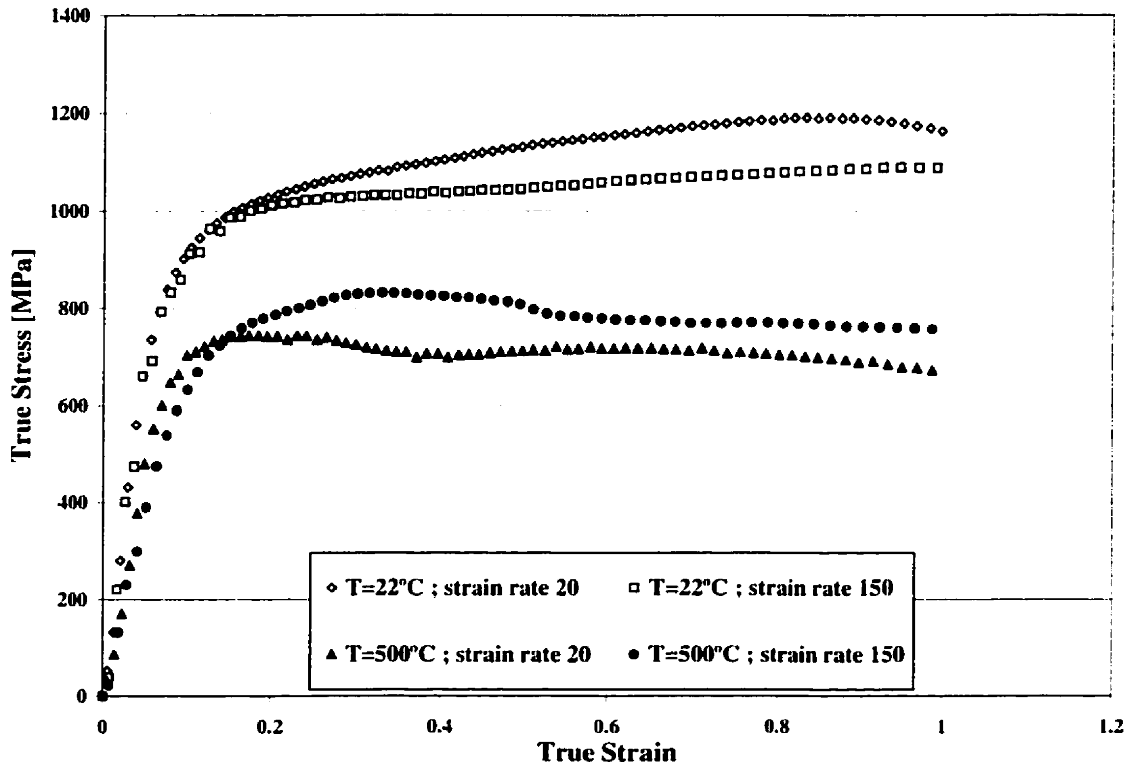

Figure 6.3 Heat 4 as-rolled. CP true stress-true strain results.

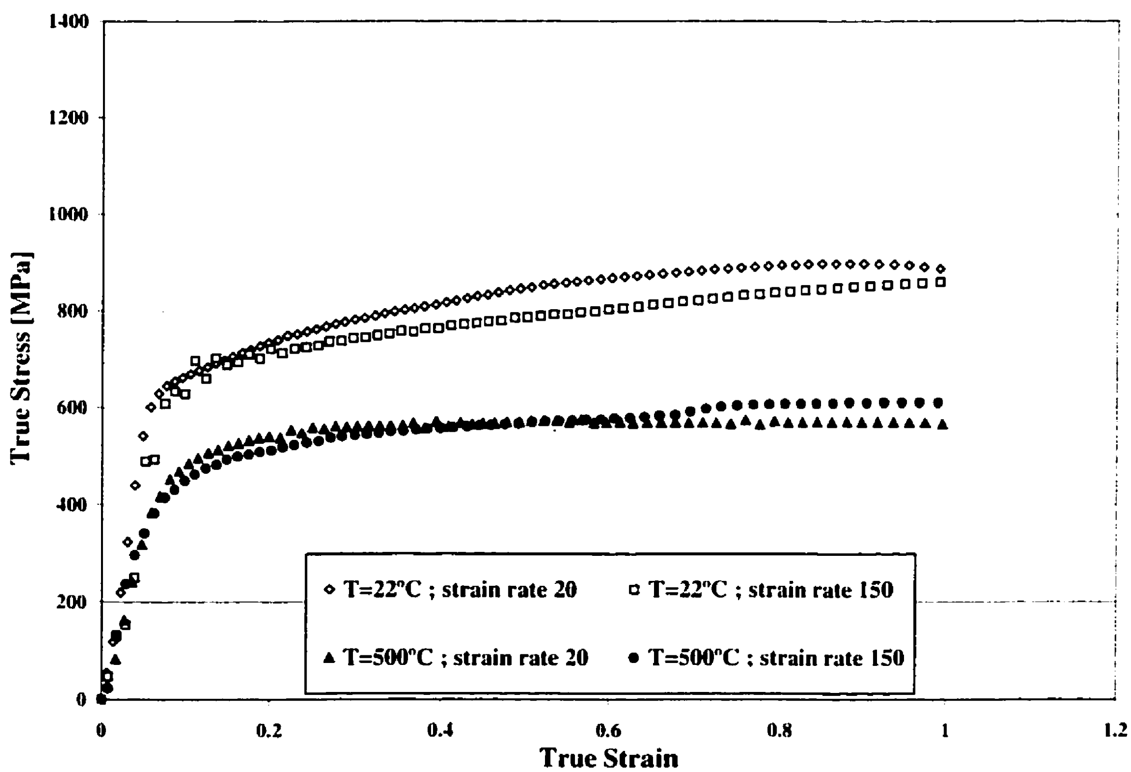

Figure 6.4 Heat 4 spheroidized. CP true stress-true strain results.

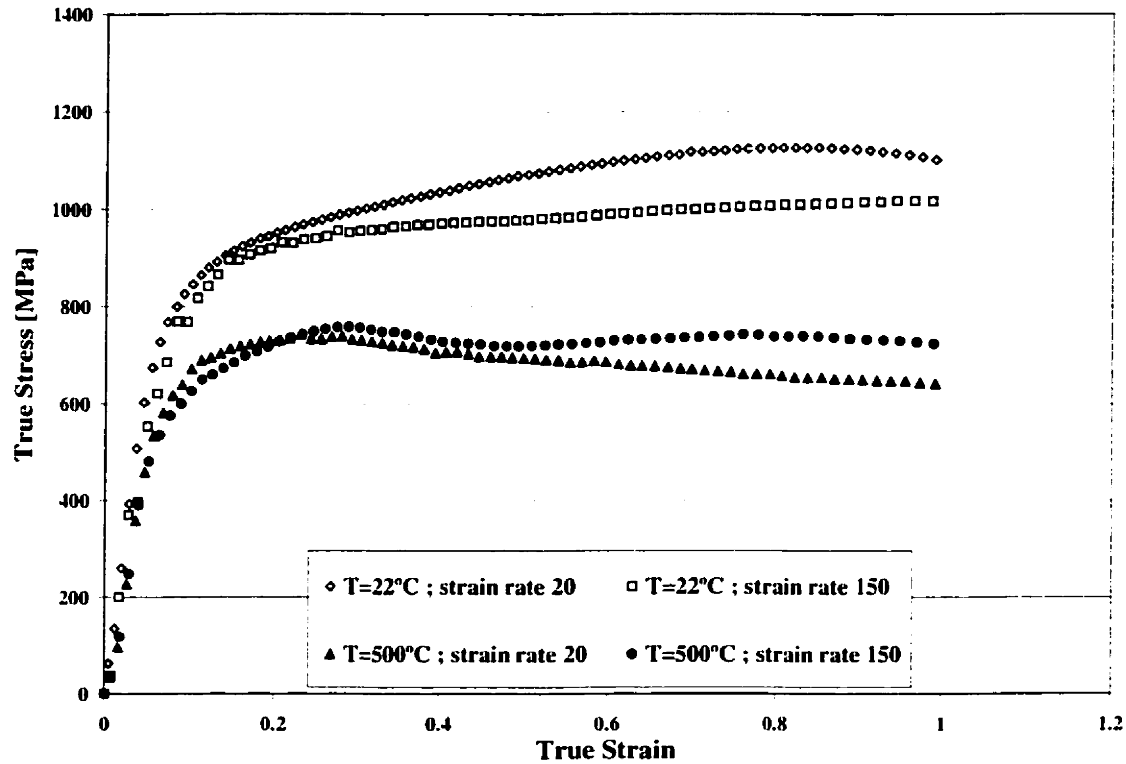

Figure 6.5 **Heat 5 as-rolled. CP true stress-true strain results.**

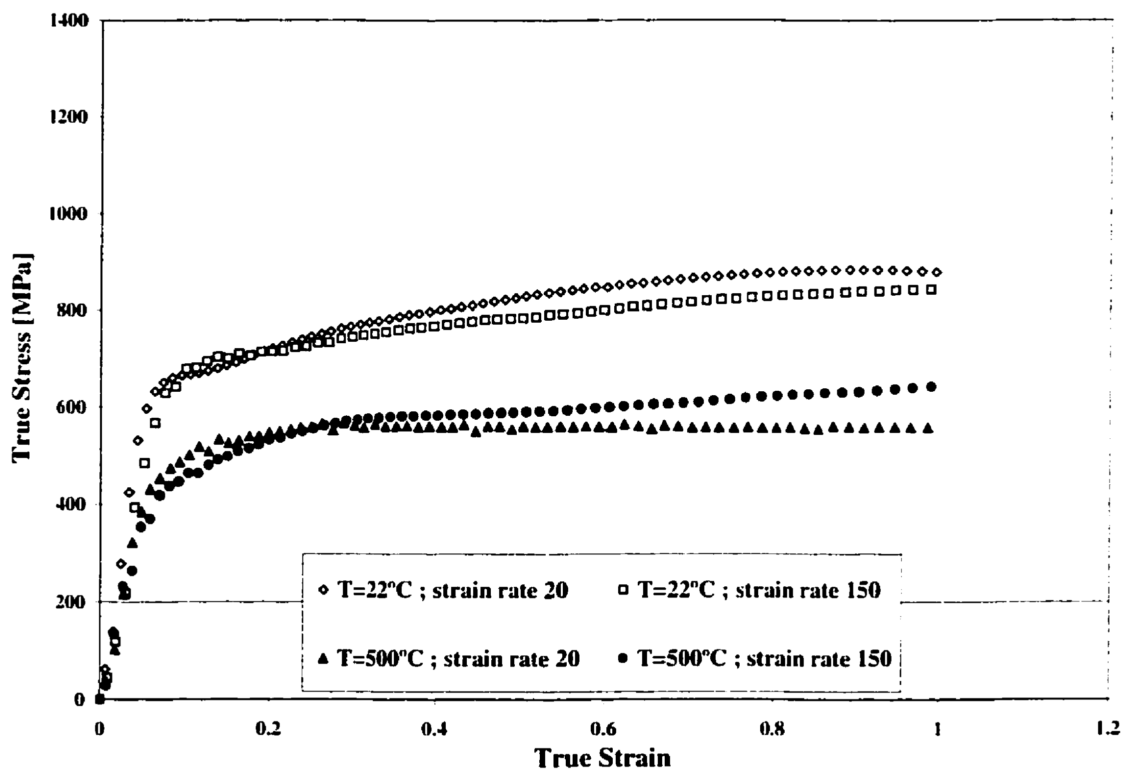

Figure 6.6 **Heat 5 spheroidized. CP true stress-true strain results.**

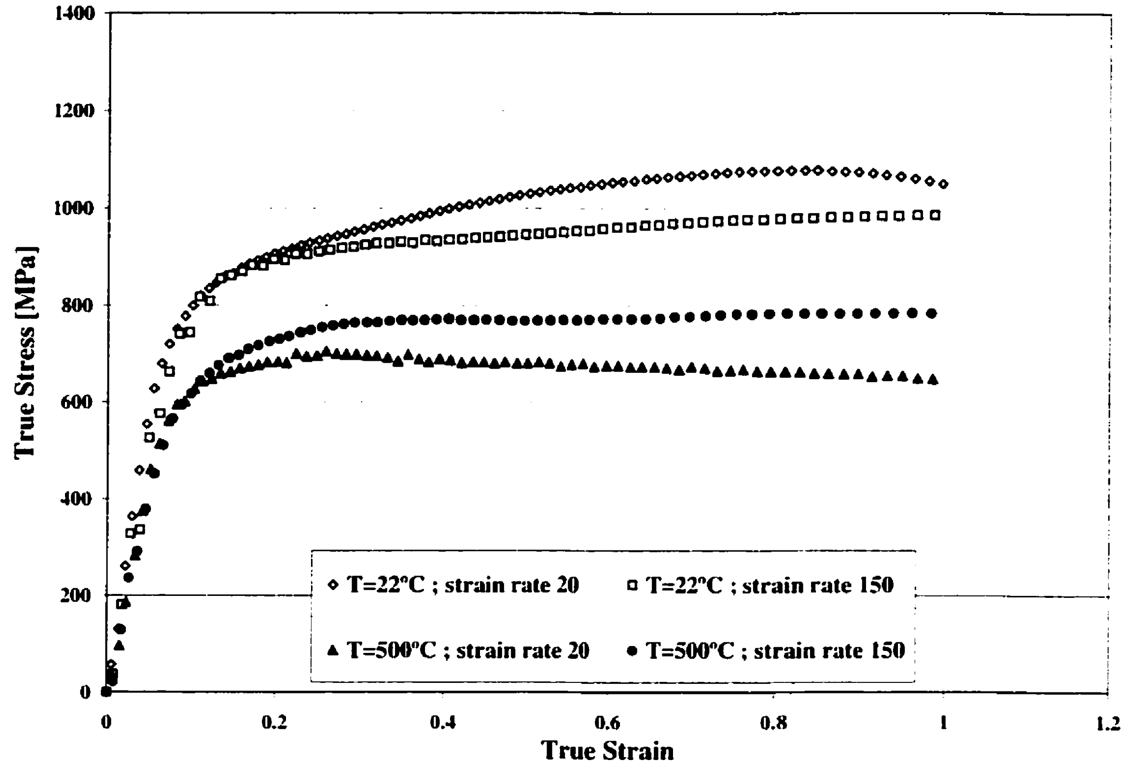

Figure 6.7 Heat 6 as-rolled. CP true stress-true strain results.

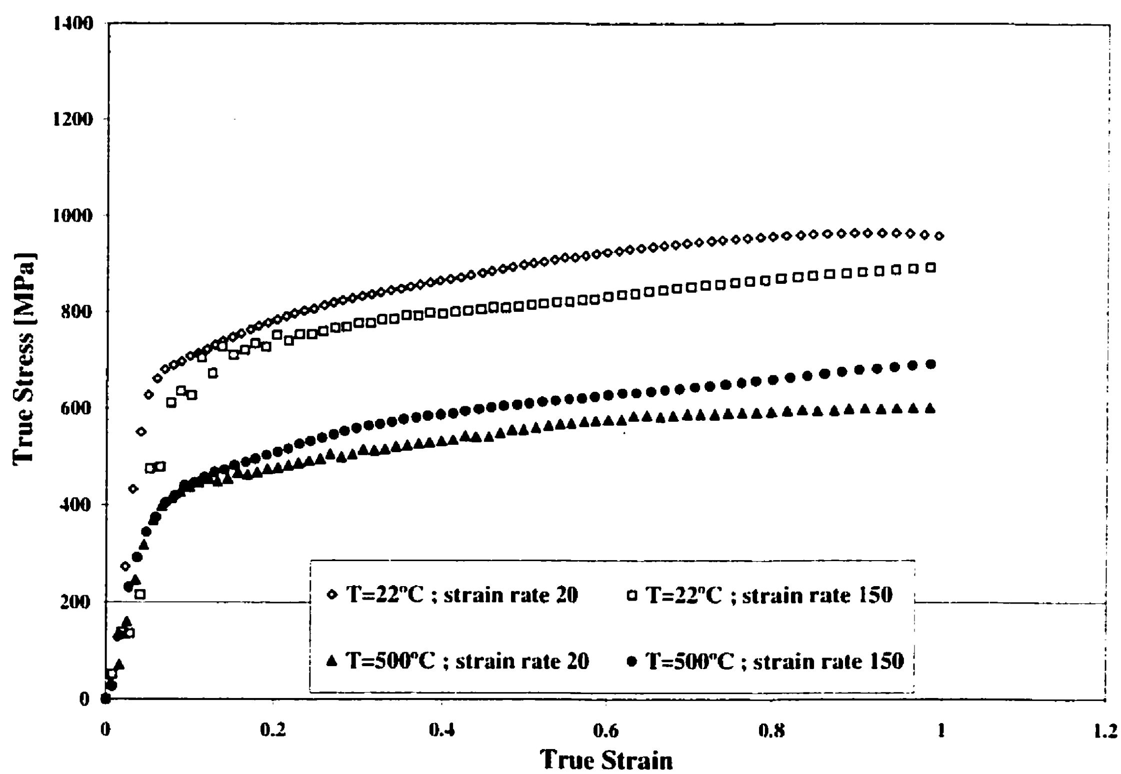

Figure 6.8 Heat 6 spheroidized. CP true stress-true strain results.

For all four heats, the flow curves for spheroidize annealed materials are about 200 MPa lower than those for as-rolled materials. This behavior is expected since a structure with spheroidal cementite is more ductile than one with lamellar cementite.

The *ambient temperature* CP tests on the as-rolled materials show higher flow stresses for the 20 s^{-1} strain rate tests compared to the 150 s^{-1} tests. At strains above roughly 0.4, this difference is 75 MPa for Heat 6 and 100 MPa for the higher residual content materials (Heats 1, 4 and 5). This is contrary to the expected behavior since higher strain rates are known to yield higher flow stresses. Deformation heating does not appear to be a factor since the heat developed with both of these high strain rates should be similar. For spheroidize annealed materials, the same behavior is observed. The ambient temperature tests show higher flow stresses (25-75 MPa) for the 20 s^{-1} strain rate tests compared to the 150 s^{-1} tests.

The *high temperature* CP tests on the as-rolled materials show flow stresses of 300 to 400 MPa lower than flow stresses obtained during ambient temperature testing. The much lower flow stresses in the as-rolled materials may be due to the partial spheroidization of pearlite followed by transformation to austenite. To explain this effect, it should be mentioned that the deformation heat generated during the high temperature CP tests brought the measured temperature from a nominal 500°C to 800°C. Spheroidization is known to be driven by large deformations [Meyer et al., 1997] and higher temperatures, and, of course, at temperatures above a nominal 730°C, transformation to austenite occurs. Indeed, metallographic analysis revealed the presence of martensite in some specimens that were immediately quenched after CP testing. The spheroidize annealed materials show a similar behavior between the high and ambient temperature CP tests. However, flow stresses at the higher temperature are only 200 MPa lower than the flow stresses at ambient temperature.

The *high temperature* CP tests on the as-rolled materials show a flow stress of 50 to 100 MPa higher at 150 s^{-1} as compared to the flow stress at 20 s^{-1}. For the spheroidize annealed Heats 1, 4 and 5, the flow stress at 20 s^{-1} saturates to just under 600 MPa at a strain of approximately 0.2. In contrast, Heat 6 (lower residuals) exhibits hardening throughout the strain range. A plausible explanation is that higher initial flow stresses in

Heats 1, 4 and 5 causes more energy to be dissipated in the form of heat earlier in the strain history, thereby countering the expected increase in flow stress with increasing strain. For all the spheroidize annealed materials, the flow stresses at 150 s^{-1} exhibit hardening throughout the strain range. This may be explained by the fact that there is no softening due to cementite morphology changes (indeed the structure is already spheroidized). Also, less heat is generated in view of the lower flow stresses at the higher temperature.

The reproducibility of the CP test was examined by repeating two of the 32 experiments. Heat 1 was re-tested in the as-rolled condition at ambient temperature with a nominal strain rate of 20 s^{-1} (Figure 6.9). Both curves overlap up to a strain of about 0.7, and deviate slightly thereafter. Heat 4 was re-tested in the spheroidize annealed condition at ambient temperature with a nominal strain rate of 150 s^{-1} (Figure 6.10). The curves overlap at strains beyond 0.3.

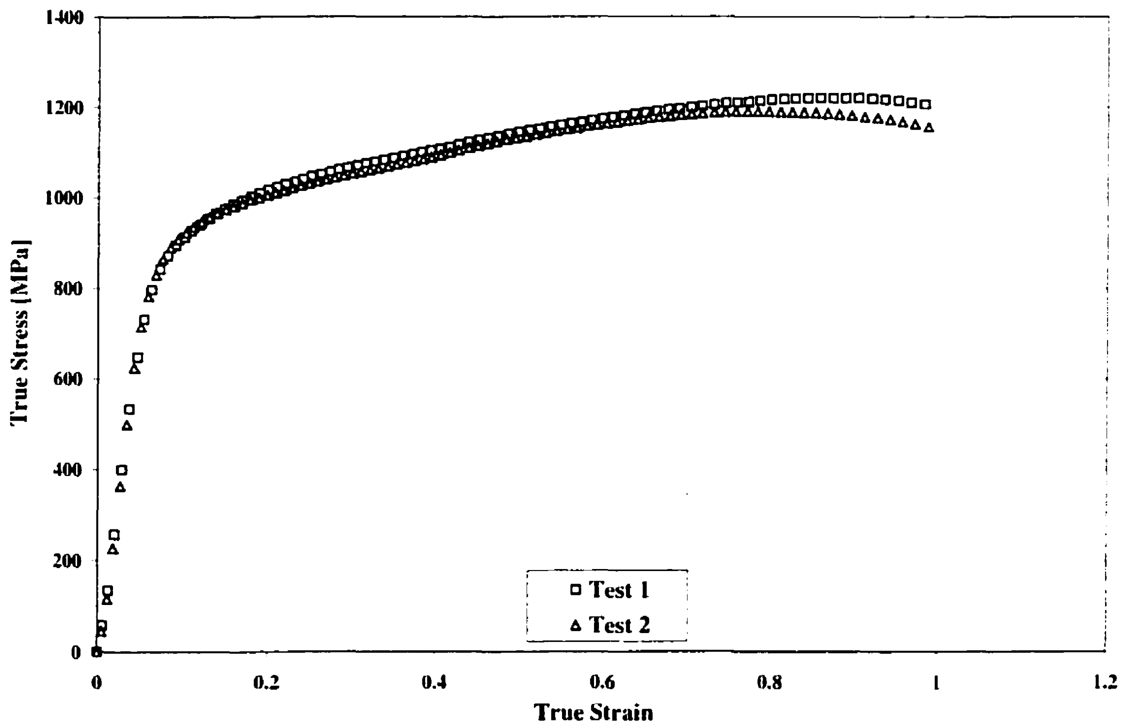

Figure 6.9 Re-test of Heat 1 as-rolled. CP true stress-true strain results at ambient temperature and strain rate 20 s^{-1}.

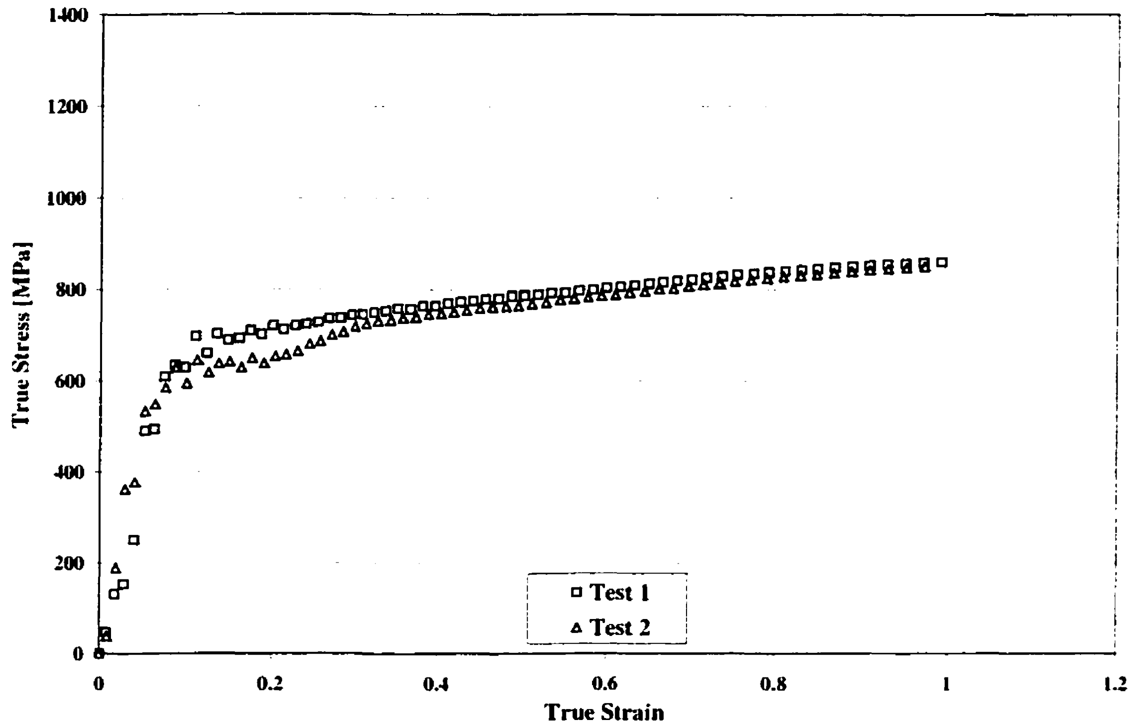

Figure 6.10 Re-test of Heat 4 spheroidized. CP true stress-true strain results at ambient temperature and strain rate of 150 s^{-1}.

6.1.2 Constitutive Modeling

Forge 2 uses the Norton-Hoff constitutive model described by equations 2.12 and 2.13. The only limitation of this model is that the strain rate coefficient, m, must be positive. To properly describe the dependence of flow stress on strain rate, described in Figures 6.1 to 6.8, it is necessary to allow negative excursions of the strain rate coefficient. Therefore, it was not possible to derive a strain rate coefficient consistent with the full spectrum of flow stress results, and for all the materials the coefficient was set to 0.02, a typical value for steel over the experimental temperature range.

Throughout the CP tests, temperatures did not remain constant due to deformation heating and die contact cooling. This temperature variation is compatible with the non-isothermal process conditions encountered in cold heading. The temperature increase was calculated at each data point by integrating the stress-strain curve at each strain increment to obtain the work per unit volume, and equating this to the enthalpy ($\rho C_p \Delta T$). A density, ρ, of 7800 kgm^{-3} and a heat capacity, C_p, of 500 $Jkg^{-1}K^{-1}$ were used.

Constitutive modeling examined the full range of deformation heating, from zero to 100% heat recovery (adiabatic heating). Using 100% heat recovery had an adverse effect on the fit between the experimental CP curves and the calculated curves. Therefore, modeling was performed at the nominal test temperature using zero heat recovery.

Analysis of flow curve test results showed that the curves obtained from testing from nominal ambient temperature and with a strain rate of 150 s^{-1} are the most representative of the process conditions observed during upsetting in cold heading. The ambient and high (500°C) temperature tests carried out at a strain rate of 150 s^{-1} were therefore selected for non-linear root mean square analysis to determine the flow curve parameters for input into the FEM models. There is a quasi-linear relationship between the 150 s^{-1} strain rate flow curves at the two test temperatures that enables determination of a reliable beta constant.

The strain range between 0.10 and 1 was used for the analysis to avoid cam profile corrections in the compliance region, and to obtain calculated flow curves consistent with the experimental curve. The strain region between 0 and 0.1 is small in comparison to the strain region beyond 0.1 that is achieved during cold heading. The calculated flow curves resulted in a better approximation of the expected elastic-plastic behavior. This is discussed in more detail in Chapter 7.

The results of the non-linear root mean square analysis yielded the flow curve parameters presented in Table 6.2. These analyses were performed using Microsoft Excel Solver. This function uses the nonlinear optimization code, Generalized Reduced Gradient 2, developed by Lasdon and Waren, Cleveland State University [Fylstra et al., 1998]. The Forge2 strain hardening regulation term, ε_o, was set at 0.0001 for all the analyses.

The Norton-Hoff parameters listed in Table 6.2 are strain rate sensitivity (m), work hardening coefficient (n), strength coefficient (K_o), and beta coefficient (β).

The strain rate sensitivity was set to 0.2, as mentioned earlier.

The spheroidize annealed materials exhibit larger work hardening coefficients ($0.10 < n < 0.13$) than do as-rolled materials ($0.03 < n < 0.06$). While the work hardening coefficients for the spheroidize annealed materials are closely grouped, the coefficients for the as-rolled materials are somewhat more erratic, perhaps because of the inherently less uniform as-rolled microstructure.

The as-rolled materials exhibit higher strength coefficients (326 MPa $< K_o <$ 362 MPa) than do the spheroidized materials (261 MPa $< K_o <$ 286 MPa). This is expected since the flow stress of the as-rolled materials is higher than the flow stress of the spheroidize annealed materials.

The as-rolled materials have a wider range of beta coefficients (102 K $< \beta <$ 161 K) than do the spheroidized materials (138 K $< \beta <$ 156 K), perhaps because of the inherently less uniform as-rolled microstructure.

Table 6.2 also presents the objective function (OF) and the number of data points (N) used in the analysis.

The objective function is defined by:

$$OF = \sqrt{\frac{\Sigma\left(\sigma_{cal} - \sigma_{exp}\right)^2}{N}} \tag{6.1}$$

where

N = number of data points in the analysis
σ_{cal} = stress calculated by Norton-Hoff relation
σ_{exp} = stress from CP testing

The objective function equals zero for a perfect fit between calculated and experimental values. It provides a benchmark for the goodness of fit between the experimental and calculated flow curves.

The as-rolled materials have higher OF values than their spheroidized counterparts, again perhaps because of the inherently less uniform as-rolled microstructure. The OF values for the eight materials ranged from 6 to 33 MPa. The non-linear analysis was also performed without fixing the strain rate coefficient (m) at 0.02. Some of the materials yielded a slightly negative m-value. However, the OF values were notably higher (>100), and the calculated flow curves did not agree with the experimental curves.

Material	m	n	K_o [MPa]	β	OF [MPa]	N
Heat 1 as-rolled	0.02	0.05	328	161	23	117
Heat 1 spheroidized	0.02	0.13	267	148	13	115
Heat 4 as-rolled	0.02	0.03	344	141	33	119
Heat 4 spheroidized	0.02	0.11	261	156	6	115
Heat 5 as-rolled	0.02	0.05	326	140	22	117
Heat 5 spheroidized	0.02	0.10	275	138	8	120
Heat 6 as-rolled	0.02	0.06	362	102	18	118
Heat 6 spheroidized	0.02	0.13	286	145	15	113

Table 6.2 Flow curve parameters from non-linear fit analysis using the Norton-Hoff relation.

Figures 6.11 to 6.18 show the calculated true stress-true strain curves superimposed on the experimental ones for the four as-rolled and spheroidize annealed materials. In the strain range of interest (0.1 to 1), a good fit is observed for all the curves. Additional computations were performed beyond this strain range to insure that the constitutive equations behave acceptably for the FEM simulations.

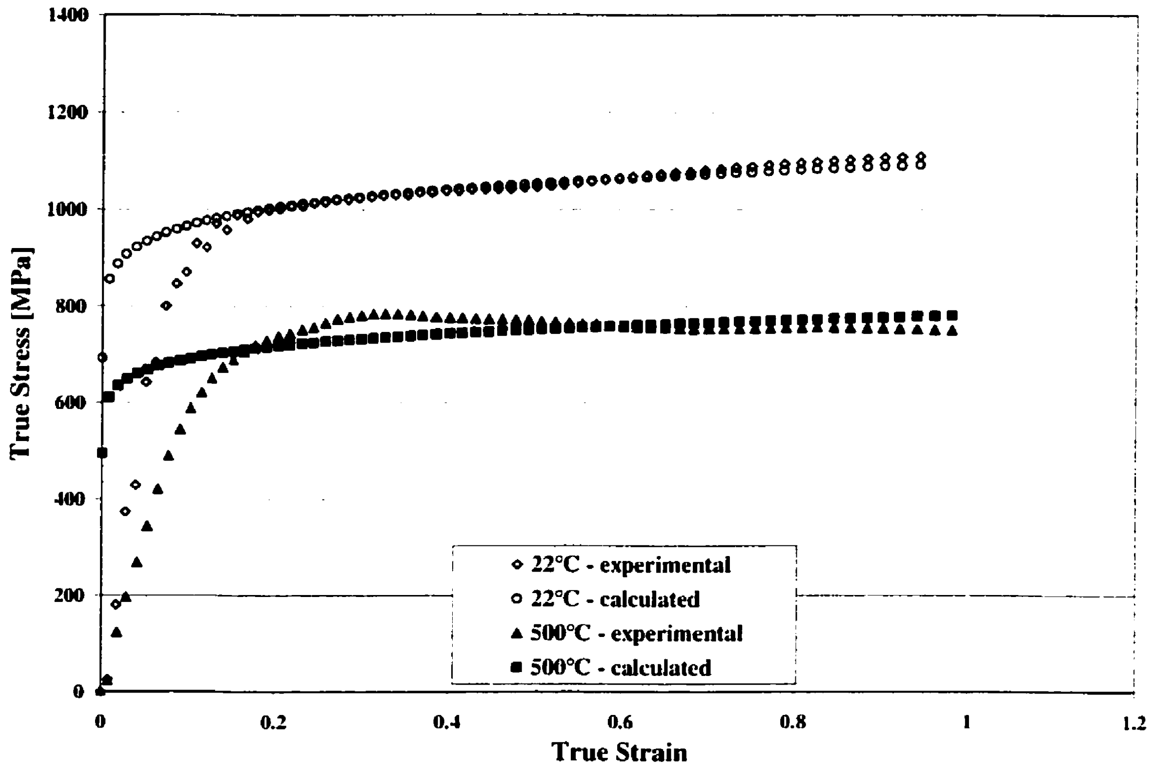

Figure 6.11 **Heat 1 as-rolled. Experimental and calculated true stress-true strain results at 150 s^{-1}.**

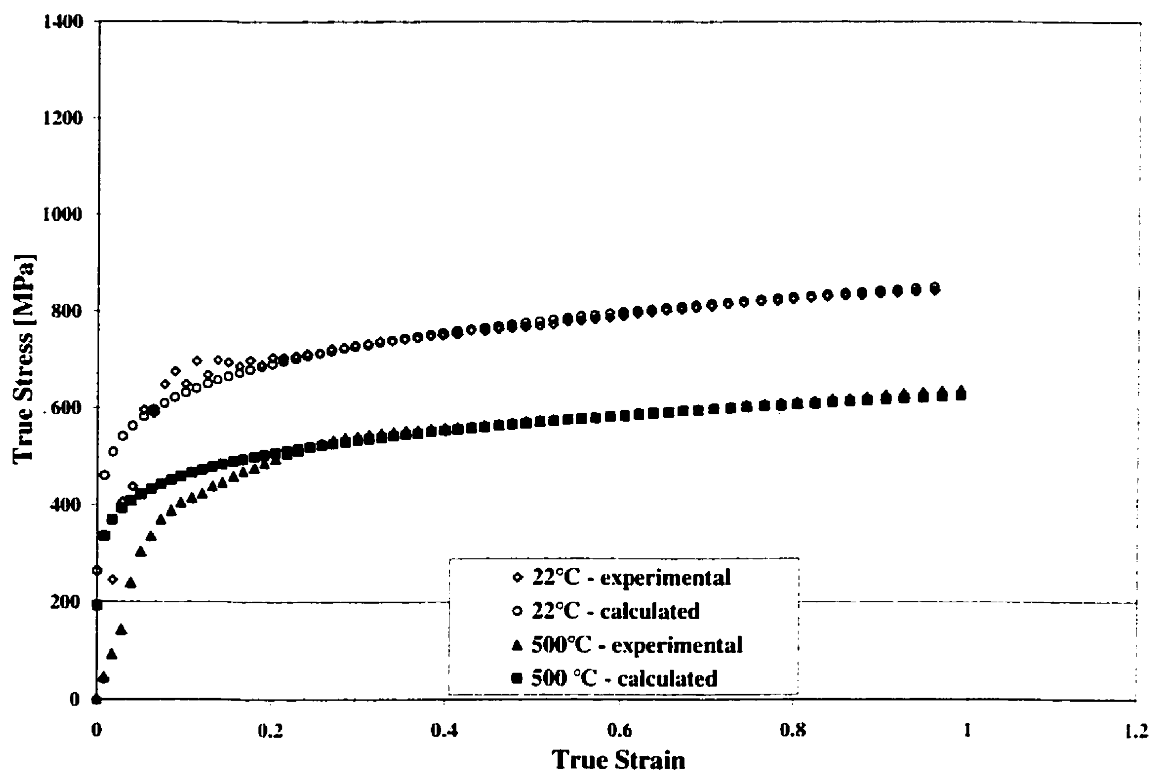

Figure 6.12 **Heat 1 spheroidized. Experimental and calculated true stress-true strain results at 150 s^{-1}.**

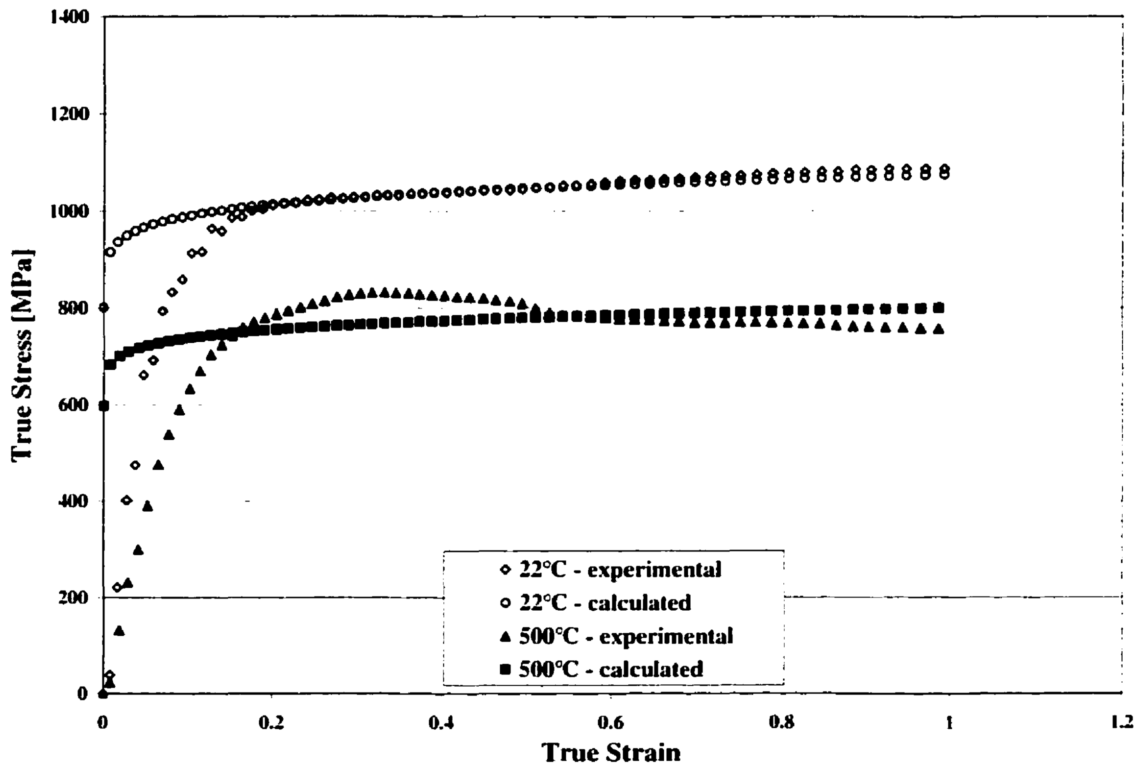

Figure 6.13 Heat 4 as-rolled. Experimental and calculated true stress-true strain results at 150 s^{-1}.

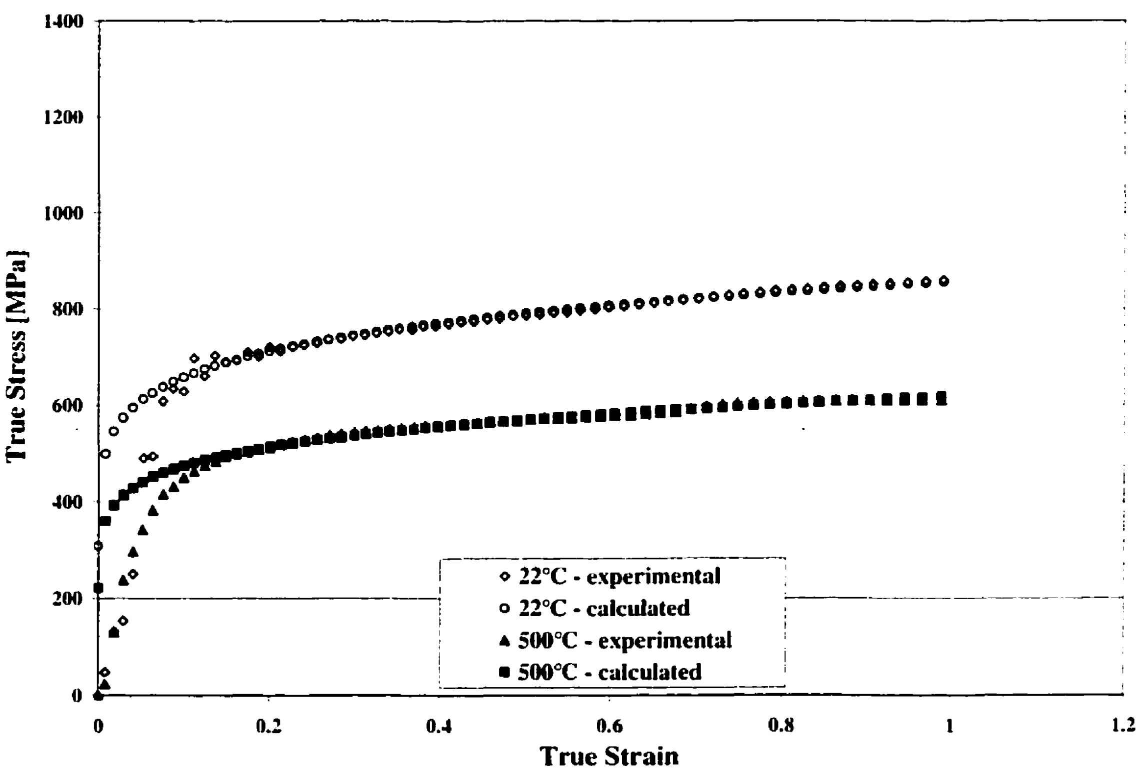

Figure 6.14 Heat 4 spheroidized. Experimental and calculated true stress-true strain results at 150 s^{-1}.

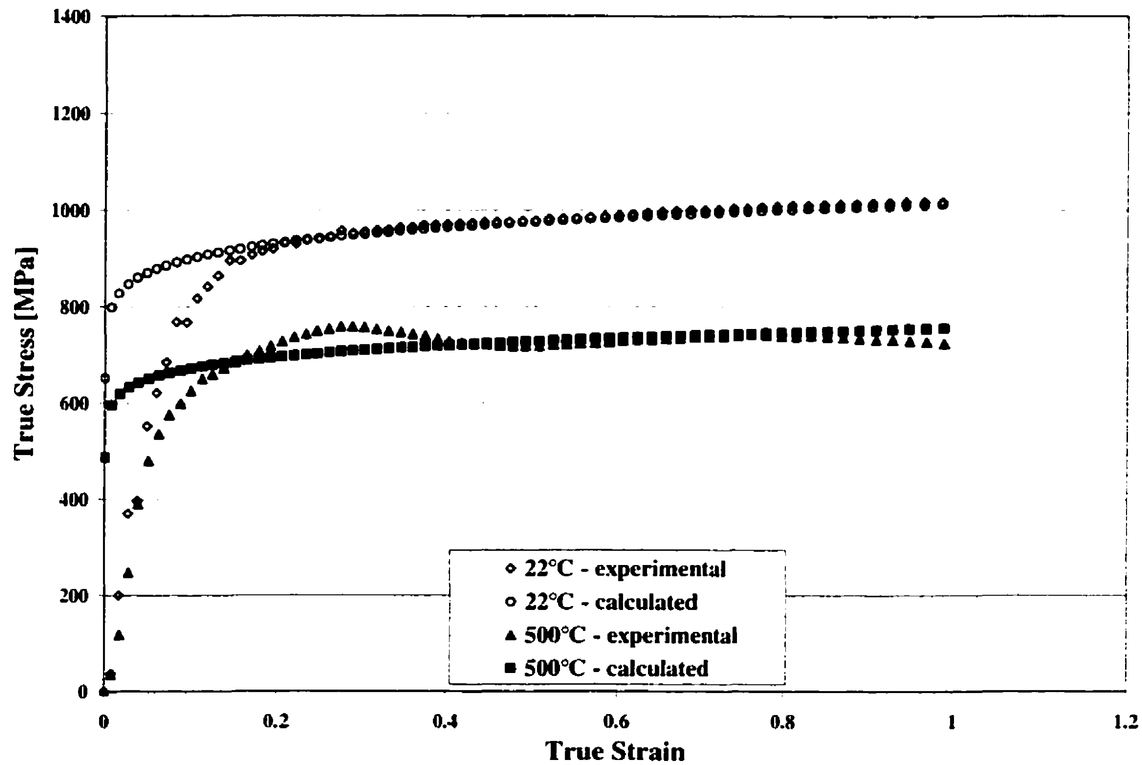

Figure 6.15 Heat 5 as-rolled. Experimental and calculated true stress-true strain results at 150 s^{-1}.

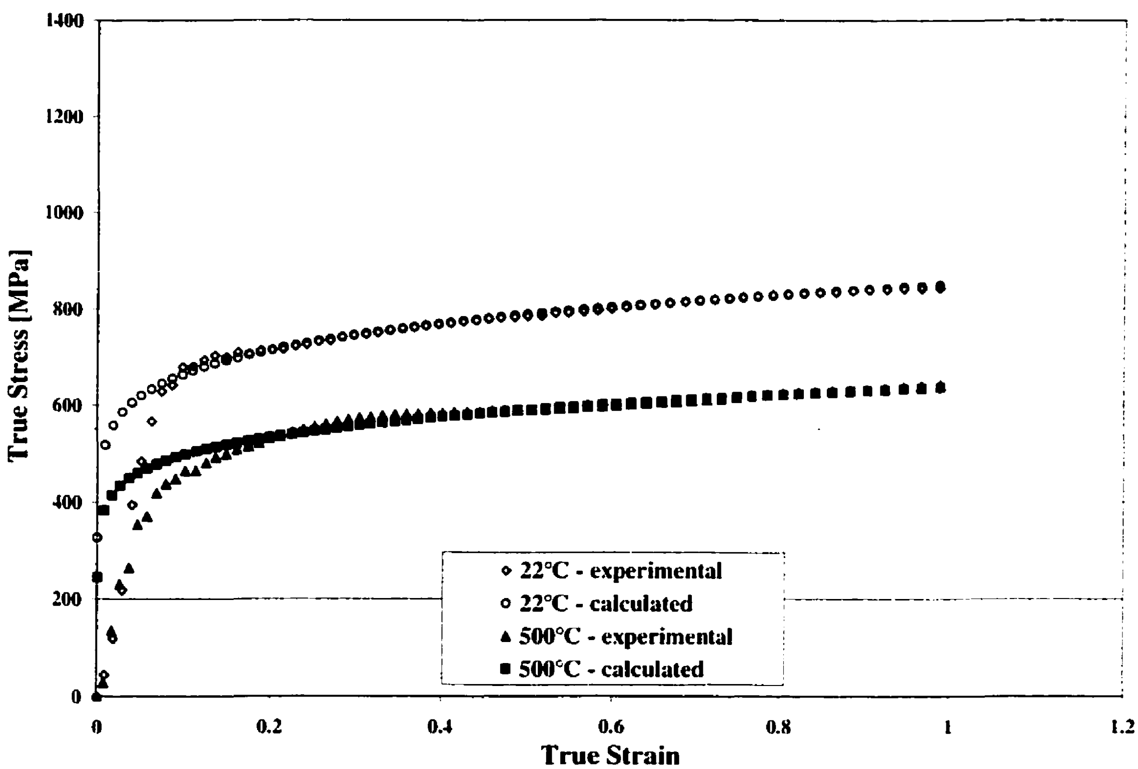

Figure 6.16 Heat 5 spheroidized. Experimental and calculated true-versus true strain results at 150 s^{-1}.

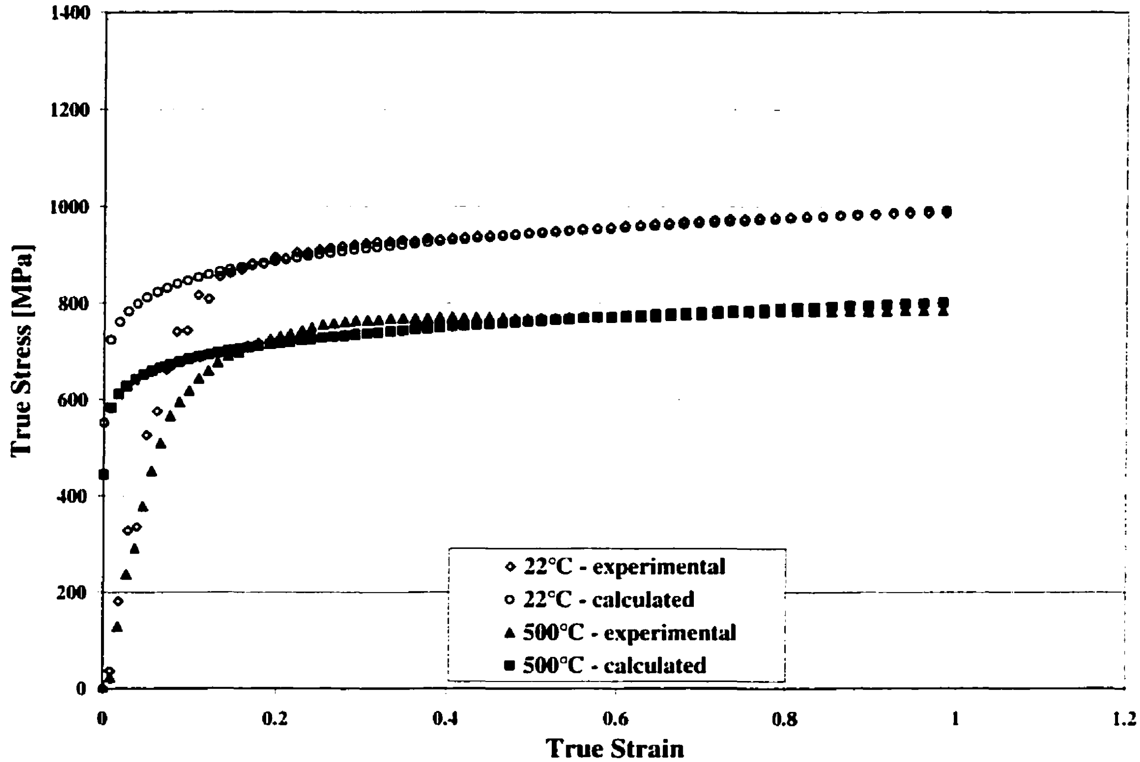

Figure 6.17 Heat 6 as-rolled. Experimental and calculated true stress-true strain results at 150 s^{-1}.

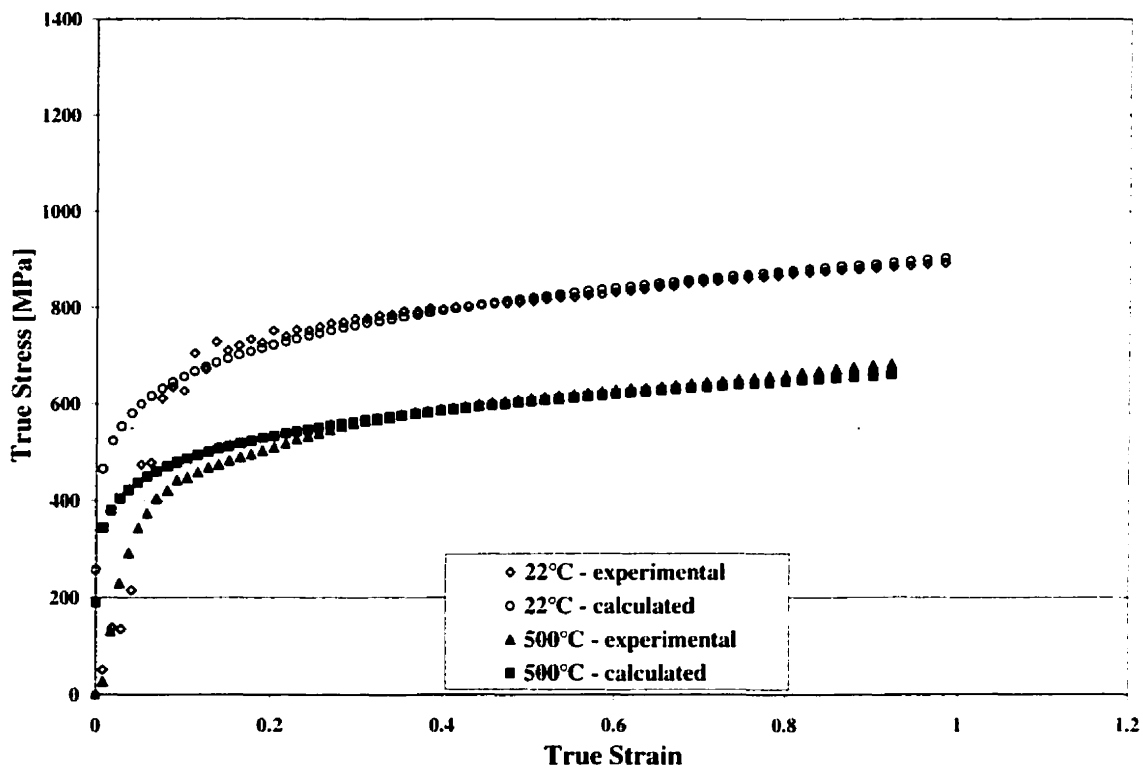

Figure 6.18 Heat 6 spheroidized. Experimental and calculated true stress-true strain results at 150 s^{-1}.

6.2 Drop Weight Compression

The drop weight compression results are presented in this section. The section is broken up into 3 sub-sections: Compression to Fracture, Load History, and Velocity.

6.2.1 Compression to Fracture

DWT testing was performed on the 7 heats. Six of these heats (1 to 5, and 7) were tested in the as-rolled and spheroidize annealed conditions. Heat 6 was only tested in the as-rolled condition. The specimens from Heat 7 were purposely decarburized during spheroidize annealing to observe the effect of decarburization on wire rod workability.

All heats were tested at an aspect ratio of 1.3. Fracture results for all the heats could then be compared at the same aspect ratio. For Heats 4 and 5, three aspect ratios, 1.0, 1.3 and 1.6, were selected for testing the materials. Testing at the two extreme aspect ratios, 1.0 and 1.6, was necessary to validate a fracture criterion generated by the FEM computations. Indeed, the fracture criterion should be independent of aspect ratio. Experimental CP data, friction conditions, and kinematic DWT parameters *at fracture* from Heat 4 as-rolled and Heat 4 spheroidized materials were chosen for subsequent FEM modeling.

An objective of the DWT experiments was to determine the sensitivity of the DWT to chemistry, microstructure, surface soundness, and decarburization for each material and aspect ratio by compressing specimens to obtain the global axial and hoop strains *at fracture*.

Special attention was required in establishing the point at which cracks initiated by viewing the specimens at a magnification of X25 using a stereo microscope and Figure 5.10 as a basis for comparison. To eliminate evaluation bias, specimens were coded and therefore evaluated without knowledge of either material source or DWT parameters.

Preliminary DWT experiments were performed to determine the mass and height that would bracket crack initiation. Masses in the range 10 to 20 kg, and a drop height of

1.5 m, were found to be suitable for all materials, heat treatments and aspect ratio. A constant drop height gave a constant initial strain rate: 630 s^{-1} for an aspect ratio of 1.6 to 820 s^{-1} for an aspect ratio of 1.3.

Interchangeable weight plates were used to vary test energy in search of the critical fracture mass. Testing was performed in two stages, coarse and fine. The coarse stage involved testing through a range of mass increments in multiples of 2.3 kg. The fine stage was performed using mass increments of 0.3 and 0.6 kg. Repeat experiments were also performed.

For Heat 4, the fine stage was performed with the aid of a load cell coupled to an oscilloscope to check the results of FEM modeling. The voltage-time data was converted to load-time and load-displacement information presented in Sections 6.2.2 and 6.2.3.

During upsetting, some specimen material went towards filling the difference between the die and specimen volumes in the die pockets. Indeed, to facilitate sample retrieval, the die pockets were 5.30 mm at the lip, and 5.25 mm at the base, while wire drawn specimens were 5.21 mm. This difference was about 0.5 mm^3, less than 0.6%, and therefore had a negligible impact on global strain calculations.

Table 6.3 illustrates the DWT fracture ranges for Heats 1, 2 and 3 (Ivaco). The fracture range has an upper limit defining the strain at which fracture occurred, and a lower limit defining the highest strain achieved without fracture. The fracture strain for a given material and specimen aspect ratio rests between these extremes.

Figures 6.19 and 6.20 show global axial and circumferential strain results for Heats 1 and 2 calculated using equations 2.2 and 2.3. A complete table of results is provided in Appendix A.

For Heat 1 as-rolled materials, the average global axial and circumferential strains are respectively 0.65 and 0.33. For spheroidized materials, the average global axial and circumferential strains are respectively, 0.77 and 0.41, i.e., 18% and 24% larger. *The DWT is thus demonstrably sensitive to microstructure.*

Heat No.	Heat Treatment	Aspect Ratio	Fracture Range for Axial Strain	Fracture Range for Circumferential Strain
1	as-rolled	1.3	0.62 - 0.67	0.32 - 0.34
1	spheroidized	1.3	0.74 - 0.80	0.39 - 0.42
2	as-rolled	1.3	0.76 - 0.82	0.41 - 0.43
2	spheroidized	1.3	1.03 - 1.04	0.52 - 0.53
3	as-rolled	1.3	less than 0.26	less than 0.16
3	spheroidized	1.3	less than 0.57	less than 0.31

Table 6.3 DWT fracture range results for Heats 1, 2, and 3.

For Heat 2 as-rolled materials, the average global axial and circumferential strains are respectively 0.79 and 0.42. For spheroidized materials, the average global axial and circumferential strains are respectively, 1.035 and 0.525, i.e., 31% and 25% larger.

Comparing Heats 1 and 2, the average global axial and circumferential strains to fracture are respectively 22% and 27% higher for Heat 2 as-rolled, and 34% and 28% higher for Heat 2 spheroidized. The fracture strain differences between the two heats may be related to the nitrogen content. Indeed, the residual element content of the two heats is the same (0.51%), while the nitrogen content of Heat 1 is almost double that of Heat 2. *The DWT is thus demonstrably sensitive to the deleterious impact of nitrogen.*

Heat 3 was selected to ascertain the sensitivity of the DWT to residual elements, particularly copper. For this heat, major cracking occurred even with the minimum available crosshead mass at the testing height of 1.5 m. Exploratory testing was performed at drop heights down to 0.9 m. Even at this height and at the minimal available crosshead mass, the equatorial surface exhibited cracking. Three types of defects were observed: longitudinal cracks, shear cracks, and slivering. The longitudinal cracks and the slivering were evident on all the specimens. The shear cracks were only observed on highly deformed (axial strains > 2.0) specimens, suggesting that these fractured due to instability. One explanation for the instability is that nitrogen can be responsible for dynamic strain aging, which leads to negative rate sensitivities that contribute to instability. The other heats did not exhibit shear cracking or slivering.

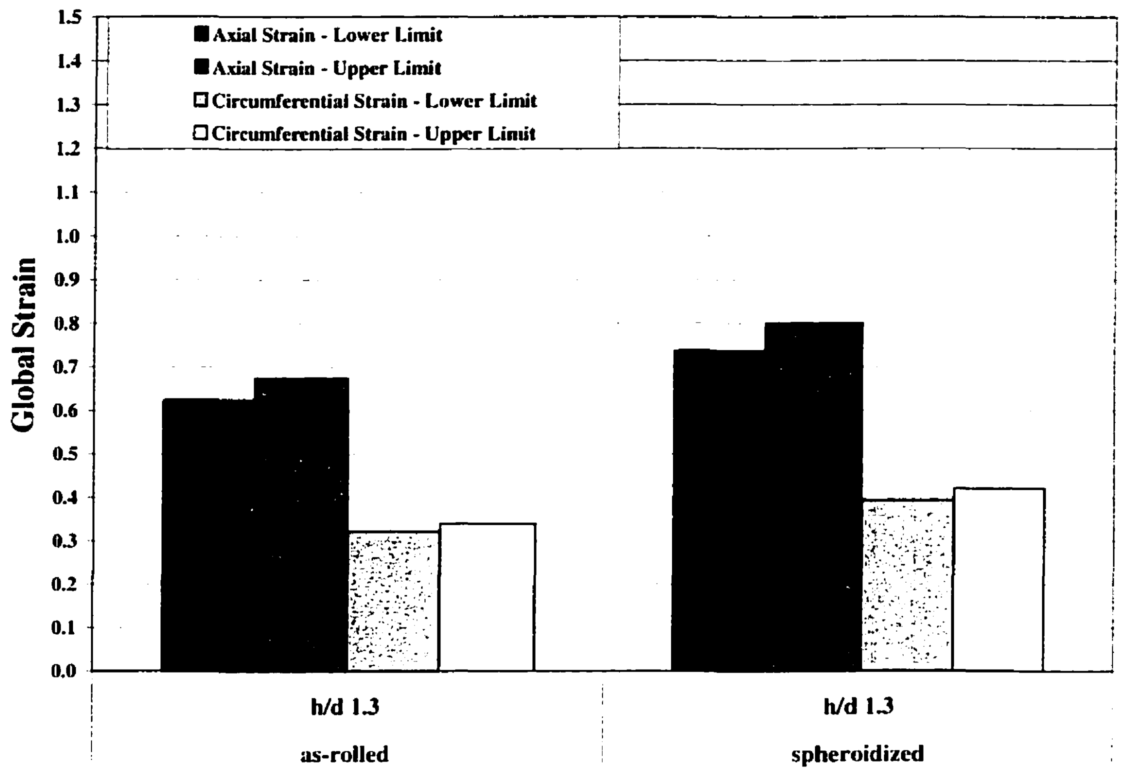

Figure 6.19 Histogram of DWT fracture results for Heat 1.

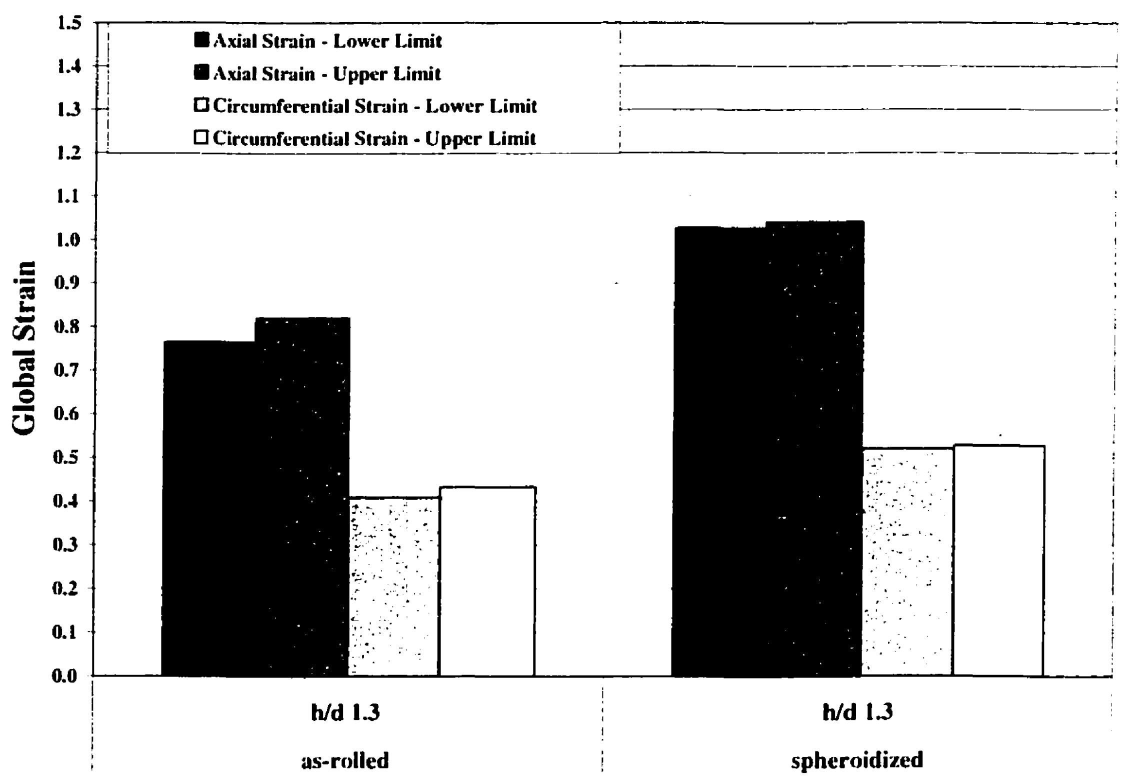

Figure 6.20 Histogram of DWT fracture results for Heat 2.

The slivering observed in the Heat 3 materials may be attributed to the presence of intergranular phases resulting from hot shortness. Hot shortness occurs during billet re-heating and rolling when low melting point compounds are present at grain boundaries because of segregation phenomena [Dieter, 1997]. In Heat 3, the hot shortness is probably due to the high copper content (0.35%). It is well known that steels with such high copper content frequently exhibit hot shortness [Yalamanchili et al., 1999; Lankford et al., 1985]. *The DWT is thus demonstrably sensitive to the deleterious impact of copper.*

The fractured specimens were photographed using a JEOL JSM-840A. Figure 6.21 illustrates an SEM photograph of the undeformed surface of typical test specimen. Surface imperfections such as die scratches are not present.

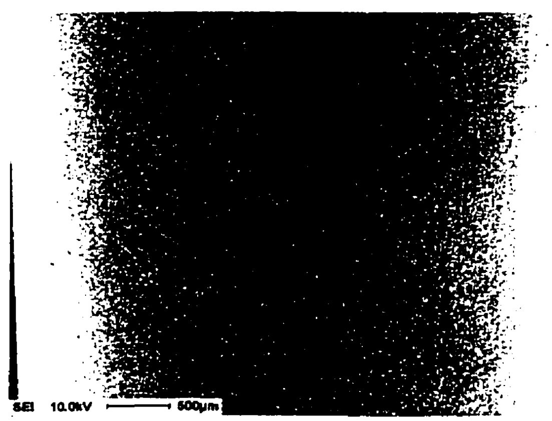

Figure 6.21 SEM photographs of undeformed surface of DWT specimens.

All the fractures observed on the specimens from Heats 1 and 2 were parallel to the specimen axis (longitudinal). Figures 6.22 and 6.23 illustrate the onset of fracture that was observed on the as-rolled and spheroidized DWT specimens from Heat 1.

Figure 6.24 illustrates the onset of fracture observed on the as-rolled DWT specimen from Heat 2. Figures 6.25 and 6.26 illustrate the progression of fracture on the as-rolled and spheroidized DWT specimens from Heat 3. Shear cracking is only observed on the specimens DWT tested with a mass of 42.9 kg.

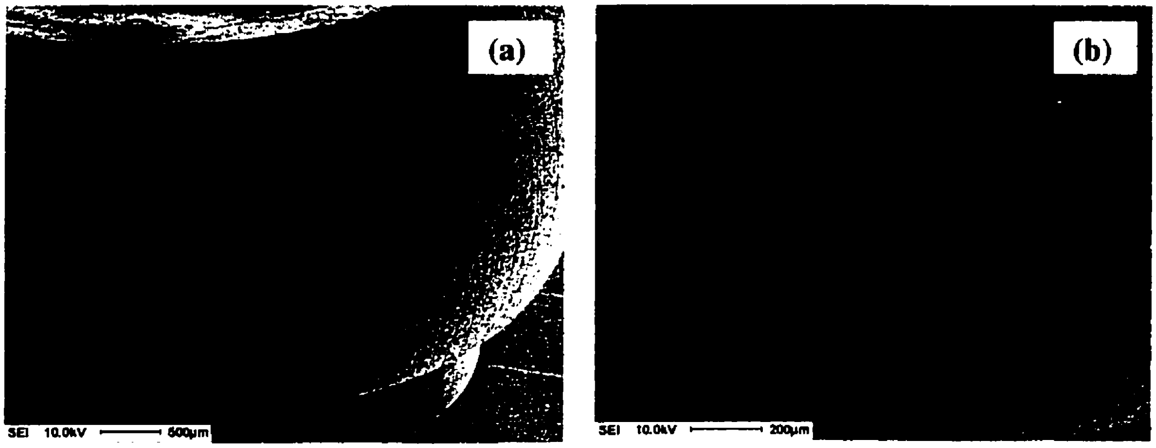

Figure 6.22 SEM micrograph of fracture initiation on Heat 1 as-rolled: (a) low magnification (b) high magnification.

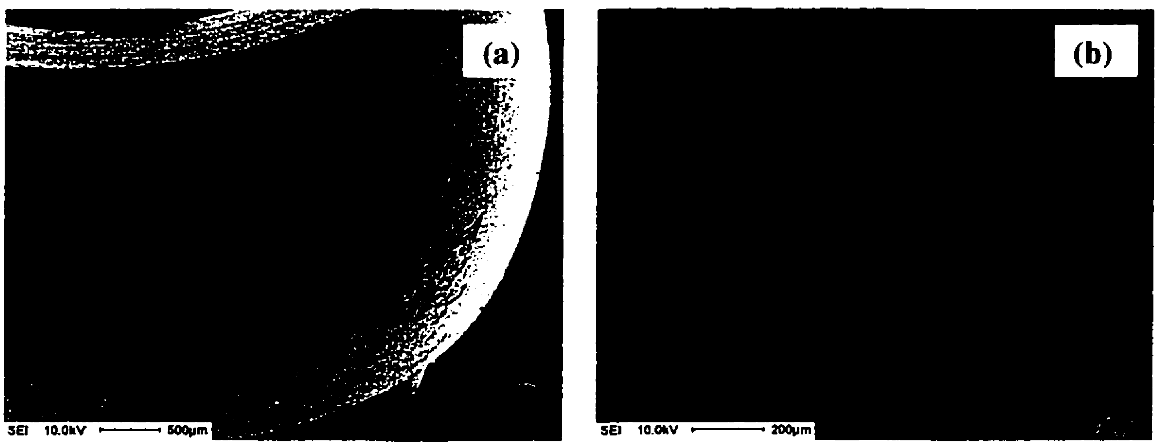

Figure 6.23 SEM micrograph of fracture initiation on Heat 1 spheroidized: (a) low magnification (b) high magnification.

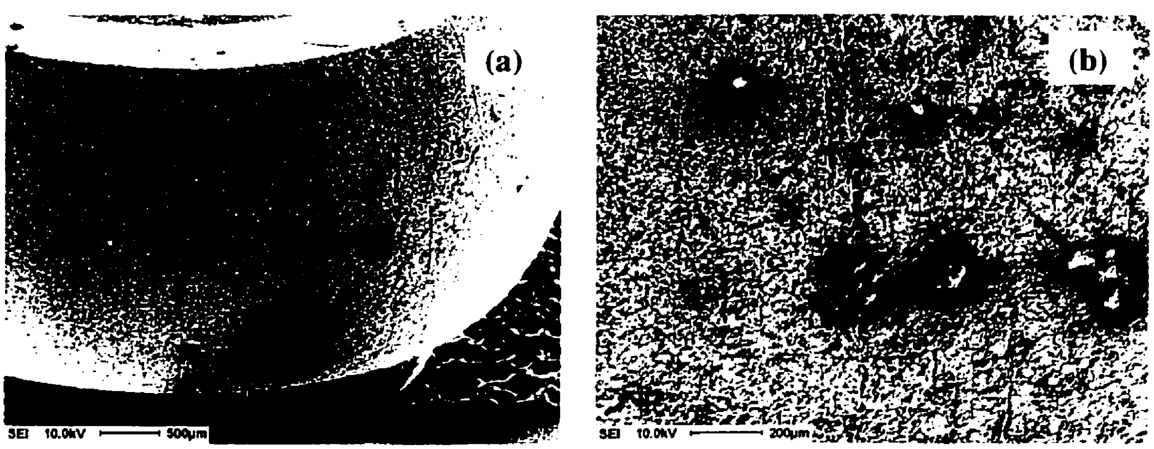

Figure 6.24 SEM micrograph of fracture initiation on Heat 2 as-rolled: (a) low magnification (b) high magnification.

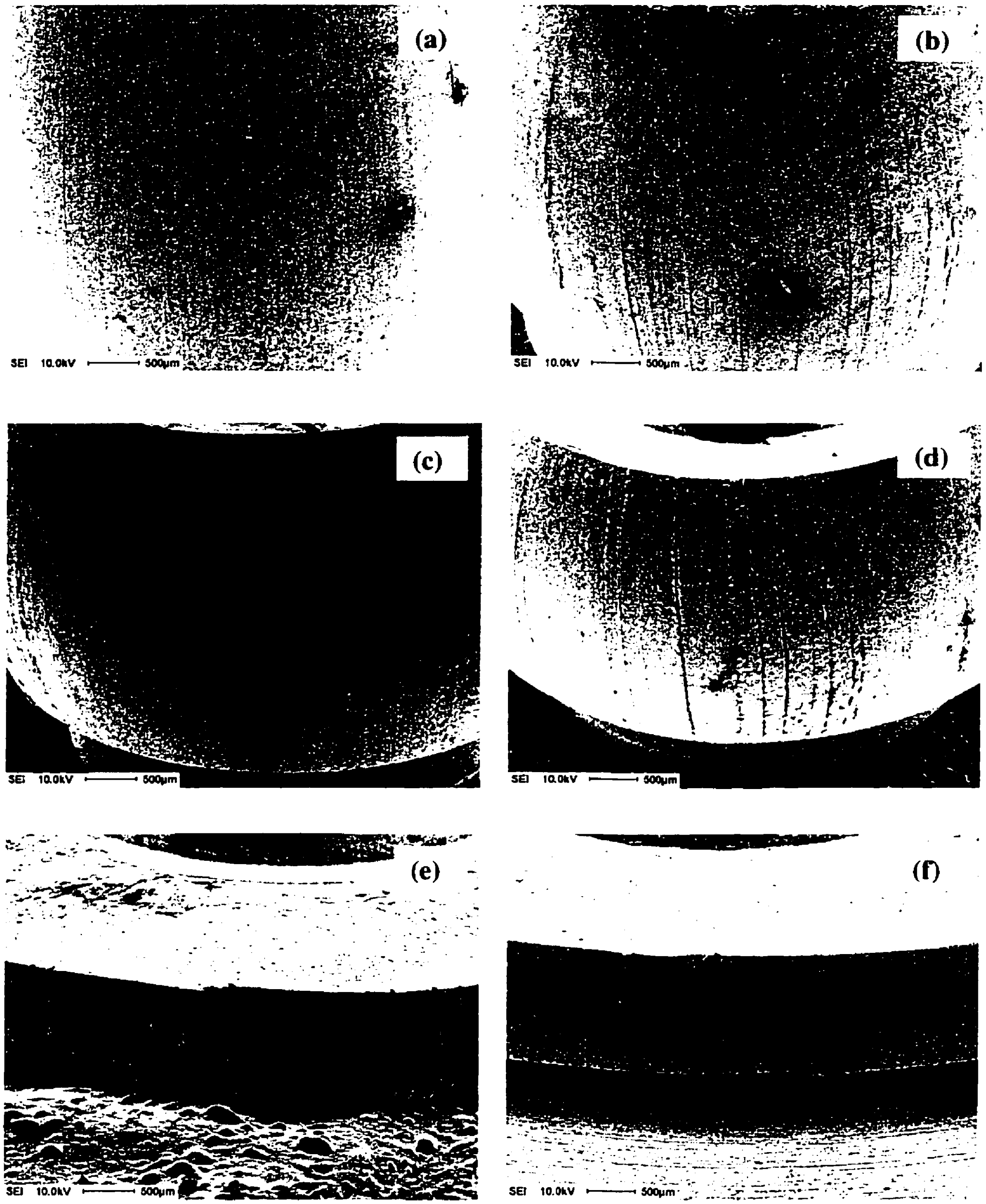

Figure 6.25 SEM micrographs – progression of fracture on Heat 3 as-rolled: longitudinal fractures and slivers on DWT specimens from 1.5 m: (a) 11.8 kg. (b) 14.1 kg. (c) 16.4 kg. (d) 18.8 kg. (e) & (f) shear fractures on DWT specimens from 1.5 m. and 42.9 kg.

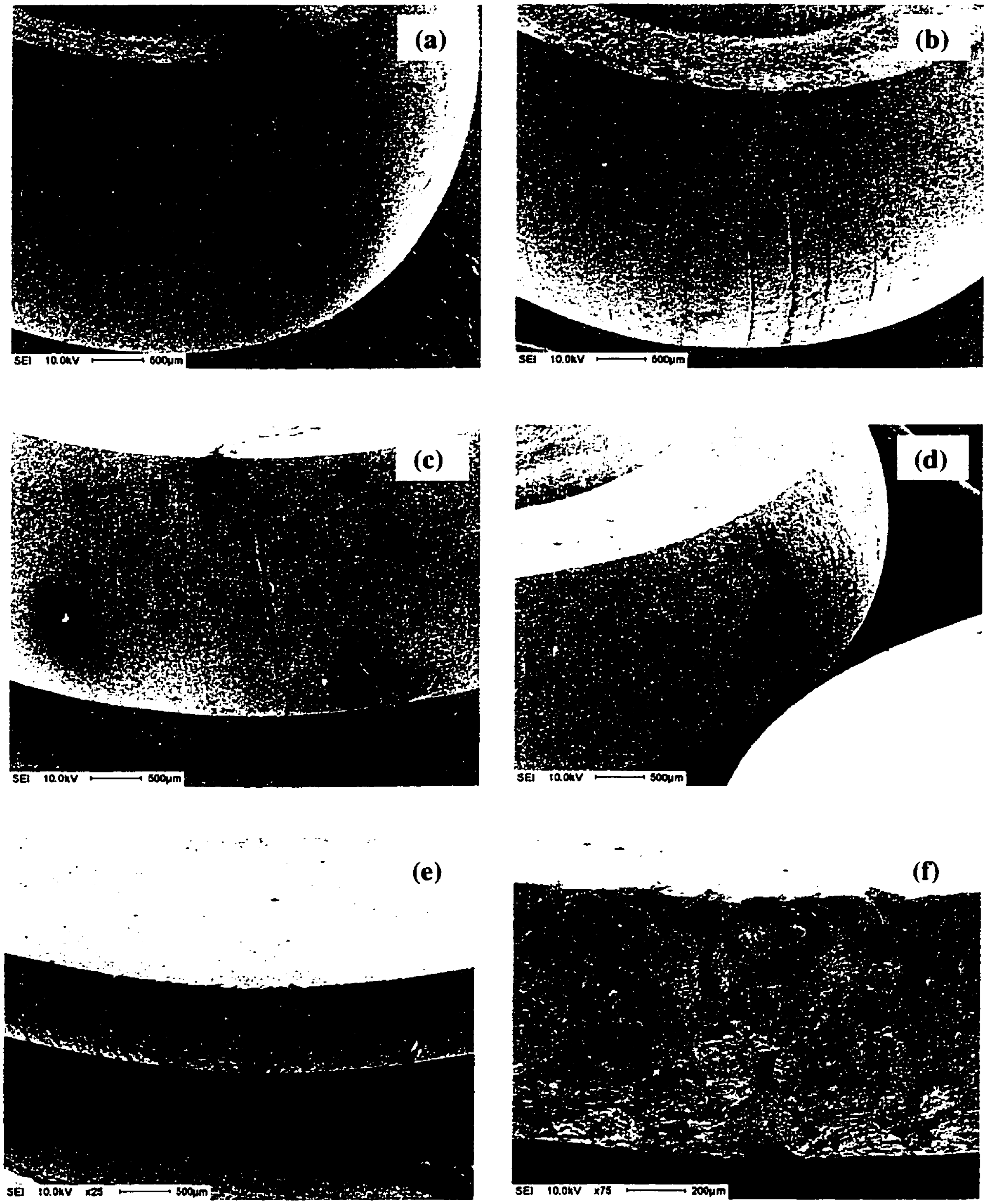

Figure 6.26 SEM micrographs – progression of fracture on Heat 3 spheroidize annealed: longitudinal fractures and slivers on DWT specimens from 1.5 m: (a) 11.8 kg. (b) 14.1 kg. (c) 16.4 kg. (d) 18.8 kg. (e) & (f) 42.9 kg.

Table 6.4 shows DWT fracture results for Heats 4 and 5. Figures 6.27 and 6.28 are graphical representations of this data. For the extreme aspect ratios, 1.0 and 1.6, three DWT experiments were conducted for each material to gauge the variability about the fracture range limits. Worse case standard deviations for both axial and circumferential fracture strain range limits are remarkably low at around 1%.

Heat No.	Heat Treatment	Aspect Ratio	Fracture Range for Axial Strain	Fracture Range for Circumferential Strain
4	as-rolled	1.0	0.88 ± 0.009 - 0.94 ± 0.006	0.44 ± 0.001 - 0.46 ± 0.003
4	spheroidized	1.0	1.07 ± 0.005 - 1.12 ± 0.004	0.52 ± 0.001 - 0.54 ± 0.003
5	as-rolled	1.0	1.02 ± 0.002 - 1.04 ± 0.008	0.50 ± 0.002 - 0.51 ± 0.001
5	spheroidized	1.0	1.11 ± 0.001 - 1.14 ± 0.005	0.55 ± 0.004 - 0.56 ± 0.005
4	as-rolled	1.3	0.98 - 1.02	0.51 - 0.52
4	spheroidized	1.3	1.20 - 1.23	0.59 - 0.61
5	as-rolled	1.3	1.08 - 1.14	0.54 - 0.57
5	spheroidized	1.3	1.28 - 1.32	0.63 - 0.65
4	as-rolled	1.6	0.99 ± 0.008 - 1.03± 0.009	0.51 ± 0.001 - 0.53 ± 0.006
4	spheroidized	1.6	1.26 ± 0.006 - 1.30 ± 0.004	0.64 ± 0.002 - 0.65 ± 0.001
5	as-rolled	1.6	1.14 ± 0.009 - 1.18 ± 0.004	0.58 ± 0.001 - 0.60 ± 0.002
5	spheroidized	1.6	1.31 ± 0.004 - 1.34 ± 0.004	0.66 ± 0.003 - 0.67 ± 0.001

Table 6.4 DWT fracture range results for Heats 4 and 5.

For Heats 4 and 5, global axial and circumferential fracture strains for the as-rolled materials are lower than those for the spheroidized materials. This is true for all three aspect ratios. For Heat 4, the axial and circumferential fracture strains are roughly 20% higher for the spheroidized materials. For Heat 5, the strains are roughly 13% higher for the spheroidized materials. *As observed with Heats 1 and 2, the DWT is sensitive to microstructure.*

Comparing Heats 4 and 5, the average global axial and circumferential strains to fracture are approximately 11% higher for Heat 5 as-rolled, and 5% higher for Heat 5 spheroidized. These differences between the two heats may be related to the nitrogen content. Indeed, the residual element content of the two heats is the same (0.17%), while the nitrogen content of Heat 4 is more than double that of Heat 5. *Again, the DWT is sensitive to nitrogen level.*

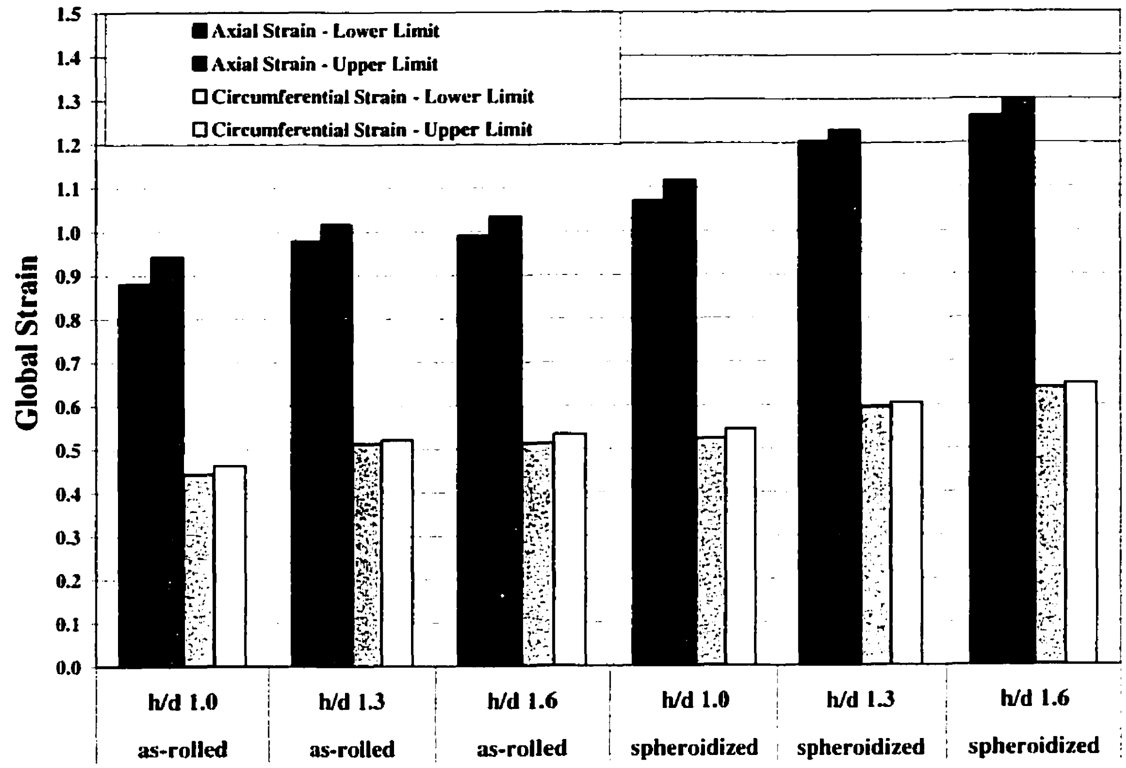

Figure 6.27 Histogram of DWT fracture results for Heat 4.

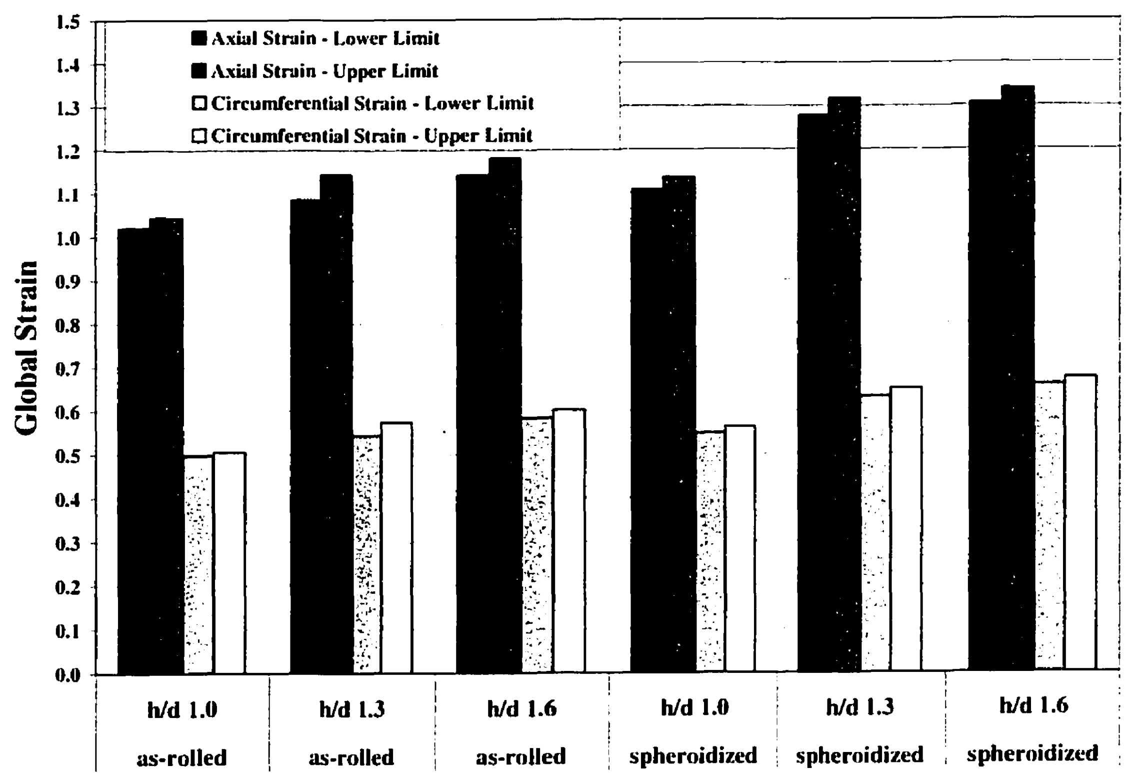

Figure 6.28 Histogram of DWT fracture results for Heat 5.

Comparing fracture strain results for the three aspect ratios, it is clear that the lower the aspect ratio, the smaller the strain to fracture. This is true for Heats 4 and 5, and for both as-rolled and spheroidized microstructures. Between aspect ratios of 1.0 and 1.3, the increase in fracture strain (axial and circumferential) is about 12%. The increase from an aspect ratio of 1.3 to a ratio of 1.6 is smaller (4%). This is an important finding, and it is consistent with the literature, in particular with the fracture limit diagram discussed in Section 2.5.2.

The fracture strains of Heats 4 and 5 were roughly 50% higher than those of Heats 1 and 2 for both as-rolled and spheroidized materials. This is consistent with the three-fold difference in sum of residuals (0.51% for Heats 1 and 2, and 0.17% for Heats 4 and 5). *The DWT is sensitive to residual element content.*

To summarize at this point, the fracture results for Heats 1 to 5 show that the sensitivity of the DWT is sufficient to differentiate between materials on the basis of microstructure, nitrogen, copper, residual element content, and even aspect ratio.

Fractured specimens were photographed at low and high magnifications using an SEM. Typical photographs are presented in Figures 6.29 and 6.30 to illustrate the onset of fracture observed on the as-rolled DWT specimens from Heats 4 and 5.

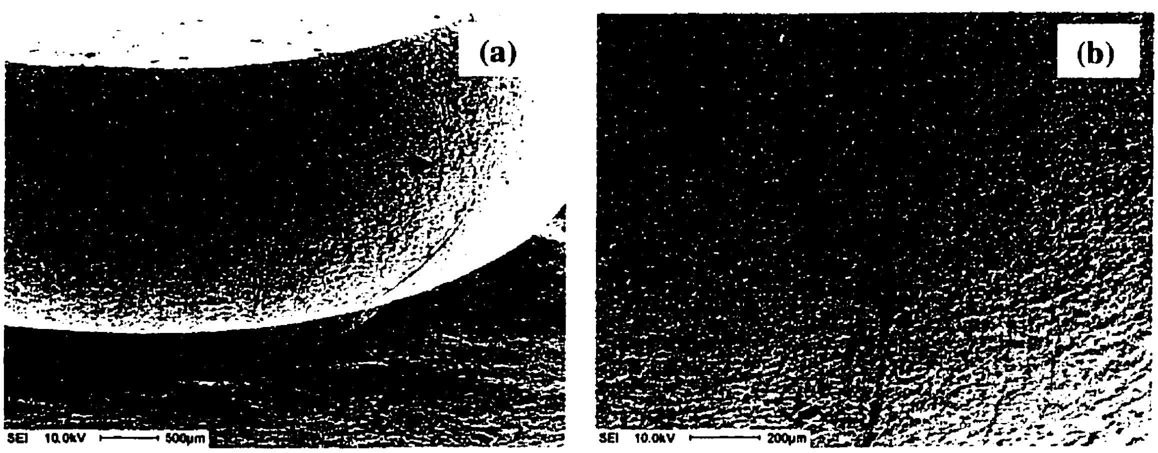

Figure 6.29 SEM micrograph of fracture initiation on Heat 4 as-rolled - aspect ratio 1.30: (a) low magnification (b) high magnification.

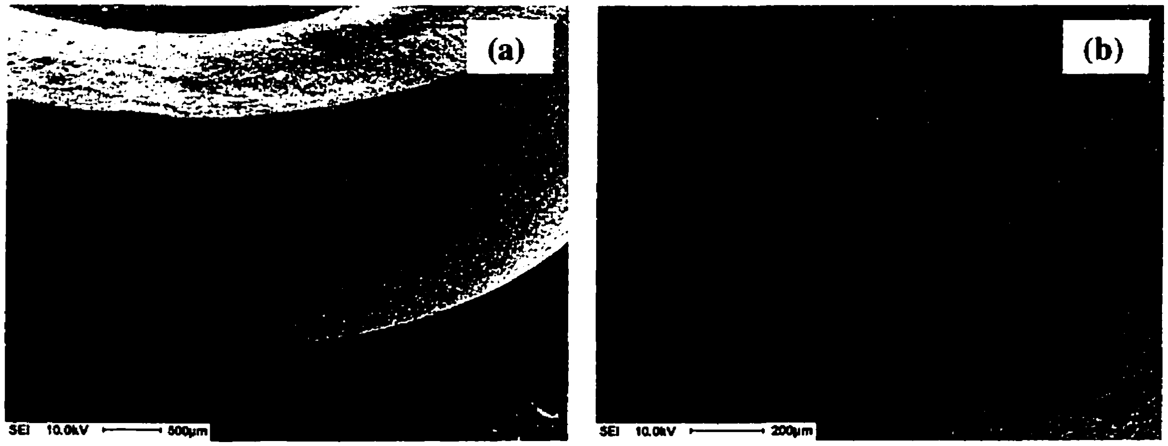

Figure 6.30 SEM micrograph of fracture initiation on Heat 5 as-rolled - aspect ratio 1.30: (a) low magnification (b) high magnification.

Table 6.5 gives the DWT fracture results for Heats 6 and 7 (Açominas heats). Figure 6.31 is a graphical representation of the data.

Heat No.	Heat Treatment	Aspect Ratio	Fracture Range for Axial Strain	Fracture Range for Circumferential Strain
6	as-rolled	1.3	0.53 - 0.55	0.28 - 0.29
7	as-rolled	1.3	1.05 - 1.08	0.52 - 0.53

Table 6.5 DWT fracture range results for Heats 6 and 7.

As mentioned in Section 4.1, the surface quality of Heat 6 specimens was substandard. Optical microscopy revealed a corroded and pitted wire rod surface. During the wire drawing operation, iron-oxide particles embedded themselves into the wire die, and introduced longitudinal scratches on the wire, as often occurs in industry. This heat was retained to test the sensitivity of the DWT to surface imperfections that act as local stress raisers [Broek, 1989]. Figure 6.32 shows the drawing scratches on a DWT specimen from Heat 6. This defect was observed in the portion of material located in the die pocket during testing, indicating that the defect was present before testing.

For Heat 6, the global axial and circumferential fracture strains for the as-rolled materials are respectively 0.53 to 0.55, and 0.28 to 0.29. For Heat 7, the global axial and circumferential fracture strains for the as-rolled materials are respectively 1.05 to 1.08, and 0.52 to 0.53. The upper limits of strain to fracture for Heat 7 are 80 to 100% higher than those of Heat 6. The residual element and nitrogen contents of the two heats are similar (0.06% and 35 ppm for Heat 6, and 0.04% and 40 ppm for Heat 7). Therefore the difference in fracture strains can only be due to surface quality. *The sensitivity of the DWT machine is thus sufficient to discriminate between surfaces of different qualities.*

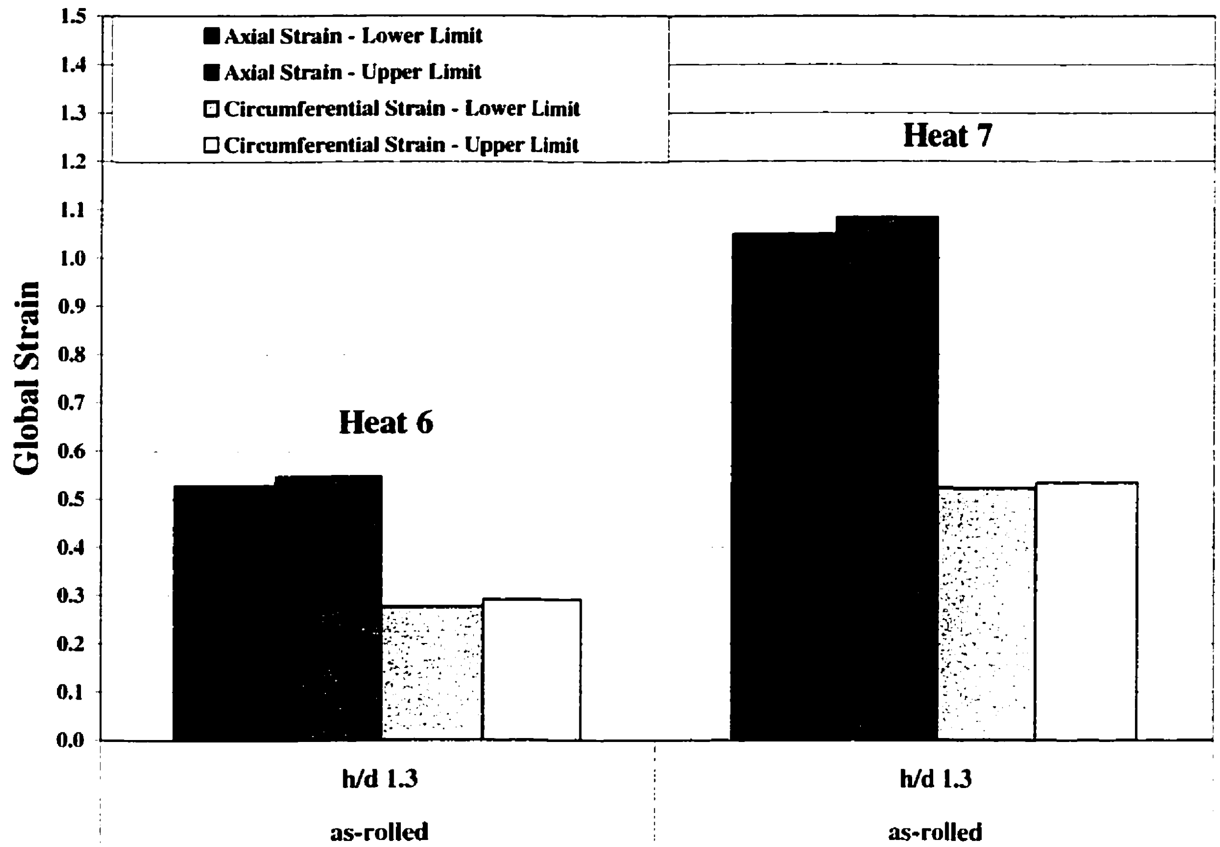

Figure 6.31 Histogram of DWT fracture results for Heats 6 and 7.

The upper limits of strain to fracture for Heat 7 are approximately 15% higher than those of Heat 4, and about 5% lower than those of Heat 5. The difference in fracture strains between Heat 7 and Heats 4 or 5 may be due to the much lower residual element content (0.04% for Heat 7 and 0.17% for Heats 4 and 5). Figure 6.33 illustrates the onset of fracture on a DWT specimen from Heat 7.

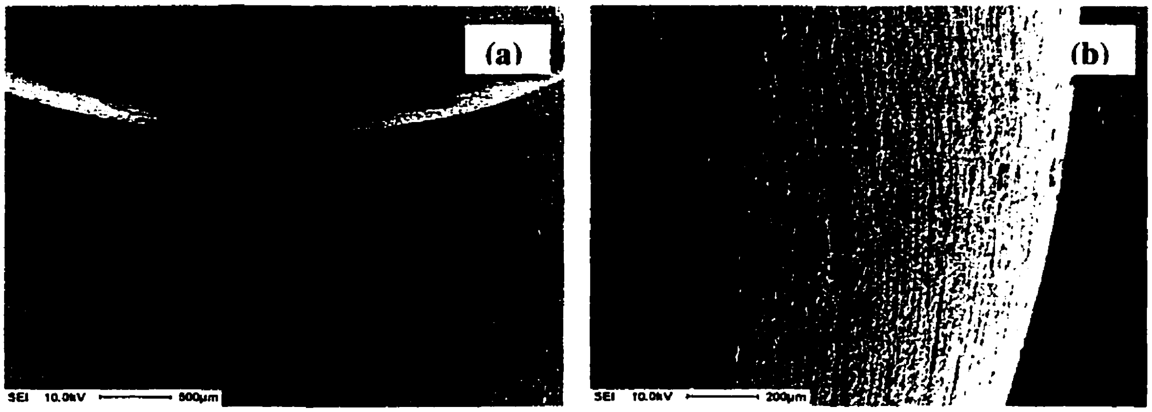

Figure 6.32 SEM micrograph of fracture initiation on Heat 6 as-rolled: (a) low magnification showing drawing die scratches in the DWT die pocket material and pitted surface (b) high magnification.

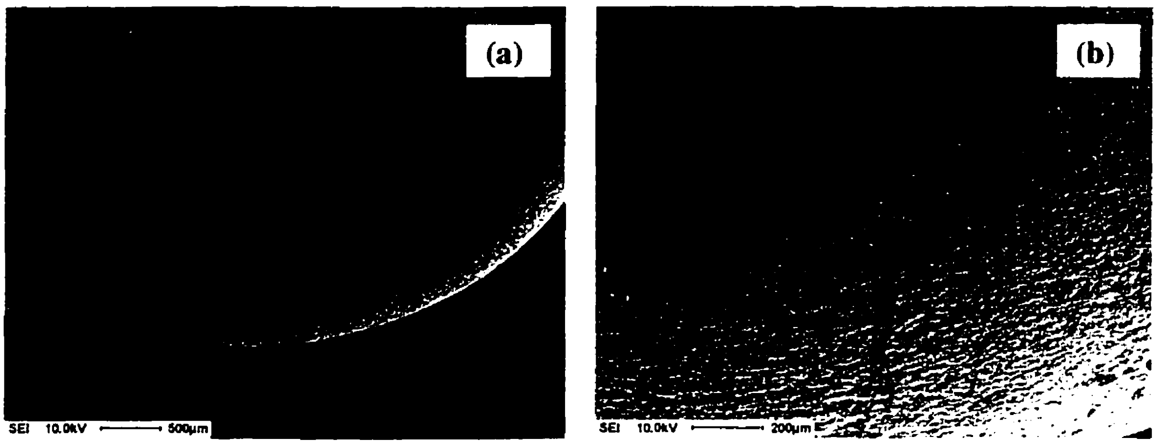

Figure 6.33 SEM micrograph of fracture initiation on Heat 7 as-rolled - aspect ratio 1.30: (a) low magnification (b) high magnification.

The deleterious effect of decarburization was discussed in Section 2.2.5. In order to gauge the sensitivity of DWT to decarburization, wire rod specimens from Heat 7 were exposed to oxygen during the spheroidize annealing.

For these specimens, axial strains to fracture during DWT went beyond 1.6, a 20% increase over spheroidized material from Heat 5. *Thus, the DWT machine reacts to the presence of decarburization.*

Decarburization might appear to be advantageous in cold heading, providing additional local ductility in the region of highest stress during testing. However, the barreled surfaces of these specimens were quite rough as shown in the SEM micrographs,

Figure 6.34. The resultant surface is not appealing, and the carbon required to harden the workpiece to the desired specification in subsequent quench and tempering is lacking.

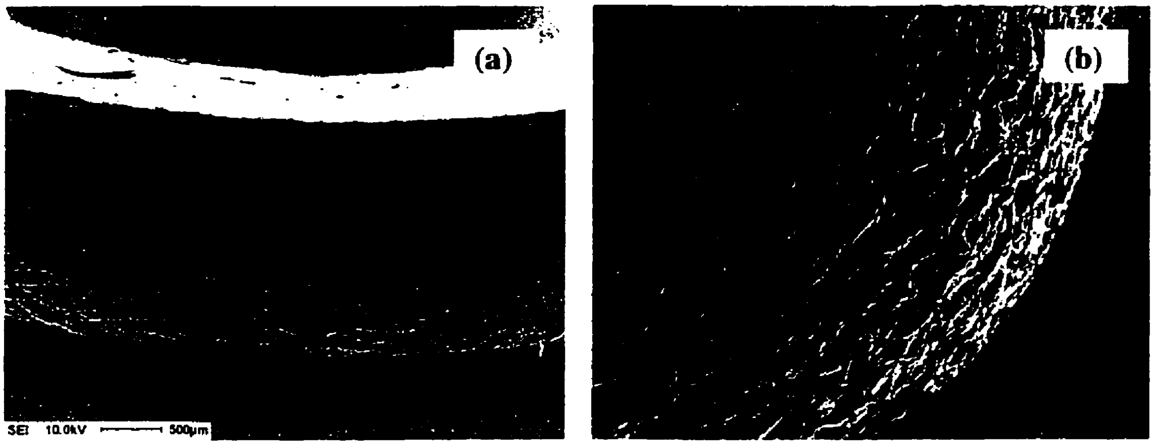

Figure 6.34 SEM micrograph of rough surface due to surface decarburization on Heat 7 spheroidized - aspect ratio 1.30: (a) low magnification (b) high magnification.

To uncover the presence of shear bands and/or internal microcracks, DWT specimens exhibiting surface cracks were examined using an SEM.

The specimens were mounted in Lucite, ground along the longitudinal axis using silicon carbide papers, polished using 6 and 1 μm diamond paste, and etched in a 4% nital solution.

None of the specimens exhibited internal microcracks. Shear bands were more intense in the as-rolled materials, but localization was not sufficient to initiate internal cracking. Furthermore, the temperature increase due to deformation heating was not enough to promote transformation to austenite, and thence to martensite. The absence of shear bands and internal microcracks indicates that shear band formation occurs at higher deformation than that required for surface cracking.

Exploratory DWT testing to reveal shear bands was performed at higher deformations. For example, Heat 4 was tested with a 40 kg mass released from a height of 2.2 m. The resultant axial and circumferential strains were respectively 2.1 and 1.1, a two-fold increase over the strains required for surface fracture.

Figure 6.35 illustrates a pronounced shear band in which internal microcracks are present. As the microstructure in the band could not be resolved using an SEM, microhardness testing was performed to shed light on the nature of this constituent. The hardness in the band was 610 VHN (tensile strength of about 2030 MPa or 295 ksi) while the hardness in the region away from the band was 213 VHN. This suggests that the shear band had transformed to martensite, i.e., the larger strains had resulted in a highly localized deformation with local temperatures above the transformation point.

Fastener head failures due to the presence of martensite may become more frequent with the advent of faster cold headers and stronger steels. In addition, improvements in the quality of cold heading materials, particularly to the surface and sub-surface integrity of cold heading materials, may also raise the formability limit for upsetting during cold heading in such a way that internal microstructural mechanisms may play a larger role. *Clearly, the DWT machine is capable of generating transformation bands during upset testing with large deformations.*

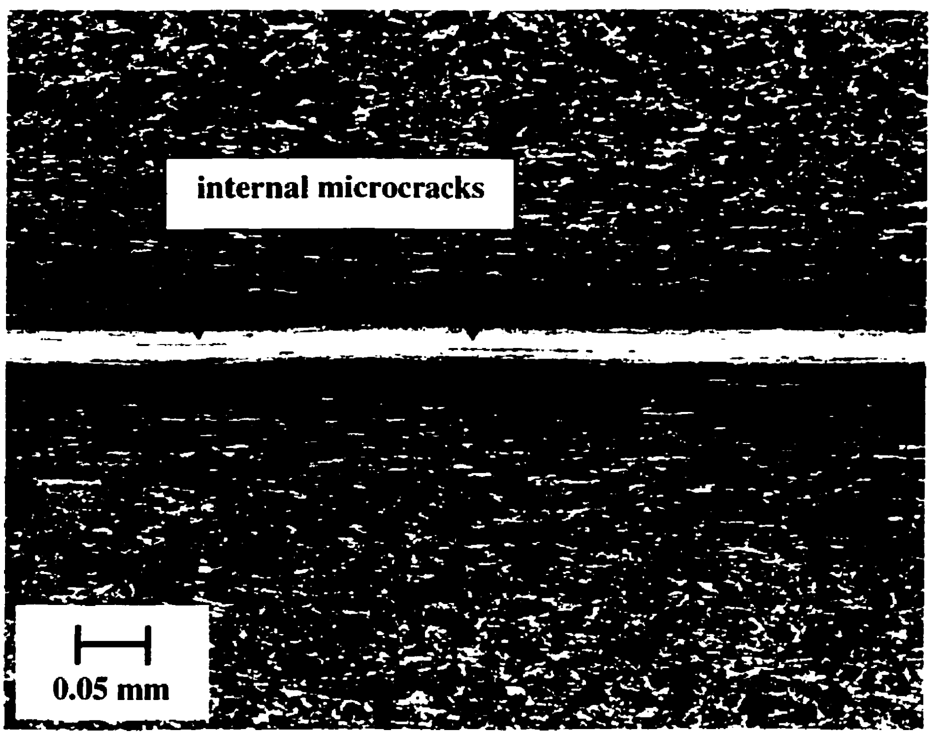

Figure 6.35 SEM micrographs of transformed shear band and internal microcracks on DWT specimen from Heat 4 – as-rolled.

6.2.2 Load-Time History

The DWT performed on Heat 4 as-rolled and spheroidized specimens with aspect ratios of 1.6 was instrumented using a load cell and an oscilloscope, as mentioned earlier. The purpose of these experiments was to check FEM modeling performed on these two materials. Load-time history was obtained using the methods described in Section 5.2.

The load-time history for the two materials is presented in Figures 6.36 and 6.37. The curves have a similar form. As the specimen is compressed, work hardening and cross-sectional area increase. The initial sharp rise is followed by oscillations that dampen as they approach the maximum load. The oscillations may be due to the spring-like response of the DWT equipment and the specimen to the load, and stops and starts due to friction. The as-rolled material displays larger oscillations than the spheroidized material, possibly reflecting a dynamic strain aging contribution.

The rise to the maximum load is steeper for spheroidize annealed material. This is consistent with the CP results that showed doubling or tripling of the work hardening coefficient for spheroidized materials (n value in Table 6.2). Following the maximum load, the curves drop without oscillation to zero load.

Displacement-to-fracture results from the DWT are presented with the maximum load and the elapsed time to peak load in Table 6.6. The load-time curves are used in a later section to check the FEM models.

Material	Mass for Fracture [kg]	Initial Specimen Height [mm]	Final Specimen Height [mm]	Displacement-to-Fracture [mm]	Max Load [kN]	Elapsed Time to Peak Load [s]
as-rolled	16.99	10.31	4.94	5.37	67.6	0.00194
spheroidized	18.16	10.30	4.25	6.05	81.4	0.00200

Table 6.6 Heat 4 DWT and load-time data for aspect ratio 1.6.

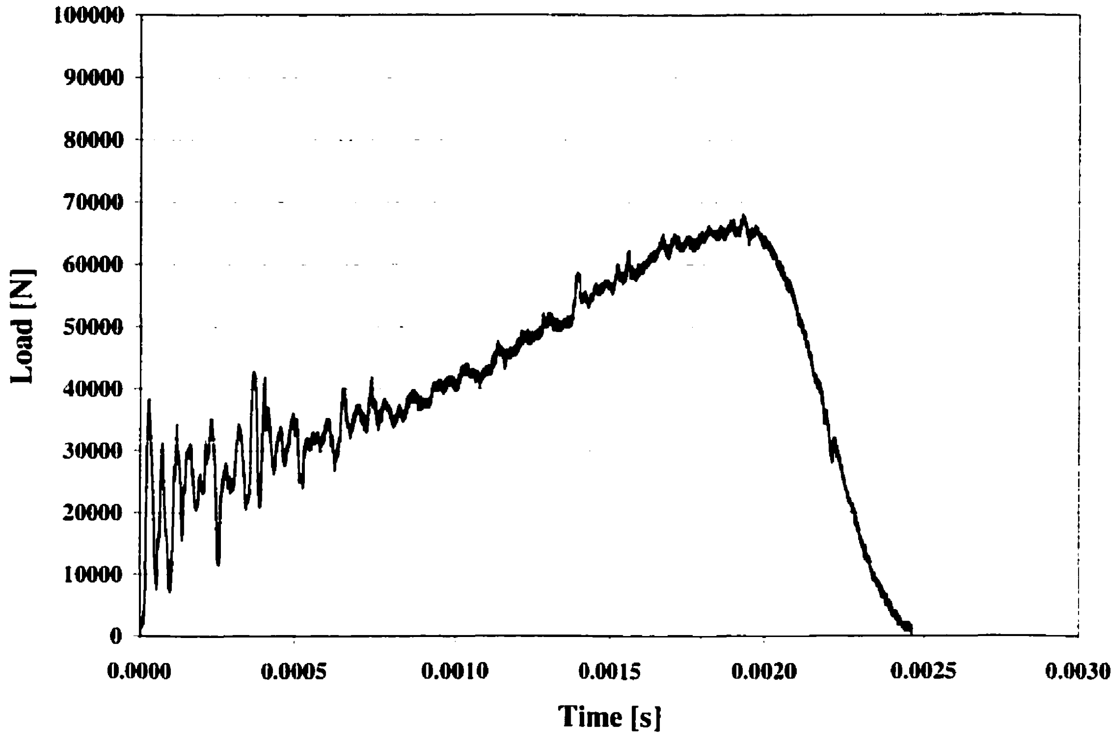

Figure 6.36 Load versus time DWT results for Heat 4 as-rolled – aspect ratio 1.6.

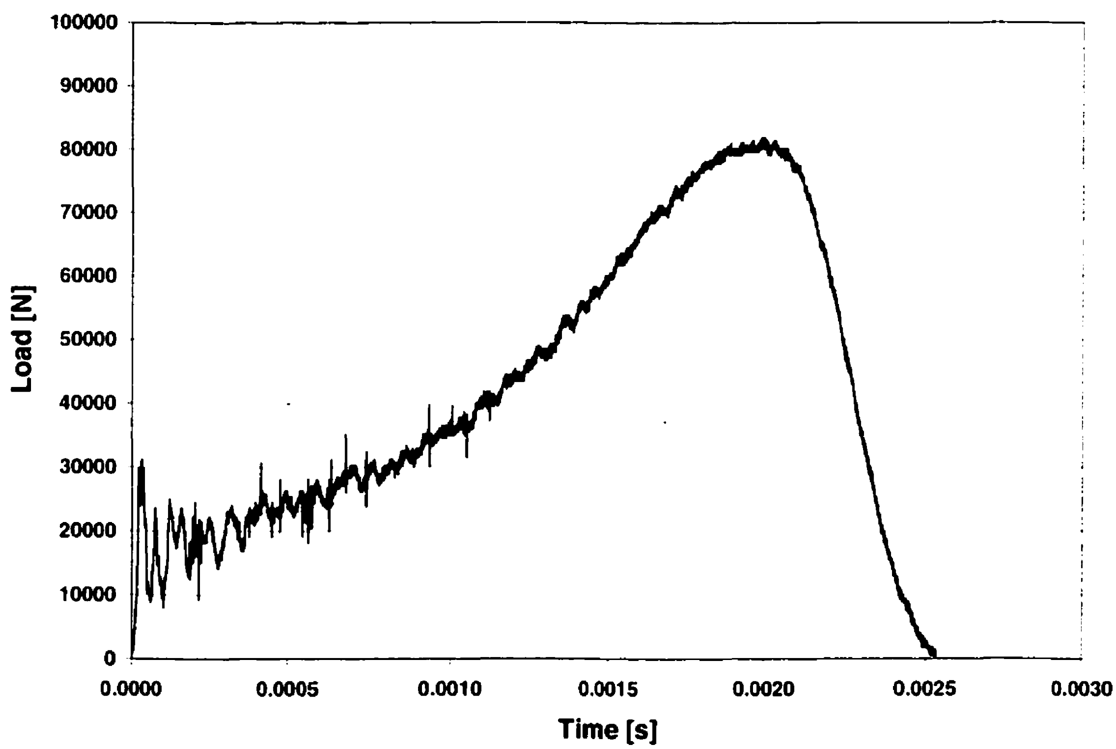

Figure 6.37 Load versus time DWT results for Heat 4 spheroidized – aspect ratio 1.6.

It is evident from Table 6.6 that the maximum load required to initiate fracture is greater by 13.8 kN for the spheroidized material. This may seem surprising since spheroidized materials are known to be more ductile. However, Table 6.6 suggests that the larger mass required to promote fracture (18.16 kg versus 16.99 kg) influenced the peak load.

Friction effects at the die-specimen interface have an increasing influence on the load-time curves as deformation progresses and contact area increases. However, the two experiments were performed under similar conditions of lubrication (sticking friction in the die pockets and molybdenum disulphide lubricant on the flat surface). Therefore, frictional conditions should have a similar influence on both load-time curves.

Repeatability of load-time data was checked using load-time curves for small mass increments above and below the onset of fracture, and found to be satisfactory.

6.2.3 Velocity

Five experiments were conducted to determine the impact velocity of the falling mass using the standard drop height of 1.5 m, and a mass of 11.7 kg. The results are presented in Table 6.7.

Experiment No.	Time [s]	Impact Velocity [ms^{-1}]
1	0.576	5.21
2	0.570	5.26
3	0.560	5.36
4	0.570	5.26
5	0.560	5.36
Average	0.567	5.29
Standard Deviation	0.007	0.07

Table 6.7 Impact velocity measurements from drop height of 1.5 m.

The theoretical initial velocity of 5.42 ms^{-1} was calculated by equating the potential and kinetic energies of the falling mass. The experimental impact velocity was 0.13 ms^{-1}

lower than the theoretical maximum. This is due to friction between the crosshead bearings and the support bars. As expected, none of the measured velocities exceeded the theoretical maximum velocity.

The measured impact velocity was used in equation 5.18 to convert the load-time curves to velocity-time curves. Velocity-time curves for the Heat 4 as rolled and spheroidized materials are presented in Figures 6.38 and 6.39. At the latter stage of deformation, the velocity changes sign, and becomes positive. It is believed that this sign change reflects the rebounding of the crosshead.

Equation 5.19 was employed to compute the displacement-history from the velocity-time data. Load-displacement curves for Heat 4 materials are presented in Figures 6.40 and 6.41. Table 6.8 gives the DWT experimental and calculated final displacements of these materials.

The DWT experimental displacements-to-fracture are between 1.1 and 1.2 mm smaller than the calculated displacements. This difference may be due to specimen unloading, and compliance of the DWT machine and its substructure. This implies that the load-history curves are not representative of the DWT specimen alone: they represent the response to the load developed by the full system, i.e., the DWT specimen, the DWT machine, and the substructure that supports the DWT machine, as it resists the impacting mass.

Material	**Aspect Ratio**	**DWT Experimental Displacement-To-Fracture [mm]**	**Calculated Displacement-To-Fracture [mm]**	**Difference [mm]**
as-rolled	1.6	5.37	6.49	1.12
spheroidized	1.6	6.05	7.29	1.24

Table 6.8 DWT experimental and calculated displacements for Heat 4.

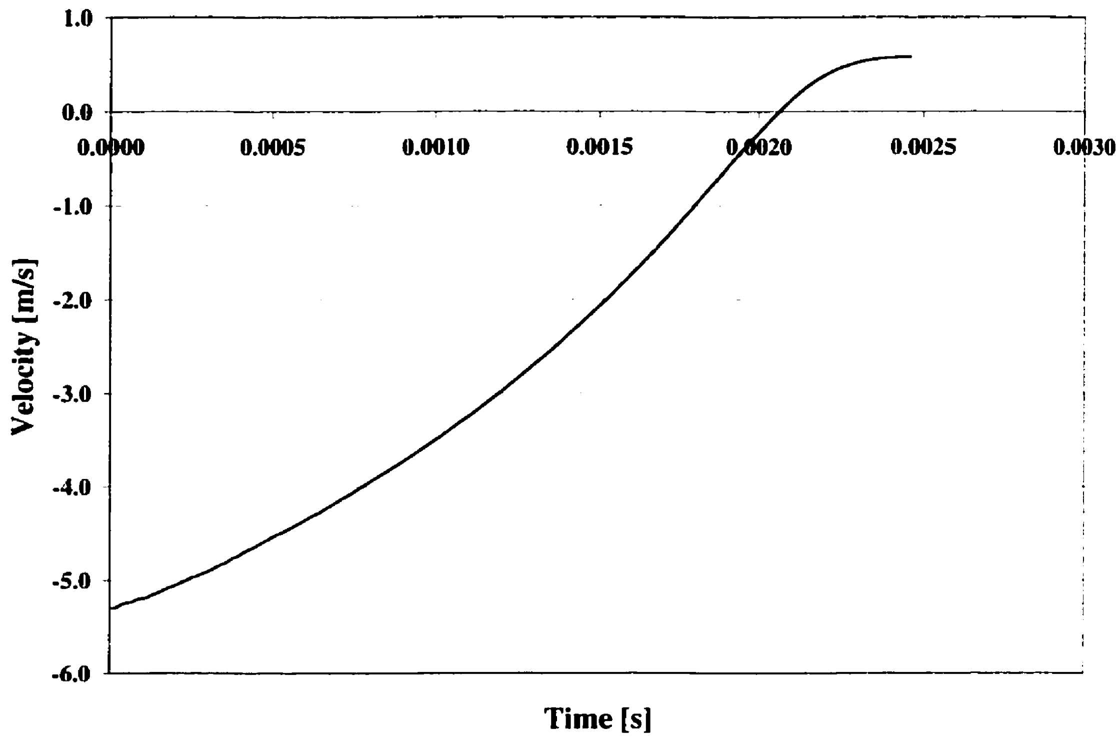

Figure 6.38 Velocity versus time DWT results for Heat 4 as-rolled – aspect ratio 1.6.

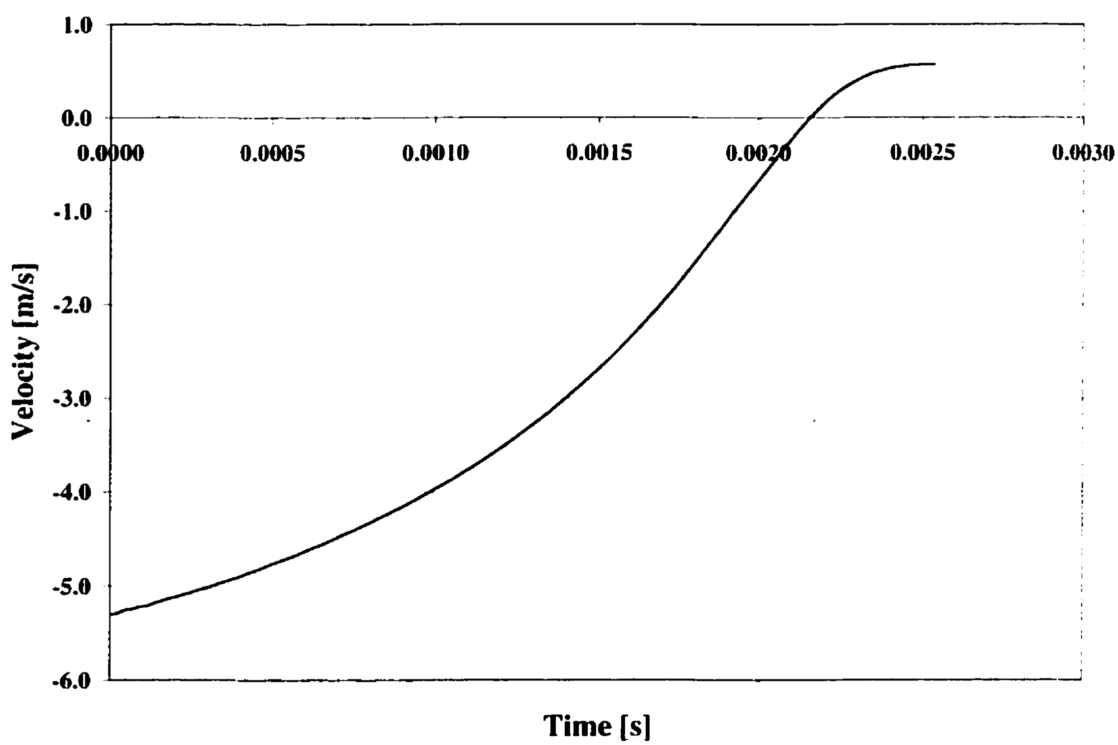

Figure 6.39 Velocity versus time DWT results for Heat 4 spheroidized – aspect ratio 1.6.

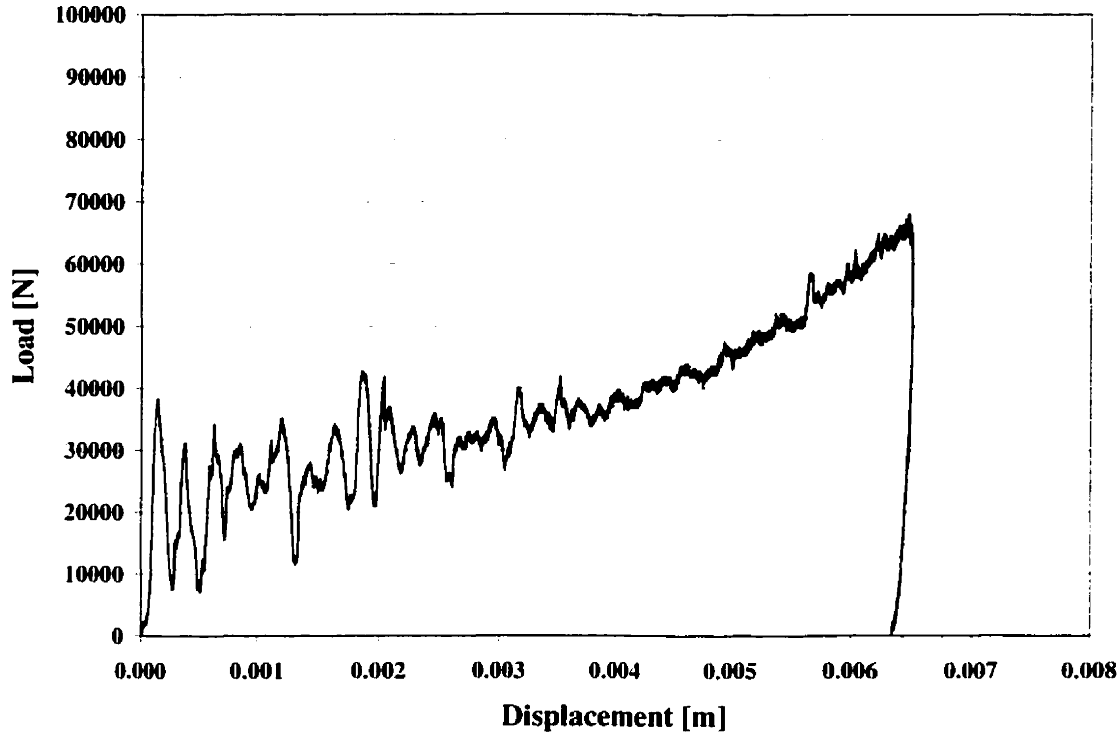

Figure 6.40 Load versus displacement DWT results for Heat 4 as-rolled – aspect ratio 1.6.

Figure 6.41 Load versus displacement DWT results for Heat 4 spheroidized – aspect ratio 1.6.

Given that the mass of the test specimen is significantly smaller than the mass of the DWT machine base and substructure, a 1-degree-of-freedom system was assumed in the analysis presented in Section 5.2.2. In effect, the DWT is a complex mass-spring-damper system. An in-depth analysis of such a system would facilitate the interpretation of results. A recommendation for future work is the derivation of a mass-spring-damper model of the DWT.

6.3 Friction Parameter

FRT experiments were performed on spheroidize annealed Heat 4 material in accordance with the methods described in Section 5.3. Ring specimens were prepared to a ratio of 6.00:2.89:1.95, close to the ratio of 6:3:2 recommended in the literature. FRT experiments were performed on the DWT machine equipped with a set of flat dies using a drop height of 1.5 m and a drop mass of 11.8 kg. The die material, the surface finish, and the molybdenum disulphide lubricant were identical to those employed in DWT with the pocket die-set. FRT results are presented in Table 6.9.

Experiment No.	Initial Outer Diameter [mm]	Initial Inner Diameter [mm]	Initial Height [mm]	Final Outer Diameter [mm]	Final Inner Diameter [mm]	Final Height [mm]
1	5.21	2.51	1.69	6.74	2.67	0.92
2	5.21	2.51	1.70	6.54	2.78	0.92
average	5.21	2.51	1.69_5	6.64	2.72_5	0.92

Table 6.9 FRT results for Heat 4 spheroidize annealed material.

The internal diameter of the deformed ring specimen is 9% larger than the initial diameter, thus indicating low friction. A 45% reduction in height was achieved using a 0.92 mm. thick impact stopper.

FEM simulations of the FRT were performed using Forge2. The velocity factor, P, was set to zero, thereby forcing the friction parameter, $\alpha^{\prime}$, to equal the shear friction factor,

$\overline{m}$. The values of the friction parameter were changed until the inner ring diameters of the FEM simulations and the FRT experiments matched.

The flow behavior of the material was described by the constitutive parameters K_o, m, n, and beta established by CP testing. The initial mesh size of the simulation ring restricted individual elements to an area of 0.47 mm^2. Subsequent mesh sizes used an area of 0.20 mm^2 for additional precision.

The results of the FRT FEM simulations are presented in Table 6.10.

FEM Simulation	α^1 Parameter	Final Height [mm]	Final Outer Diameter [mm]	Final Inner Diameter [mm]
1	0.20	0.92	6.67	2.44
2	0.15	0.92	6.73	2.64
3	*0.13*	*0.92*	*6.77*	*2.73*
4	0.10	0.91	6.84	2.87

Table 6.10 FRT FEM simulation results.

Referring to Tables 6.9 and 6.10, a friction parameter of 0.13 generates a ring configuration that corresponds closely to that obtained during FRT experimentation. The final outer diameter is roughly 2% larger; the final inner diameter is only 0.15% larger. A friction parameter of 0.13 was therefore retained for FEM simulations of the DWT.

Figure 6.42 is a composite of the initial and deformed FEM meshes for the cases where friction parameters were 0.2 and 0.13. The inner diameter using a friction parameter of 0.2 shows a slight contraction, while the inner diameter using a friction parameter of 0.13 shows a 9%, expansion, the latter corresponding to the experimental FRT.

Figure 6.43 shows that superimposing the experimental FRT results (45% reduction in height and 9% expansion of the initial diameter) on the theoretical friction ring calibration chart presented in Figure 5.13, yields a shear friction factor, $\overline{m}$, equal to 0.13. This is the equivalent to the value found with the FEM simulations.

It is interesting to note that Dieter [1997] stated that the use of polished steel dies with molybdenum disulphide solid lubricant should yield a shear friction factor of about 0.08, only marginally different from the value arrived at in this work.

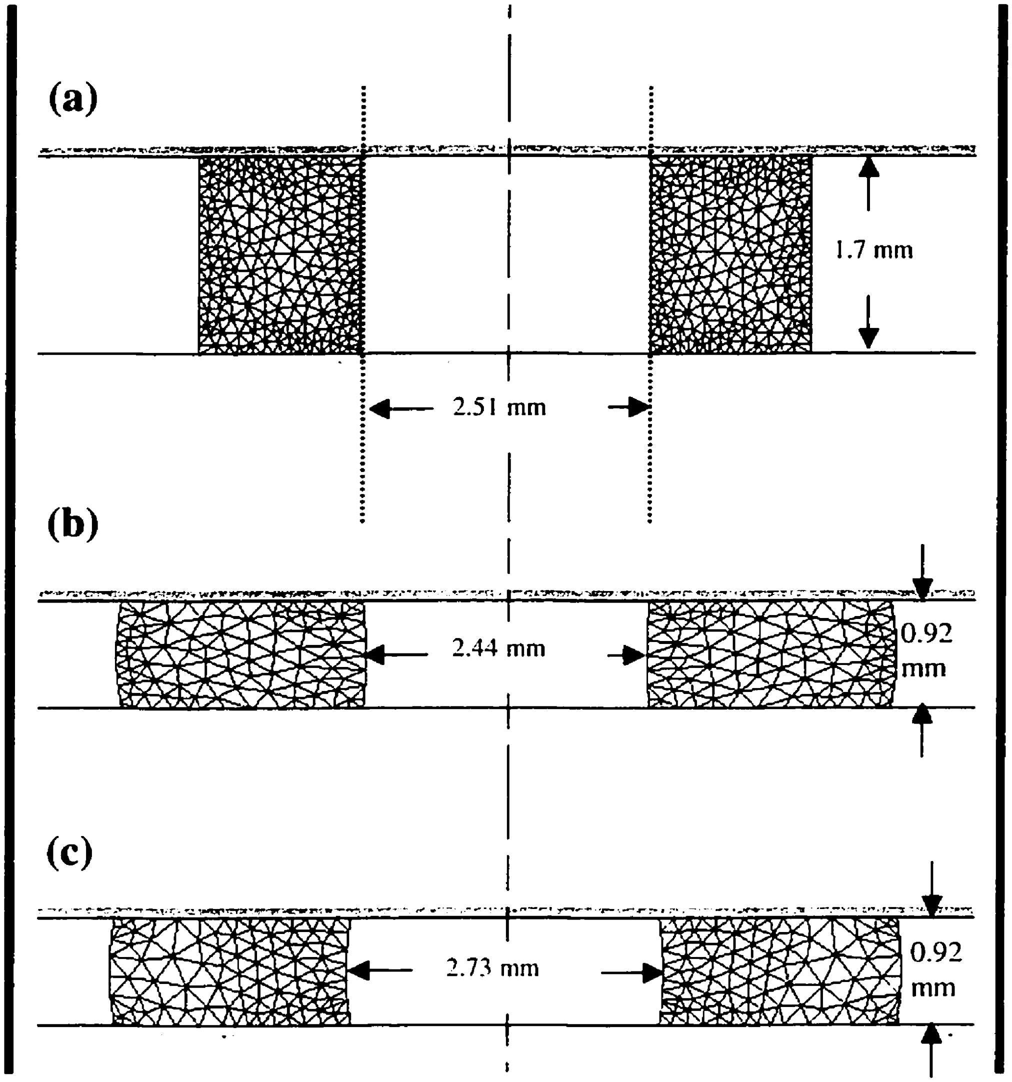

Figure 6.42 Composite of friction ring FEM plots showing (a) undeformed mesh, (b) final mesh for $\alpha^{1} = 0.2$, and (c) final mesh for $\alpha^{1} = 0.13$.

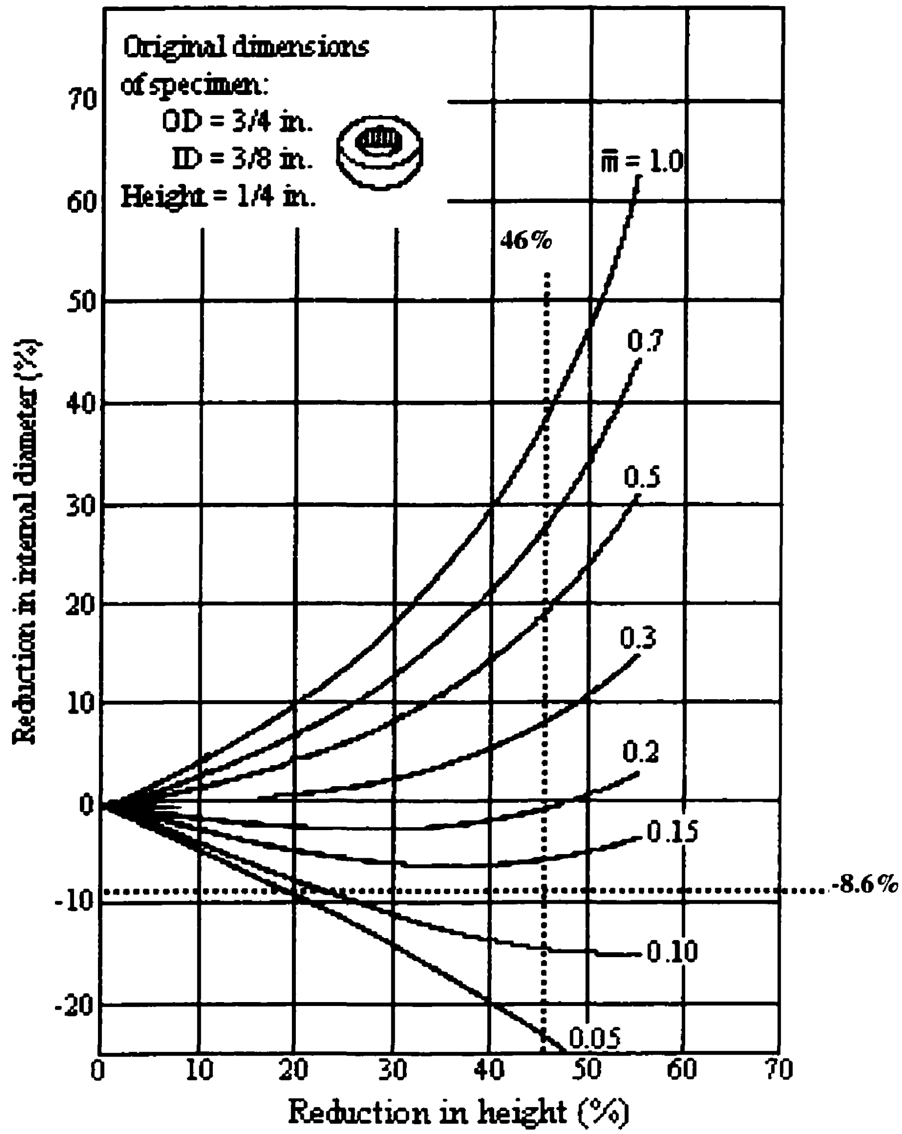

Figure 6.43 Experimental FRT results superimposed on theoretical friction ring calibration chart for the 6:3:2 geometry.

6.4 Finite Element Calculations

Forge2, a commercial FEM software package, was employed to simulate the upsetting of DWT specimens. Experimental determination of the main input parameters, namely, flow stress behavior and friction conditions, was discussed in earlier sections. A rigid-plastic model was used in the FEM simulations.

6.4.1 Heat 4 FEM Results

Heat 4 data for as-rolled and spheroidize annealed materials were selected for the FEM simulations carried out at the two extreme aspect ratios, 1.0 and 1.6. The objective of this work was to model the stress and strain behavior of these materials subjected to upsetting using the pocket die-set configuration, and ultimately to demonstrate the validity of the Cockcroft and Latham ductile fracture criterion.

The initial mesh was generated using the automatic mesh generation function. Quadratic six-node triangular elements were used. Triangular elements can be used to model a two-dimensional problem with curved boundaries by approximating the curve with a series of straight lines [Buchanan, 1995]. Table 6.11 presents the initial mesh parameters employed for the FEM modeling.

Mesh Parameter	Aspect Ratio 1.0	Aspect Ratio 1.6
plane area [mm^2]	18.8	26.8
axisymmetric volume [mm^3]	153.5	219.6
number of corner nodes	272	290
number of elements	458	486
nodes of quadratic triangular element	1001	1065
initial mesh maximum element size [mm]	0.43	0.52
remesh maximum element size [mm]	0.25	0.25

Table 6.11 Initial mesh parameters for FEM models.

Various mesh refinement rates were tested for solution convergence before final selection of the initial mesh parameters. In these preliminary simulations homogeneous upsetting was performed using frictionless flat dies. The accuracy of the FEM solution improves as the number of elements is increased. However, the number of elements is limited by the computer time and memory. Beyond a certain mesh refinement limit, refining the mesh yields little improvement in solution accuracy. In fact, Rowe et al. [1991] state that for axisymmetric plasticity problems, it is usually unnecessary to use more than 1000 elements.

Figure 6.44 shows initial meshes and the pocket dies.

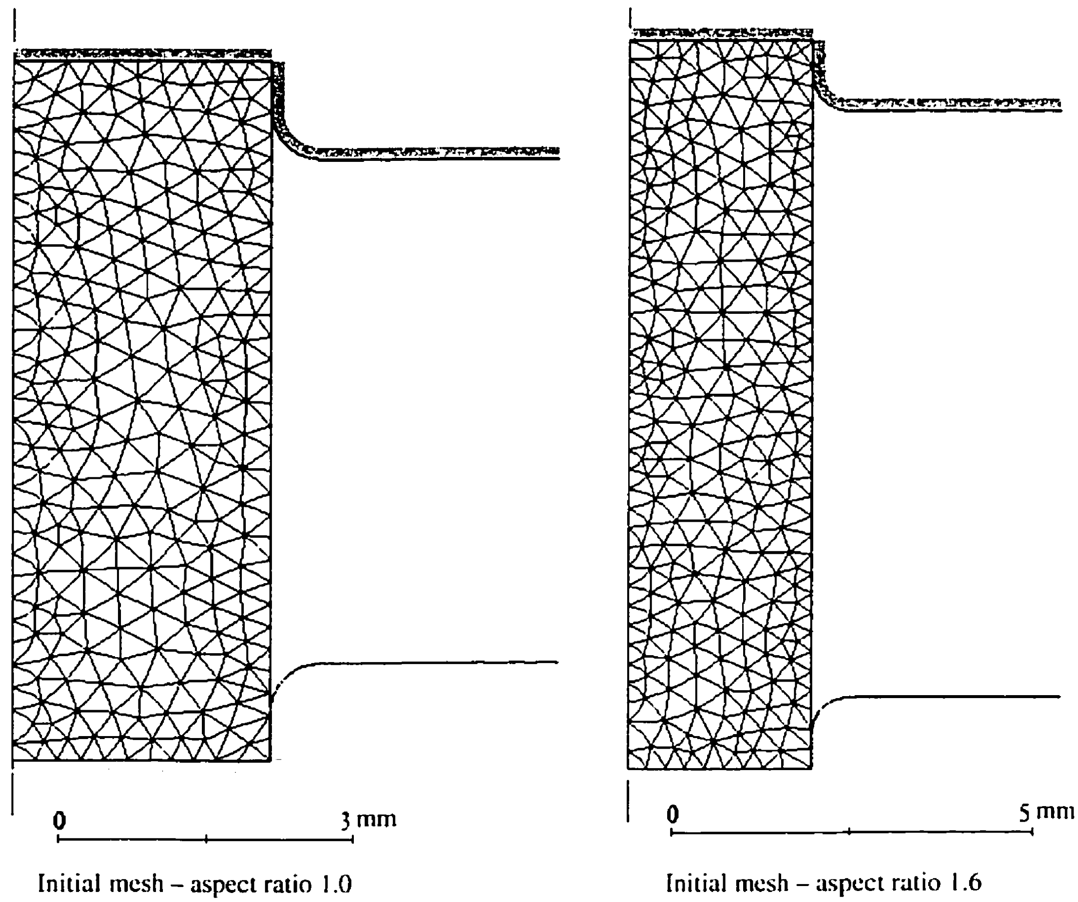

Figure 6.44 Initial mesh and die geometry for aspect ratios of 1.0 and 1.6.

The results for Heat 4 simulations are presented in the form of plots with an abscissa of equivalent strain. All the plots were derived from the history of a material point on the equatorial surface of the specimens. Automatic remeshing occurred when the code was no longer able to perform additional computations due to mesh distortion or mesh penetration into the dies.

All simulations were carried at a constant drop height of 1.5 m, and used the actual DWT drop mass required to fracture a given specimen.

The reference velocity, v_o, in the tool-drop piloting mode is equal to:

$$v_o = \sqrt{2gh} \tag{6.2}$$

where

g = gravitational constant [ms^{-2}]
h = drop height = 1.5 [m]

FEM simulation calculations ended when the drop tool velocity decreased to the reference velocity divided by 100,000. That is, Forge2 continuously updated the velocity until $v = v_o/100{,}000$ using:

$$\frac{1}{2}Mv^2 + W_{total} = \frac{1}{2}Mv_o^2 \tag{6.3}$$

where

$$W_{total} = \text{strain energy} = \int_0^t \dot{W}_{strain}\, dt \tag{6.4}$$

The FEM simulations predicted final specimen heights that were lower than those observed in the actual DWT experiments. The height discrepancies (see Table 6.12) were roughly 1.1 mm. These are attributed to DWT machine compliance. Nevertheless, the results (i.e. stress and strain components, fracture criterion) of the FEM simulations were taken up to the point of fracture as dictated by the final specimen height from the DWT results.

Material	**experimental DWT final height [mm]**	**FEM Simulations final height [mm]**
Heat 4 as-rolled – aspect 1.0	4.03	3.01
Heat 4 as-rolled – aspect 1.6	4.97	3.90
Heat 4 spheroidized – aspect 1.0	3.72	2.69
Heat 4 spheroidized – aspect 1.6	4.28	3.13

Table 6.12 Final specimen height – DWT testing versus FEM simulations.

The equivalent stress versus equivalent strain plots for nodes at the equatorial surface from the Heat 4 FEM simulations are presented in Figure 6.45. The two sets of curves, as-rolled and spheroidized, resemble the true stress versus true strain curves from CP testing (see Figures 6.3 and 6.4). Predictably, the equivalent stress results are independent of the aspect ratio of the material.

At the equatorial surface, the radial component of the stress should vanish. It is evident from Figure 6.46 that the radial stress is essentially zero for all four simulations. These results are in accordance with the expected behavior, and provide additional confidence in the FEM simulation results.

Figures 6.47 and 6.48 are plots of hoop ($\sigma_{\theta\theta}$) and axial (σ_{zz}) stress components versus equivalent strain. From Figure 6.47, it is evident that the hoop stress rises faster for the two materials with the small aspect ratio. This is in accordance with the workability diagram (see Figure 2.9), where a quicker rise in the hoop strain for smaller aspect ratios is observed. Also, for a given aspect ratio, the hoop stress for as-rolled materials rises faster than the hoop stress for spheroidized materials. The hoop stress for all four materials rises to a maximum, decreases to a minimum, and rises again. The onset of the decrease in hoop stress occurs as the material comes in contact with the die face, as will be shown in a later section.

Similar decreases were obtained with the axial stress plot (Figure 6.48). The axial stress also rises faster for the two materials with the smaller aspect ratio. Contrary to the hoop stress, the axial stress for the as-rolled materials rises more slowly than the axial stress for spheroidized materials at a given aspect ratio.

At the start of deformation, the axial stress component should be near the negative of the yield stress according to the von Mises yield criterion. The axial stresses for the as-rolled and spheroidized materials are 800-900 MPa and 550-600 MPa, respectively. These values are comparable to the yield stresses as estimated from Figure 6.45.

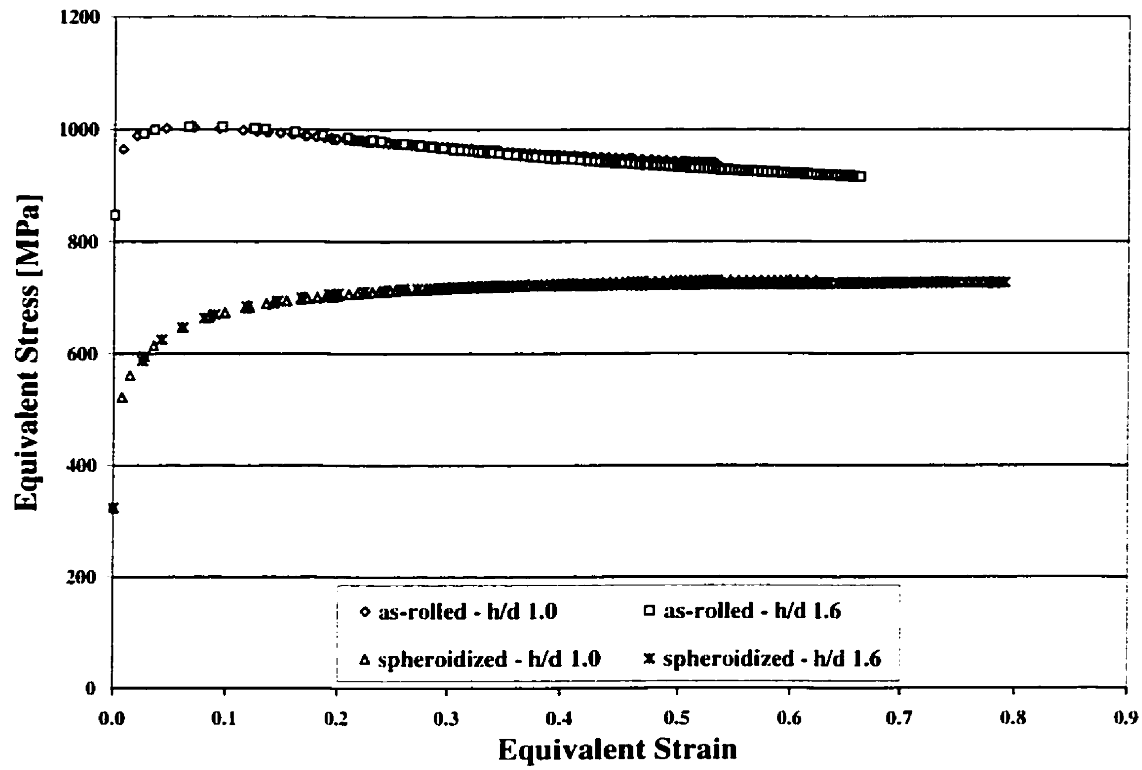

Figure 6.45 Equivalent stress versus equivalent strain for Heat 4 FEM simulations.

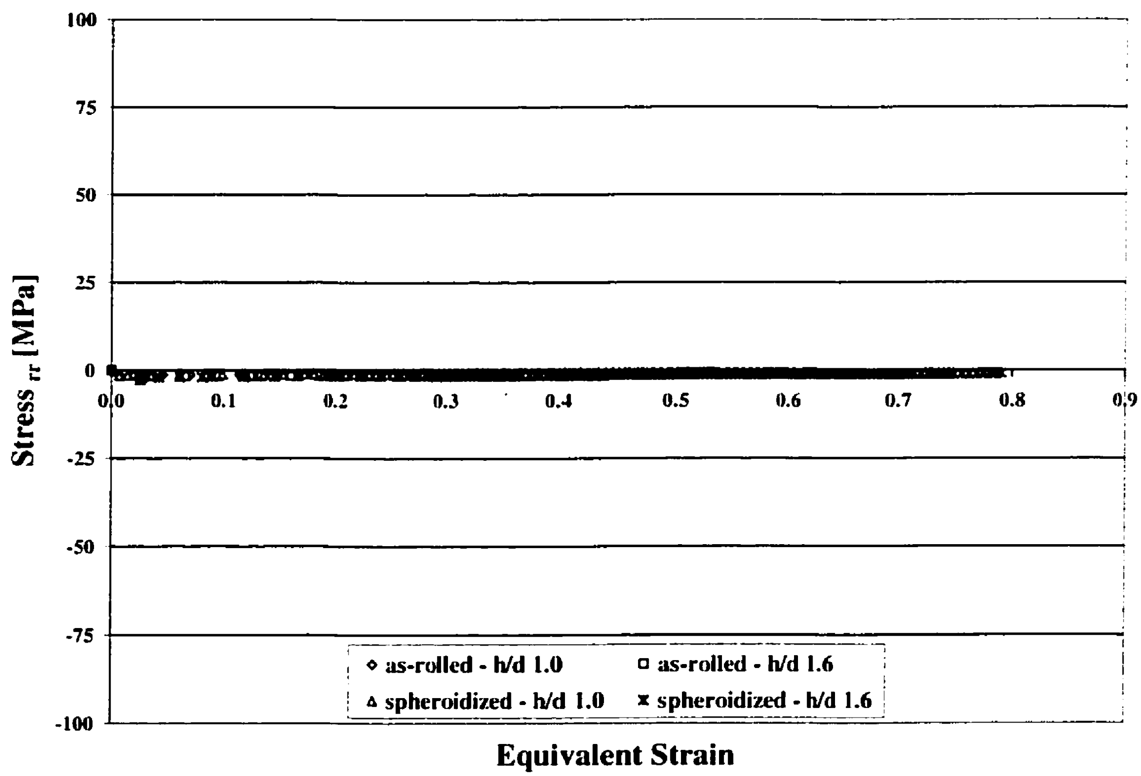

Figure 6.46 Radial stress (σ_{rr}) versus equivalent strain for Heat 4 FEM simulations.

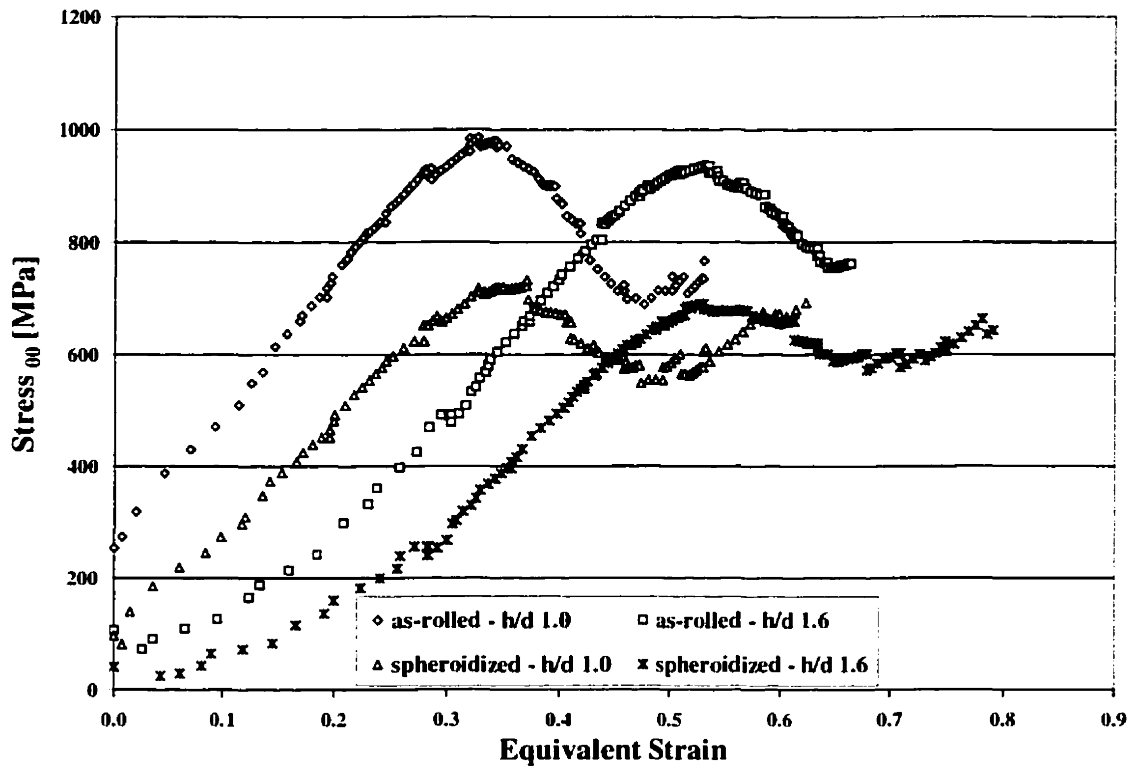

Figure 6.47 Hoop stress ($\sigma_{\theta\theta}$) versus equivalent strain for Heat 4 FEM simulations.

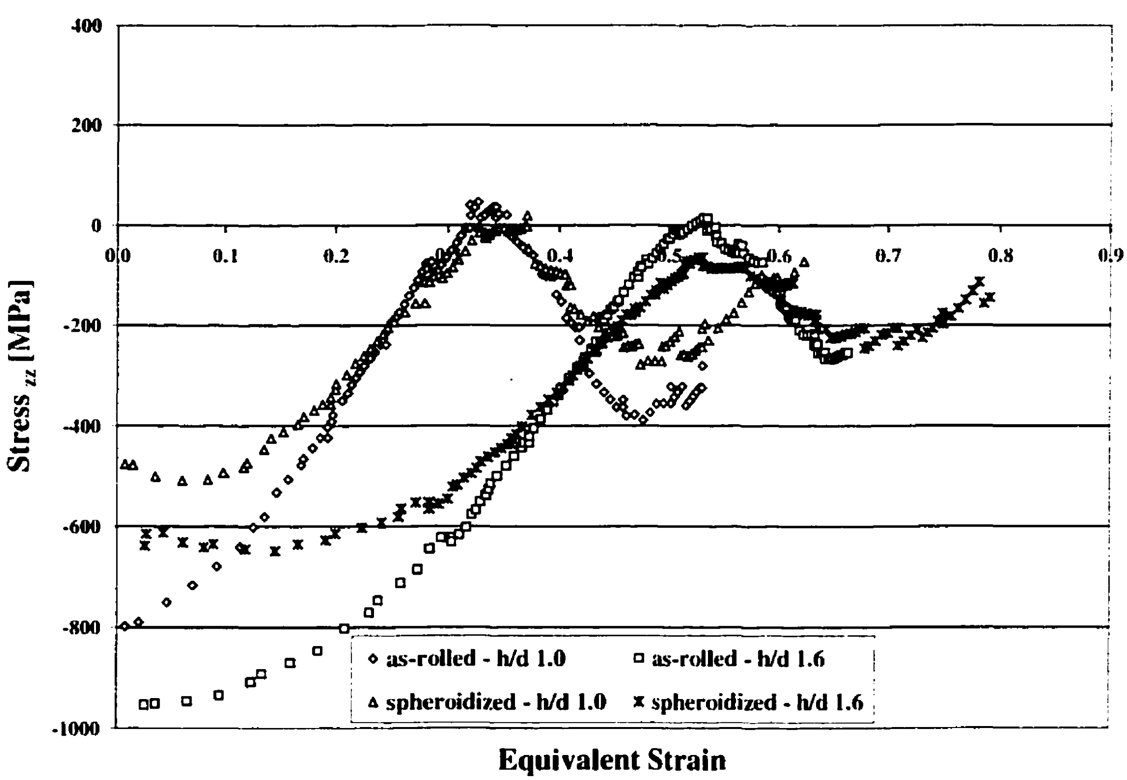

Figure 6.48 Axial stress (σ_{zz}) versus equivalent strain for Heat 4 FEM simulations.

Additional work was performed in order to determine the origin of the decreases. This is presented below, following the analysis of the Heat 4 materials.

The assumption of incompressibility of metals dictates that the hydrostatic component of the stress does not influence yielding. It is known, however, that the hydrostatic stress can have a marked impact on deformation and fracture. Indeed, application of a large hydrostatic pressure during tensile testing can promote uninterrupted necking where the specimen draws down to a point [Hertzberg, 1996]. Figure 6.49 is a plot of the stress triaxiality (hydrostatic/equivalent stress) versus equivalent strain to fracture. The as-rolled materials reach a higher tensile state of stress triaxiality. Therefore, compared to spheroidized materials, as-rolled materials have a larger propensity for fracture. The tensile character of the stress triaxiality makes it a candidate for insertion into a ductile fracture criterion such as the Oyane criterion. In this case, the contribution of this parameter to fracture is similar to that of the hoop stress.

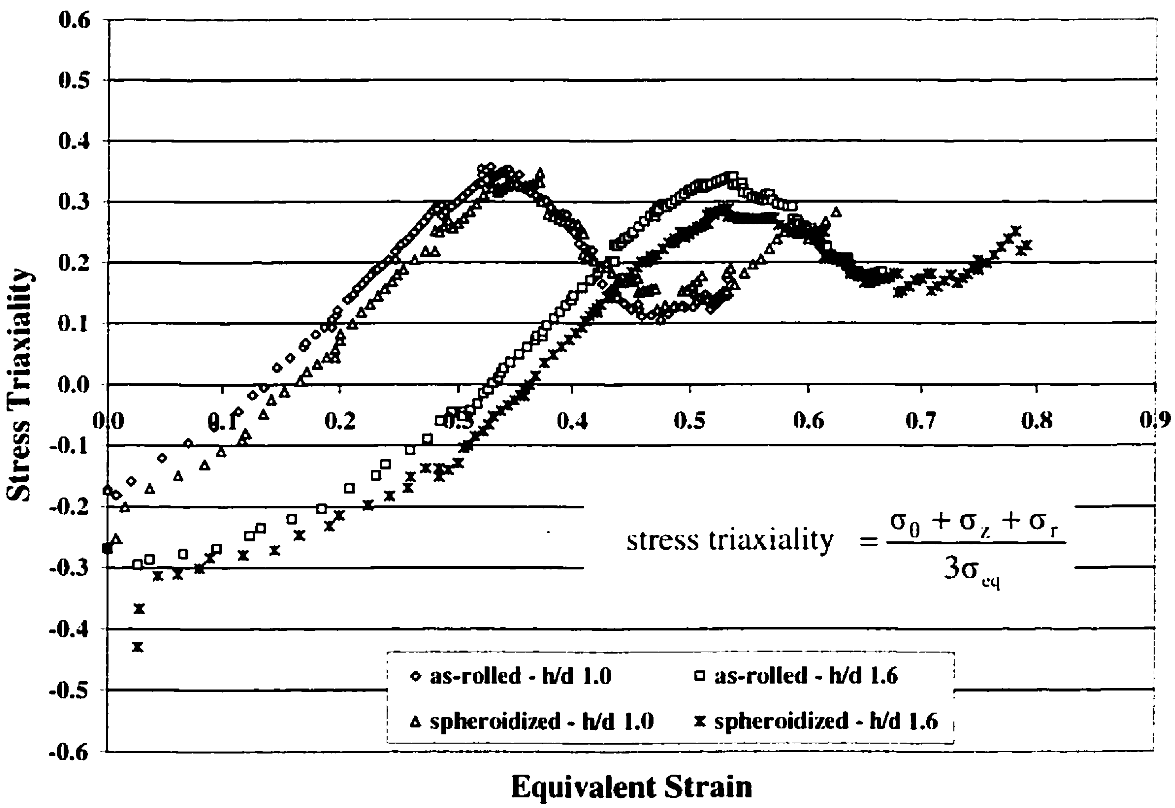

Figure 6.49 Stress triaxiality versus equivalent strain for Heat 4 FEM simulations.

6.4.2 Fracture Criterion Determination

The global approach to ductile fracture, whereby the stress and strain fields calculated at each stage of the deformation process are incorporated into the ductile fracture criterion, was used in this work.

The ductile fracture criterion proposed by Cockcroft and Latham was chosen. This criterion, equation 2.8, states that fracture will occur when the work done by the maximum tensile stress attains a critical energy per unit volume, 'C'. It is important to note this is a material property. In upsetting, the maximum tensile stress is the hoop stress component at the equatorial surface, as discussed earlier.

The Cockcroft and Latham criterion was numerically evaluated using the FEM simulations. In the case of upsetting, the Cockcroft and Latham constant is the area under the hoop stress versus equivalent strain curve (Figure 6.47). For a particular material, the criterion should yield the same cumulative energy to fracture for upset testing regardless of specimen aspect ratio. Should this not be the case, a 2-parameter criterion such as the Oyane fracture criterion might prove to be more successful.

Figure 6.50 presents a plot of the Cockcroft and Latham criterion versus equivalent strain. The Cockcroft and Latham constant remains unaffected by the variation in hoop stresses observed in Figure 6.47.

The Cockcroft and Latham constants were evaluated at the experimental DWT displacement to fracture for the four Heat 4 materials (as-rolled and spheroidized, and aspect ratio of 1.0 and 1.6). These are presented in Tables 6.13 and 6.14. Comparing the FEM results for the as-rolled materials at the two aspect ratios, there is only a 6% difference in Cockcroft and Latham constants for a 25% difference in equivalent strains to fracture. Comparing the spheroidized materials at the two aspect ratios, there is only a 1% difference in the constants for a 29 % difference in equivalent strains to fracture. These results are significant in view of the large equivalent strain differences between the aspect ratios. *These findings suggest that the Cockcroft and Latham criterion is valid for upsetting in cold heading.*

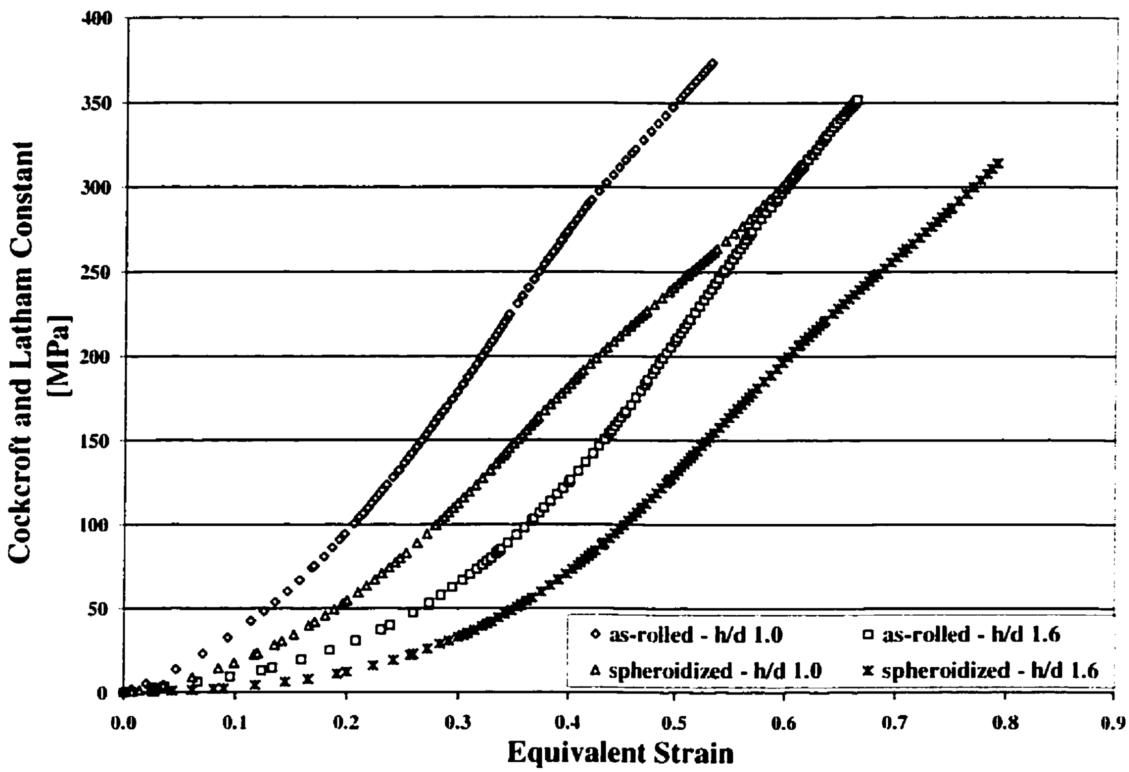

Figure 6.50 Cockcroft and Latham constant versus equivalent strain for Heat 4 FEM simulations.

Heat 4 Material	Cockcroft and Latham constant at fracture [MPa]	Equivalent Strain at Fracture
as-rolled – aspect ratio 1.0	373.4	0.531
as-rolled – aspect ratio 1.6	351.6	0.664
difference	-6%	25%

Table 6.13 Cockcroft and Latham constants at fracture for Heat 4 as-rolled.

Heat 4 Material	Cockcroft and Latham constant at fracture [MPa]	Equivalent Strain at Fracture
spheroidized – aspect ratio 1.0	319.6	0.624
spheroidized – aspect ratio 1.6	323.5	0.805
difference	-1%	29%

Table 6.14 Cockcroft and Latham constants at fracture for Heat 4 spheroidized.

The Cockcroft and Latham constant for the as-rolled material is 11% *larger* than that for the spheroidized annealed material, while the axial strain to fracture is *lower* for the as-rolled materials, as the DWT results of Section 6.2 clearly show. To enable comparison of the Cockcroft and Latham constants between materials, this author proposes that the constants be normalized, i.e., be divided by the respective yield stresses of the materials.

The yield stress used in the normalization is K_o, the strength coefficient determined from CP testing and the Norton-Hoff constitutive relation (equations 2.16 and 2.17).

Table 6.15 shows normalized Cockcroft and Latham constants for Heat 4.

Parameter	Heat 4 as-rolled	Heat 4 spheroidized
Cockcroft and Latham constant (average) [MPa]	362.5	321.6
K_o [MPa]	344	261
normalized Cockcroft and Latham constant	1.05	1.23

Table 6.15 Normalized Cockcroft and Latham results.

The normalized Cockcroft and Latham constant for the spheroidized material is now 15% greater than that for the as-rolled material, indicating a more ductile material. This value is similar to the difference in equivalent strain to fracture for the as-rolled and spheroidized materials (15% and 18% for aspect ratios of 1.0 and 1.6, respectively). Future testing could determine whether this agreement is soundly based or fortuitous.

In a FEM study of upset testing, Dung [1984] normalized the stress components with respect to the yield stress. However, Dung did not apply such a procedure to a fracture criterion.

The Cockcroft and Latham constants obtained in this work are comparable to those found in the literature. For example, Frater and Petrus [1990] determined a Cockcroft and Latham fracture constant of 395 MPa for an as-rolled grade 1045 steel in tension. This value is only 9% greater than the results for the grade 1038 steel tested in this work.

6.4.3 Contour Plot Illustration

In previous sections, the history of a material point on the upset specimen equator was investigated. This section presents FEM results in terms of the full specimen configuration. Figures 6.51 to 6.56 are contour plots of an upset simulation for a Heat 4 as-rolled material specimen, with an aspect ratio of 1.0 and using the experimentally determined friction parameter, i.e., 0.13.

Figure 6.51 is the contour plot of the equivalent strain at fracture. The triangular identifier points to the maximum equivalent strain to fracture at the center of the specimen. The fact that the maximum is not located at the surface implies that any fracture criterion based solely on the equivalent strain is not adequate for upsetting in cold heading.

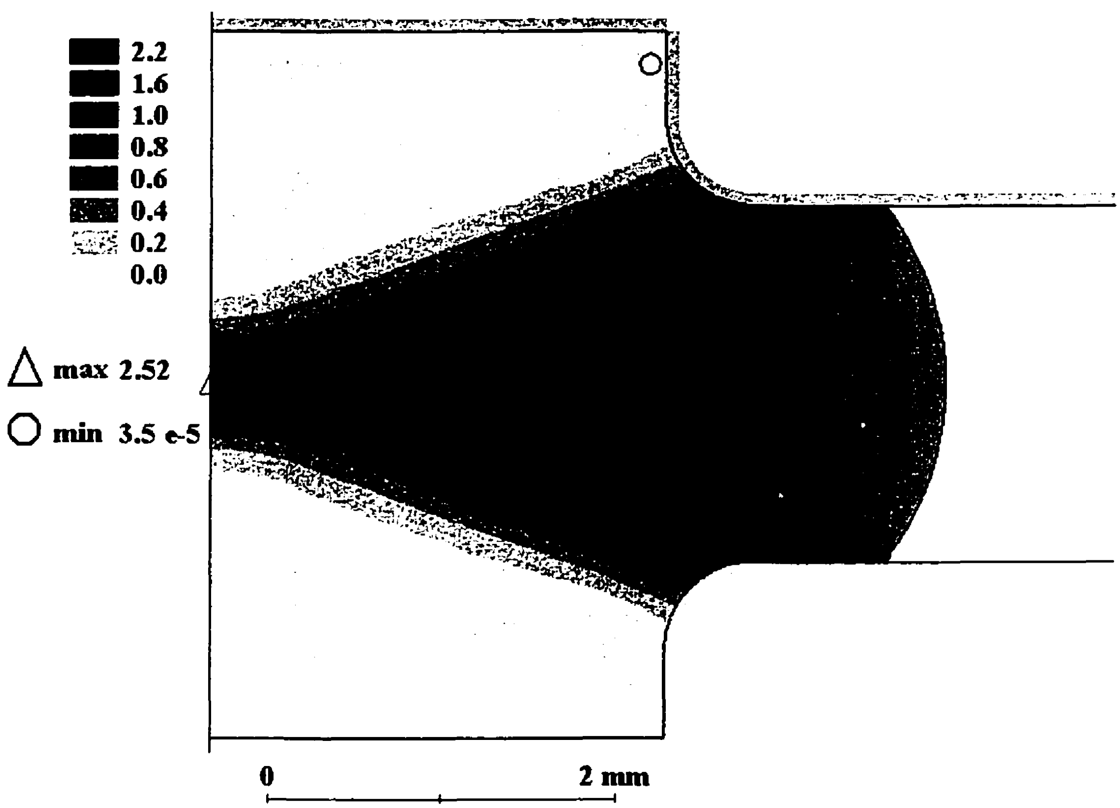

Figure 6.51 Contour plot of equivalent strain at fracture.

Figure 6.52 shows that the maximum equivalent stress is located at the surface, the subsurface and just above and below the horizontal axis of symmetry of the specimen.

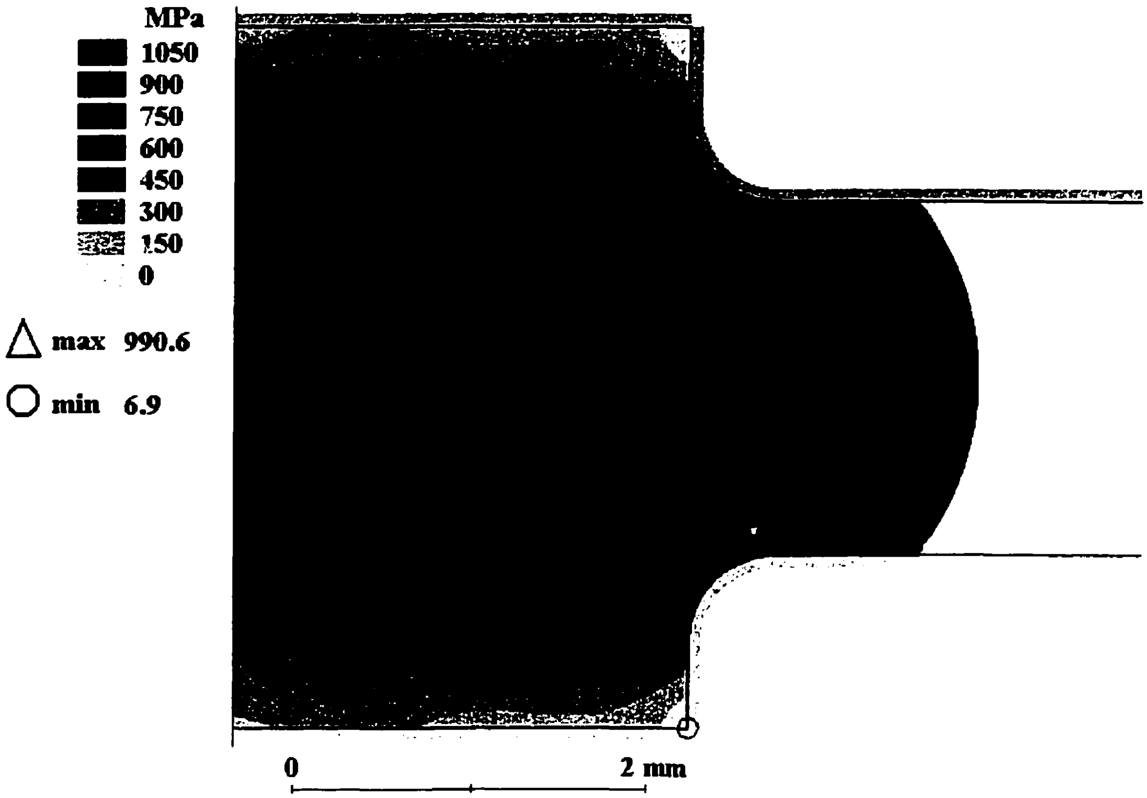

Figure 6.52 Contour plot of equivalent stress at fracture.

Figure 6.53 is a contour plot of the hoop stress component. The central volume of the specimen is in compression, thereby indicating that it is capable of withstanding large loads even after fracture initiation. The volume just under the barreled surface is in tension. The maximum hoop stress is tensile, and is located on the equatorial surface where fracture is known to occur.

Figure 6.54 is a contour plot of the axial stress component. The axial stress at the equatorial surface is in compression, and therefore does not contribute to fracture. Figure 6.55 is a contour plot of the Cockcroft and Latham constant calculated by numerical integration to fracture of the maximum hoop stress and the equivalent strain product. Here, the maximum is located at the equatorial surface, the location at which fracture occurred during DWT testing.

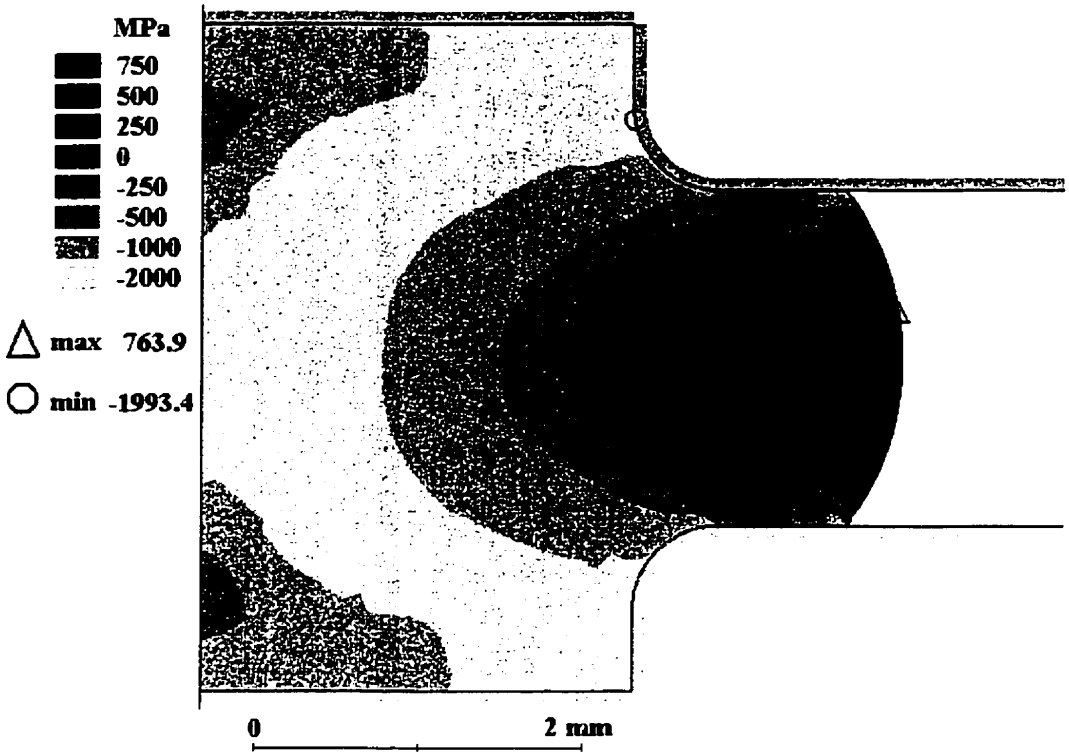

Figure 6.53 Contour plot of hoop stress at fracture.

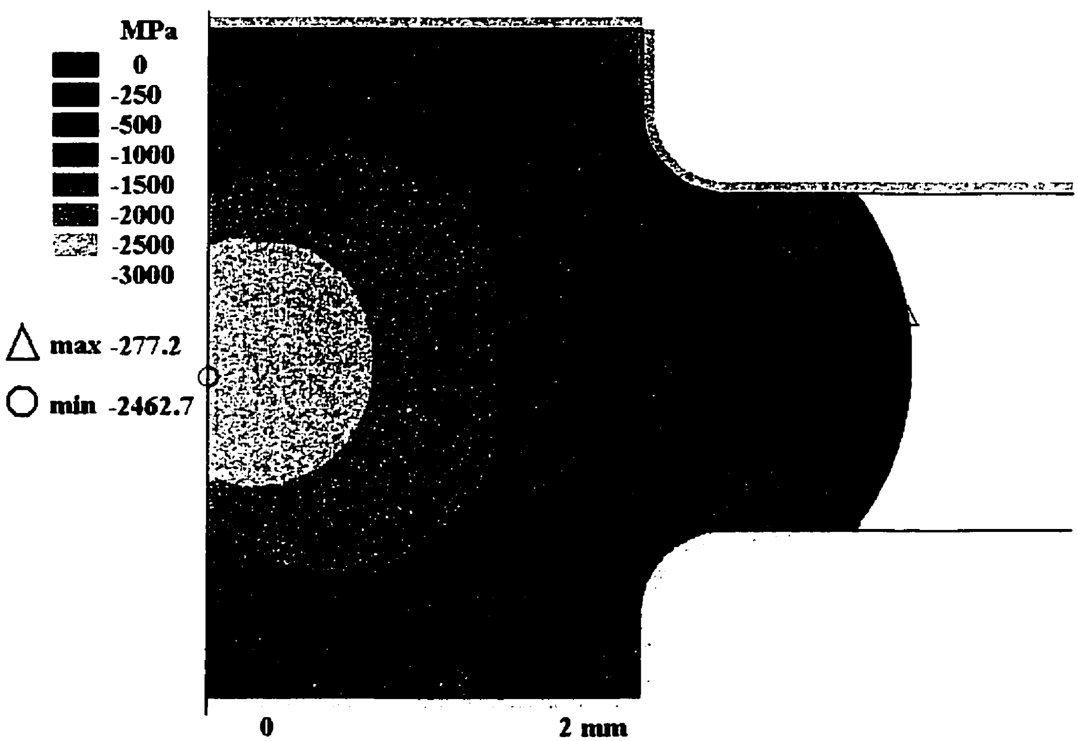

Figure 6.54 Contour plot of axial stress at fracture.

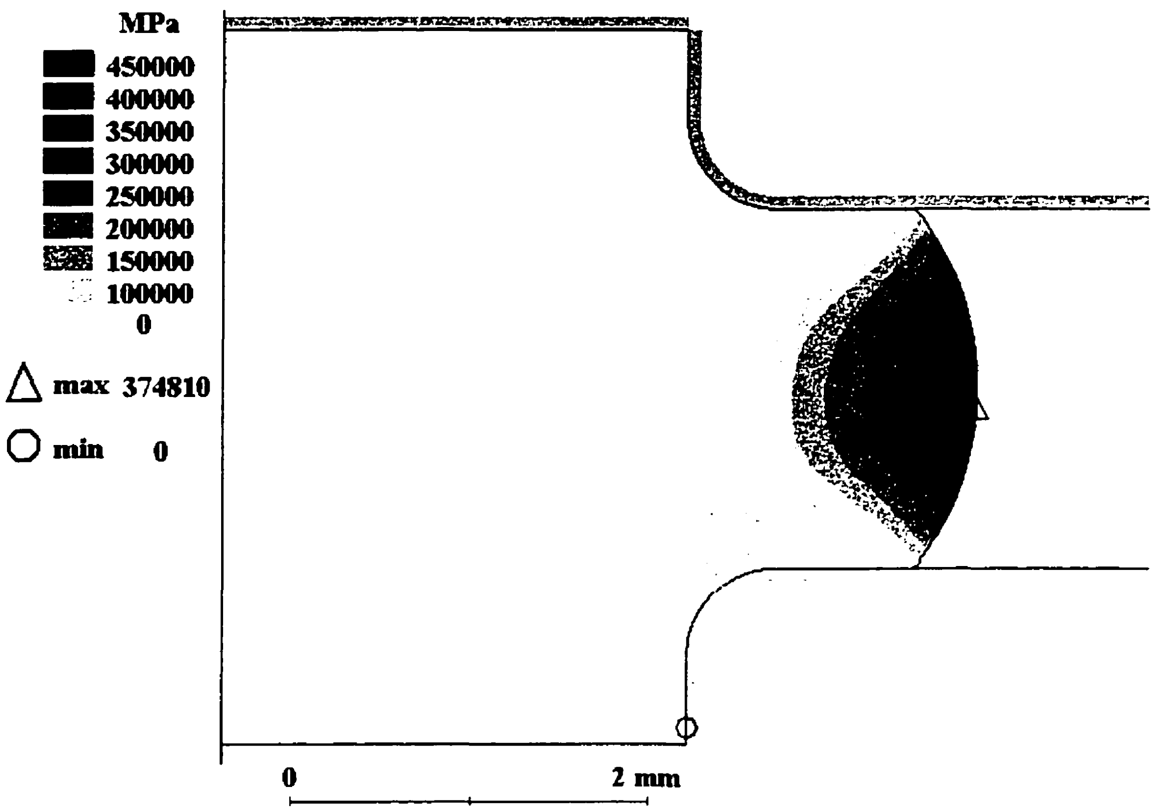

Figure 6.55 Contour plot of Cockcroft and Latham constant at fracture.

Figure 6.56 shows the temperature distribution at the instant of fracture. The temperature exceeds 500°C at the center of the specimen, where the maximum strain occurs. These results agree with the findings of Hartley et al. [1986] and Osakada [1989].

The temperature of about 540°C attained in this simulation is by no means the maximum possible, either in DWT testing or in FEM simulations. Figure 6.35 in Section 6.2 shows a transformed shear band produced during exploratory DWT; hence, by inference, temperatures in excess of the Ac_1 temperature were attained. Moreover, Verreman et al. [2000] produced FEM contour plots where the temperature at the center of the upset part exceeded 800°C under extreme conditions. Shear bands are of concern to the fastener industry since they cannot be identified by normal inspection procedures. The advent of faster cold heading machines and the current industry trend of reducing the number of operations in a heading sequence may heighten concerns over transformed shear bands.

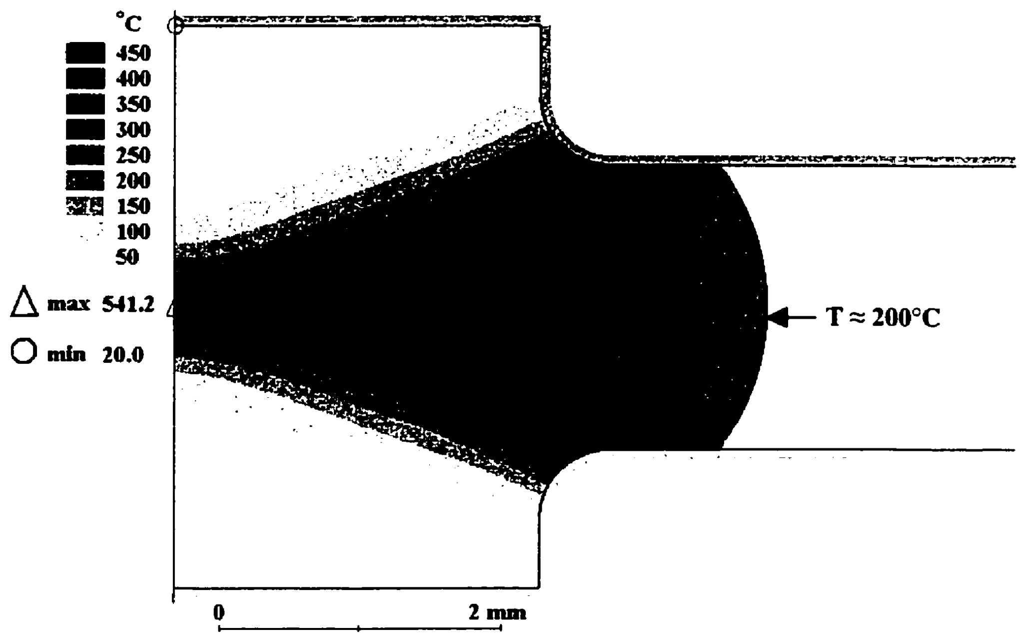

Figure 6.56 Contour plot of temperature at fracture.

6.4.4 Effect of Friction on FEM Results

The importance of friction conditions has been discussed in Section 2.5.2 with respect to the workability diagram (Figure 2.9). Friction effects were simulated using as-rolled material from Heat 4 at an aspect ratio of 1.0. Figure 6.57 is a plot of the hoop stress versus equivalent strain for five friction conditions which varied from alpha = 0 (no friction) to alpha = 1.0 (full friction). The hoop stress component remains tensile at the surface throughout the deformation. The behavior of the curves is influenced by the friction conditions; the lower the value of alpha, the greater the drop in stress following the maximum.

Figure 6.58 is a plot of axial stress versus equivalent strain. A similar behavior is observed for this stress component. Axial stresses at the start of deformation converge to the material yield stress for all five friction conditions. The behavior of both stress components suggests the presence of near sticky friction conditions ($\alpha^{\prime} = 1$; $P = 0$) until contact develops between the material and the die face. The theory of the workability diagram states that the strain path is related to the friction conditions. Steeper strain paths result in additional barreling and smaller barrel radii.

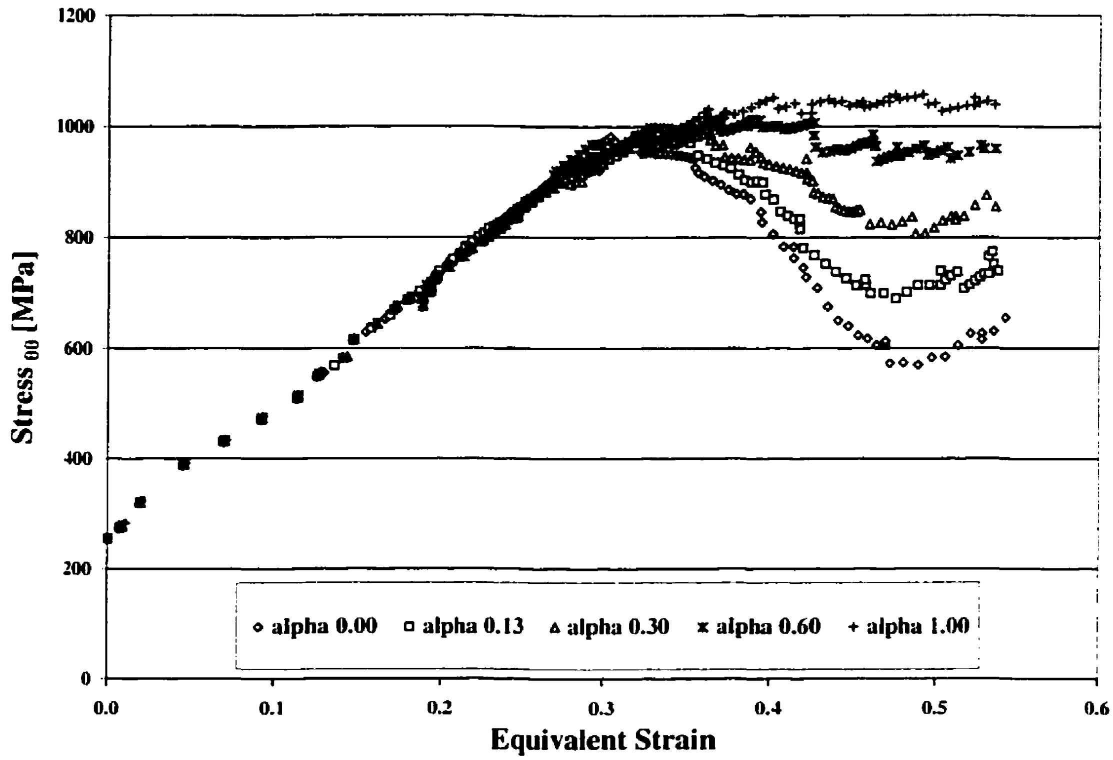

Figure 6.57 Hoop stress versus equivalent strain for 5 friction conditions for as-rolled Heat 4 material, aspect ratio 1.0.

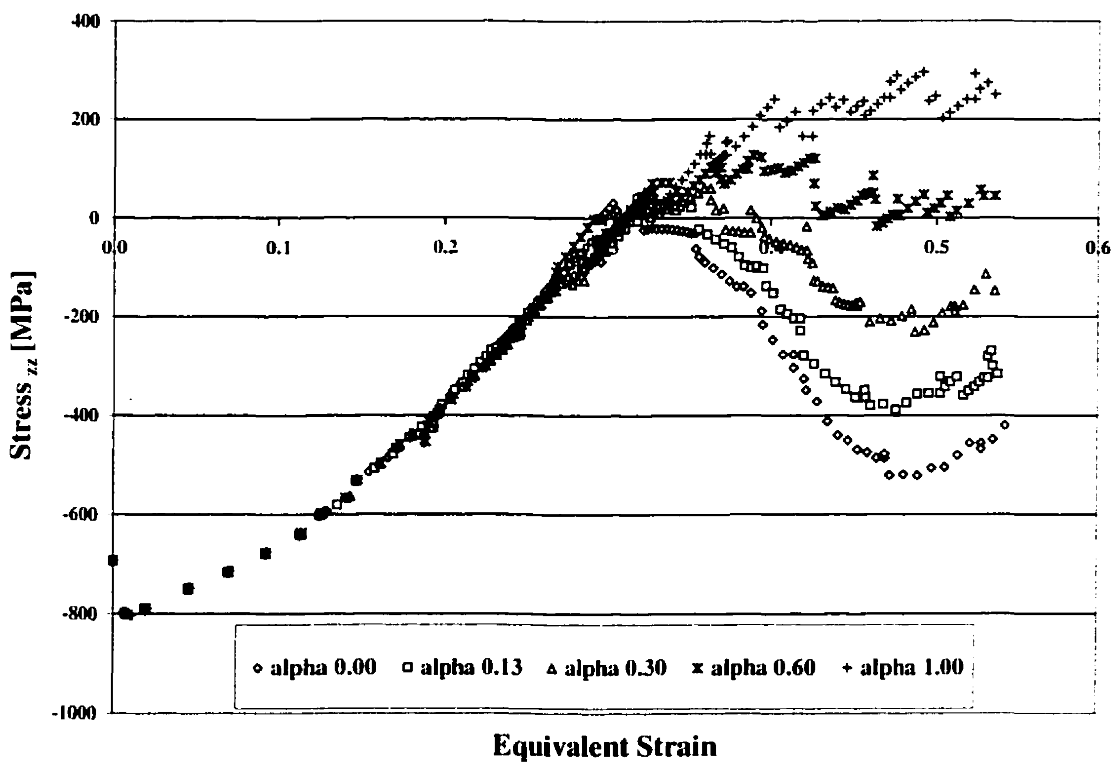

Figure 6.58 Axial stress versus equivalent strain for 5 friction conditions for as-rolled Heat 4 material, aspect ratio 1.0.

It is possible to estimate the equivalent strain to fracture values for various friction conditions from the experimental Cockcroft and Latham constant presented in Section 6.4.2. The fact that the Cockcroft and Latham constant is independent of friction makes it reasonable to assume that had all 5 friction conditions been tested, the strain to fracture would have diminished with an increase in the α^{I} parameter.

For a friction parameter of $\alpha^{I} = 0.30$, an equivalent strain to fracture locus of 0.518 was calculated by matching the areas under the hoop stress versus equivalent strain curves for the experimentally determined curve, i.e., for $\alpha^{I} = 0.13$, and for the calculated curve, i.e., $\alpha^{I} = 0.30$. Table 6.16 lists the results of similar calculations for 4 different theoretical friction conditions.

friction parameter	calculated equivalent strain to fracture locus
$\alpha^{I} = 0.00$	0.563
$\alpha^{I} = 0.13$	0.537 (experimental)
$\alpha^{I} = 0.30$	0.518
$\alpha^{I} = 0.60$	0.500
$\alpha^{I} = 1.00$	0.495

Table 6.16 Calculated and experimentally determined equivalent strain to fracture for five friction conditions.

As predicted, the smaller the friction parameter, the larger the calculated equivalent strain to fracture. The difference in calculated equivalent strain to fracture locus between the two extreme theoretical friction conditions is 12%.

Figure 6.59 is a plot of hoop stress versus equivalent strain that includes the calculated fracture loci presented in Table 6.16. Evidently, proper lubrication (i.e. low friction parameter) has a marked and beneficial effect on strain to fracture during upsetting.

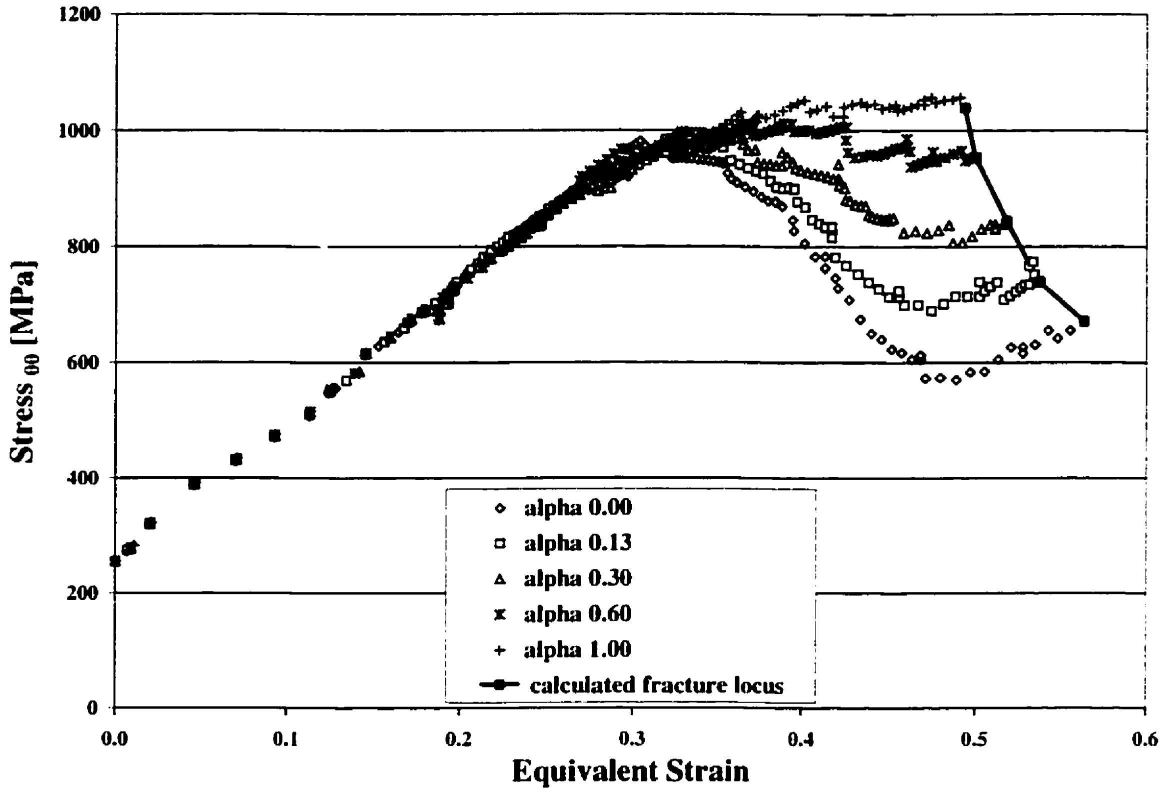

Figure 6.59 Hoop stress versus equivalent strain for 5 friction conditions including calculated fracture loci.

Figure 6.60 illustrates barrel radius progression as a function of equivalent strain and hoop stress for as-rolled Heat 4, aspect ratio 1.0 with high ($\alpha^{I} = 1.0$) and low ($\alpha^{I} = 0.13$) friction. The barrel radius is a measure of the stress on the equatorial surface.

The barrel radius for *high* friction progression decreases appreciably (from A to D) as the hoop stress stabilizes at about 1050 MPa. The barrel radius for the *low* friction progression decreases at a much lower rate from equivalent strain 0.38 to 0.48 (A to C) while the hoop stress decreases.

The composite images marked 'E' in Figure 6.60 summarize barrel radius progressions. The images were produced by overlapping the surfaces from illustrations 'A', 'B', 'C', and 'D'.

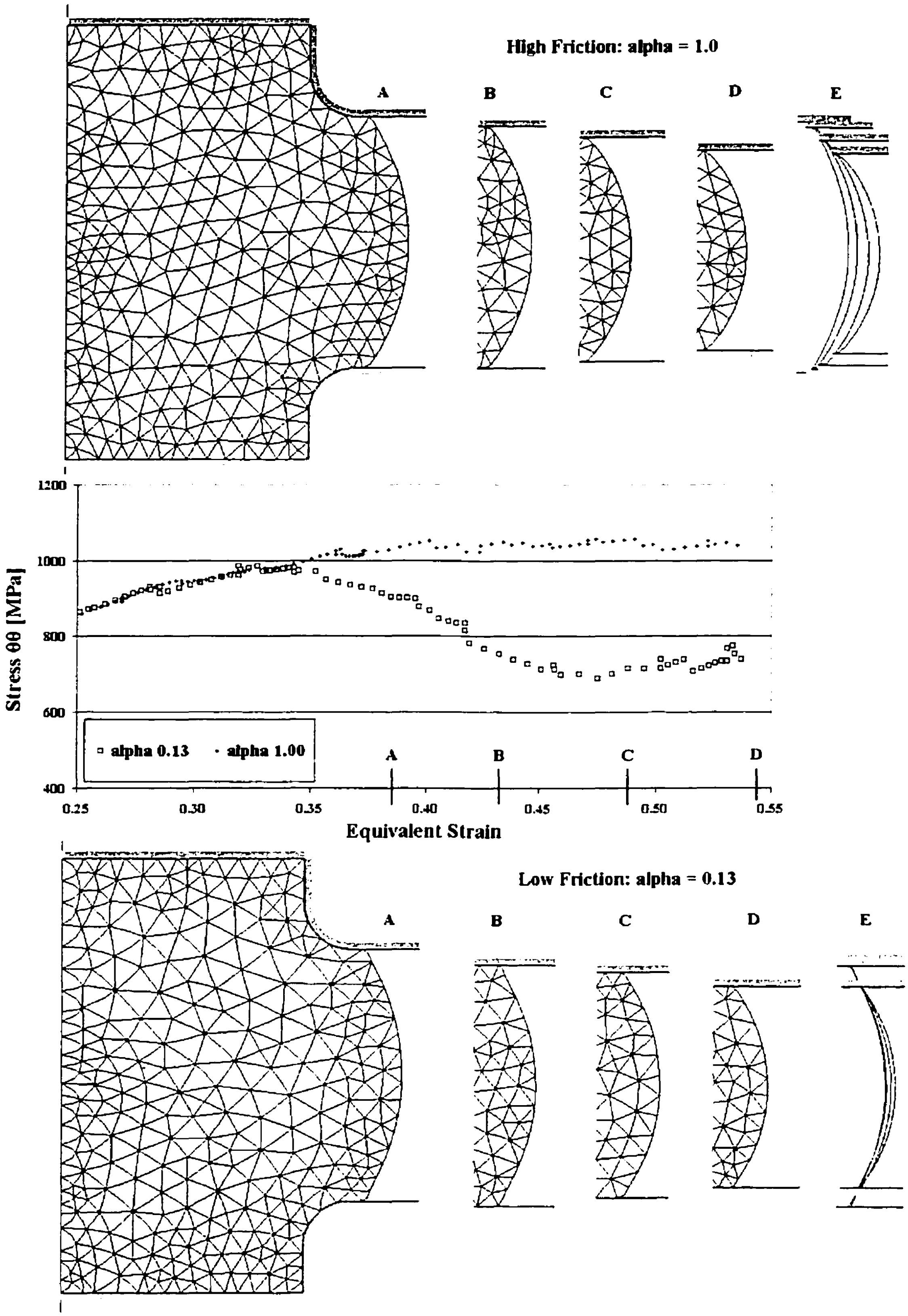

Figure 6.60 Barrel radius progression as a function of equivalent strain and hoop stress for as-rolled Heat 4, aspect ratio 1.0 with high and low friction ($\alpha^{l} = 0.13$ and $\alpha^{l} = 1.0$).

Figure 6.61 shows the differences in the stress component behaviors for the various friction conditions in the workability diagram (hoop strain versus axial strain) for Heat 4 as-rolled material. The diagram illustrates that at low friction (α^{l} = 0.13) and at a given aspect ratio the hoop strain component increases more slowly than when high friction (α^{l} = 1.0) conditions apply. This is due to the fact that there is less barreling at the equatorial surface. Under high friction conditions, the slope is steeper and the hoop strain component increases faster due to the increased barreling.

The two simulations performed with the experimental friction conditions (α^{l} = 0.13) and with aspect ratios of 1.0 and 1.6 exhibit fracture loci that are approximately parallel to the homogeneous (frictionless) compression line as predicted by the workability diagram theory. The fracture locus crosses the ordinate at a hoop strain of 0.33 for the grade 1038 steel used in this work. It is interesting to note that Kuhn [1978] determined the hoop strain intercept to be 0.28 for grade 1045 and 0.32 for grade 1022 steels.

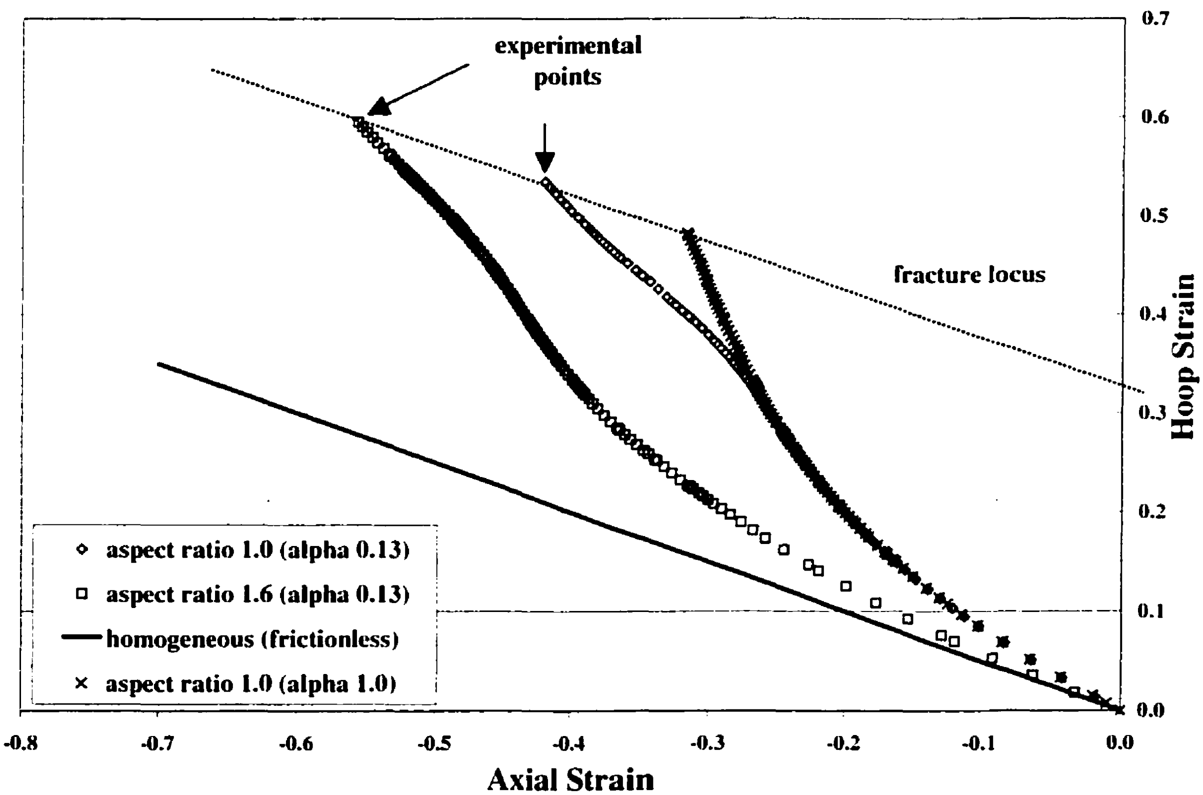

Figure 6.61 Hoop strain versus axial strain for Heat 4 as-rolled.

Figure 6.62 is a workability diagram plot for spheroidize annealed Heat 4 material. The fracture locus is again approximately parallel to homogeneous (frictionless) compression. The fracture locus crosses the ordinate at about 0.35 hoop strain, indicating that the material is slightly more ductile. The difference in fracture locus intercept between the two microstructures is less than 9%. This difference is based on an extended extrapolation of the fracture locus to the ordinate, and is therefore tenuous. *The workability diagram does not discriminate between the microstructures as well as does the normalized Cockcroft and Latham criterion (see Section 6.4.2).*

Another interesting observation is that larger aspect ratio specimens approach homogeneous compression more closely, thereby delaying barreling and consequential fracture, a behavior predicted by the workability diagram theory.

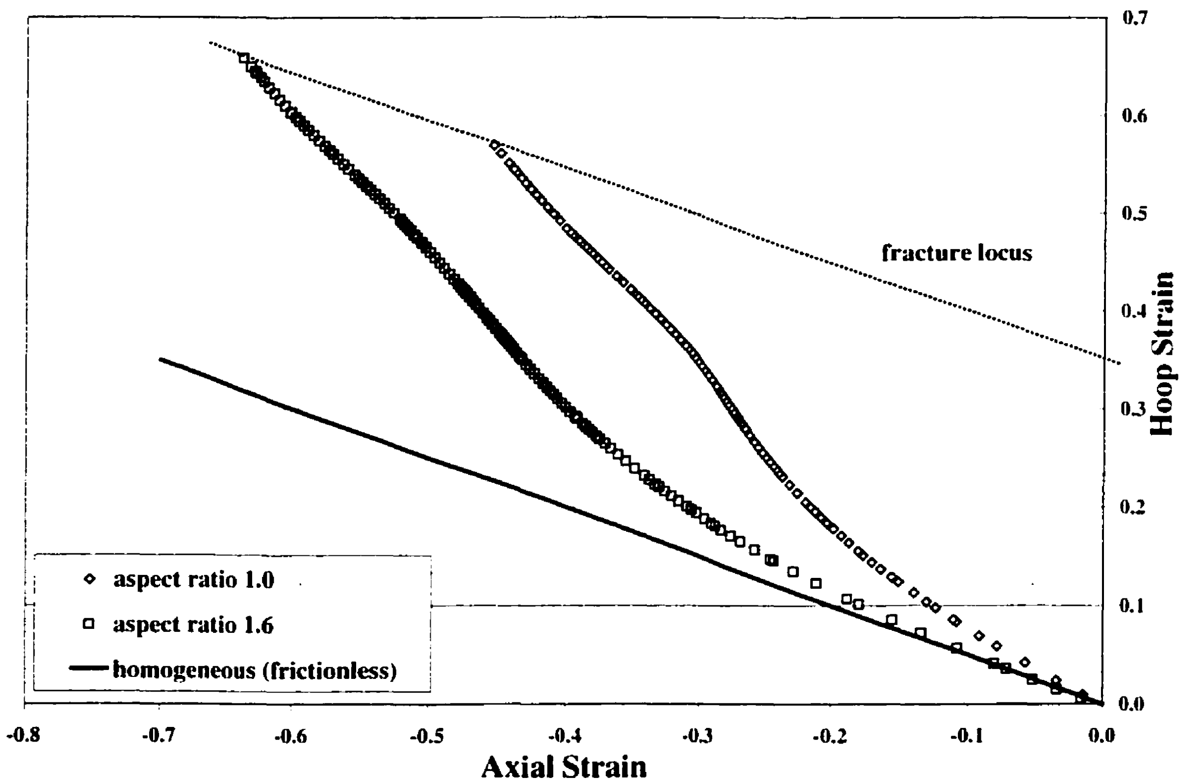

Figure 6.62 Hoop strain versus axial strain for Heat 4 spheroidized.

From the Levy-Mises relations [Olsson et al., 1986]:

$$\sigma_z = \frac{\sigma_{eq}}{\sqrt{3}} \frac{1+2K}{\sqrt{1+K+K^2}} \tag{6.6}$$

$$\sigma_\theta = \frac{\sigma_{eq}}{\sqrt{3}} \frac{2+K}{\sqrt{1+K+K^2}} \tag{6.7}$$

where K is the instantaneous strain ratio:

$$K = \frac{d\varepsilon_z}{d\varepsilon_\theta} \tag{6.8}$$

$$\frac{\sigma_z}{\sigma_\theta} = \frac{1+2K}{2+K} \tag{6.9}$$

From the workability diagram, it is evident that the instantaneous strain ratio, K, varies from 0 with very high friction to -2 for no friction (homogeneous compression). Therefore, as the instantaneous strain ratio decreases, the ratio of the stress components (σ_z/σ_θ) decreases.

Figure 6.63 is a plot of the stress ratio (σ_z/σ_θ) versus equivalent strain for the Heat 4 materials. It is evident that the larger aspect ratio specimens begin deforming at a smaller stress ratio. This is also true for the softer material (spheroidize annealed).

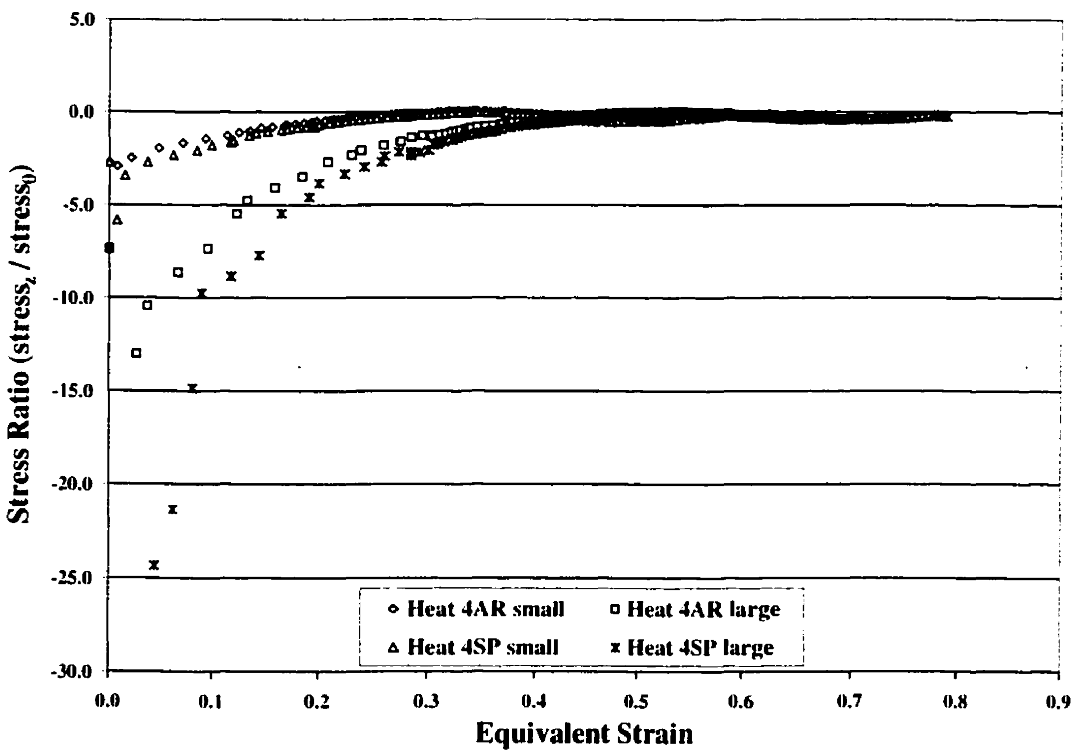

Figure 6.63 Stress ratio (σ_z/σ_θ) versus equivalent strain for Heat4 materials.

This plot can be discussed in terms of the von Mises yield surface in two-dimensions (see Figure 6.64). The larger aspect ratio specimens begin deforming closer to point 'A' on the yield surface. A similar behavior would be expected for lower friction conditions. As deformation proceeds, the stress ratio for the as-rolled materials becomes progressively larger. Thus, the stress state moves upwards along the yield surface until it passes a state of uniaxial tension at point 'B' (stress ratio of 0). A slight state of biaxial tension (positive stress ratio) is then reached, before the stress ratio falls back to just below zero, as shown in the previous figure.

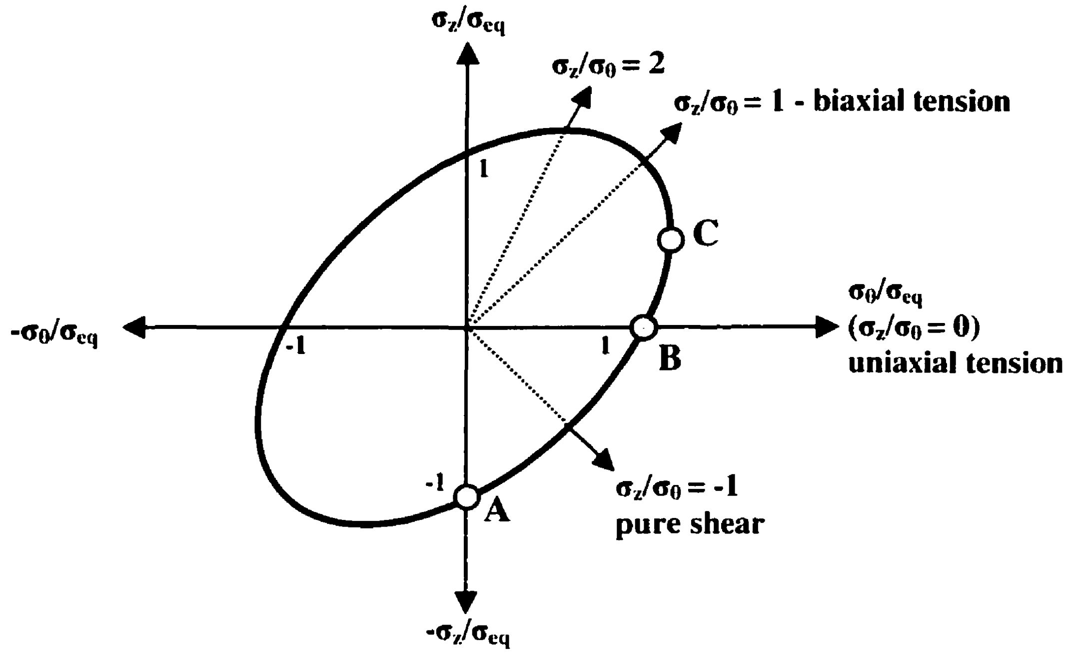

Figure 6.64 Stress ratio (σ_z/σ_θ) progression on the von Mises yield surface in two-dimensions (σ_r=0).

The progression of stress triaxiality at the equatorial surface was presented earlier in Figure 6.49. This is presented again in Figure 6.65, and further discussed in terms of the von Mises yield surface. Three stress triaxiality levels are identified on this figure. These levels correspond to points marked 'A', 'B', and 'C' on the yield surface in Figure 6.64.

The stress states at those three levels can be represented by:

stress at level A	**stress at level B**	***stress at level C** $\sigma_\theta=2\sigma_z$

$$\begin{pmatrix} \sigma_r=0 & & \\ & \sigma_\theta=0 & \\ & & \sigma_z=-\sigma_{eq} \end{pmatrix} \begin{pmatrix} 0 & & \\ & +\sigma_{eq} & \\ & & 0 \end{pmatrix} \begin{pmatrix} 0 & & \\ & 1.155\sigma_{eq} & \\ & & 0.577\sigma_{eq} \end{pmatrix}$$

* Hosford and Caddell [1983B]

The stress triaxiality equals the hydrostatic stress divided by the equivalent stress. Therefore, the stress triaxiality levels at points 'A', 'B', and 'C' are equal to –0.33, +0.33, and +0.58, respectively. The highest level, point 'C', indicates the maximum possible state of biaxial tension and stress triaxiality. From Figure 6.65, the larger aspect ratio materials rise from a lower stress triaxiality level (i.e. closer to point 'A') as was observed with the stress ratio plot.

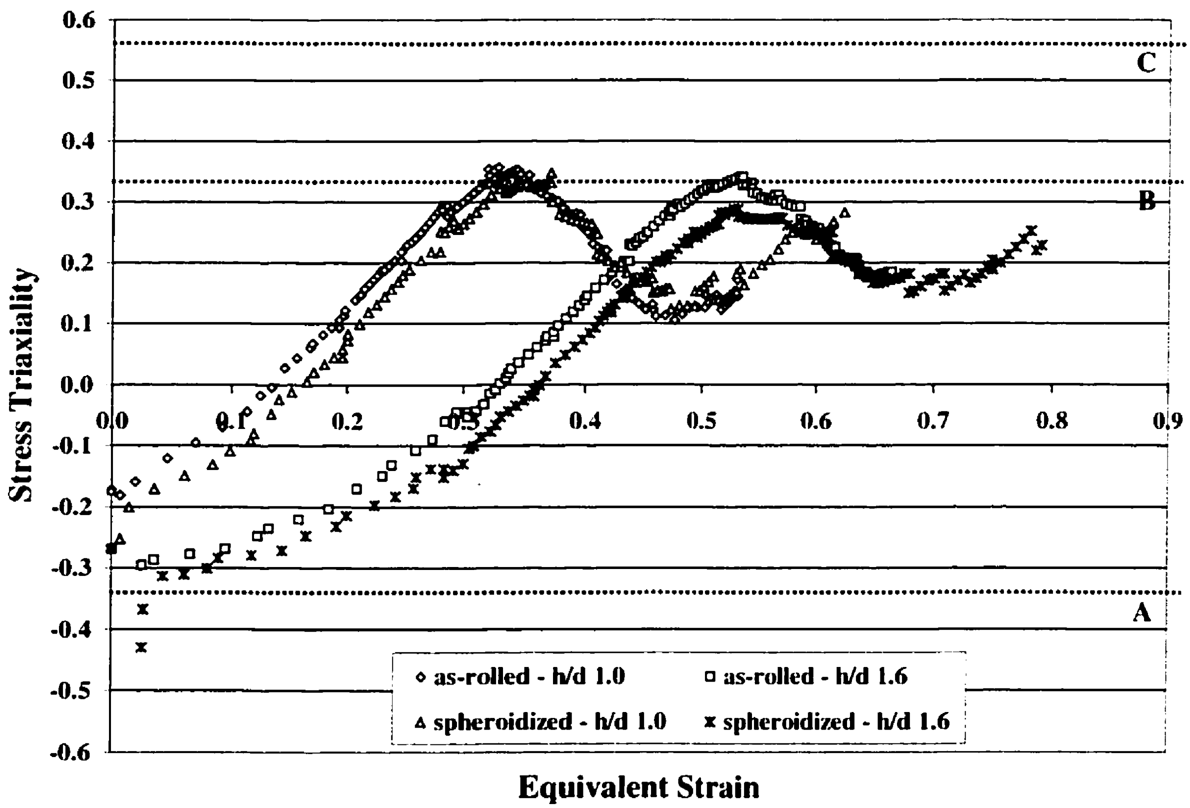

Figure 6.65 Stress triaxiality versus equivalent strain for Heat 4 simulations with regard to the von Mises yield surface.

6.4.5 Comparison of Flat-Die and Pocket-Die Configurations

The performance of the pocket die-set used in this work is compared to that of the more common flat die in this section. One material (Heat 4 as-rolled, aspect ratio 1.0) was selected for this exploratory work. Two friction conditions were tested; α' equal to 0.0 and 1.0. Figure 6.66 shows the initial mesh for the flat die. The specimen height was adjusted to 5.2 mm in order to yield an aspect ratio of 1.0.

Figures 6.67 and 6.68 show contour plots of equivalent strain using a flat die configuration and two friction conditions, ($\alpha' = 0.0$ and $\alpha' = 1.0$). The $\alpha' = 0.0$ friction condition contour plot displays no barreling, indicating that the hoop strain at the equatorial surface remains at zero throughout the deformation. In addition, the equivalent strain is the same throughout the specimen. The $\alpha' = 1.0$ friction condition contour plot reveals severe barreling at the equatorial surface and a maximum equivalent strain at the center.

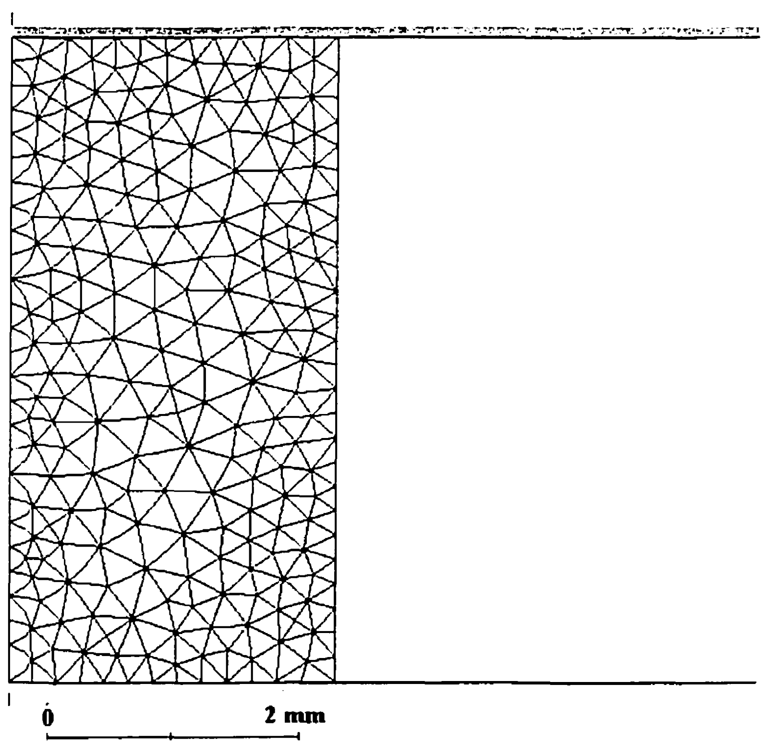

Figure 6.66 Initial mesh and flat die configuration.

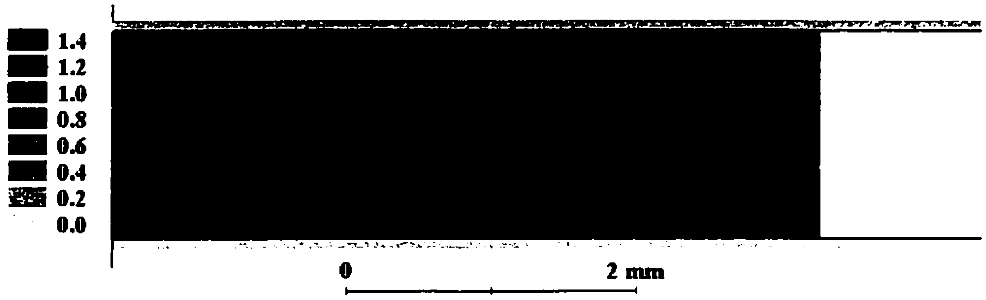

Figure 6.67 Contour plot of equivalent strain using the flat die configuration and a friction condition of $\alpha^1 = 0.0$.

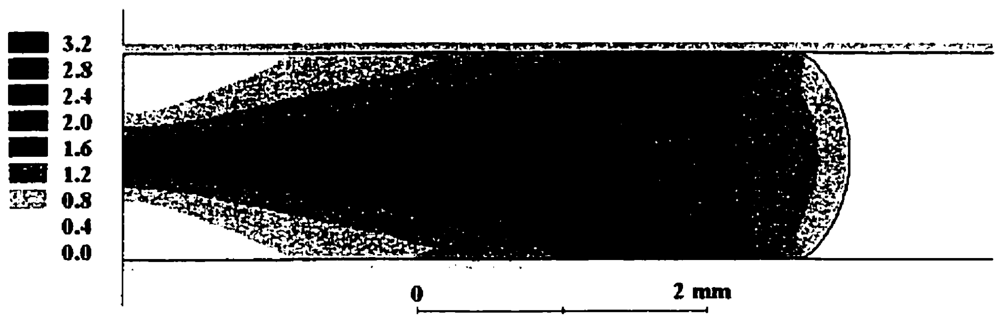

Figure 6.68 Contour plot of equivalent strain using the flat die configuration and a friction condition of $\alpha^1 = 1.0$.

Figures 6.69 and 6.70 are plots of the hoop (σ_θ) and axial (σ_z) stress components versus equivalent strain at the equatorial surface. As expected, the hoop stress remains at zero throughout the deformation with the absence of barreling during frictionless compression. The Cockcroft and Latham integral therefore equates to zero during frictionless upsetting, predicting that no fracture can occur under frictionless conditions. During frictionless compression, the axial stress component is equal to the negative of the yield stress of the material (~1000 MPa). Since all the stress components are compressive during frictionless compression, fracture is theoretically not possible.

The hoop stress component for the $\alpha^1 = 1.0$ friction condition rises to a maximum (~1000 MPa), and remains there until the end of the simulation. This behavior is comparable to that of the pocket die-set simulation with the same friction conditions, Figure 6.57. Under high friction conditions, the behavior of the axial stress component is also comparable to that of the pocket die-set simulation, Figure 6.58.

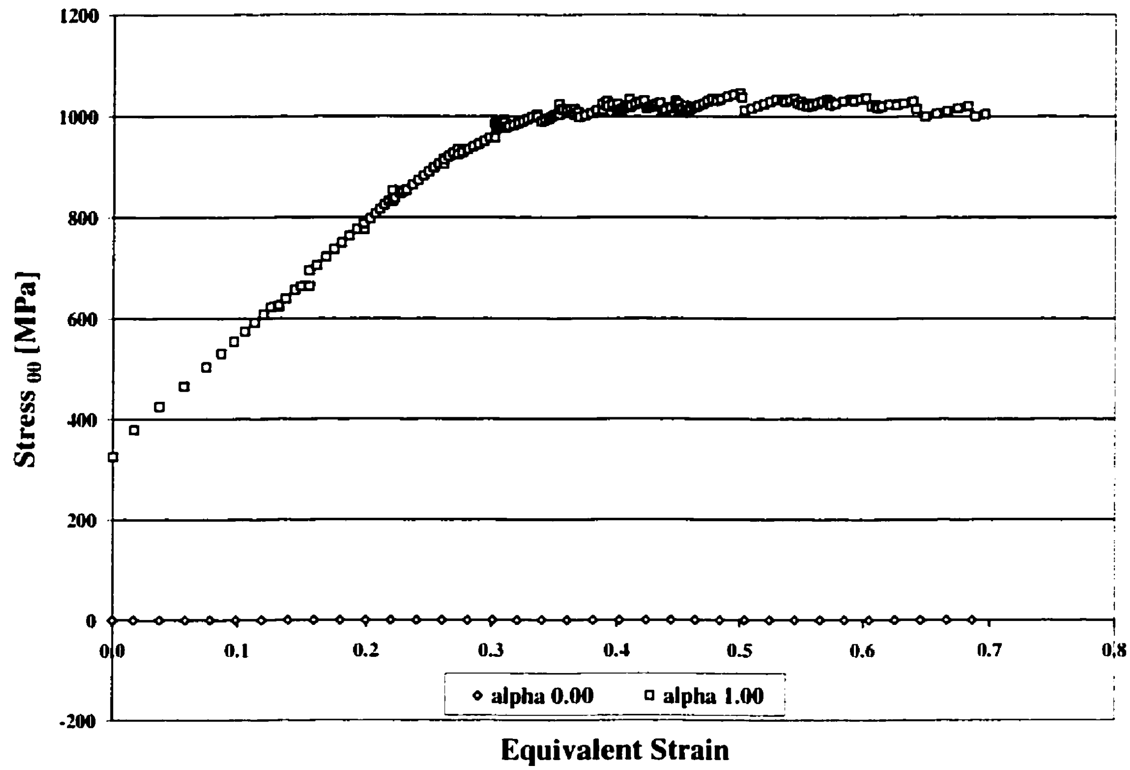

Figure 6.69 Hoop stress (σ_θ) versus equivalent strain for simulations using the flat die configuration.

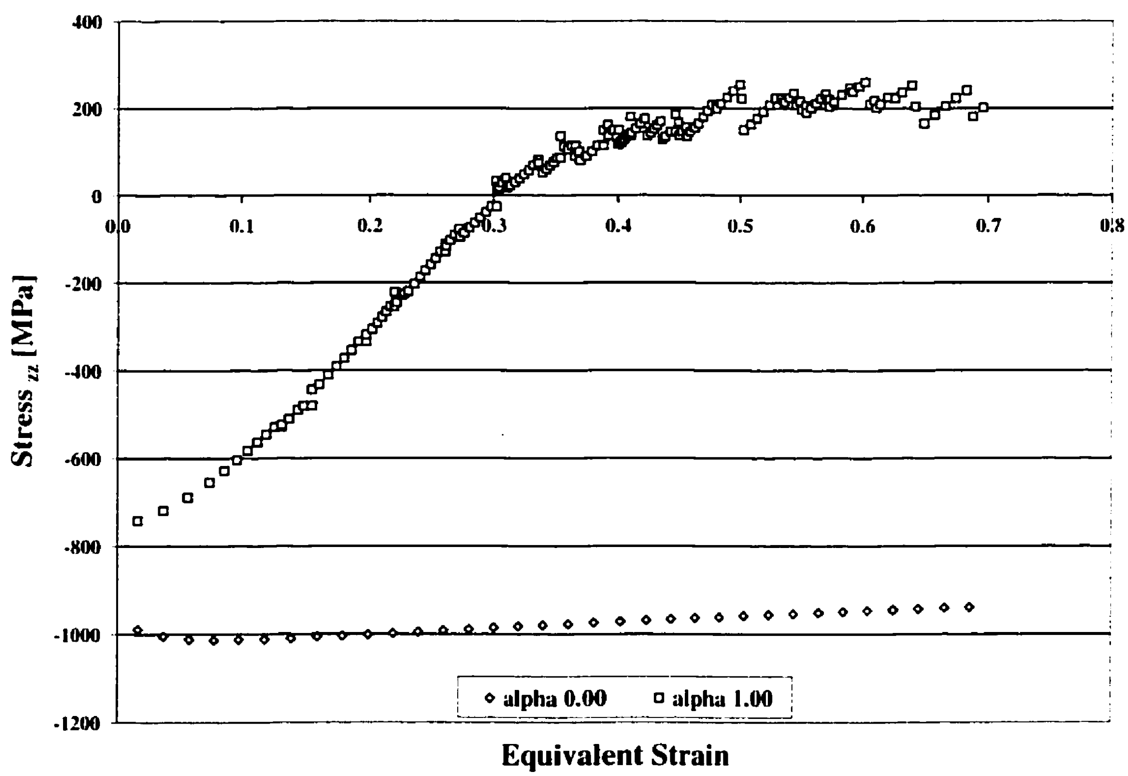

Figure 6.70 Axial stress (σ_z) versus equivalent strain for simulations using the flat die configuration.

The workability diagram of Figure 6.71 is a plot of axial strain versus hoop strain for the flat die simulations on Heat 4 (aspect ratio 1.0) for the two simulated extreme friction conditions and for the experimental pocket-die simulation ($\alpha' = 0.13$). During the onset of compressive deformation (see Section 2.5.2), the deformation is homogeneous (ε_θ=0) and $d\varepsilon_\theta = d\varepsilon_r$. The constant volume ($d\varepsilon_\theta + d\varepsilon_r + d\varepsilon_z = 0$) relation may be expressed as $2d\varepsilon_\theta + d\varepsilon_z = 0$. From this, $d\varepsilon_z/d\varepsilon_\theta = -2$ (equation 2.4).

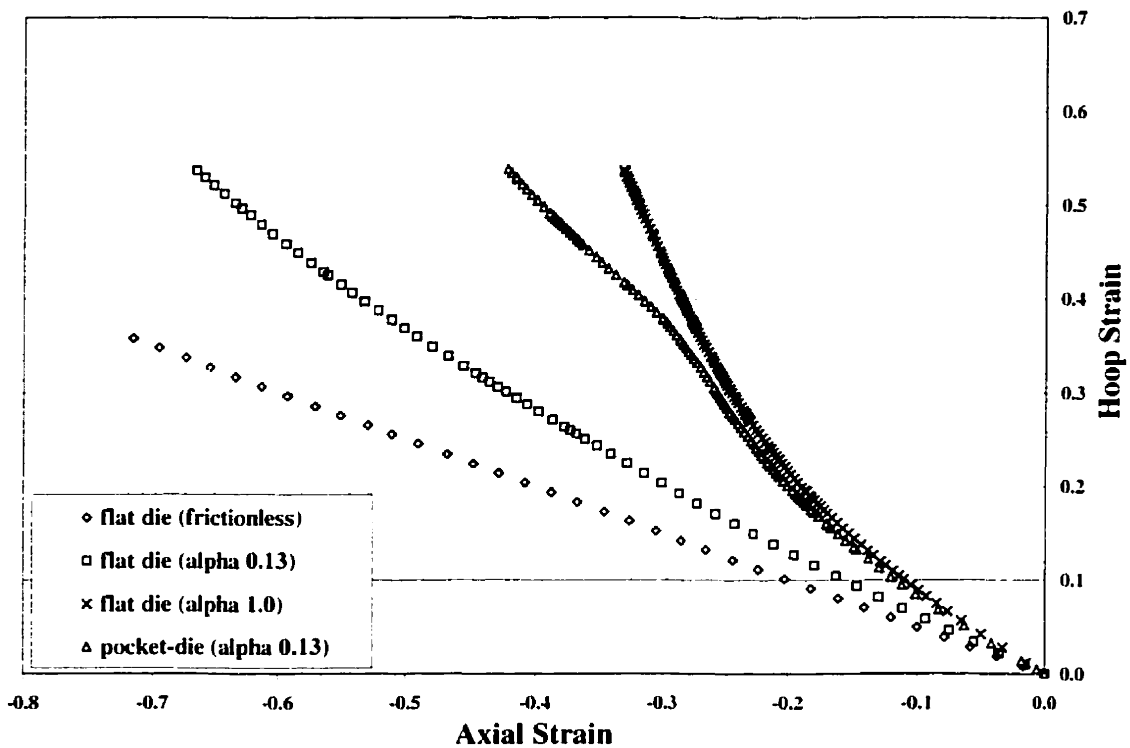

Figure 6.71 Hoop strain versus axial strain for Heat 4 (aspect ratio 1.0) as-rolled simulations using flat and pocket die-set configurations.

Since frictionless deformation is homogeneous, the strain ratio is expected to remain constant at –2. In fact, this is the case. Under maximum friction conditions, the strain path is the steepest possible for the particular aspect ratio and material.

The flat versus pocket die-set configurations for the same material, aspect ratio and friction conditions are also compared. It is evident that the pocket die-set configuration is much more severe in terms of fracture initiation since deformation begins further from the homogeneous deformation conditions.

The choice of this die-set configuration was justified since the main objective was to obtain failure. It is interesting to note the inflection in the slope of the strain path at the point where specimen material and die-face come into contact. From this point onwards, the strain path follows the same slope as the flat die simulation for the same friction condition.

6.4.6 Load-Time Evaluation

In section 6.2.2, selected load-time curves were presented from the experimental DWT for Heat 4 (aspect ratio 1.6). These were doubly integrated to yield displacement-time curves. From this, experimental DWT load-displacement curves were obtained.

These load-displacement curves are compared to Heat 4 simulation curves (see Figures 6.40 and 6.41).

Figures 6.72 and 6.73 are plots comparing the simulation and the experimental DWT load versus displacement results for as-rolled and spheroidize annealed Heat 4 materials (aspect ratio of 1.6). Note that S_{data} represents the final displacement of DWT test specimens as measured with the use of a micrometer. On the other hand, S_{final} represents either the calculated final displacement from DWT experiments as predicted by double-integration of the load-time curves (see Section 5.2.2) or the final displacement as predicted by the simulation.

In general, there is a quick step-rise to the yield point followed by a gradual rise to the maximum load. The load-time behavior of the simulation corresponds to the behavior of the experimental DWT between the start of the deformation and a displacement equal to about 4.7-4.8 mm for both the as-rolled and spheroidize annealed materials. Following this, the simulation loads rise faster than those from the experimental DWT. This may indicate that the simulation has overestimated the flow stress at larger strains and at higher temperatures.

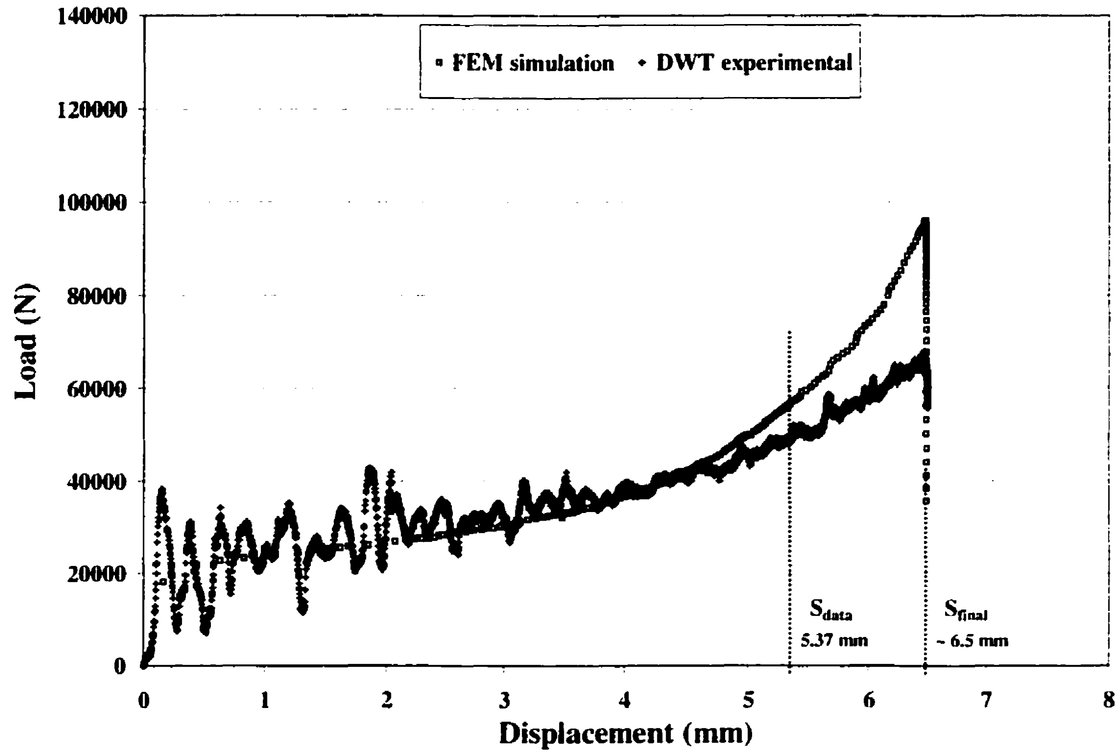

Figure 6.72 Load versus displacement plot for simulation and experimental DWT for Heat 4 as-rolled material with aspect ratio of 1.6.

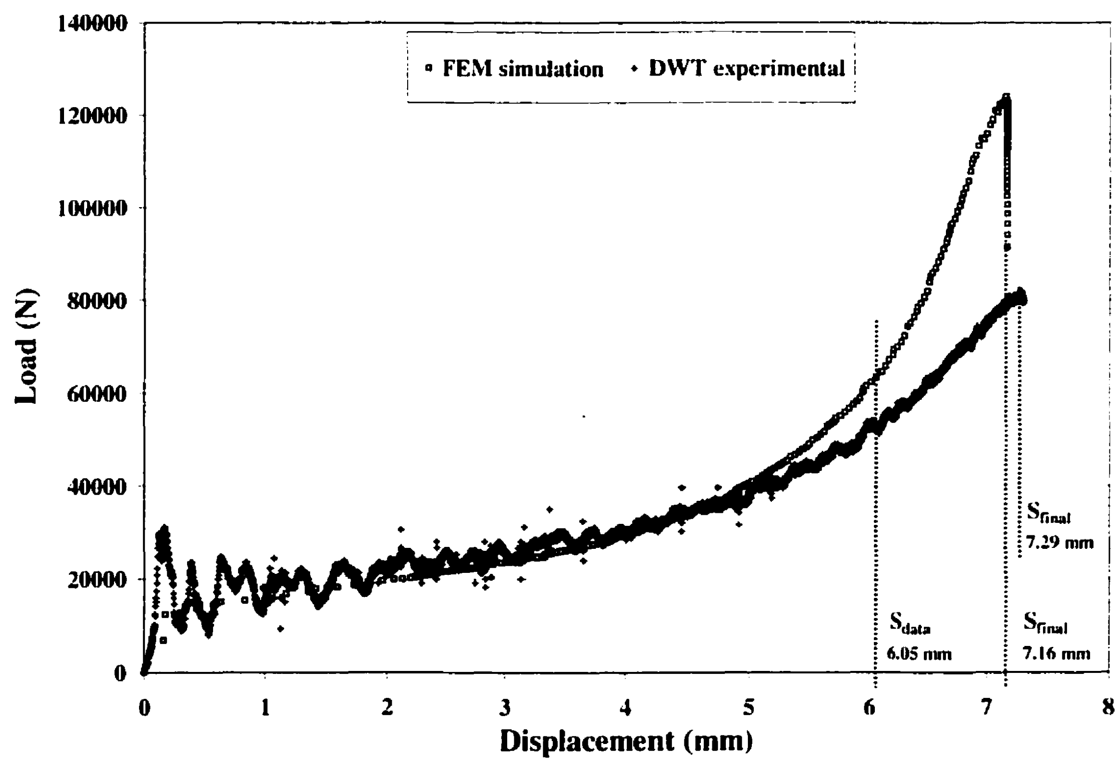

Figure 6.73 Load versus displacement plot for simulation and experimental DWT for Heat 4 spheroidized material with aspect ratio of 1.6.

The DWT oscilloscope curves are used as a basis for comparison. The load cell actually measures the load developed by the full system as it resists the impacting mass. The full system comprises the specimen, the base, and the floor that supports the DWT machine. This system is represented in terms of energy by equations 6.10 to 6.12.

$$E_{DWT} = \frac{1}{2}Mv_o^2 = E_{SP} + E_{BASE} + E_{LOST} \tag{6.10}$$

where

E_{DWT} = energy of DWT experiment (area under load-displacement curves)
E_{SP} = energy absorbed by the test specimen
E_{BASE} = energy absorbed by the base and floor
E_{LOST} = energy lost as heat, friction, and noise

Since

$$E = \int_{S_o}^{S} F dS \tag{6.11}$$

the terms in equation 6.10 can be expanded to give:

$$\int_{S_o}^{S_{DWT}} F_{DWT} dS_{DWT} = \int_{S_o}^{S_{SP}} F_{SP} dS_{SP} + \int_{S_o}^{S_{BASE}} F_{BASE} dS_{BASE} + E_{LOST} \tag{6.12}$$

where

F_{DWT} = force measured from DWT experiment (oscilloscope)
F_{SP} = resistive force of the specimen
F_{BASE} = resistive force of the base and the floor (machine compliance)
S_{DWT} = displacement from DWT experiment
S_{SP} = displacement of the specimen
S_{BASE} = displacement of the base and the floor (machine compliance)

The left-hand side of equation 6.12 is obtained by double-integration of the experimentally determined load-time curve. The energy lost (E_{LOST}) is not known, but is small as will be seen below.

To obtain the functionality of the specimen on its own (E_{SP}), one requires knowledge of the functionality of E_{BASE}. This is not known since the compliances of the DWT machine and the substructure are not known. In fact, the specimen and base act as two parallel springs that absorb the energy of the impacting mass. What is known, however, is that in the absence of any machine or substructure compliance, the load-time curves would have achieved a higher load with a shorter test duration. This is in fact what is observed with the simulation load-time curves since the dies are rigid.

The uncorrected DWT experimental curves predict lower peak loads and larger displacements. The lower peak loads and larger displacements are due to the compliance of the DWT machine and the substructure. On the other hand, the FEM curves are highly dependent on the validity of the constitutive parameters. In addition, the simulation utilizes the full amount of available energy ($\frac{1}{2}Mv_o^2$) with no provision for energy lost as heat, friction, and noise (E_{LOST}).

Fracture initiation on the actual test specimens occurred at a known and measured displacement. This is represented in Figures 6.72 and 6.73 as S_{data}. By cropping the FEM simulation curves at this particular displacement it is possible to obtain simulation data representative of the stress-strain state of the material at the time of fracture initiation, assuming the flow stress and friction conditions are representative of the actual DWT.

Table 6.17 presents experimental DWT and simulation maximum load results for the Heat 4 materials. The simulations predict roughly 40-50% larger peak loads than those from the DWT experiments. However, it is known that the peak loads for the DWT experiments are lower because of the absorbing actions of the DWT machine base and the substructure, as mentioned earlier. Therefore, the DWT peak load results do not represent the response of the actual test specimen. Instead, they represent the response of the full system, and therefore are not directly comparable.

Heat 4 Material	DWT experiment Maximum Load [kN]	FEM simulation Maximum Load [kN]	% Difference
as rolled	67.6	96.1	-42.2
spheroidized	81.4	123.9	-52.2

Table 6.17 Experimental DWT and FEM simulation maximum load results.

Table 6.18 presents experimental DWT and simulation maximum load results at the final DWT specimen displacement (at S_{data}) for Heat 4 material with an aspect ratio of 1.6. The simulations predict peak loads that are between 12 and 16% larger than those from the DWT experiments. This method of comparison yields a much smaller difference between the two sets of curves.

Heat 4 Material	DWT experiment maximum load at S_{data} [kN]	FEM simulation maximum load at S_{data} [kN]	% Difference
as rolled	50.3	56.3	-11.9
spheroidized	53.4	62.2	-16.5

Table 6.18 Experimental DWT and simulation maximum load results at final DWT specimen displacement (S_{data}).

The higher loads with the simulations may be attributed to discrepancies between the experimental test conditions (i.e. strain rate, flow behavior) and the simulations at higher strains ($\varepsilon > 1$). Figure 6.74 illustrates the calculated true stress versus true strain results (using constitutive parameters from CP testing) extended into the larger strain regions experienced by the central region of the DWT specimens.

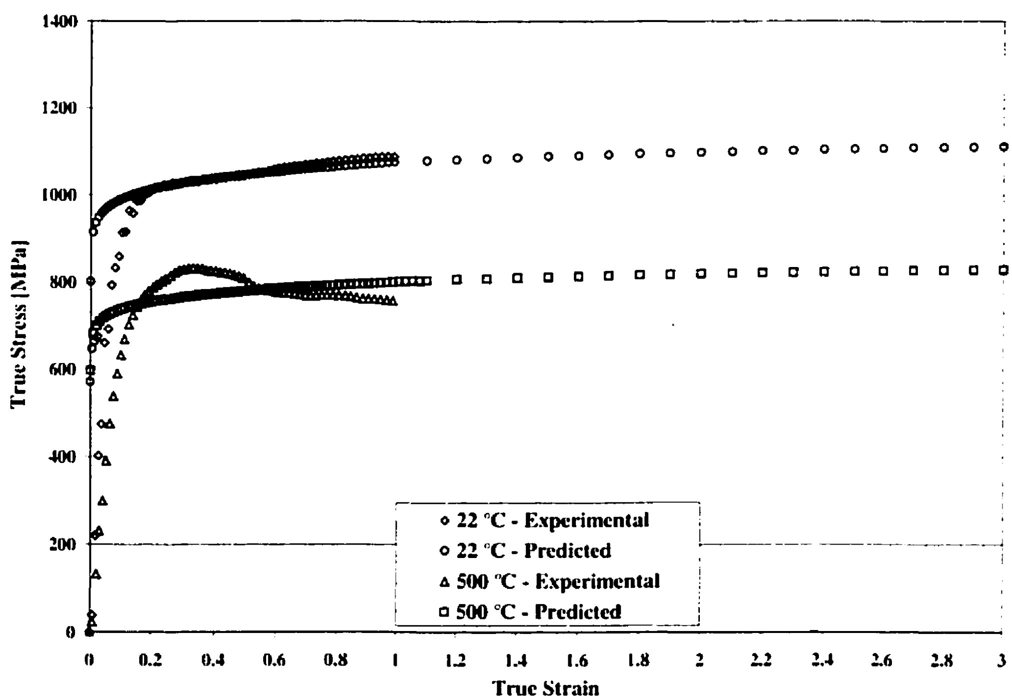

Figure 6.74 Heat 4 as-rolled – true stress versus true strain results for CP testing with extended strain range.

The stress continues to increase in the larger strain regions. Here, the stress is expected to saturate or decrease.

Negative rate sensitivity could not be modeled with the Norton-Hoff relation. Many unsuccessful attempts were made to correct for the flow behavior at larger strains. Nevertheless, the fact that stress continues to increase in the larger strain regions helps explain the slightly higher loads with the simulations.

Energy is represented by the area under the load-displacement curves. The experimental DWT and FEM simulation curves were integrated up to S_{final} for both the as-rolled and spheroidize annealed Heat 4 materials. The results are presented in Table 6.19.

Heat 4 Material	DWT experiment total energy [J]	FEM simulation total energy [J]	% Difference
as rolled	237.7	248.2	-4.4
spheroidized	253.6	264.1	-4.1

Table 6.19 Experimental DWT and FEM simulation total energy results.

It is evident from Table 6.19 that the total energy absorbed during DWT experimentation is only about 4% smaller than that absorbed by the FEM simulation for both the as-rolled and spheroidize annealed materials. This value provides an indication of the energy lost as heat, friction, and noise (E_{LOSS}) during DWT testing.

Table 6.20 presents experimental DWT and simulation energy results at the final DWT specimen displacement (S_{data}) for Heat 4 materials with aspect ratio of 1.6. The energy from DWT experimentation is only about 3-5% larger than the FEM simulation energy for both the as-rolled and spheroidize annealed materials. This small difference supports the assertion that the simulations are representative of the DWT experiments, at least with regards to energy absorbed.

Heat 4 Material	**DWT experiment energy at S_{data} [J]**	**FEM simulation energy at S_{data} [J]**	**% Difference**
as rolled	174.0	164.7	5.3
spheroidized	169.9	164.1	3.4

Table 6.20 Experimental DWT and FEM simulation energy results at final DWT specimen displacement (S_{data}).

CHAPTER 7

DISCUSSION

7.1 Cam Plastometer Results

The objective of this work was to ascertain the effect of chemistry on flow behavior. The cam plastometer (CP) was employed to obtain the compressive stress-strain relations for a selection of matrix materials tested in representative stress states, and at appropriate strain rates and temperatures. From this, constitutive relations were developed and flow curve parameters were determined for input into the FEM models. Flow curves were obtained for 4 of the 7 matrix materials in the as-rolled as well as in the spheroidize annealed conditions. These included the two QIT heats (high and low nitrogen), the high nitrogen Ivaco heat, and one of the Açominas heats.

For all 4 materials, the flow curve levels for the spheroidize annealed materials were found to be approximately 200 MPa lower than those for the as-rolled materials. This behavior was expected since it is well known that a spheroidal cementite microstructure is less resistant to flow than a lamellar cementite microstructure. This explains the motivation for spheroidize annealing of steels prior to cold heading. The downside to spheroidization is that it represents a notable portion of the cost of producing a fastener. Furthermore, the lower flow stress does not usually allow the required final properties, e.g., strength, to be achieved. A quench and temper operation is then required following the heading operation.

For the room temperature tests, the as-rolled materials revealed a lower flow stress when tested at the higher strain rate (150 s^{-1}). This is counter-intuitive as one would expect an increase in flow stress at higher strain rates. For the high temperature tests, the as-rolled materials exhibited the expected behavior: the flow stress increased with increasing strain rate. In general, the as-rolled materials show a notable decrease in flow stress of about 350 MPa when tested at high temperatures. This is due to the thermal softening effect.

At room temperature, the spheroidized materials also displayed a higher flow stress at the lower strain rate, although the differential was smaller. At high temperatures, the flow stresses of spheroidized materials are similar at high and low strain rates. This may be attributed to the ease of dislocation movement through the spheroidal microstructure when aided by thermal activation.

It is evident from the stress-strain plots that the loading slopes, i.e., up to yielding, do not correspond to the value of Young's modulus. In fact, the apparent Young's modulus is too low by over an order of magnitude. With the CP, the sample height is measured at the end of each test. This is the value achieved with the machine play and slack that must be taken up at the start of a test. Therefore, the achieved sample deformation is smaller by a certain amount due to the apparent deformation associated with bedding down of the tools. This bedding down is associated with the play between the different interfaces, e.g., wedge, bearings, pins, in the system that makes up the CP, and is responsible for the discrepancy during the initial stages of the test.

At the onset of deformation (i.e. at low strains < 0.1), the slack is not known, and therefore not included in the formulation used to calculate the strain. This is not a serious issue here since a rigid viscoplastic model is used in the FEM modeling.

A non-linear root mean square analysis was performed on the CP data to obtain the flow curve parameters of the Norton-Hoff relation. The objective functions were between 6 and 33 MPa for the eight materials. This indicates that the parameters of the constitutive model provide theoretical flow curves that are representative of the experimental curves. The goodness of fit between the experimental and theoretical flow curves was also demonstrated in Figures 6.11 to 6.18, at least for the strain range of greatest interest (0.1 to 1.0). In the range from yielding to a strain of about 0.1, the lack of agreement can be attributed to the absence of a correction for machine setting during the initial stages of the test, as mentioned earlier. In addition, elastic deformation is not included in the model.

7.2 *Drop Weight Compression*

The problem of quantifying material ductility for cold heading has been the subject of many studies. Conventional laboratory tests such as tensile testing and simple compression have limitations for assessing cold headability. This can be attributed to stress state, strain rate, and temperature conditions that are not representative of industrial conditions.

The literature review uncovered numerous efforts made to assess the cold headability of steels. One major shortcoming of the simple compression test is the difficulty in producing cracks on the equatorial surface, even though failure incidence with cold heading materials in industry is easily over 1%.

A major research focus in the field of compression testing has been to increase the tensile hoop strain through various workpiece and test designs [Dannenmann and Blaich, 1980; Shivpuri et al., 1988A, 1988B]. One of these is the collared cylinder (Figure 2.11) used by Sowerby et al. [1984] and Nguyen [1984] that eliminates the need for a surface grid since the axial and circumferential strains can be obtained by measuring the diameter and thickness of the collar. This design was found to be successful in increasing the hoop strains at the equatorial surface. However the workpiece geometry is altered, thereby changing the process conditions [Shivpuri et al., 1988A, 1988B].

Some researchers worked with experimental data available in the literature [Shabara et al., 1996; Wifi et al., 1998], possibly because of the absence of a test and die design capable of producing fracture. Other researchers expanded their matrix of materials to include higher carbon steels (C > 0.55%), resulphurized steels, aluminum, and even brass [Nguyen, 1984; Darvas, 1984; Brownrigg et al., 1981; Sowerby et al., 1984]. In fact, much of the work done on upsetting has been on non-ferrous materials, particularly aluminum [Ettouney and Hardt, 1983; Narayanasamy and Pandey, 1997]. These are interesting studies, but they evade the issue of steel upsettability.

Olsson et al. [1979], Dannenmann and Blaich [1980], and Thibau et al. [1999] resorted to surface notching to readily produce fracture on cylindrical steel specimens. The presence of surface discontinuities gives rise to a fracture mechanics problem, rather than a formability problem. Kuhn [1978] stated that surface notching is not recommended since only the interior material is tested instead of the as-received surface. Brownrigg et al. [1981] also discourage the practice of surface notching since there is a strong dependence of notch root ductility on microstructure.

One of the major objectives of this work was to develop a test methodology to evaluate the formability of materials. The test methodology involved the simulation of upsetting in cold heading and associated material conditioning operations found in industrial practice. The focus of the test methodology was the development of a drop weight testing apparatus and a die-set configuration representative of industrial cold heading environments. The critically important characteristic of the testing apparatus, i.e., the DWT, is that it is capable of generating the large loads required to promote fracture on steel specimens

The material matrix was designed to evaluate the impact of varying material parameters, i.e., aspect ratio, surface quality, copper level, nitrogen content, microstructure, and steel sources, i.e., ingot and continuous cast, on fracture behavior during upsetting of grade 1038 steel. Material preparation and conditioning included hot rolling, controlled rod cooling, descaling, straightening, lime coating and lubricating, and wire drawing. The spheroidization of test specimens was performed in an industrial batch furnace using an industrial heat treatment cycle.

Spheroidize annealing 30 cm rod lengths in an industrial batch furnace proved to be a challenge. Several trials were conducted by inserting the rod lengths directly in the batch furnace, before the capsule design incorporating a carbon source was conceived and implemented. In the absence of carbon source, the capsule assembly does not function properly, resulting in a decarburized surface.

The absence of representative industrial material preparation and conditioning would certainly have resulted in skewed results. For example, Sugondo et al. [1991] employed pre-draw reductions ranging from 36 to 72% on test specimens to bring out the effect of texture on low carbon cold heading steels. Such large reductions are not employed in industry, at least with conventional cold heading materials. Other examples discussed earlier include grinding and shaving specimens, altering the specimen geometry, and the use of unrepresentative dies.

Unguided die-set configurations were attempted before arriving at the current configuration. During this exploratory testing phase the unguided die-sets proved to be inadequate. Die failure was experienced after only a few compression experiments, on the most part, prior to material fracture.

A guided die-set sleeve design was then devised and constructed. This configuration proved to be very successful; *well over two thousand upset tests were performed without experiencing a single die failure.* In fact, all the matrix materials were tested using the same die-set. This design is clearly a very valuable contribution since many researchers have found die failures to be a major obstacle [Sarruf, 2000; Shivpuri et al., 1988A].

For the purposes of this work, the presence of a ghost-line crack at X25 using stereo microscopy signaled the onset of fracture. This definition of fracture onset is more stringent than the one employed in industry. Nevertheless, it was necessary in this work to define the stress-strain state at the precise moment of fracture initiation. Many of the studies found in the literature employ a 'naked eye' visual assessment to define the onset of fracture [Tozawa et al., 1981; Dannenmann and Blaich, 1980; Lee and Kuhn, 1973]. Such an interpretation overestimates the fracture stress. The use of stereo microscopy also reveals extraneous fractures related to surface notches that would otherwise go unnoticed. Approximately 5% of the specimens tested during this study were found to possess unwanted surface discontinuities. These specimens were discarded.

DWT was performed on the 7 test matrix heats. The specific objective of these experiments was to determine the strain to fracture for each material, and to determine the sensitivity of the DWT to aspect ratio, chemistry in terms of copper content and nitrogen level, microstructure, surface soundness, and surface decarburization. Three aspect ratios, i.e., 1.0, 1.3 and 1.6, were selected for testing the materials from Heats 4 and 5, while an aspect ratio of 1.3 was used for the balance of the materials. The 1.3 aspect ratio tests were used as a basis for comparing the axial strain to fracture ($\ln H/H_o$) for the various materials. The results from Heats 4 and 5 were used to ascertain the effect of aspect ratio on fracture strain.

The drop weight test results for the 1.3 aspect ratio experiments that were described in Chapter 6 are consolidated and presented in Figure 7.1.

It is evident that the low nitrogen content heats, i.e., Heats 2 and 5, performed markedly better in terms of global strain to fracture than their high nitrogen content counterparts, i.e., Heats 1 and 4. This is true for both the as-rolled and the spheroidized materials. The high copper heat, i.e., Heat 3, performed poorly compared to the other heats. In fact, none of the DWT tests performed on this heat passed the visual failure criterion (Level 0). This behavior was attributed to hot shortness due to the high copper content. Heat 6, the Açominas material with induced surface scratches, did not perform well either. This was as expected since the defects act as stress concentrators, and promote premature fracture. The 'good' Açominas heat, i.e., Heat 7, performed well in terms of global axial strain to fracture, but not quite as well as the low nitrogen QIT heat, i.e., Heat 5. This result is counter-intuitive since the Açominas material contains lower residual and nitrogen contents. Both materials had similar surface decarburization results, cleanliness ratings, and reduction-of-area results from tensile testing (see Chapter 4). It is evident from Figures 4.8 and 4.10 that the Heat 5 material microstructure is finer than that of the Heat 7 material. The superior performance of Heat 5 can therefore be attributed to this factor. In general, the spheroidized materials yielded strains-to-fracture that are about 25% higher than those of the as-rolled materials. One possible explanation for this behavior is that the flow stress for the spheroidized materials from CP testing was found to be lower by about 350-400 MPa. This also conforms with the superior performance of spheroidized materials in industry.

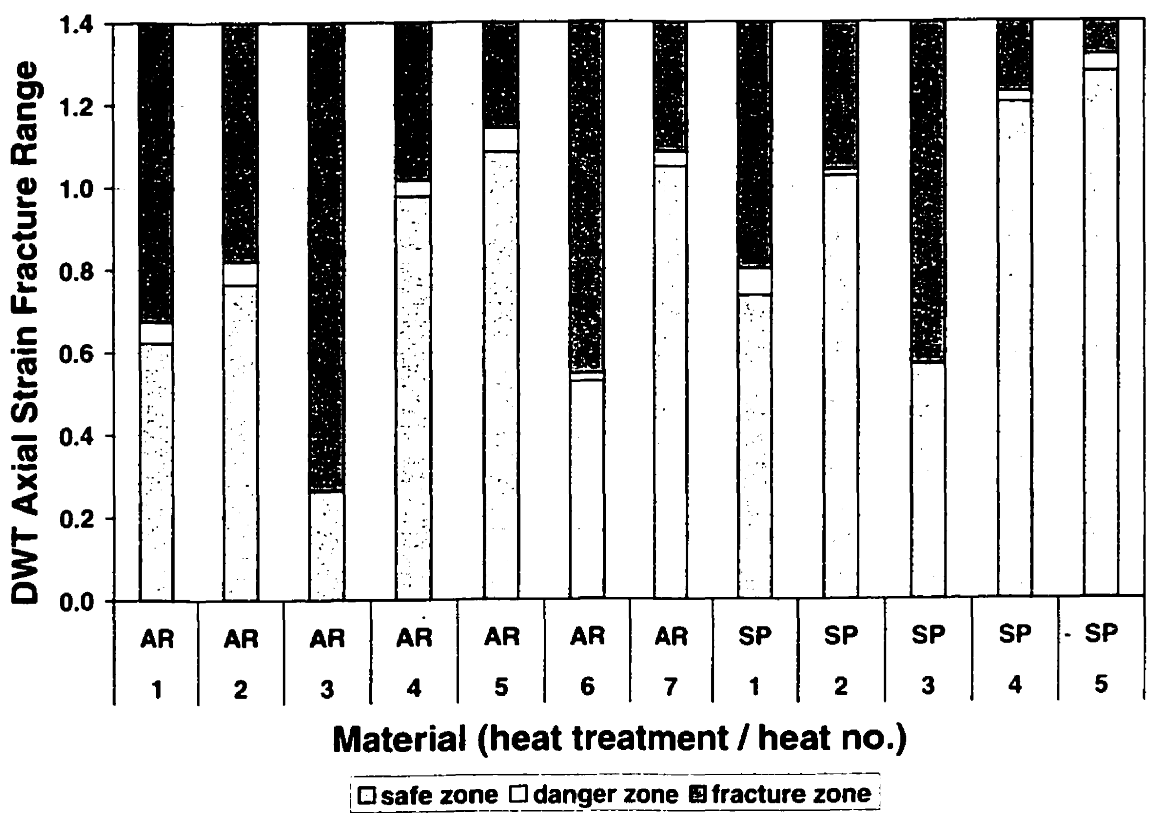

Figure 7.1 **Histogram of DWT fracture results for all heats and an aspect ratio of 1.3.**

Figure 7.2 is a histogram of the Heat 4 DWT fracture results for all three aspect ratios.

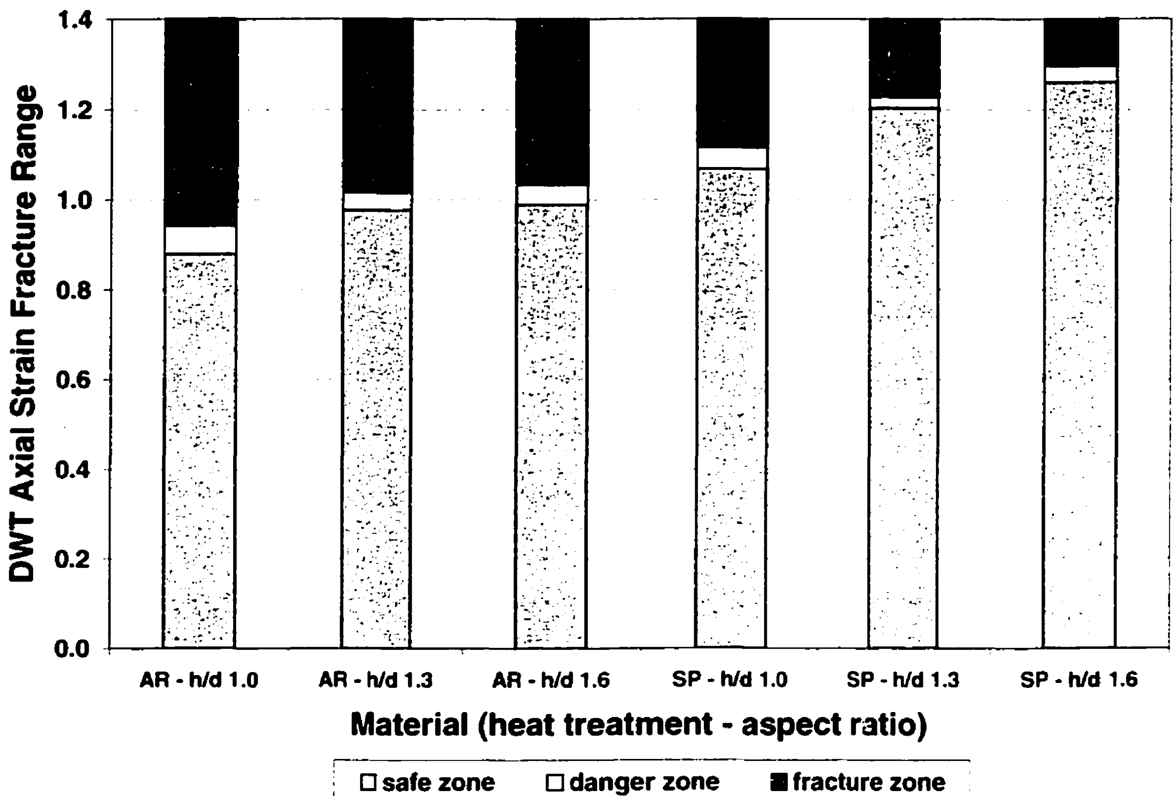

Figure 7.2 Histogram of DWT fracture results for Heat 4 by aspect ratio.

In general, there is an increase in axial strain to fracture with increasing aspect ratio, as predicted by the theory of the workability diagram (see Figure 2.9). Lower friction values and higher aspect ratios decrease bulge curvature and the degree of non-uniformity, thereby delaying fracture. Figure 7.2 also illustrates the differences in axial strain to fracture between the as-rolled and spheroidized materials for all three aspect ratios (~0.2 strain).

It is evident that aspect ratio significantly affects fracture strain. *Hence, in evaluating materials using the DWT, comparisons should be made only between specimens of the same aspect ratio, as was presented in Figure 7.1.*

All test specimens exhibited longitudinal cracks at the moment of fracture initiation. Heat 3, the high copper heat, exhibited shear cracking as well, but only at very large deformations, much after the initiation of longitudinal fracture (see Figures 6.25 and 6.26). Although not reported in the results section, specimens from all seven heats were tested with much larger masses than those required for crack initiation. Only the Heat 3 specimens exhibited shear cracks.

It is well known that longitudinal cracks are due to the exhaustion of material ductility, and that shear cracks are due to localization induced by flow softening and plastic instability. From the crack orientation, i.e., longitudinal, on the DWT specimens, it can be concluded that flow in the matrix materials did not localize sufficiently to cause shear cracking. The exhaustion of material ductility was the limiting factor for all the materials tested. Heat 3 materials were possibly more prone to localization, because the high residual element content and the relatively high nitrogen content raised the flow stress, promoting deformation heating and flow softening at the latter stages of upsetting.

The tensile test is the most commonly employed test to evaluate the suitability of cold heading materials in industry. However, numerous academic and industrial studies conclude that there is no correlation between tensile properties and the cold headability of materials. These findings motivated the initiation of the present work. In Section 2.5.1, it was confirmed that the tensile test is of limited use for evaluating the cold headability.

Tensile test results for the matrix materials were presented in Chapter 4. The reduction-of-area (ROA) results for the as-rolled and spheroidized materials were presented in Tables 4.3 and 4.5. Reduction-of-area results are commonly used as a measure of material ductility. DWT fracture results for specimen aspect ratio 1.3, and the tensile test reduction-of-area results are compared in Figure 7.3. The error bars in this figure indicate ± 3 standard deviations for the reduction-of-area results.

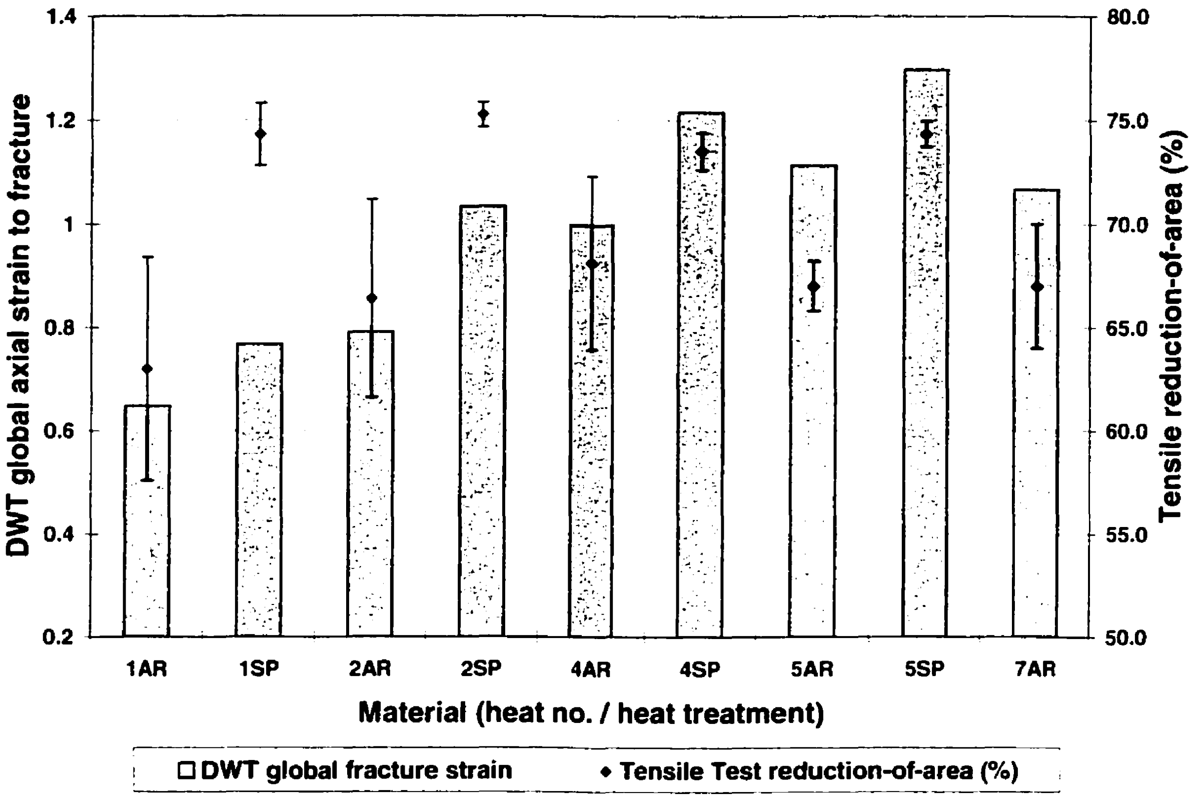

Figure 7.3 Plot of DWT fracture results (aspect ratio 1.3) versus tensile reduction-of-area results.

It is evident from Figure 7.3 that there is some degree of correlation between the results of the two sets of tests, particularly with respect to microstructure. The spheroidized materials yielded higher ROA values than their counterpart as-rolled materials. Therefore, the ROA parameter discriminates between the microstructures. Heat 3 results were not plotted since a strain for which fracture did not occur could not be found. Heat 6 results were also not plotted since tensile testing was performed prior to inducing die scratches on that material.

When comparing materials with a particular microstructure, it is evident that the parameter is deficient. For example, Heat 4 yielded the highest ROA of all the as-rolled materials even though the DWT results show that the axial strain to fracture for this heat is about 12% lower than that of Heat 5, the best DWT performer. Even though the DWT results for Heat 7 are nearly 5% lower than those for Heat 5, the tensile results yield the same ROA values for the two heats. Similar examples are also evident with the spheroidized materials. The most notable of these is the comparison of the results for Heats 1 and 2. Heat 2 exhibited DWT axial strains to fracture that were 26% greater than those from Heat 1, yet, the ROA results are only 1% different. Finally, Heats 5 as-rolled and 7 as-rolled behave far worse in tensile testing than would be expected from their DWT results.

It can therefore be concluded that the tensile reduction-of-area results are not totally reliable as a measure of material ductility for cold heading. This agrees with studies by Dieter [1961A], Bhatnagar [1978, Ollilainen [1995], Hosford and Caddell [1983], Osakada [1989], Ring Screw Works Co. [1998], Olsson et al. [1986], and Turner et al. [1984], mentioned in Chapter 2.

One of the critical factors influencing material performance is surface integrity of the test materials. The literature shows that surface preparation techniques vary considerably. Many researchers employ grinding techniques to shave test specimens, usually for proper fit in a particular die set [Olsson et al., 1979; Ohmori et al., 1997; Shah, 1974; Darvas, 1984; Brownrigg et al, 1981; Dhers et al., 1992]. This results in an altered surface prone to surface discontinuities that may alter strain path and act as stress raisers promoting premature fracture. Indeed, Shah and Kuhn [1986] state that machining the specimen surface influences fracture initiation. The present study has demonstrated that it is critically important to test specimens with their natural surfaces intact.

Another important consideration that is on the most part ignored by researchers is the pre-draw operation. This operation must be taken into account since it affects the flow stress and perhaps even the intrinsic ductility of the material, which is strain-history dependent. The pre-draw operation serves to strengthen the less work hardened regions of a fastener, i.e., the shank. It invariably work hardens the upset region of the fastener and therefore promotes a higher flow stress behavior during upsetting. The pre-draw operation also improves surface finish and also renders the material more axisymmetric, a critical requirement for testing. In some cases, the pre-draw can increase material ductility for subsequent operations [Jenner and Dodd, 1981]. An explanation is that the pre-draw operation allows the material to overcome Lüders band instabilities [Jonas, 1997], a phenomenon that only occurs in tension and in shear. During an upset operation, the equatorial surface is in a tensile stress state, and therefore Lüders band instabilities are possible. The pre-draw operation allows the material to strain beyond this point of instability during a fully compressive drawing operation during which Lüders bands cannot form. *The pre-draw operation is therefore an important consideration for upsetting.* A 10% pre-draw was employed for all the materials tested in this work, and therefore the effect of pre-draw on upsettability was not determined. A quantitative evaluation of the effect of pre-drawing on fracture could be of benefit to industry.

Much of the work reported in the literature was performed using servo-hydraulic machines with limited load and strain rate capacity, unable to generate strain rates representative of industrial cold heading. The drop tower, on the other hand, employs a falling weight to apply a compressive load to a specimen, and has the capability of generating the large loads required to promote fracture on steel specimens. In addition, the DWT can generate strain rates representative of industrial cold heading.

Another advantage of the DWT is that the application of force is similar in the drop weight testing machine and in an industrial cold heading machine. In the DWT, the deforming specimen itself arrests the crosshead, while in an industrial cold heading machine, the machine limits the deformation of the component. *In both cases, the application of energy is similar, i.e., the deformation rate slows to zero, albeit with minor differences depending on the cam configuration of the cold heading machine.*

The DWT is able to exaggerate cold heading loading rates to promote fracture on otherwise "good" materials. The test height for this study remained constant at 1.5 m, yielding initial strain rates between 600 and 1000 s^{-1}, depending on the aspect ratio. These values are between 4 and 6 times the overall strain rates observed in industry, i.e., ~150 s^{-1};

nevertheless, they are much more characteristic of cold heading than the strain rates associated with servo-hydraulic machines, i.e., 0.1-1 s^{-1}.

The DWT and guided pocket-die conceived and developed for this study have been shown to be sensitive to critical cold heading parameters. These include surface quality, chemical composition in terms of residual elements (i.e. copper) and nitrogen content, microstructure, decarburization, and specimen aspect ratio. The DWT developed for this work is highly satisfactory for evaluating the fracture behavior under industrial cold heading conditions, i.e., strain rate, deformation heating, and stress state of deformation. *The guided pocket-die design is representative of industrial cold heading practice, and is capable of yielding hoop stresses that are large enough to promote fracture on the equatorial surface. Die-set longevity was found to be exceptional.*

7.3 Friction Parameter

The purpose of the FRT was to determine the friction parameter, α^{l}, using representative test conditions for input into the finite element models. FRT were performed using the drop weight tower on Heat 4 spheroidize annealed specimens with an approximate geometry of 6:3:2 as recommended by the literature. The die set material, surface finish, and lubrication conditions were identical to those employed in the DWT.

The results were characterized by an increase in internal diameter of approximately 9%. FEM simulations of the FRT were performed using Forge2 to determine the friction parameter. This was accomplished by varying the friction parameter until the final mesh geometry matched the experimental one. A friction parameter of 0.13 yielded the best match.

A friction ring calibration chart was also consulted as an additional check. From this, the shear friction factor, $\overline{m}$, was determined to be about 0.13. The shear friction factor is equivalent to the friction parameter, α^{l}, when the velocity factor, P, is set to zero, as was the case with the FEM modeling. *There is very good agreement between the FEM model results and the friction ring calibration curves. The friction parameter determined in this work agrees well with typical values found in the literature.*

7.4 Finite Element Forge2 Results

The simulation of upsetting during cold heading involved numerous inputs, including the stress-strain relationship during the heading operation (constitutive model parameters), a fracture criterion for the material in question, and a friction parameter. These inputs were obtained for the matrix materials with the aid of several specialized tests. The CP was employed to determine the flow stress of the matrix materials at low and high strain rates, and at two nominal temperatures. The DWT was employed to compress test specimens to failure and to determine the fracture limit of the matrix materials; finally, the FRT was utilized to determine the friction parameter (α^{l}) for input into the FEM models.

FEM modeling was performed using two extreme aspect ratios (1.0 and 1.6) for the Heat 4 materials (as-rolled and spheroidized). Plots of the hoop (σ_{θ}) and axial (σ_z) stress components versus equivalent strain were presented in Chapter 6. The hoop and axial stresses rise faster for the two materials with the lower aspect ratio, in accordance with the workability diagram. The hoop stresses of as-rolled materials rise faster than the hoop stresses of spheroidized materials for a given aspect ratio. The opposite behavior is found with the axial stresses. All eight curves rise to a maximum, decrease to a minimum, and rise again. The onset of the decrease corresponds to the point at which the material contacts the die face.

FEM simulations were performed by varying the friction parameter, α^{l}, from zero to 0.20. The results showed that the steep decrease is a function of the friction conditions at the tool/die interface. This is an important finding, since it demonstrates the critical influence of the friction conditions on the fracture behavior during cold heading. *The FEM* *simulation results displayed good agreement with the workability diagram theory: the lower the friction, the larger the strain to fracture.* Improved lubrication reduces barreling and the tensile hoop stress on the surface, thereby enabling materials to endure larger deformations before the onset of fracture. A comparable effect can be obtained by increasing the aspect ratio. However, in practice, this parameter is usually dictated by the final component geometry.

A global approach to ductile fracture was taken whereby the stress and strain fields were numerically integrated by Forge2 at each stage of the deformation process, and incorporated into the Cockcroft and Latham ductile fracture criterion. The latter was validated for differing specimen aspect ratios. The Cockcroft and Latham constant results (at fracture) for the Heat 4 as-rolled materials showed that there is only a 6% difference in the constants for the two extreme aspect ratios, even though there is a 25.0% difference in the equivalent strains to fracture. A difference of only 1% in the Cockcroft and Latham constants was found for the spheroidized materials pertaining to the two aspect ratios, while there was a 29.0% difference in the equivalent strains to fracture. These results are quite remarkable. *From the standpoint of aspect ratio, one can conclude that the Cockcroft and Latham criterion is valid for upsetting in cold heading, at least for the pocket die-set employed in this work.*

The Cockcroft and Latham constant is not a value that can be used in its raw form to compare various materials. This is evidenced by the results that showed that the Cockcroft and Latham constant for the as-rolled material is about 11% larger than the value found for the spheroidize annealed material. To say that a lower constant is better would also be incorrect. This is due to the fact that materials cannot be compared without somehow normalizing the Cockcroft and Latham constants. Cockcroft and Latham [1968] determined this constant for an unstrained aluminum alloy (3% Mg), and found it to be approximately 160 MPa, almost 60% lower than the value found for Heat 4 as-rolled. Such an alloy would certainly be more ductile than steel. However, the final mechanical properties would fall short of those required for a steel component application. *The*

Cockcroft and Latham criterion is only one portion of the material selection process. Indeed, final mechanical properties must be achieved during the cold heading operation (e.g. dual phase steels), or by subsequent heat treatment.

Normalization of the Cockcroft and Latham constant was proposed in the Chapter 6, where the constant for a given material is divided by a measure of its yield strength for comparison purposes. In fact, Cockcroft and Latham [1968] demonstrated that the constant did not change when a material was tensile tested with various levels of pre-strain, even though the yield strengths were vastly different. This indicates that the yield strength does not have an influence on fracture.

The normalized Cockcroft and Latham constant for the spheroidized material yielded a normalized constant value that was 15% greater than that for the as-rolled material. The fact that this difference coincides with the difference in equivalent strain to fracture for the two materials possibly indicates that it is a good measure of upset ductility. Experimentation with vastly different materials (i.e. copper, aluminum) is needed to verify the validity of the proposed normalization method.

The load-time curves obtained from the DWT were used as a basis for comparison with the curves obtained from the FEM models. The load-time behavior of the FEM simulation corresponded well with the behavior of the experimental DWT between the start of the deformation and displacement equal to about 4.7 - 4.8 mm for both the as-rolled and spheroidize annealed materials. Following this displacement, the simulation loads rose faster than the experimental DWT loads.

The experimentally obtained DWT load-time curves were actually a measure of the load developed by the full system, i.e., the specimen, the base, and the floor supporting the DWT machine, as it resisted the impacting mass. Therefore, the FEM load-displacement curves exhibited lower peak loads and larger displacements than those experienced by the actual

DWT specimens. Thus, the FEM simulation curves were cropped at the fracture initiation displacements measured on the actual DWT specimens.

The FEM simulations predicted peak loads that were only 12 to 16% larger than those from the DWT experiments. The higher loads with the FEM simulations may be attributed to discrepancies between the experimental test conditions, i.e., strain rate and flow behavior, and the FEM simulations at higher strains ($\varepsilon > 1$). The energy differences between the DWT experimentation and the FEM simulations were calculated to be only about 3-5% for both the as-rolled and spheroidize annealed materials. This is fortunate since the Cockcroft and Latham ductile fracture criterion is in essence an energy term.

One recommendation for future work is to improve the DWT machine so that reliable flow data can be obtained during testing. Indeed, the ideal method of obtaining flow data at these higher strains and strain rates is to use the DWT machine itself. This would require a better understanding of the compliance of the full system, a technique to monitor the crosshead position during testing, and the ability to heat-up a specimen and to monitor its temperature.

Dies used for upsetting are another critical consideration. Many researchers, such as Shah and Kuhn [1986], employed a flat-die configuration not representative of industrial cold heading in terms of metal flow and die shape [Shivpuri et al., 1988A]. In actuality, for most cold heading operations, only the volume of material that is part of the upset is left unsupported in the die assembly during deformation [National Machinery Co., 1999]. This necessitates that at least one end of the component be constrained.

A fully constrained die set in the form of pocket dies was selected for the present study. Exploratory FEM work compared the strain paths for flat and pocket dies for the same material, aspect ratio, and friction conditions. It was demonstrated that the flat-die configuration is much less severe in terms of the development of hoop strain and fracture initiation by virtue of the fact that the strain path lies closer to homogeneous deformation conditions. *Since a major objective of this work was to produce failure in specimens while approximating industrial cold heading conditions, the selection of a pocket die-set configuration seems justified.*

Grid marks are used by some researchers to measure the amount of surface deformation. There is a limit on the fineness of the grid that may affect the accuracy of the results. In addition, the measurement of the final grid marks on deformed specimens is laborious, and may also be inaccurate due to the barreled surface. FEM modeling eliminates the need to apply grid marks to undeformed specimens. With FEM modeling, mesh size is the equivalent of grid marking. FEM solution accuracy improves as the number of elements is increased. However, the number of elements is limited by the computer time and memory.

The FEM model of the present upset test configuration is yet another important contribution of this investigation, in that predictions are compared with results from DWT. FEM allows the determination of the stress and strain behavior throughout the component. This can be very valuable in the selection and design of die sequences, and may assist the design engineer to reduce the number of stages required to produce a component. This allows for better use of machinery and production time. FEM modeling can also serve as an important tool for the analysis of repeating component failures during cold heading.

Through FEM modeling, it is possible to model a full heading sequence that may include a combination of extrusion and threading operations. The resulting strain accumulation is critical to the application of a ductile fracture criterion in the case where two or more deformation steps are required. Indeed, several separate 'hits' are generally preferable to a single one. When the final strain is applied in several steps, the temperature rise associated with deformation heating can be dissipated, at least in part, a phenomenon that can be modeled with FEM.

On average, 13 re-meshes were required for each DWT simulation. *The Forge2 FEM software package with its re-mesh capability proved to be an invaluable tool in this work.*

7.5 Concluding Remarks

The results support the conclusion that the combination of the DWT and the guided die-set configuration developed in this work is a significant contribution to the understanding of cold heading. The DWT approximates the upsetting portion of the cold heading process in terms of material stress state and strain rate, and is relatively easy to use on a production basis. *Coupled with FEM modeling, the DWT has the potential to become very valuable to the wire rod industry.*

Other uses for the DWT include the optimization of cold heading chemical compositions, microstructures, spheroidization levels, percent draft (draw) prior to heading, lubrication conditions, and die geometry. Finally, the behavior of casting or rolling defects during cold heading can be studied.

CHAPTER 8

CONCLUSIONS

1. Drop weight testing can be used to evaluate the formability of materials for upsetting in cold heading.

2. The drop weight test exaggerates the loads and the strain rates employed in industrial cold heading to promote fracture.

3. The drop weight test is sensitive to surface integrity, to microstructural differences between as-rolled and spheroidize annealed materials, and to the deleterious impact of nitrogen and copper levels on the fracture behavior of cold heading materials.

4. In terms of strain path and fracture initiation, pocket-dies are more representative of upsetting in cold heading than flat dies.

5. Die-set guiding raises pocket-die longevity to a practical level.

6. The Cockcroft and Latham fracture criterion has been found to be valid for evaluating materials destined for upsetting processes in cold heading.

7. Finite element method simulations revealed a large dependence of strain path on friction at the material-die interface. Thus, the low friction conditions promote large deformations to fracture at constant Cockcroft and Latham values. This is in accordance with the workability diagram, and conforms to industrial knowledge. Friction conditions at the material-die interface must therefore be properly accounted for during simulation.

8. Drop weight testing and finite element modeling act synergistically as a powerful tool for selecting materials and processes.

RECOMMENDATIONS FOR FUTURE WORK

1. All testing was performed on 5.5 mm wire rod drawn down to 5.2 mm diameter wire rod. This size represents only a small portion of the diameter range of interest to industry. Since the material ductility is independent of aspect ratio, the results are valid. However, the use of the DWT machine in its current form is limited, since it is not capable of testing large diameter wire on a production basis. The construction of a larger DWT machine for industrial use is therefore recommended.

2. Model the compliance of the DWT equipment and integrate load instrumentation to enable accurate acquisition of flow stress data at representative strains and strain rates.

3. The present investigation was performed on grade 1038 steel. This grade represents a small fraction of the grades used in industry. It is recommended that fracture constants be determined on a range of grades of industrial importance. The resulting database would be of use to engineers for designing die progressions and in the material selection process. As well, more insight would be developed regarding the effect of the material parameters of cold-headability. Such research would also lead to a greater understanding of fracture mechanisms in general.

4. Torx-head fasteners are considered to be some of the more difficult components to produce in industry. In this case, the critical stress concentration may be in the fastener head, where sharp radii exist. The test methodology developed needs to be expanded to include torx-head applications.

5. Exploratory work showed that drop weight testing is capable of causing shear bands to be produced. Shear bands may become more frequent with the advent of faster cold headers, and therefore an in-depth study of this phenomenon would be useful.

6. Pre-draw is another operation that affects the cold headability of materials. An in-depth study quantifying the effect of pre-draw would be of considerable use to the cold heading industry.

7. The normalized Cockcroft and Latham fracture criterion proposed in this work should be applied on various ferrous and non-ferrous materials to verify its validity.

STATEMENT OF ORIGINALITY AND CONTRIBUTIONS TO KNOWLEDGE

1. An instrumented drop weight test machine equipped with a guided pocket die-set configuration capable of producing fracture during the physical modeling of upsetting for cold heading applications, was designed and constructed. The test was found to be sensitive to surface quality, residual element and solute nitrogen contents, microstructure, and level of decarburization.

2. A guided die-set configuration representative of constrained upsetting was designed and commissioned. It is capable of deforming cylindrical steel specimens to fracture repeatedly without die failure.

3. A comprehensive test methodology to physically and numerically model upsetting in cold heading was defined. It includes:

    a. A drop weight machine and guided pocket die-set to determine the axial strain to fracture of cylindrical steel specimens;

    b. A cam plastometer to determine flow behavior at strain rates representative of upsetting in cold heading;

    c. A friction ring test using the drop weight machine to obtain a parameter representative of die/specimen friction;

    d. A finite element method model of the drop weight test and die-set configuration to obtain the fracture criterion constants.

4. The Cockcroft and Latham fracture criterion was validated for upsetting in cold heading using a pocket die-set configuration at extreme aspect ratios.

REFERENCE LIST

Alberti, N., A. Barcellona, L. Cannizzaro, and F. Micari (1994) *Prediction of Ductile Fractures in Metal Forming Processes: An Approach Based on Damage Mechanics*, CIRP Annals - College International de Recherches pour la Production, vol. 43, no. 1, pp. 207-211.

Altan, T., S. Oh, and H.L. Gegel (1983) Metal Forming – Fundamentals and Applications, ASM, Metals Park, Ohio, pp. 83-88.

Andersson, K., S. Kivivuori, and A.S. Korhonen (1996) *Effect of the Heat-Transfer Coefficient in Ring-Compression Tests*, Journal of Materials Processing Technology, pp. 10-13, 62.

ASTM E45 (1997) *Standard Test Methods for Determining the Inclusion Content of Steel*, American Society for Testing and Materials (ASTM), Philadelphia, Pennsylvania.

ASTM E1077 (1997) *Standard Test Methods for Estimating the Depth of Decarburization Of Steel Specimens*, American Society for Testing and Materials (ASTM), Philadelphia, Pennsylvania.

Lankford, W.T. Jr., N.L. Samways, R.F. Craven, and H.E. McGannon [editors] (1985) The Making, Shaping and Treating of Steel, Association of Iron and Steel Engineers, 10th Edition, United States Steel, Pittsburgh, Pennsylvania, p. 1317.

Atack, P.A. (1984) *Problems Involved in Determining Deformation Resistance Using the Cam Plastometer*, International Symposium on Plasticity and Resistance to Metal Deformation (4th), pp. 66-82.

Avitzur, B. (1968) Metal Forming: Processes and Analysis, McGraw Hill, New York, New York, pp. 77-153.

Bai, Y. and B. Dodd (1992) Adiabatic Shear Localization: Occurrences, Theories and Applications, Pergamon Press, New York, New York, pp. 1-74.

Baragar, D.L. (1989) *The MTL Cam Plastometer – Theory and Operation*, Report MTL 89-25(TR), Materials Technology Laboratories, CANMET.

Barrett, R. (1997) *Getting a Grip on Fasteners*, Metal Bulletin Monthly, pp. 38-43.

Bhatnagar, S.S. (1978) *Cold Heading of Steels*, Tool & Alloy Steels, vol. 12, no. 4, pp. 121-125.

Blake, A. (1986) Threaded Fasteners - Materials and Design, Marcel Dekker, New York, New York, p. 62.

Brimacombe J.K. and K. Sorimachi (1977) *Crack Formation in the Continuous Casting of Steel,* Metallurgical Transactions B, vol. 8B, pp. 489-505.

Broek, D. (1989) The Practical Use of Fracture Mechanics, Kluwer Academic Publishers, The Netherlands, pp. 22-47.

Brownrigg, A., J. Havranek, and M. Littlejohn (1981) *Cold Forgeability of Steel,* BHP Tech. Bull, vol. 25, no. 2, pp. 16-24.

Buchanan, P.J., V. Randle, and P.E.J. Flewitt (1997) *A Simple Procedure for the Assessment of Plastic Strain in Electron Back-Scatter Diffraction Patterns,* Scripta Materialia, vol. 37, no. 10, pp. 1511-1518.

Cao, B.H., J.J. Jonas, P.R. Hastings, and N. Nickoletopoulos (1998) *Effect of Boron Addition on the Dynamic Strain Aging Behavior of a Medium Carbon Steel Wire Rod,* Materials Science Forum, vol. 284-286, pp. 543-550.

Cescutti, J.P. (1986) *Les Essais Mécaniques,* Plasticité et mise en forme des métaux – Tome I, Chapter G, Centre de Mise en Forme Des Matériaux (CEMEF), Paris, France, pp. G1-G30.

Chin, B. (1997) Finite Element Analysis of the Rolling of Hot Steel Rods and its Application to Microstructural Prediction, Masters Thesis, McGill University, pp. 40-62.

Cockcroft M.G. and D.J. Latham (1968) *Ductility and the Workability of Metals,* Journal of the Institute of Metals, vol. 96, pp. 33-39.

Davis, J. [Senior Editor] (1988) *Cold Heading* ASM Metals Handbook, Volume 14: Forming and Forging, 9th edition, Metals Park, Ohio, pp. 291-297.

Dallavia, A., A. Bugini, E. Gentili, and R. Pacagnella (1977) *Stress/Strain Curves and Friction Evaluation From the Ring Test,* Metallurgia and Metal Forming, pp. 442-446.

Danckert, J. and T. Wanheim (1988) *Analysis of the Ring Test Method for the Evaluation of Frictional Stresses in Bulk Metal Forming Processes,* CIRP Annals, vol. 37, no. 1, pp. 217-220.

Dannenmann, E. and M. Blaich (1980) *Method for Determining Cold Heading Suitability,* Wire, vol. 29, pp. 84-89.

Darvas, Z. (1984) *The Forming Limit and the Fracture Mode in Cold Upsetting*, Material Science and Engineering, vol. 70, pp.101-111.

Dhers, J., B. Thivard, and A. Genta (1992) *Improvement of Steel Wire for Cold Heading*, Wire Journal International, vol. 25, no. 10, pp.73-77.

Dieter, G.E. (1984A) *Overview of Workability*, Workability Testing Techniques, American Society for Metals (ASM), Metals Park, Ohio, pp. 1-19.

Dieter, G.E. (1984B) *Tension Testing*, Workability Testing Techniques, American Society for Metals (ASM), Metals Park, Ohio, pp. 20-35.

Dieter, G.E. (1997) *Bulk Workability Testing*, ASM Handbook, Volume 8, Mechanical Testing, Metals Park, Ohio, pp. 571-597.

Dieter, G.E Jr. (1961A) Mechanical Metallurgy, McGraw-Hill, New York, New York, pp. 237-272.

Dieter, G.E Jr. (1961B) Mechanical Metallurgy, McGraw-Hill, New York, New York, pp. 55-57.

Dove, A.B. (1989A) Ferrous Wire – Volume 1: The Manufacture of Ferrous Wire, The Wire Association International, Guilford, Connecticut, pp. 45-61.

Dove, A.B. (1989B) Ferrous Wire – Volume 2: The Manufacture of Ferrous Wire Products, The Wire Association International, Guilford, Connecticut, pp. 415-441.

Dudder, G.B. (1985) *Drop Tower Compression Test*, Mechanical Testing, ASM Handbook, 9th Edition, vol. 8, Metals Park, Ohio, pp. 196-198.

El-Magd, E., H. Scholles, and H. Weisshaupt (1997) *Dynamic Ductility of Metals*, Journal de Physique – Colloques, vol. 7, no. 3, pp. 349-354.

Ellingson, J.L. (1999) Experimental Research and Computational Modeling of Deformation Processing, Ph.D. Thesis, University of Minnesota.

Ettouney, O. and D.E. Hardt (1983) *A Method for In-Process Failure Prediction in Cold Upset Forging*, J. Eng. Ind. (Trans. ASME), vol. 105, no. 3, pp. 161-167.

Follansbee, P.S. (1989) *High Strain Rate Compression Testing*, ASM Metals Handbook, Volume 8: Mechanical Testing, 9th edition, Metals Park, Ohio, pp. 190-207.

Forge2 (1998) *Forge2 User's Manual*, CEMEF - Ecole de Mines de Paris, Version 2.8.

Frater, J.L. and G.J. Petrus (1990) *Combining Finite Element Methods and the Cockcroft and Latham Criterion to Predict Free Surface Workability of Cold Forgings*, Transactions of NAMRI/SME, pp. 97-102.

Fylstra D., L. Lasdon, J. Watson, and A. Waren (1998) *Design and Use of the Microsoft Excel Solver*, Interfaces, vol. 28, no. 5, pp. 29-55.

Gilormini, P. and F. Montheillet (1985) *Discussion of Macroscopic Fracture Criteria. In Search of a Macroscopic Initiation Criterion*, Matériaux et Techniques (Paris), vol. 73, no. 8-9, pp. E73-E76.

Goetz, R.L, V.K. Jain, J.T. Morgan, and M.W. Wierschke (1991) *Effects of Material and Processing Conditions Upon Ring Calibration Curves*, Wear, vol. 143, no. 1, pp. 71-86.

Guthrie, M. (1981) *An Analysis of the Effect on Cold Headers and Cold Headed Products of Using Annealed Versus Non-Annealed Boron-Treated Steel*, Wire Association International 51st Annual Conference, Atlanta, GA, pp.195-207.

Hartley, K.A., J. Duffy, and R.H. Hawley (1986) *Measurement of the Temperature Profile During Shear Band Formation in Steels Deforming at High Strain Rates*, Army Research Office, no. DAAG 29-85-K-0003/2, Brown University.

Hawkyard, J.B. and W. Johnson (1967) *An Analysis of the Changes in Geometry of a Short Hollow Cylinder During Axial Compression*, International Journal of Mechanical Science, vol. 9, pp.163-182.

Hertzberg, R.W. (1996) Deformation and Fracture Mechanics of Engineering Materials, 4th Edition, John Wiley & Sons, New York, New York, pp. 22-28.

Hosford, W.F. and R.M. Caddell (1983A) Metal Forming - Mechanics and Metallurgy, Prentice Hall, Englewood Cliffs, New Jersey, pp. 246-247.

Hosford, W.F. and R.M. Caddell (1983B) Metal Forming - Mechanics and Metallurgy, Prentice Hall, Englewood Cliffs, New Jersey, pp. 32-34.

IFI-140 (1993) *Carbon and Alloy Steel Wire, Rods and Bars for Mechanical Fasteners*, Industrial Fasteners Institute (IFI), Cleveland, Ohio, pp. 1-23.

Jenner, A. and B. Dodd (1981) *Cold Upsetting and Free Surface Ductility*, Journal of Mechanical Working Technology, vol. 5, pp. 31-43.

Joffret, N. and J. Perrier (1996) *Frappe à Froid de L'Acier*, Techniques de L'Ingénieur, traité Métallurgie, Imprimerie Strasbourgeoise, Paris, France, M 628, 12 pp.

Jonas, J.J. (1997) Private Communication, McGill University.

Kalpakjian, S. (1984A) Manufacturing Processes for Engineering Materials, Addison-Wesley Publishing Company, Reading, Massachusetts, pp. 200-205.

Kalpakjian, S. (1984B) Manufacturing Processes for Engineering Materials, Addison-Wesley Publishing Company, Reading, Massachusetts, pp. 27-50.

Kobayashi, S., S. Oh, and T. Altan (1989) Metal Forming and the Finite Element Method, Oxford University Press, New York, New York, pp. 151-172.

Kudo, H., K. Sato, and K. Aoi (1968) *On Cold Forgeability Test*, CIRP Annals, vol. 16, pp. 309-318.

Kuhn, H.A. (1978) Workability Testing and Analysis for Bulk Forming Processes, Formability Topics – Metallic Materials, ASTM STP 647, pp. 206-219.

Kurko, M. and N. Nickoletopoulos (1998) Ring Screw Works Co./Ivaco Rolling Mills, Private Communication.

Latham, D.J., M.G. Cockcroft, and E.S. Tweedie (1968A) *An Assessment of the Compression Test for Determining Mechanical Properties*, Metal Forming, pp. 196-200.

Latham, D.J., M.G. Cockcroft, and E.S. Tweedie (1968B) *An Assessment of the Compression Test for Determining Mechanical Properties*, Metal Forming, pp. 221-225.

Lee, P.W. and H.A. Kuhn (1973) *Fracture in Cold Upset Forging - A Criterion and Model*, Metallurgical Transactions, vol. 4, pp. 969-973.

Lee, P.W. and H.A. Kuhn (1984) *Cold Upset Testing*, Workability Testing Techniques, American Society for Metals (ASM), Metals Park, Ohio, Chapter 3, pp. 37-50.

Le Floc'h, A. (1986) *Simulation*, Plasticité et Mise en Forme des Métaux – Tome I, Chapter I, Centre de Mise en Forme Des Matériaux (CEMEF), Paris, France, pp. I1-I32.

Levaillant, C. (1986) *Ductilité*, Plasticité et mise en forme des métaux – Tome I, Chapter H, Centre de Mise en Forme Des Matériaux (CEMEF), Paris, France, pp. H1-H25.

Maheshwari, M.D., B. Dutta, and T. Mukherjee (1978) *Quality Requirements for Cold Heading Grades of Steel*, Tool & Alloy Steels, pp. 247-251.

Male A.T. and V. DePierre (1970) *The Validity of Mathematical Solutions for Determining Friction from the Ring Compression Test*, Transactions of the ASME – Journal of Lubrication Technology, pp. 389-397.

Matsunaga, T. and K. Shiwaku (1980) *Manufacturing of Cold Heading Quality Wire Rods and Wires*, SEAISI Quarterly Journal, vol. 9, no. 1, pp. 45-55.

Meyer, L.W., A. Weise, and F. Hahn (1997) *Comparison of Constitutive Flow Curve Relations in Cold and Hot Forming*, Journal de Physique –Colloques, vol. 7, no. 3, p.13-21.

Meyers, M.A. (1994) Dynamic Behavior of Materials, John Wiley & Sons, New York, New York, pp. 448-488.

Meyers, M.A. and K.K. Chawla (1999) Mechanical Behavior of Materials, Prentice Hall, Englewood Cliffs, New Jersey, pp.116-121.
Muzak, N., K. Naidu, and C. Osborne (1996) *New Methods for Assessing Cold Heading Quality*, Wire Journal International, vol. 29, no. 10, pp. 66-72.

Narayanasamy, R. and K.S. Pandey (1997) *Phenomenon of Barreling in Aluminium Solid Cylinders During Cold Upset-Forming*, Journal of Materials Processing Technology, vol. 70, no. 1-3, pp. 17-21.

National Machinery Co. (1997) Private Communication, (report: *Parts From Wire*).

National Machinery Co. (1999) seminar: *Cold Forming Principles*, Tiffin, Ohio.

Naumann, F.K. (1983) Failure Analysis – Case Histories and Methodology, Dr. Riederer-Verlag GmbH and American Society for Metals, Metals Park, Ohio, pp. 479-481.

Nguyen L. D. (1984) *Finite Element Modeling of Upsetting Test*, Forsch. Ing., vol. 50, pp. 55-62.

Nickoletopoulos N., R.B. Rogge, J.A. Nemes, and M. Hone (2000) *Determination of Residual Stresses in a Steel Fastener by Neutron Diffraction*, Wire Journal International, pp. 220-226.

Nickoletopoulos, N., Y. Verreman, M. Hone, J.A. Nemes, J.J. Jonas, S. Yue, and P. Wanjara (2000) *Development of a Fracture Criterion For Cold Heading*, Wire Association International, 70th Annual Conference Proceedings, pp. 65-74.

Ohmori, A., A. Matsuzaki, and K. Amano (1997) *Effect of Cu, Sn and Sb on Cold Forgeability of a 0.5% Carbon Steel*, ISIJ International, vol. 37, no. 3, pp. 302-304.

Okamoto, T., T. Fukuda, and H. Hagita (1973) *Material Fracture in Cold Forging - Systematic Classification of Working Methods and Types of Cracking in Cold Forging*, The Sumitomo Search, no. 9, pp. 216-227.

Ollilainen, V. (1995) *Assessment of the Cold Formability of Ferritic Steels Using Parameters Determined in Uniaxial Tensile Testing*, Journal of Material Engineering and Performance, vol. 4, no. 6, pp. 745-755.

Olsson, K., S. Karlsson, and A. Melander (1986) *The Influence of Notches, Testing Geometry, Friction Conditions, and Microstructure on the Cold Forgeability of Low Carbon Steels*, Scandinavian Journal of Metallurgy, vol. 15, no. 5, pp. 238-256.

Osakada, K. (1989) *Analysis of Cold Forging Operations*, Plasticity and Metal-Forming Operations, Elsevier Applied Science, New York, New York, pp. 241-262.

Oyane, M. (1972) *Criteria of Ductile Fracture Strain*, Bull. Japan Soc. Mech. Eng., 15, (90), pp. 1507-1513.

Oyane M., T. Sato, and K. Okimoto (1980) *Criteria for Ductile Fracture and Their Applications*, Journal of Mechanical Working Technology, pp. 65-81.

Roessig, K.M. and J.J. Mason (1999A) *Adiabatic Shear Localization in the Dynamic Punch Test, Part I: Experimental Investigation*, International Journal of Plasticity, 15, pp. 241-262.

Roessig, K.M. and J.J. Mason (1999B) *Adiabatic Shear Localization in the Dynamic Punch Test, Part II: Experimental Investigation*, International Journal of Plasticity, 15, pp. 263-283.

Rogers, H.C. (1983) *Adiabatic Shearing - General Nature and Material Aspects*, Material Behaviour Under High Stress and Ultrahigh Loading Rates, Plenum Press, New York, New York, pp. 101-118.

Rogge, R.B., R.W.L. Fong, and N. Nickoletopoulos (2000) *Use of Neutron Diffraction to Evaluate the Thermal-Mechanical Processing of Industrial Components*, submitted for Conference of Processing and Manufacturing of Advanced Materials (THERMEC 2000).

Rowe, G.W., C.E.N. Sturgess, P. Hartley, and L. Pillinger (1991) Finite-Element Plasticity and Metalforming Analysis, Cambridge University Press, Cambridge, Massachusetts, p. 17.

Sahi, M., R. Rahouadj, R. Herbach, and D. Choulier (1996) *The Influence of Viscoplasticity in the Interpretation of the Ring Test*, Journal of Materials Processing Technology, vol. 58, no. 2-3, pp. 286-292.

Samuels, L.E. (1980) Optical Microscopy of Carbon Steels, American Society for Metals, Metals Park, Ohio, pp. 225-243.

Samuels, L.E. (1988) Metals Engineering – A Technical Guide, ASM International, Metals Park, Ohio, pp. 422-427.

Sarruf, Y., B. Cao, J.J. Jonas, and N. Nickoletopoulos (1998) *Criteria and Tests for Cold Headability*, Wire Association International, Conference Proceedings, 68th Annual Convention, pp. 141-148.

Sarruf, Y. (2000) Criteria and Tests for Cold Headability, Masters Thesis, McGill University.

Semiatin, S.L., G.D. Lahoti, and S.I. Oh (1983) *The Occurrence of Shear Bands in Metalworking*, Material Behaviour Under High Stress and Ultrahigh Loading Rates, Plenum Press, New York, New York, pp. 119-159.

Semiatin, S.L. and J.J. Jonas (1984) Formability and Workability of Metals – Plastic Instability & Flow Localization, American Society for Metals (ASM), Metals Park, Ohio, pp. 43-119.

Shabara, M.A., A.A. El-Domiaty, and A. Kandil (1996) *Validity Assessment of Ductile Fracture Criteria in Cold Forming*, Journal of Materials Engineering and Performance, vol. 5, no. 4, pp. 478-488.

Shabaik, A.H., M. Abdel-Rahman, F.F.A. Elaziz, and M.A. Chaban (1993) *Effect of the Pre-Gained Volume Strain Ratio on the Strain-Path Configuration of AISI 1045 Steel in Upsetting*, Journal of Materials Processing Technology, vol. 37, no. 1-4, pp. 337-347.

Shah, D.C. (1974) *The Flow and Fracture of Steel in Cold Upsetting*, Conf., Mechanical Working and Steel Processing XII, Illinois, The Metallurgical Society / A.I.M.E., pp. 285-300.

Shah, J.J. and H.A. Kuhn (1986) *An Empirical Formula for Workability Limits in Cold Upsetting and Bolt Heading*, Journal of Applied Metalworking, vol. 4, no. 3, pp. 255-261.

Shivpuri, R., A. Tietmann, E. Kropp, and B. Lilly (1988A) *Investigation of a New Upset Test to Study the Formability of Steels for Cold Forging*, NAMRAC Conference, XVI, Illinois.

Shivpuri, R., E. Kropp, and B. Lilly (1988B) *Formability Testing of Steels for Cold Forming*, Near Net Shape Manufacturing Conference, Ohio, ASM International, pp. 169-177.

Sowerby, R., I. O'Reilly, N. Chandrasekaran, and N.L. Dung (1984) *Material Testing for Cold Forging*, Journal of Engineering Materials and Technology, vol. 106, pp. 101-106.

Sugondo, J.A. Szpunar, and P. Gangli (1991) *Development of Texture in Low-Carbon Steels for Cold Heading*, Journal of Materials Processing Technology, vol. 26, no. 3, pp. 305-321.

Taheri, A.K., T.M. Maccagno, and J.J. Jonas (1995A) *Effect of Cooling Rate After Hot Rolling and of Multistage Strain Aging on the Drawability of Low-Carbon-Steel Wire Rod*, Metallurgical and Materials Transactions A, vol. 26A, pp. 1183-1193.

Taheri, A.K., T.M. Maccagno, and J.J. Jonas (1995B) *Effect of Quench Aging on Drawability in Low Carbon Steels*, Material Science and Technology, vol. 11, pp. 1139-1146.

Takuda, H., K. Mori, H. Fujimoto, and N. Hatta (1997) *Fracture Prediction in Stretch Forming Using Finite Element Simulation Combined with a Ductile Fracture Criterion*, Archives of Applied Mechanics - Ingénieur Archive, vol. 67, no. 3, pp. 143-150.

Tan, X., P.A.F. Martins, N. Bay, and W. Zhang (1998) *Friction Studies at Different Normal Pressures with Alternative Ring-Compression Tests*, Journal of Materials Processing Technology, vol. 80-81, pp. 292-297.

Thibau, R., A. Trudel, D. Baragar, and P.R. Hastings (1999) *Development of a Test to Evaluate the Formability of CHQ Wire*, Wire Association International 69th Annual Conference Proceedings, pp. 232-241.

Thirukkonda, M., R. Srinivasan, and L. Weiss (1994) *Instability and Flow Localization During Compression of a Flow Softening Material*, Journal of Materials Engineering and Performance, vol. 3, no. 4, pp. 514-527.

Thomason, P.F. (1990A) Ductile Fracture of Metals, Pergamon Press, New York, New York, pp. 152-175.

Thomason, P.F. (1990B) Ductile Fracture of Metals, Pergamon Press, New York, New York, pp. 30-39.

Thomason, P.F. (1990C) Ductile Fracture of Metals, Pergamon Press, New York, New York, pp. 130-131.

Tozawa, Y., T. Kato, and N. Kato (1981) *Effect of Upsetting Speed on the Upsetting Limit*, CIRP Annals, vol. 30, pp. 203-207.

Turner, A.F., C.S. Betteridge, and J. Avery (1984) report: *Development of Steels for the Fastener and Cold Forging Markets by Testing Under Fastener Production Conditions*, Commission of the European Communities - British Steel Corporation.

Upsetting (no year) National Machinery Co. Literature Item 215-C.

Verreman, Y. (1996) *Simulation of Metal Forming Using Forge2*, Proceedings of the International Symposium on Hot Workability of Steels and Light Alloys-Composites, Montreal, Canada, pp. 358-366.

Verreman, Y. (1998) Class Notes, 1998.

Verreman, Y., N. Nickoletopoulos, and M. Hone (2000) *Prediction of Fracture in Cold Headed Steel Fasteners by Numerical Simulation*, 39th Annual Conference of Metallurgists, Conference Proceedings: Symposium on Mathematical Modeling in Metal Processing and Manufacturing, Paper 2, Ottawa, Canada.

Wagoner H.W. and J.L. Chenot (1996) Fundamentals of Metal Forming, John Wiley & Sons, New York, New York, pp. 1-38.

Wifi, A.S., A. Abdel-Hamid, and N. El-Abbasi (1998) *Computer-Aided Evaluation of Workability in Bulk Forming Processes*, Journal of Materials Processing Technology, vol. 77, no. 1-3, pp. 285-293.

Woodall, S.M and J.A. Schey (1974) *Determination of Ductility for Bulk Deformation*, Formability Topics - Metallic Materials, ASTM STP 647, pp. 20.

Wright, R.N., T.A. Kircher, and J.R. Vervlied (1987) *Modeling Bulk Workability Under Complex Conditions*, Journal of Metals, vol. 39, no. 10, pp. 26-29.

Yalamanchili, B., P.M. Power, and J.B. Nelson Jr. (1999) *Effect of Residual Elements on Low Carbon Rod Quality and Implications to the End User*, Wire Journal International, vol. 32, no. 5, pp. 100-106.

Yoo, S.J., D.L. Lee, and D.T. Chung (1997) *Prediction of Cold Heading Quality with High Strain Rate Compression Tester*, Wire Journal International, vol. 30, no. 9, pp. 84-89.

APPENDIX A

DROP WEIGHT TEST DATA

The following represent selected data obtained from drop weight testing.

Heat Number	Heat Treatment	H_0 net (mm)	D_0 (mm)	Aspect Ratio	Mass (kg)	Drop Height (m)	H net (mm)	Axial Strain $\ln(H/H_0)$	D (mm)	Circumferential Strain $\ln(D/D_0)$	Surface Defect (Yes or No)
1	as rolled	6.63	5.21	1.27	11.777	1.143	3.83	0.549	6.91	0.282	N
1	as rolled	6.53	5.21	1.25	11.777	1.270	3.60	0.595	7.09	0.308	N
1	as rolled	6.56	5.21	1.26	11.777	1.397	3.52	0.623	7.19	0.322	N
1	as rolled	6.61	5.21	1.27	11.777	1.499	3.37	0.674	7.32	0.340	Y
1	as rolled	6.63	5.21	1.27	12.332	1.499	3.12	0.754	7.65	0.384	Y
1	as rolled	6.55	5.21	1.26	12.942	1.499	2.91	0.811	7.83	0.407	Y
1	as rolled	6.61	5.21	1.27	13.497	1.499	2.81	0.855	8.04	0.434	Y
1	spheroidized	6.62	5.21	1.27	11.777	1.270	3.17	0.736	7.72	0.393	N
1	spheroidized	6.63	5.21	1.27	11.777	1.397	2.98	0.800	7.94	0.421	Y
1	spheroidized	6.66	5.21	1.28	11.777	1.499	2.81	0.863	8.15	0.447	Y
1	spheroidized	6.61	5.21	1.27	12.332	1.499	2.72	0.888	8.33	0.469	Y
1	spheroidized	6.61	5.21	1.27	12.942	1.499	2.56	0.949	8.55	0.495	Y
1	spheroidized	6.63	5.21	1.27	13.497	1.499	2.45	0.996	8.78	0.522	Y

Table A1: Selected DWT results for Heat 1 as-rolled and spheroidized.

Heat Number	Heat Treatment	H_o net (mm)	D_o (mm)	Aspect Ratio	Mass (kg)	Drop Height (m)	H net (mm)	Axial Strain $\ln(H/H_o)$	D (mm)	Circumferential Strain $\ln(D/D_o)$	Surface Defect (Yes or No)
2	as rolled	6.65	5.21	1.28	11.777	1.499	3.23	0.722	7.64	0.383	N
2	as rolled	6.61	5.21	1.27	12.332	1.499	3.08	0.764	7.84	0.409	N
2	as rolled	6.56	5.21	1.26	12.942	1.499	2.89	0.820	8.03	0.433	Y
2	as rolled	6.55	5.21	1.26	13.212	1.499	2.83	0.839	8.06	0.436	Y
2	as rolled	6.62	5.21	1.27	13.497	1.499	2.79	0.864	8.22	0.456	Y
2	as rolled	6.54	5.21	1.26	14.107	1.499	2.65	0.903	8.35	0.472	Y
2	spheroidized	6.59	5.21	1.26	11.777	1.499	2.63	0.919	8.31	0.467	N
2	spheroidized	6.63	5.21	1.27	12.332	1.499	2.56	0.952	8.45	0.484	N
2	spheroidized	6.61	5.21	1.27	12.942	1.499	2.37	1.026	8.76	0.520	N
2	spheroidized	6.60	5.21	1.27	13.497	1.499	2.33	1.041	8.83	0.528	Y
2	spheroidized	6.61	5.21	1.27	14.107	1.499	2.25	1.078	9.04	0.551	Y
2	spheroidized	6.62	5.21	1.27	14.662	1.499	2.11	1.143	9.18	0.566	Y
2	spheroidized	6.57	5.21	1.26	15.272	1.499	2.04	1.170	9.34	0.584	Y

Table A2: Selected DWT results for Heat 2 as-rolled and spheroidized.

Heat Number	Heat Treatment	H_o net (mm)	D_o (mm)	Aspect Ratio	Mass (kg)	Drop Height (m)	H net (mm)	Axial Strain $\ln(H/H_o)$	D (mm)	Circumferential Strain $\ln(D/D_o)$	Surface Defect (Yes or No)
3	as rolled	6.63	5.21	1.27	11.777	0.914	5.09	0.264	6.12	0.161	Y
3	as rolled	6.61	5.21	1.27	11.777	1.397	4.37	0.414	6.63	0.241	Y
3	as rolled	6.59	5.21	1.26	11.777	1.346	4.40	0.404	6.56	0.230	Y
3	as rolled	6.57	5.21	1.26	14.107	1.346	3.86	0.532	7.04	0.301	Y
3	as rolled	6.55	5.21	1.26	16.437	1.346	3.38	0.662	7.38	0.348	Y
3	as rolled	6.59	5.21	1.26	18.767	1.346	3.01	0.784	8.02	0.431	Y
3	as rolled	6.56	5.21	1.26	21.097	1.346	2.57	0.937	8.44	0.482	Y
3	as rolled	6.60	5.21	1.27	26.245	1.346	2.12	1.136	*na	*na	Y
3	spheroidized	6.62	5.21	1.27	11.777	0.914	3.75	0.568	7.10	0.310	Y
3	spheroidized	6.57	5.21	1.26	11.777	1.397	2.96	0.797	8.01	0.430	Y
3	spheroidized	6.63	5.21	1.27	11.777	1.346	3.15	0.744	7.76	0.398	Y
3	spheroidized	6.57	5.21	1.26	14.107	1.346	2.42	0.999	8.78	0.522	Y
3	spheroidized	6.71	5.21	1.29	16.437	1.346	2.18	1.124	9.18	0.566	Y
3	spheroidized	6.51	5.21	1.25	18.767	1.346	1.81	1.280	9.92	0.644	Y
3	spheroidized	6.61	5.21	1.27	21.097	1.346	1.66	1.382	10.33	0.684	Y
3	spheroidized	6.75	5.21	1.30	26.245	1.346	1.43	1.552	11.22	0.767	Y

* specimen distorted due to large cracks

Table A3: Selected DWT results for Heat 3 as-rolled and spheroidized.

Heat Number	Heat Treatment	H_o net (mm)	D_o (mm)	Aspect Ratio	Mass (kg)	Drop Height (m)	H net (mm)	Axial Strain $\ln(H/H_o)$	D (mm)	Circumferential Strain $\ln(D/D_o)$	Surface Defect (Yes or No)
4	as rolled	5.20	5.21	1.00	12.332	1.499	2.17	0.874	8.11	0.443	N
4	as rolled	5.24	5.21	1.01	12.332	1.499	2.16	0.886	8.12	0.444	N
	avg.						*2.165*	*0.880*	*8.115*	*0.443*	
	std. dev.						*0.007*	*0.009*	*0.007*	*0.001*	
4	as rolled	5.20	5.21	1.00	12.942	1.499	2.04	0.936	8.24	0.458	Y
4	as rolled	5.23	5.21	1.00	12.942	1.499	2.03	0.946	8.29	0.464	Y
4	as rolled	5.22	5.21	1.00	12.942	1.499	2.03	0.944	8.27	0.462	Y
	avg.						*2.033*	*0.942*	*8.267*	*0.462*	
	std. dev.						*0.006*	*0.006*	*0.025*	*0.003*	
4	as rolled	5.22	5.21	1.00	13.497	1.499	1.91	1.005	8.46	0.485	Y
4	as rolled	5.19	5.21	1.00	14.107	1.499	1.83	1.042	8.63	0.505	Y
4	as rolled	8.64	5.21	1.28	14.662	1.499	2.51	0.977	8.70	0.513	N
4	as rolled	8.63	5.21	1.28	15.272	1.499	2.41	1.016	8.77	0.521	Y
4	as rolled	6.64	5.21	1.27	15.827	1.499	2.29	1.065	8.97	0.543	Y
4	as rolled	6.65	5.21	1.28	16.437	1.499	2.25	1.084	9.05	0.552	Y
4	as rolled	6.64	5.21	1.27	16.992	1.499	2.19	1.109	9.12	0.560	Y
4	as rolled	6.69	5.21	1.28	18.157	1.499	2.06	1.178	9.36	0.586	Y
4	as rolled	6.68	5.21	1.28	19.322	1.499	1.88	1.268	9.62	0.613	Y
4	as rolled	6.63	5.21	1.27	19.932	1.499	1.82	1.293	9.81	0.633	Y
4	as rolled	8.34	5.21	1.60	15.827	1.499	3.19	0.961	8.62	0.504	N
4	as rolled	8.31	5.21	1.60	16.437	1.499	3.12	0.980	8.70	0.513	N
4	as rolled	8.33	5.21	1.60	16.437	1.499	3.09	0.992	8.72	0.515	N
4	as rolled	8.33	5.21	1.60	16.437	1.499	3.08	0.995	8.71	0.514	N
	avg.						*3.097*	*0.989*	*8.710*	*0.514*	
	std. dev.						*0.021*	*0.008*	*0.010*	*0.001*	
4	as rolled	8.33	5.21	1.60	16.992	1.499	2.99	1.025	8.83	0.528	Y
4	as rolled	8.36	5.21	1.60	16.992	1.499	2.95	1.042	8.89	0.534	Y
4	as rolled	8.34	5.21	1.60	16.992	1.499	2.96	1.036	8.93	0.539	Y
	avg.						*2.967*	*1.034*	*8.883*	*0.534*	
	std. dev.						*0.021*	*0.009*	*0.050*	*0.006*	
4	as rolled	8.28	5.21	1.59	18.157	1.499	2.78	1.091	9.18	0.566	Y
4	as rolled	8.36	5.21	1.60	19.322	1.499	2.59	1.172	9.46	0.596	Y
4	as rolled	8.40	5.21	1.61	19.932	1.499	2.53	1.200	9.59	0.610	Y
4	as rolled	8.33	5.21	1.60	20.487	1.499	2.45	1.224	9.69	0.621	Y

Table A4: Selected DWT results for Heat 4 as-rolled.

Heat Number	Heat Treatment	H_o net (mm)	D_o (mm)	Aspect Ratio	Mass (kg)	Drop Height (m)	H net (mm)	Axial Strain $\ln(H/H_o)$	D (mm)	Circumferential Strain $\ln(D/D_o)$	Surface Defect (Yes or No)
4	spheroidized	5.22	5.21	1.00	12.332	1.499	1.80	1.065	8.79	0.523	N
4	spheroidized	5.23	5.21	1.00	12.332	1.499	1.79	1.072	8.80	0.524	N
	avg.						*1.795*	*1.068*	*8.795*	*0.524*	
	std. dev.						*0.007*	*0.005*	*0.007*	*0.001*	
4	spheroidized	5.24	5.21	1.01	12.942	1.499	1.71	1.120	9.01	0.548	Y
4	spheroidized	5.25	5.21	1.01	12.942	1.499	1.72	1.116	8.95	0.541	Y
4	spheroidized	5.26	5.21	1.01	12.942	1.499	1.73	1.112	8.97	0.543	Y
	avg.						*1.720*	*1.116*	*8.977*	*0.544*	
	std. dev.						*0.010*	*0.004*	*0.031*	*0.003*	
4	spheroidized	5.25	5.21	1.01	13.497	1.499	1.65	1.157	9.15	0.563	Y
4	spheroidized	5.23	5.21	1.00	14.107	1.499	1.56	1.210	9.27	0.576	Y
4	spheroidized	6.65	5.21	1.28	14.107	1.499	2.15	1.129	9.17	0.565	N
4	spheroidized	6.65	5.21	1.28	14.662	1.499	2.09	1.157	9.23	0.572	N
4	spheroidized	6.63	5.21	1.27	15.272	1.499	1.99	1.203	9.45	0.595	N
4	spheroidized	6.66	5.21	1.28	15.827	1.499	1.95	1.228	9.54	0.605	Y
4	spheroidized	6.63	5.21	1.27	16.437	1.499	1.88	1.260	9.76	0.628	Y
4	spheroidized	6.62	5.21	1.27	16.992	1.499	1.84	1.280	9.84	0.636	Y
4	spheroidized	6.65	5.21	1.28	17.602	1.499	1.73	1.346	10.04	0.656	Y
4	spheroidized	8.32	5.21	1.60	14.107	1.499	3.04	1.007	8.77	0.521	N
4	spheroidized	8.34	5.21	1.60	15.272	1.499	2.73	1.117	9.28	0.577	N
4	spheroidized	8.34	5.21	1.60	16.437	1.499	2.55	1.185	9.48	0.599	N
4	spheroidized	8.33	5.21	1.60	17.602	1.499	2.37	1.257	9.86	0.638	N
4	spheroidized	8.31	5.21	1.60	17.602	1.499	2.34	1.267	9.89	0.641	N
4	spheroidized	8.33	5.21	1.60	17.602	1.499	2.37	1.257	9.85	0.637	N
	avg.						*2.360*	*1.260*	*9.867*	*0.639*	
	std. dev.						*0.017*	*0.006*	*0.021*	*0.002*	
4	spheroidized	8.35	5.21	1.60	18.157	1.499	2.28	1.298	9.95	0.647	Y
4	spheroidized	8.29	5.21	1.59	18.157	1.499	2.26	1.300	9.96	0.648	Y
4	spheroidized	8.34	5.21	1.60	18.157	1.499	2.29	1.293	9.96	0.648	Y
	avg.						*2.277*	*1.297*	*9.957*	*0.648*	
	std. dev.						*0.015*	*0.004*	*0.006*	*0.001*	
4	spheroidized	8.36	5.21	1.60	18.767	1.499	2.23	1.321	10.09	0.661	Y
4	spheroidized	8.37	5.21	1.61	19.322	1.499	2.19	1.341	10.15	0.667	Y

Table A5: Selected DWT results for Heat 4 spheroidized.

Heat Number	Heat Treatment	H_o net (mm)	D_o (mm)	Aspect Ratio	Mass (kg)	Drop Height (m)	H net (mm)	Axial Strain $\ln(H/H_o)$	D (mm)	Circumferential Strain $\ln(D/D_o)$	Surface Defect (Yes or No)
5	as rolled	5.18	5.21	0.99	12.942	1.499	1.98	0.962	8.29	0.464	N
5	as rolled	5.23	5.21	1.00	13.497	1.499	1.89	1.018	8.56	0.497	N
5	as rolled	5.22	5.21	1.00	13.497	1.499	1.88	1.021	8.59	0.500	N
	avg.						*1.885*	*1.020*	*8.575*	*0.498*	
	std. dev.						*0.007*	*0.002*	*0.021*	*0.002*	
5	as rolled	5.24	5.21	1.01	13.767	1.499	1.84	1.047	8.63	0.505	Y
5	as rolled	5.20	5.21	1.00	13.767	1.499	1.85	1.033	8.64	0.506	Y
5	as rolled	5.25	5.21	1.01	13.767	1.499	1.84	1.048	8.64	0.506	Y
	avg.						*1.843*	*1.043*	*8.637*	*0.505*	
	std. dev.						*0.006*	*0.008*	*0.006*	*0.001*	
5	as rolled	5.23	5.21	1.00	14.107	1.499	1.73	1.106	8.87	0.532	Y
5	as rolled	6.68	5.21	1.28	15.827	1.499	2.26	1.084	8.97	0.543	N
5	as rolled	6.64	5.21	1.27	16.437	1.499	2.12	1.142	9.24	0.573	Y
5	as rolled	6.67	5.21	1.28	16.992	1.499	2.09	1.160	9.28	0.577	Y
5	as rolled	6.65	5.21	1.28	17.602	1.499	2.05	1.177	9.38	0.588	Y
5	as rolled	6.64	5.21	1.27	18.157	1.499	1.98	1.210	9.54	0.605	Y
5	as rolled	6.66	5.21	1.28	18.767	1.499	1.94	1.233	9.61	0.612	Y
5	as rolled	8.34	5.21	1.60	15.827	1.499	3.21	0.955	8.52	0.492	N
5	as rolled	8.33	5.21	1.60	16.437	1.499	2.95	1.038	8.90	0.535	N
5	as rolled	8.36	5.21	1.60	16.992	1.499	2.89	1.062	9.05	0.552	N
5	as rolled	8.33	5.21	1.60	17.602	1.499	2.82	1.083	9.17	0.565	N
5	as rolled	8.34	5.21	1.60	18.157	1.499	2.69	1.132	9.32	0.582	N
5	as rolled	8.31	5.21	1.60	18.157	1.499	2.63	1.150	9.33	0.583	N
5	as rolled	8.33	5.21	1.60	18.157	1.499	2.66	1.142	9.34	0.584	N
	avg.						*2.660*	*1.141*	*9.330*	*0.583*	
	std. dev.						*0.030*	*0.009*	*0.010*	*0.001*	
5	as rolled	8.30	5.21	1.59	18.767	1.499	2.56	1.176	9.49	0.600	Y
5	as rolled	8.33	5.21	1.60	18.767	1.499	2.55	1.184	9.52	0.603	Y
5	as rolled	8.34	5.21	1.60	18.767	1.499	2.56	1.181	9.51	0.602	Y
	avg.						*2.557*	*1.180*	*9.507*	*0.601*	
	std. dev.						*0.006*	*0.004*	*0.015*	*0.002*	
5	as rolled	8.37	5.21	1.61	19.322	1.499	2.42	1.241	9.73	0.625	Y

Table A6: Selected DWT results for Heat 5 as-rolled.

Heat Number	Heat Treatment	H_o net (mm)	D_o (mm)	Aspect Ratio	Mass (kg)	Drop Height (m)	H net (mm)	Axial Strain $\ln(H/H_o)$	D (mm)	Circumferential Strain $\ln(D/D_o)$	Surface Defect (Yes or No)
5	spheroidized	5.22	5.21	1.00	12.332	1.499	1.79	1.070	8.89	0.534	N
5	spheroidized	5.17	5.21	0.99	12.942	1.499	1.71	1.106	8.99	0.546	N
5	spheroidized	5.21	5.21	1.00	12.942	1.499	1.72	1.108	9.04	0.551	N
	avg.						*1.715*	*1.107*	*9.015*	*0.548*	
	std. dev.						*0.007*	*0.001*	*0.035*	*0.004*	
5	spheroidized	5.23	5.21	1.00	13.497	1.499	1.68	1.136	9.09	0.557	Y
5	spheroidized	5.18	5.21	0.99	13.497	1.499	1.67	1.132	9.16	0.564	Y
5	spheroidized	5.23	5.21	1.00	13.497	1.499	1.67	1.142	9.18	0.566	Y
	avg.						*1.673*	*1.136*	*9.143*	*0.562*	
	std. dev.						*0.006*	*0.005*	*0.047*	*0.005*	
5	spheroidized	5.18	5.21	0.99	14.107	1.499	1.53	1.220	9.45	0.595	Y
5	spheroidized	6.66	5.21	1.28	15.272	1.499	2.05	1.178	9.41	0.591	N
5	spheroidized	6.63	5.21	1.27	15.827	1.499	1.92	1.239	9.65	0.616	N
5	spheroidized	6.67	5.21	1.28	16.437	1.499	1.86	1.277	9.80	0.632	N
5	spheroidized	6.68	5.21	1.28	16.992	1.499	1.79	1.317	9.98	0.650	Y
5	spheroidized	6.65	5.21	1.28	17.602	1.499	1.76	1.329	10.04	0.656	Y
5	spheroidized	6.69	5.21	1.28	18.157	1.499	1.70	1.370	10.19	0.671	Y
5	spheroidized	6.68	5.21	1.28	18.767	1.499	1.66	1.392	10.32	0.684	Y
5	spheroidized	8.22	5.21	1.58	15.272	1.499	2.67	1.124	9.27	0.576	N
5	spheroidized	8.34	5.21	1.60	15.827	1.499	2.59	1.169	9.46	0.596	N
5	spheroidized	8.30	5.21	1.59	16.437	1.499	2.49	1.204	9.59	0.610	N
5	spheroidized	8.33	5.21	1.60	16.992	1.499	2.41	1.240	9.81	0.633	N
5	spheroidized	8.30	5.21	1.59	17.602	1.499	2.36	1.258	9.90	0.642	N
5	spheroidized	8.38	5.21	1.61	18.157	1.499	2.27	1.306	10.03	0.655	N
5	spheroidized	8.31	5.21	1.60	18.157	1.499	2.24	1.311	10.08	0.660	N
5	spheroidized	8.31	5.21	1.60	18.157	1.499	2.26	1.302	10.06	0.658	N
	avg.						*2.257*	*1.306*	*10.057*	*0.658*	
	std. dev.						*0.015*	*0.004*	*0.025*	*0.003*	
5	spheroidized	8.28	5.21	1.59	18.767	1.499	2.18	1.335	10.20	0.672	Y
5	spheroidized	8.34	5.21	1.60	18.767	1.499	2.18	1.342	10.23	0.675	Y
5	spheroidized	8.30	5.21	1.59	18.767	1.499	2.17	1.342	10.22	0.674	Y
	avg.						*2.177*	*1.339*	*10.217*	*0.673*	
	std. dev.						*0.006*	*0.004*	*0.015*	*0.001*	

Table A7: Selected DWT results for Heat 5 spheroidized.

Heat Number	Heat Treatment	H_o net (mm)	D_o (mm)	Aspect Ratio	Mass (kg)	Drop Height (m)	H net (mm)	Axial Strain $\ln(H/H_o)$	D (mm)	Circumferential Strain $\ln(D/D_o)$	Surface Defect (Yes or No)
6	as rolled	6.64	5.21	1.27	11.777	0.826	3.92	0.527	6.87	0.277	N
6	as rolled	6.61	5.21	1.27	11.777	0.902	3.83	0.546	6.98	0.292	Y
6	as rolled	6.68	5.21	1.28	11.777	1.003	3.70	0.591	7.13	0.314	Y
6	as rolled	6.65	5.21	1.28	11.777	1.143	3.48	0.648	7.34	0.343	Y
6	as rolled	6.61	5.21	1.27	11.777	1.270	3.18	0.732	7.58	0.375	Y
6	as rolled	6.64	5.21	1.27	11.777	1.499	2.86	0.842	8.04	0.434	Y
6	as rolled	6.58	5.21	1.26	14.107	1.499	2.33	1.038	8.80	0.524	Y
6	as rolled	6.60	5.21	1.27	16.437	1.499	2.02	1.184	9.41	0.591	Y
6	as rolled	6.61	5.21	1.27	18.767	1.499	1.84	1.279	9.86	0.638	Y
7	as rolled	6.64	5.21	1.27	11.777	1.499	2.98	0.801	7.88	0.414	N
7	as rolled	6.65	5.21	1.28	12.332	1.499	2.83	0.854	8.07	0.438	N
7	as rolled	6.66	5.21	1.28	12.942	1.499	2.71	0.899	8.33	0.469	N
7	as rolled	6.64	5.21	1.27	14.107	1.499	2.51	0.973	8.56	0.497	N
7	as rolled	6.65	5.21	1.28	15.272	1.499	2.33	1.049	8.80	0.524	N
7	as rolled	6.62	5.21	1.27	15.827	1.499	2.24	1.084	8.89	0.534	Y
7	as rolled	6.66	5.21	1.28	16.437	1.499	2.18	1.117	9.12	0.560	Y
7	as rolled	6.63	5.21	1.27	15.827	1.499	2.23	1.090	8.92	0.538	Y
7	as rolled	6.64	5.21	1.27	15.827	1.499	2.22	1.096	8.81	0.525	Y
7	as rolled	6.66	5.21	1.28	15.827	1.499	2.25	1.085	8.87	0.532	Y

Table A8: Selected DWT results for Heat 6 and 7 as-rolled.